



Doctoral Thesis

The Thin-Disk Laser for the 2S – 2P Measurement in Muonic Helium

Author(s):

Schuhmann, Karsten

Publication Date:

2017-09-24

Permanent Link:

<https://doi.org/10.3929/ethz-b-000208477> →

Rights / License:

[In Copyright - Non-Commercial Use Permitted](#) →

This page was generated automatically upon download from the [ETH Zurich Research Collection](#). For more information please consult the [Terms of use](#).

DISS. ETH NO. 24327

The thin-disk laser for the 2S – 2P measurement in muonic helium

A thesis submitted to attain the degree of
DOCTOR OF SCIENCES of ETH ZURICH
(Dr. sc. ETH Zurich)

presented by
Karsten Reinhard Fürchtegott Schuhmann

Dipl. Phys, Goethe Universität Frankfurt

born on
06.07.1974

citizen of
Germany

accepted on the recommendation of:

Professor Klaus Stefan Kirch

Professor Thomas Graf

2017

II The thin-disk laser for the $2S - 2P$ measurement in muonic helium

Abstract

In the project presented in this thesis, a laser system for the spectroscopy of muonic helium ions has been developed. Five 2S-2P transitions were successfully measured in 2013 and 2014 using this laser system. Eventually the alpha particle and the helion charge radii will be deduced from these measurements with accuracies of few parts per thousand. These values will be benchmarks for nuclear structure theories, and bear information contributing to the solution of the so-called proton radius puzzle.

The laser system developed is composed of a thin-disk laser operated at a wavelength of 1030 nm pumped with a high-power diode laser. The pulses of the thin-disk laser are frequency-doubled and used to pump a Ti:sapphire laser. The pulsed Ti:sapphire laser is injection-seeded by a frequency-stabilized cw Ti:sapphire laser with a wavelength tunable between 800 nm and 970 nm. The pulses of the Ti:sapphire laser are then transported and coupled into the multi-pass cavity surrounding the volume the muons are stopped at.

The most challenging building block of the laser system is the thin-disk laser. A thin-disk laser was developed based on a Q-switched oscillator followed by a multi-pass amplifier. The thin-disk laser has to deliver pulses with 100 mJ of energy, at average repetition rates of at least 200 Hz with stochastically distributed (in time) triggers having a minimal delay time between pulses down to 1.2 ms. In addition, pulse-to-pulse fluctuations smaller than a few % are required, as well as a latency time between trigger and emission of the pulse of < 500 ns, and good transverse beam mode quality of $M^2 < 1.1$ for efficient frequency doubling.

Special emphasis was devoted to the design of resonators and multi-pass amplifiers that minimizes the sensitivity to thermal lens effects. In addition, aperture effects that naturally occur in the pumped active medium have been discussed in detail in this thesis because they are usually neglected in the thin-disk laser community. Yet, they may play an important role in laser design.

The laser development that has been motivated by the muonic helium spectroscopy has also led to several additional results published in papers reproduced in the second part of this thesis.

As the first additional result, a novel multi-pass architecture is proposed that solves present energy scaling limitations of mode-locked multi-pass laser oscillators. Contrarily to the state-of-the-art layouts based on 4f-imaging, the stability region of our multi-pass resonator does not shrink with the number of passes at the active medium. Hence, our design sustains thermal lens variations that are by at least an order of magnitude larger compared to state-of-the-art multi-pass designs. This implies an order of magnitude larger output powers, and laser output pulses with mJ energy at MHz repetition rates directly from an oscillator.

As second additional result, we expose a novel limitation for the power scaling of thin-disk lasers. This limitation is related to misalignment induced by thermal lens effects. From its modeling a parameter has been obtained that can be used to design laser resonators circumventing this limitation.

IV The thin-disk laser for the 2S – 2P measurement in muonic helium

The third additional result is related to novel pump optic schemes having an increased number of passes at the thin disk as compared to standard designs while maintaining the same requirement for the pump beam quality and size of the pump optics.

Zusammenfassung

In dieser Arbeit beschreibe ich die Entwicklung eines Lasersystems für die Spektroskopie des 2S-2P-Übergangs in myonischem Helium. Mit diesem System wurden 2013 und 2014 fünf Übergänge vermessen. Aus diesen Daten lassen sich die Ladungsradien des Alpha-Teilchens und des Helions auf wenige Promille genau bestimmen. Mit diesen Werten lassen sich Kernstruktur-Theorien überprüfen und außerdem können sie dazu beitragen, das sogenannte «proton radius puzzle» zu lösen.

Das Lasersystem, das ich entwickelt habe, basiert auf der Scheibenlaser-Technologie. Das Lasersystem wird bei einer Wellenlänge von 1030 nm betrieben. Zum Pumpen werden Hochleistungsdiodenlaser verwendet. Die Pulse des Scheibenlasers werden auf eine Wellenlänge von 515 nm frequenzverdoppelt, um einen Ti:Saphir-Laser zu pumpen. Die Wellenlänge des gepulsten Ti:Saphir-Lasers ist zwischen 800 nm und 970 nm abstimmbare und wird durch Injection-Seeding mit der Ausgangsleistung eines kontinuierlich betriebenen Einfrequenz-Ti:Saphir-Lasers stabilisiert. Die Ti:Saphir-Laserpulse werden in eine Multipass-Cavity injiziert, in deren Inneren die Myonen gestoppt werden und myonisches Helium entsteht, welches dann spektroskopisch vermessen wird.

Der anspruchsvollste Teil des Lasersystems ist der Scheibenlaser. Das realisierte System besteht aus einem gütegeschalteten Oszillator, dem ein Multipass-Verstärker folgt. Der Scheibenlaser muss eine Pulsenergie von 100 mJ bei einer Repetitionsrate von mindestens 200 Hz liefern. Der Laser läuft aber nicht bei einer festen Frequenz, sondern wird stochastisch getriggert. Bei einem minimalen Puls-zu-Puls-Abstand von 1.2 ms ist eine Puls-zu-Puls-Stabilität von wenigen % erforderlich. Besonders zeichnet sich das System durch eine sehr kurze Trigger-zu-Puls-Verzögerung von weniger als 500 ns aus. Dabei ist auch eine hervorragende Strahlqualität von $M^2 < 1.1$ erforderlich, um eine effiziente Frequenzverdopplung zu gewährleisten.

Besonderer Wert wurde auf das Design des Multipass-Laser-Verstärkers gelegt, um die Sensitivität für thermisch induzierte Linsen und die Dejustierung zu minimieren. Der Einfluss von weichen Aperturen auf die Laser-Stabilität wird detailliert diskutiert, insbesondere, weil dieser Effekt normalerweise ignoriert wird.

Auch wenn die Laserentwicklung durch die Spektroskopie an myonischem Helium motiviert wurde, hat die Beschäftigung mit diesem Thema auch zu mehreren Ergebnissen von allgemeinem Interesse geführt. Diese wurden in verschiedenen Veröffentlichungen publiziert und bilden den zweiten Teil dieser Arbeit.

Als erstes dieser Ergebnisse stellen wir eine neuartige Multipass-Oszillator-Architektur vor, die eine erhebliche Leistungssteigerung für modengekoppelte Laser ermöglichen wird. Im Gegensatz zu aktuellen Designs auf Basis multipler 4f-Abbildung, reduziert sich der Stabilitätsbereich nicht mit der Anzahl der Reflektionen an der Scheibe, wodurch die Ausgangsleistung um mindestens eine Größenordnung gesteigert werden kann.

Beim zweiten Ergebnis handelt es sich um eine neuartige Limitierung der Leistungsskalierung eines Scheibenlasers, die auf der Dejustierung des Lasers aufgrund der thermischen Linse beruht. Im Weiteren werden Laserdesigns vorgestellt, die diese Limitierung umgehen.

VI The thin-disk laser for the 2S – 2P measurement in muonic helium

Im dritten Ergebnis wird ein neuartiges Design einer Pumpoptik für Scheiben vorgestellt, welches die Anzahl der Durchgänge durch das aktive Medium bei minimalen Anforderungen an die Strahlqualität des Pumpstrahls und die Größe der Pumpoptik vergrößern kann.

Acknowledgment

I would like to express my gratitude to Klaus Kirch for giving me the opportunity to work in his group and for his support in all these years.

I am indebted to my dear friend Aldo Antognini for his trust and his support that went far beyond anything I could have hoped for. I want to thank for his patience with all my shortcomings and his willingness to follow my strange solutions in my quest to further optimize the laser.

I could not have carried out this development without the technical help of Helmut Brückner for various adaptations of his electronics, Hanspeter von Gunten and Ulf Röser for their support in the development of the Pockels cell. Furthermore, I want to thank Andreas Stuker, Bernhard Morath and Roy Hunziker for realizing mechanical components with astonishing precision.

I also want to thank all the members of the CREMA collaboration for providing me with an exciting task and environment, which allowed my personal development. Special thanks to Franz Kottmann, Francois Nez, Randolph Pohl, Thomas Graf and Marwan Abdou Ahmed.

I want to thank my father Wolfgang Schuhmann who taught me to combine inspiration and technical knowledge to practical technical solutions, and I want to thank my mother Brunhild who taught me that clear logic thinking brings you further than traded knowledge.

But most of all, I want to thank Xiaowen my beloved wife who enabled me to finish this work, who supported me when I did not believe in myself, and kept my feet on the ground when I took myself too seriously. Finally, I want to thank my two sons, Timo and Leon, for showing me that there is more to life than just work.

VIII The thin-disk laser for the $2S - 2P$ measurement in muonic helium

Table of contents

Abstract	III
Zusammenfassung.....	V
Acknowledgment	VII
Table of contents.....	IX
1. Summary	1
2. Motivation.....	6
2.1. Spectroscopy of muonic hydrogen and the proton radius	6
2.2. The “proton radius puzzle”	7
2.3. Spectroscopy of muonic helium.....	10
3. The muonic helium experiment.....	14
3.1. The low-energy muon beam line	15
3.2. The target region.....	17
3.3. The laser system.....	18
3.4. Requirements for the laser system	23
4. The active medium of the thin disk.....	26
4.1. Principle of the thin-disk laser.....	27
4.2. Amplified spontaneous emission (ASE).....	30
4.3. Thermal lens.....	37
4.4. Analytical model of the bending of the thin disk	45
5. Impact of apertures on laser design	56
5.1. Motivation	57
5.2. Transmissivity of apertures.....	61
5.3. Diffraction at apertures.....	65
5.4. Gaussian, Super-Gaussian and flattop apertures.....	66
5.5. ABCD-Matrix formalism and Gaussian apertures	71
5.6. Losses at apertures.....	77
5.7. Multi-pass amplifiers with apertures	78
5.8. Resonator design with apertures	83
6. Q-switched thin-disk oscillator.....	92

X The thin-disk laser for the 2S – 2P measurement in muonic helium

6.1.	The oscillator dynamics	93
6.2.	The oscillator eigenmode and cavity layout.....	98
6.3.	The Pockels cell.....	100
6.4.	Results	108
7.	Thin-disk laser multi-pass amplifier.....	112
7.1.	Introduction.....	112
7.2.	Amplifier concept	114
7.3.	Comparison to other concepts.....	116
7.4.	Realization of the multi-pass amplifier.....	117
7.5.	Measurement of laser operation	118
7.6.	Misalignment sensitivity.....	119
7.7.	Summary.....	122
8.	Multi-pass oscillator layout for high-energy mode-locked thin-disk lasers	123
8.1.	Motivation	123
8.2.	New multi-pass resonator design.....	125
8.3.	Proof of principle	130
8.4.	A simple way to improve the multi-pass resonator based on 4f imaging.....	131
8.5.	Conclusions.....	132
9.	Thin-disk laser scaling limit due to thermal-lens induced misalignment instability	134
9.1.	Motivation	134
9.2.	Thermal lens at the disk	136
9.3.	Resonator reaction for end-mirror misalignment.....	139
9.4.	Resonator stability for disk as end-mirror.....	140
9.5.	Stability of V-shaped resonators	142
9.6.	Impact on typical V-shaped resonators.....	143
9.7.	Resonator designs insensitive to the thermal-induced misalignment.....	147
9.8.	Conclusion	150
9.9.	Appendix: Simulations based on finite elements methods.....	150
10.	Thin-disk laser pump schemes	152
10.1.	Motivation	152
10.2.	Simple example of a multi-pass scheme based on 4f relay imaging.....	154
10.3.	State of the art of the commercial multi-pass pump systems	155
10.4.	Two mirror pairs whose intersects meet off-axis.....	157
10.5.	Design with many more passes	158

10.6.	Particular example based on a 6×6 configuration with triangular input aperture	162
10.7.	Conclusions.....	163
11.	Appendix A: 2S-2P resonances in $\mu^3\text{He}$ and $\mu^4\text{He}$	165
12.	Appendix B: Interferometric measurement of the thermal lens	168
	References.....	A
	Curriculum vitae	Y

XII The thin-disk laser for the $2S - 2P$ measurement in muonic helium

1. Summary

Muonic atoms are atomic systems where one of the electrons is replaced by a muon: for example, muonic hydrogen (μp) is the hydrogen-like bound state formed by a negative muon and a proton. As the muon mass is about 200 times larger than the electron mass, the muon is “orbiting” the nucleus at an average distance 200 times smaller than the electron in the regular electronic atoms. Thus, there is a large overlap between the muon (atomic) wave function and the nucleus that leads to an enhanced sensitivity of the energy levels to the nuclear structure, i.e. the energy levels of the muonic atoms are strongly affected by the nuclear structure. The major energy shift related to the nuclear structure arises from the non-point-like nature of the nucleus, from the fact that the nucleus has a finite size.

By performing laser spectroscopy of the 2S-2P transition in μp [1, 2] we (the CREMA collaboration) deduced a proton charge radius with a relative precision of the order of 10^{-3} . This radius has attracted much attention not only because of its high precision but also because of its 7σ discrepancy with the values extracted from electron-proton scattering and hydrogen (H) spectroscopy [3] that are known with accuracies on the percent level.

As summarized in [4, 5, 6, 7, 8] a few hundred publications have been devoted to the so called “proton radius puzzle” ranging from studies of physics beyond the standard model [9, 10, 11], to the reanalysis of electron-proton scattering data [8, 12, 13, 14, 15, 16, 17, 18, 19, 20] [21, 22, 23], to verifications and refinements of bound-state QED calculations [24, 25, 26, 27, 28], to theories describing the complex low-energy structure of the proton [29, 30, 31, 32, 33, 34, 35, 36, 37, 38], and adjustment of fundamental constants. Considerable effort has been devoted also to the experimental side: new proposals for electron-proton scattering, electron-deuteron scattering, muon-proton scattering [39, 40, 41, 42, 43], new H spectroscopy experiments [44, 45, 46], spectroscopy of H_2 and H-D molecules [44] and alternative determination of the Rydberg constant (strongly correlated to the proton radius in the CODATA adjustment [47]) via spectroscopy of Rydberg states in highly charged ions [48] or positronium and muonium spectroscopy [49]. At present, despite all efforts, the discrepancy persists and the resolution of the proton radius puzzle remains unknown. New experimental inputs are needed to shed light into the proton radius puzzle.

To unravel the proton radius puzzle in 2010 we proposed to measure several 2S-2P transition frequencies in muonic helium ions, $\mu^4\text{He}^+$ and $\mu^3\text{He}^+$ [50], by means of pulsed laser spectroscopy. Successful measurements of two transition frequencies in $\mu^4\text{He}^+$ and three in $\mu^3\text{He}^+$ with accuracies of 50 ppm have been accomplished in two beam times in 2013 and 2014. Data analysis of the measured transitions is ongoing.

This thesis is devoted to the realization of the laser system that was required for the spectroscopy of the muonic helium ions. The development required for this laser has brought along several major innovations in the field of thin-disk lasers [51, 52, 53, 54]. Therefore, a large fraction of this thesis is also dedicated to these additional results having the potential to significantly impact the field of high-power lasers. In summary, the achievements reached in this thesis project can be subdivided into the following topics:

- **Optimization of the active medium of the thin disk.**

At first, we performed an optimization of the active medium of the thin-disk laser in collaboration with the Institut für Strahlwerkzeuge (IFSW), Stuttgart. We adapted the geometry and the doping concentration of the active medium (thin disk) for our conditions that are quite distinctive from typical operational conditions of thin-disk lasers (ultra-short and continuous wave (cw)). Pulses with energies in the order of 100 mJ are extracted with “low” repetition rates while pumped in cw-mode. As a result, we operate our thin-disk laser in the so-called fluorescence mode for the vast majority of the time. Severe challenges are related with the Amplified-Spontaneous-Emission (ASE), with the capability of storing energy in the active medium and reduction of the optical damage threshold. On the one hand, this called for an optimization of the geometry of the active medium, coating, doping and contacting of the disk to the heat sink and on the other hand, for novel layouts of the laser resonator for large beam (eigenmode) widths and reduced sensitivity to thermal lens effect.

- **Thin-disk laser development for muonic helium spectroscopy.**

We developed a thin-disk laser based on a Q-switched oscillator and multi-pass amplifier scheme needed for the 2S-2P spectroscopy of muonic helium and fulfilling the various challenging requirements in terms of pulse energy, pulse bandwidth, beam quality, repetition rates, stochastic trigger and short latency time (short delay between laser trigger and laser pulse emission).

The oscillator was operated in the so-called pre-lasing mode to guarantee a short latency time. The Q-switching dynamics were controlled by a Pockels cell developed in-house for fast switching and feedback stabilization of the pre-lasing operation.

The realized multi-pass amplifier was based on a concatenation of nearly identical optical segments where the ABCD-matrix for a roundtrip in each individual segment represents a stable optical cavity. The resulting multi-pass propagation shows stability properties significantly superior to the standard design that is typically based on 4f-imaging from disk to disk. Several mirror-array schemes to sustain the beam routing in this multi-pass amplifier have been conceived and implemented resulting in elegant, simple and stable realizations of this multi-pass architecture.

- **Realization of a Ti:sapphire laser and a multi-pass enhancement cavity.**

In collaboration with the Laboratoire Kastler Brossel (LKB), Paris, we realized an injection-locked ring-oscillator Ti:Sa laser delivering pulses with up to 15 mJ of energy, operating in a wavelength range between 800 and 960 nm with a bandwidth smaller than 100 MHz and having an rms pulse-to-pulse energy stability of 1%.

In collaboration with the Max-Planck-Institute for Quantum Optics (MPQ), Garching, we designed a multi-pass laser cavity to enhance the laser fluence in the He gas where μHe^+ is formed [55]. While the Garching group took care of the optical aspects of the

cavity, we developed the required stable mechanics to hold the cavity mirrors inside the gas target placed within the 5 T solenoid of the muon beam line.

- **Measurement of five muonic 2S-2P transitions.**

We contributed to setting up the muonic helium experiment in the $\pi E5$ area at PSI and operated the laser system successfully for two (3-month) beam times in 2013 and 2014. During these two beam times, we succeeded in measuring five transition frequencies, two in $\mu^4\text{He}^+$ and three in $\mu^3\text{He}^+$ with the proposed precision of about 50 ppm. Thus, the measurement campaign has been terminated and data analysis is ongoing. The key player in the success of this experiment was the thin-disk laser, which allowed steady operation of the laser system over the whole measurement periods.

- **Aperture effects in thin-disk laser.**

The thin-disk laser community commonly neglects aperture effects. However, in this thesis, we demonstrate their importance and we show how to include them in a simple way into the design of thin-disk resonators and multi-pass amplifiers. Simulating the laser modes accounting for apertures not only allows a more precise and realistic description of the laser mode but also the realization of novel optical architectures.

- **Additional result 1: Multi-pass resonator architecture for ultrafast lasers [52].**

The studies we performed to develop the multi-pass amplifier for muonic atoms [54] have led us to conceive a new scheme for a multi-pass resonator impacting the ultrafast laser sector. These investigations culminated in a patent application that we submitted to the “European Patent Office” [56], titled “High power multi-pass laser oscillators”.

We envisage a resonator scheme that solves present energy scaling limitations of mode-locked multi-pass laser oscillators. The multi-pass oscillator we are proposing is based on a concatenation of identical (or nearly identical) segments. Each segment is equivalent to a roundtrip in an optically stable resonator containing one pass (or more) on the same active medium, which exhibits soft-aperture effects. We demonstrate that the multi-pass oscillator is inheriting the eigenmode properties of the underlying segment as long as we consider aperture effects present in a real laser system. The multi-pass oscillator realized in this way turns out to have the same stability properties as an oscillator composed by a single segment.

Therefore, contrarily to the state-of-the-art layouts based on 4f-imaging, the stability region of our multi-pass oscillator does not shrink with the number of passes at the active medium. Hence, our design sustains variations of the thermal lens of the disk at least one order of magnitude larger than to-date multi-pass design. This opens the way for an order of magnitude increase of the output power and energy: pulses with mJ energy at MHz repetition rates directly from an oscillator become feasible.

- **Additional result 2: A novel limitation of power scaling related to the change of the thermal lens caused by the laser mode [51].**

When designing resonators and multi-pass amplifiers, thermal lens effects at the pumped medium need to be taken into account as they represent one of the limitations for power and energy scaling even for thin-disk lasers. The design of the optical layout has to be conceived to minimize the sensitivity of the laser mode to changes of the thermal lens. For resonators, the sensitivity to variations of the thermal lens is expressed using the so called “stability plot” (see Sec. 5.7.1). The resonator has to be designed well within the stability region to avoid significant changes of the eigenmode by variations of the running conditions (e.g. pump power).

However, another obstacle in power scaling of thin-disk lasers has been disclosed for the first time in this thesis. This limitation is also related to the thermal lens effects. More precisely, it is related to the self-driven growth of misalignment due to thermal lens effects. This self-driven growth of misalignment arises from an asymmetrical thermal lens (with respect to the optical axis) caused by a misalignment between the laser beam position at the thin disk and the axis of the thin disk.

From a modeling of the coupling between thermal lens effects, misalignment and resonator layout, we found a criterion which can be applied to design laser resonators that completely avoid or strongly reduce this limitation.

- **Additional result 3: Novel pump optic scheme for thin-disk lasers [53].**

4f-relay imaging is typically used to realize the multi-pass scheme of the pump light, needed to efficiently pump the active material. The standard realization of such a 4f-based propagation is accomplished using a parabolic mirror and a system of prisms. We generalized and extended this design resulting in new configurations having an increased number of passes at the thin disk as compared to standard designs.

In a standard multi-pass pump design, scaling of the number of beam passes at the disk brings about an increase in the overall size of the optical arrangement or an increase in the requirements for the beam quality of the pump source. Such increases are minimized in our scheme, making these schemes eligible for industrial applications (high efficiency and low cost) and apt for the use of novel active materials with low absorption.

Summarizing, besides having led to the measurement of five transition frequencies in muonic helium impacting the proton radius puzzle and the understanding of two of the simplest nuclei, this thesis has disclosed three major advancements in optics that address power scaling of one of the workhorses in the high-power laser sector: the thin-disk laser. This thesis is organized as follows. In Chapter 2 the so called “proton radius puzzle” is summarized. This forms the background of the experiment to determine the Lamb shift in muonic helium. Then follows a description of the motivations and goals of the spectroscopy of muonic helium as well as the main preliminary results. The experimental principle of the determination of Lamb shift in muonic helium is given in Chapter 3 together with an overview of the setup that includes the muon beam line, the laser system and the enhancement cavity.

The other chapters are dedicated solely to the development of the thin-disk laser. An introduction to thin-disk laser technology is presented in Chapter 4. Emphasis is placed on the thermal lens effects occurring in the active medium, as this constitutes the most severe limitation in power and energy scaling of thin-disk lasers. The designs of a laser showing insensitivity to thermal lens effects forms the central thread of the development carried out in this thesis project. Aperture effects occurring in the pumped active medium that are typically neglected when designing thin-disk lasers are detailed in Chapter 5. We demonstrate that their inclusion in laser design is important and in some cases even mandatory to predict the correct behavior.

In Chapter 6, there is a detailed description of the Q-switched thin-disk laser oscillator that has been realized for the spectroscopy of the muonic helium ion. The multi-pass amplifier used to boost the energy of the pulses delivered by the oscillator is presented in Chapter 7.

The remaining three chapters are dedicated to additional results of the laser development for muonic atoms: Chapter 8 exposes a novel multi-pass resonator architecture whose stability range does not scale with the number of passes, Chapter 9 a new limitation of power scaling and its consequences for laser design, and Chapter 10 describes a novel pump optics design.

2. Motivation

2.1. Spectroscopy of muonic hydrogen and the proton radius

Highly accurate measurements of atomic transition frequencies can be used as precise probes of low-energy properties of the nucleus. A particular class of atoms, called muonic atoms, offers the opportunity to extract properties of the nucleus with higher precision. Examples of such atoms are muonic hydrogen (μp), the bound system of a negative muon and a proton, and muonic helium ions ($\mu^4\text{He}^+$, $\mu^3\text{He}^+$), the bound state of a muon and an alpha particle or a helion. The properties of an atomic system are strongly affected by the orbiting particle mass m . For example, the binding energy (Bohr structure) scales linearly with m (for $m \gg M$ where M is the nuclear mass), while the Bohr radius scales with $1/m$, resulting in binding energies of several keV even for atoms with a low nuclear charge.

For hydrogen-like S states, there is a non-negligible probability that the “orbiting” particle is spending some time inside the nuclear charge distribution, thus experiencing a reduced electrostatic attraction as compared with a point-like nucleus. This reduced attraction, caused by the modification of the Coulomb potential at small distances, gives rise to a shift of the atomic energy levels. The finite-size effect refers to the difference between the energy level computed assuming a Coulomb potential and the energy level computed using the potential from the realistic charge distribution of the nucleus parameterized by the rms (root-mean square) charge radius R_E . For H-like S states, the leading-order finite-size effect is [57, 58, 59]

$$\Delta E_{finite\ size}^{n,S} = \frac{2\pi Z\alpha}{3} |\phi^2(0)|^2 = \frac{2m_r^3 (Z\alpha)^4}{3n^3} R_E^2, \quad (1)$$

where $\phi(0)$ is the wave function at the origin of the coordinate system, $m_r = mM/(m + M)$ is the reduced mass of the atomic system, α the fine structure constant, Z the charge number of the nucleus and n the principal quantum number. Simply speaking, the non-vanishing wave function of the muon inside the proton means that the muon spends some of its time “inside the proton”. Here it feels a reduced Coulomb attraction that shifts S states “upwards”, i.e. makes them less bound.

The m_r^3 dependence of Eq. (1) reveals the advantages related with muonic atoms as the muon mass is 200 times larger than the electron mass, leading to an increase in the energy shift of $m_r^3 \approx 10^7$. Thus, the muonic bound states represent ideal systems for the precise determination of nuclear rms charge radii R_E [1, 2, 4] defined as the square root of the second moments of the electric charge distributions $\rho_E(r)$

$$R_E^2 = \int d\vec{r} \rho_E(\vec{r}) r^2. \quad (2)$$

Note however that this definition is only appropriate in a non-relativistic framework. The covariant definition of the charge radii reads [4]

$$R_E^2 = -6\hbar^2 \frac{dG_E}{dQ^2} (Q^2 = 0), \quad (3)$$

where G_E is the electric Sachs form factor, and $-Q^2 = q^2$ is the four-momentum of the exchanged photon. Due to the sensitivity of the muonic S states to the finite-size effect, the measurement of the 2S-2P transition in muonic hydrogen represents a unique opportunity to deduce the charge radius of the proton independently of the gross structure, i.e. (almost) independently of the Rydberg constant. The theoretical prediction for the 2S-2P_{1/2} splitting in muonic hydrogen is summarized in [60] and reads

$$E_{2S-2P_{1/2}}^{th} = 206.0336(15) [\text{meV}] - 5.2275(10) \left[\frac{\text{meV}}{\text{fm}^2} \right] (R_E^p)^2 + 0.0332(20) [\text{meV}], \quad (4)$$

where R_E^p is the proton charge radius. The first term accounts for quantum electrodynamic (QED) contributions, the second one for finite-size effects (first order and radiative corrections to it), and the third one for the two-photon exchange (TPE) contribution which is a second-order perturbation theory contribution related with the proton structure which cannot be simply calculated in the framework of bound-state QED. By equating the theoretical prediction of Eq. (4) with the value extracted from the measurements, a proton charge radius $R_E^p = 0.84087(39)$ fm [2] has been extracted which is by an order of magnitude more accurate than the CODATA value of $R_E^p = 0.8751(61)$ fm [61]. Yet the value from muonic hydrogen is 4% smaller than derived from electron-proton scattering [18, 22, 23] and H spectroscopy [62] with a disagreement at the 7σ level. This discrepancy is nowadays referred to as “the proton radius puzzle”.

An equation similar to Eq. (4) can be formulated for the 2S-2P splittings in the muonic helium ions (see Sec. 2.3). When compared to the corresponding measurements the alpha particle and helion charge radii can then be deduced. However, before focusing on muonic helium spectroscopy we introduce first the “proton radius puzzle” which represents the horizon motivating among others the muonic helium spectroscopy experiment.

2.2. The “proton radius puzzle”

Historically, the fact that the proton has a finite size has been disclosed by scattering electrons off protons (hydrogen gas target) and observing the angular distribution of the elastically scattered electrons. The scattering distribution can be described by the electric and magnetic form factors G_E and G_M that account for the complex structure of the proton. Making use of Eq. (3) the charge radius can be obtained. This method is still used to date and provides charge radii with accuracies on the percent level [16, 17, 18].

A second way to the proton charge radius is through high-precision laser spectroscopy of the hydrogen (H) energy levels that delivers radii with 1 % relative precision [61]. The third method, our method, is based on laser spectroscopy of μp . The value extracted from μp [1, 2] with a relative precision of $5 \cdot 10^{-4}$ is by an order of magnitude more accurate than obtained by averaging the values from hydrogen [62] and electron-proton scattering. Yet, the muonic measurement exposes a 6σ variance from this average value that has been deduced by the CODATA group by performing a least square adjustment of several transition

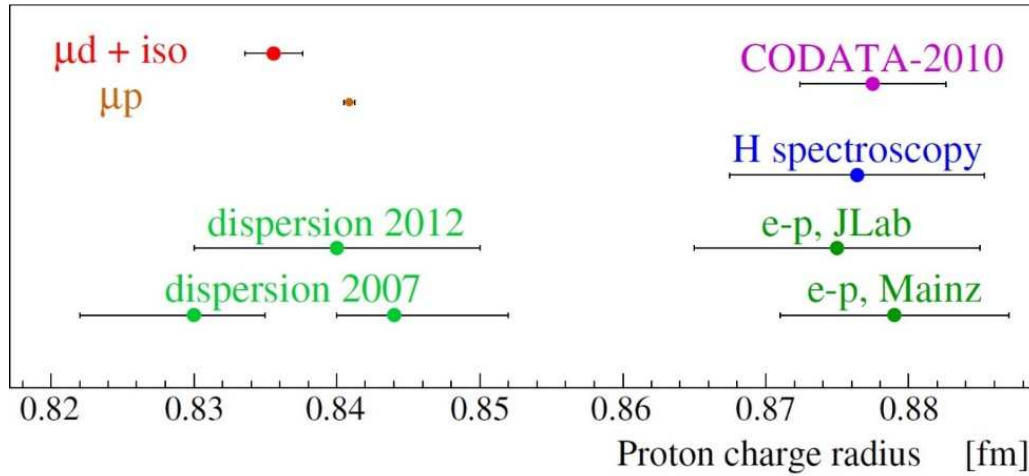


Figure 1: Proton charge radii determined from spectroscopy of muonic hydrogen (brown), from electron scattering (green) and from H/D spectroscopy (blue). An additional value (red) extracted indirectly from muonic deuterium combined with the H/D isotopic shift measurement (see main text for more details) shows the consistency of the muonic results. Many more values have been extracted recently from electron-scattering data but for the sake of simplicity we have neglected them, because some of them are controversial. (Figure reproduced from [63]).

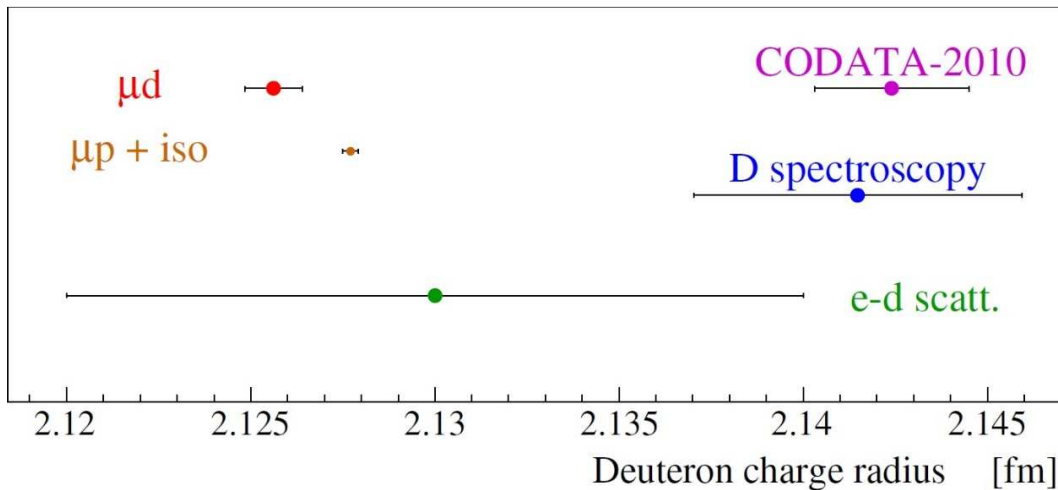


Figure 2: Deuteron charge radii determined from spectroscopy of muonic deuterium (red), from electron scattering (green) and from D spectroscopy (blue). The most precise determination of the deuteron radius (brown) comes from combining the proton radius from muonic hydrogen with the H/D isotopic shift. (Figure reproduced from [63]).

frequency measurements in H, D, and electron-proton, electron-deuterium scattering data [61]. Some values of the proton charge radius extracted from the three methods are summarized in Figure 1.

This discrepancy has attracted much attention ranging from studies of physics beyond the standard model [9, 10, 11], to reanalysis of electron-proton scattering data [12, 13, 14, 15, 16, 17, 18, 19, 64], refinements of bound-state QED calculations [24, 25, 26, 27, 28, 65, 66], and theories describing the complex low-energy structure of the proton [29, 30, 31, 32, 34, 35, 36, 37, 67].

Several new experimental activities have been initiated in response to the observed discrepancy. On the atomic physics side, these include experiments aiming at improving the laser spectroscopy in hydrogen to check for possible tiny systematic effects [44, 45, 46]. In parallel, also spectroscopy of Rydberg states in

highly ionized ions has been initiated [48] as well as spectroscopy of muonium [49] to improve on the Rydberg constant that is fully correlated to the proton radius. Recently, high-precision spectroscopy of the vibrational levels in molecular hydrogen [68, 69] has been proposed to deduce the proton charge radius, and various experiments have been launched [68].

To improve the situation in the electron-proton scattering sector, several new experiments are ongoing [39, 43]. This should serve to elucidate the tension existing between various electron-proton data analyses: some yielding radii compatible with μp [15, 19, 20, 21], some at variance [16, 17, 18, 70]. The difference between various analyses has to be ascribed in particular to the method used to extrapolate to $Q^2 = 0$ from the form factors measured at finite $Q^2 > 0$. The main challenge in these experiments is thus to precisely measure the form factors $G_E(Q^2)$ and $G_M(Q^2)$ at very low Q^2 ($Q^2 \approx 0.001 \text{ GeV}^2/c^2$). To reduce the charge radii with better precision, the new experiments therefore propose to deduce the exchanged photon momentum Q^2 in the $10^{-4} \text{ GeV}^2/c^2$ range: the JLAB experiment [39] by means of a non-magnetic calorimeter, the new MAMI [42] experiments using initial state radiation and also a windowless target.

Another approach is followed by the MUSE collaboration at PSI [40]. The plan is to measure μ^-p , μ^+p , e^-p and e^+p scattering within the same setup. In this way, not only the absolute value of the proton charge radius can be deduced but also a possible difference between the radius as extracted with electrons and with muons. Hence, these measurements hold the potential to disclose a possible violation of muon-electron universality.

Investigations of beyond standard model (BSM) physics as an explanation of the discrepancy observed are numerous, see e.g. [9, 10] and references therein. The parameter space for this BSM explanation is small. However, theories can be formulated able to explain the proton radius puzzle together with the 3.5σ discrepancy observed in the muon $g-2$ experiment [71] without conflicting with other low-energy constraints. They all predict new force carriers with masses in the MeV range.

Summarizing, currently 7 years after the first publication of the proton radius value from spectroscopy of muonic hydrogen, the discrepancy persists. On the theory side, a myriad of reevaluations and refinements of the atomic and nuclear physics have been accomplished while possible-beyond standard model physics are not convincing. At this stage, it seems that only new experimental inputs hold the potential to clarify the situation. From the experimental side, various activities have been initiated but to date no new results (besides muonic deuterium) have been presented which could confirm or solve the discrepancy.

Spectroscopy of muonic deuterium has recently provided new insights into the proton radius puzzle [63]. Similar to muonic hydrogen, in muonic deuterium we have measured three transitions between the 2S and the 2P states. The red point in Figure 2 shows the value for the deuteron charge radius extracted from these measurements. The value is at a 6σ variance from the CODATA value [61] that represents the best estimate of the deuteron radius obtained from electron scattering on protons and deuterons and precision laser spectroscopy of H and D. Although the deuteron charge radius obtained from electron-deuterium scattering is precise to the 0.5 % level [72], it is unfortunately not precise enough to pick out the value from muonic deuterium or CODATA.

It is important to note that the CODATA value of the deuteron radius is strongly linked with the CODATA value of the proton radius through the H/D isotopic shift [73]. By measuring the frequency difference (isotopic shift) of the 1S-2S transition in H and D and by combining it with the corresponding theoretical prediction, a correlation between the proton and the deuteron charge radii is obtained [73]

$$(R_E^d)^2 = (R_E^p)^2 + 3.82007(65) \text{ fm}^2, \quad (5)$$

where R_E^d is the deuteron charge radius and R_E^p the proton charge radius. Given the small uncertainty of the numerical factor in Eq. (5), the 6σ variance between the deuteron radius from muonic deuterium [63] and CODATA “simply” reflects the discrepancy of the proton radius values. It is therefore of interest to consider the value of the deuteron radius without any influence of the proton radius. When selecting only deuteron spectroscopy data the blue point in Figure 2 is obtained [74], which deviates by about 3.5σ from the muonic value [63]. This new discrepancy between the atomic physics determination of the deuteron radius from electronic deuterium and muonic deuterium is thus almost as severe as the 4.0σ discrepancy between the proton radius values from H and muonic hydrogen spectroscopy. Therefore, we are faced with a double discrepancy: one in the proton sector, one in the deuteron sector [75].

The deuteron radius from muonic deuterium provides new insight into the proton radius puzzle. In fact, when combining the deuteron charge radius from muonic deuterium with Eq. (5), another determination of the proton charge radius is obtained as shown by the red point in Figure 1. This new indirect value of the proton radius from muonic deuterium confirms the previously obtained value from muonic hydrogen. Therefore, muonic deuterium on the one hand amplifies the proton radius puzzle; on the other hand, it shows the consistency between the various muonic results. The difference of 2.6σ of the muonic values could be attributed to an incomplete treatment of the calculated polarizability contribution (two-photon exchange) in muonic deuterium, which is 50 times larger than in muonic hydrogen.

Conversely, the proton radius from muonic hydrogen can be combined with Eq. (5) to attain an indirect value of the deuteron radius (brown point in Figure 2). Because of the fair agreement between the deuteron radius extracted indirectly from muonic hydrogen and directly from muonic deuterium, we can conclude that a hypothetical new force carrier (beyond the standard model) which would explain the proton charge radius has to couple only weakly with the neutron. New physics explanations thus have to assume a preferential coupling to muons and protons but not to electrons and neutrons in order to explain the observed “double” discrepancy. Agreement between all spectroscopic results could be reached if the Rydberg constant R_∞ was shifted by $\approx 7 \sigma$ or the 1S Lamb shift contribution in H and D was corrected by 110 kHz that corresponds to about 50 times the claimed precision. Only in this way the proton and the deuteron radii from μp and μd could be brought into agreement with the ones extracted from H and D without calling for new physics explanations.

Muonic deuterium has thus provided an important information towards the resolution of the proton radius puzzle. Spectroscopy of muonic helium will have a similar impact.

2.3. Spectroscopy of muonic helium

To shed light onto the proton radius puzzle in 2010 we proposed to measure several 2S-2P energy splittings in the $\mu^3\text{He}^+$ and $\mu^4\text{He}^+$ ions. The finite-size effect in μHe^+ is about 20% of the 2S-2P energy splitting [26], to be compared with the 2% effect in muonic hydrogen (see Figure 3). Therefore, a precision measurement of the 2S-2P transition in the muonic helium ions, $\mu^4\text{He}^+$ and $\mu^3\text{He}^+$ can be used to deduce the

corresponding nuclear charge radii with high precision provided that the theoretical predictions mainly given by bound-state QED contributions are sufficiently accurate.

The theoretical prediction of the $2S - 2P_{1/2}$ and $2S - 2P_{3/2}$ energy splitting in $\mu^4\text{He}^+$ can be summarized by the following equations [76]

$$E_{(2P_{1/2}-2S_{1/2})}^{th} = 1671.50(18) - 106.357(8)(R_E^\alpha)^2 + 1.40(R_E^\alpha)^3 \text{ [meV]} \quad (6)$$

$$E_{(2P_{3/2}-2S_{1/2})}^{th} = E_{(2P_{1/2}-2S_{1/2})}^{th} + 146.192(13) \text{ [meV]} \quad (7)$$

where R_E^α is the charge radius of the alpha particle expressed in fm. The first terms on the right sides represent the sum of QED contributions and the nuclear polarizability contributions. The other two terms on the right side represent the finite-size contributions: the ones proportional to $(R_E^\alpha)^2$ arise from the one-photon exchange and are given mainly by Eq. (1), the ones proportional to $(R_E^\alpha)^3$ arise from the elastic part of the two-photon exchange contributions. Similar predictions exist for $\mu^3\text{He}^+$, but for simplicity reasons here, we only consider the $\mu^4\text{He}^+$ case.

As already mentioned, in two beam times in 2013 and 2014 we succeeded in measuring five transition frequencies: two in $\mu^4\text{He}^+$ and three in $\mu^3\text{He}^+$, the measured transitions are reported in Chapter 11. As an example, the black full dots of Figure 4 represent the measured $2P_{3/2} - 2S_{1/2}$ transition in $\mu^4\text{He}^+$. The central value of the red curve, which is the fit to the muonic resonance, will be eventually deduced with a statistical precision of about 0.05Γ , where $\Gamma \approx 320$ GHz represents the FWHM line width. Its position has to be compared with the colored horizontal bars (green, blue and purple). The green bar represents the

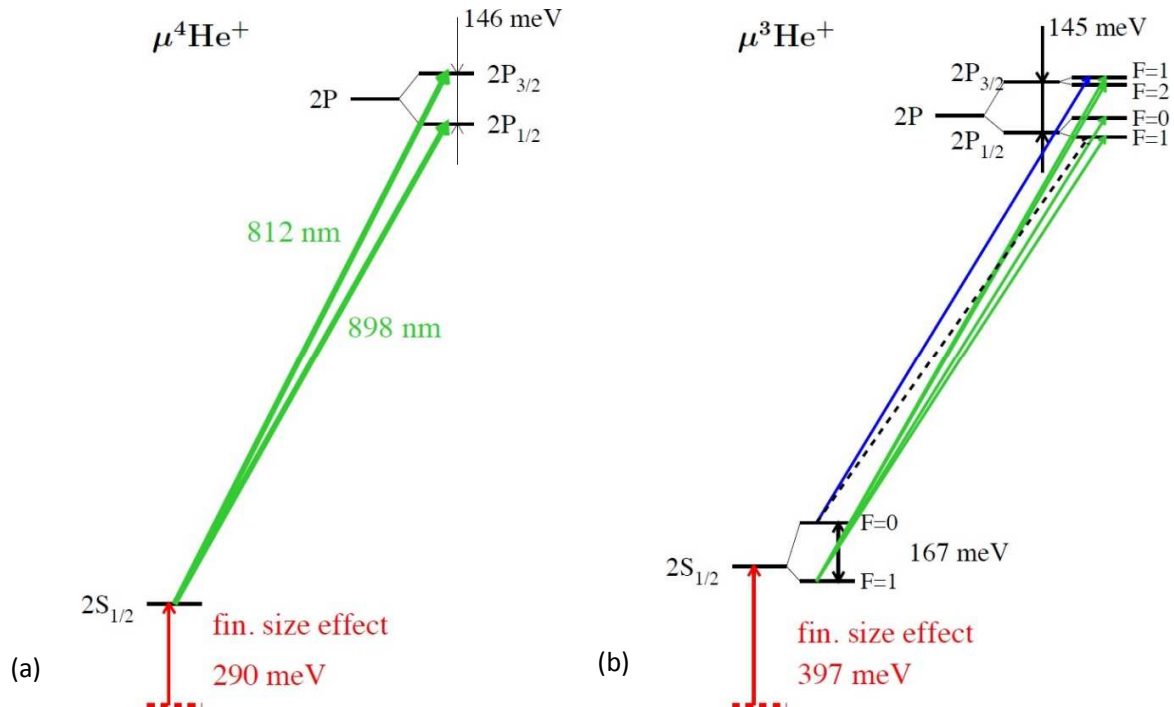


Figure 3: Sub-level structure of the $n=2$ state in $\mu^4\text{He}^+$ (a) and in $\mu^3\text{He}^+$ (b) caused by QED, fine and hyper-fine effects. Indicated are the E1 transitions which have been addressed in our experiment and the energy shifts caused by the finite-size effect. (Courtesy of R. Pohl)

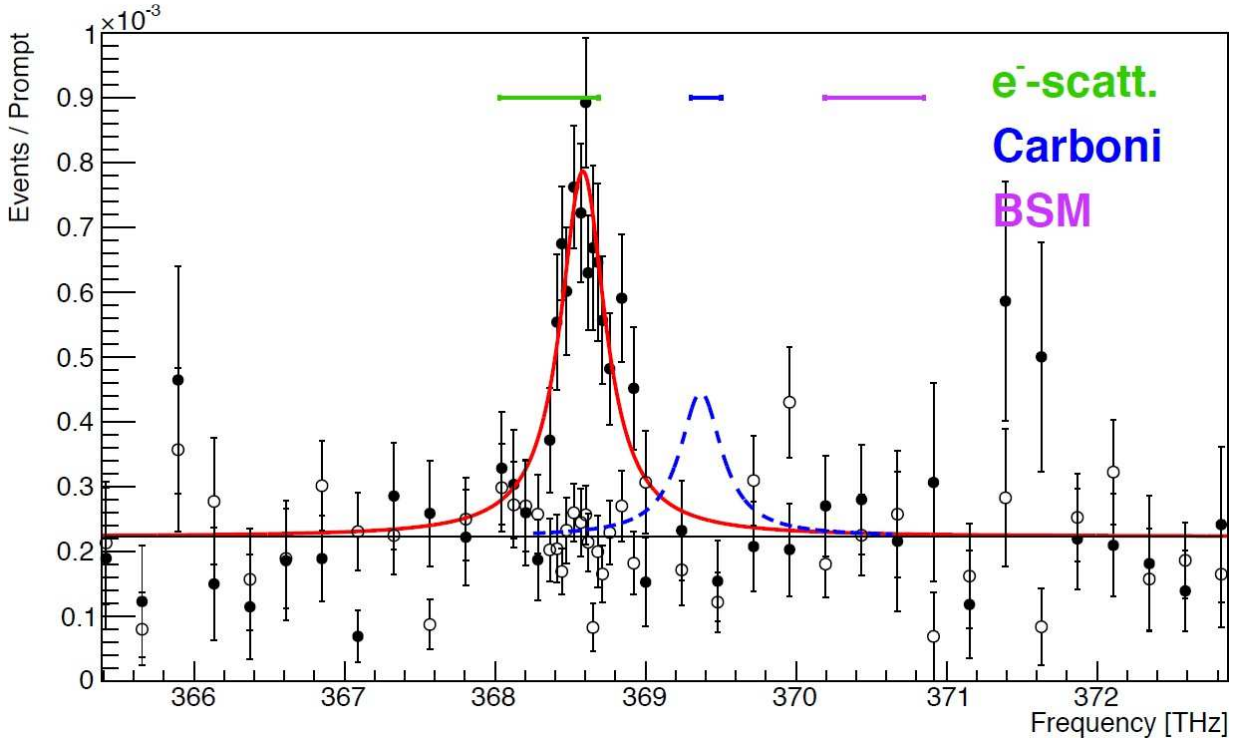


Figure 4: Measured $2P_{3/2} - 2S_{1/2}$ transition in $\mu^4\text{He}^+$. The black dots represent the muonic resonance line that has been fitted by the red curve. The empty circles represent data where the laser was not shot. They can be used for a precise determination of the background level. The various horizontal bars are explained in the main text. (Reproduced from [76]).

position of the muonic transition assuming the bound-state QED theory of Eq. (6) and the alpha-particle charge radius from electron-He scattering [77]. Its width is given by $\pm 1 \sigma$ of the theoretical uncertainty that is largely dominated by the uncertainty of the alpha-particle charge radius. This time, differently from muonic hydrogen, agreement is found between the results from electron scattering and spectroscopy of muonic atoms. This agreement will strongly constrain the room for BSM physics.

The purple bar also assumes the alpha particle value from electron scattering. However, in this case a beyond-standard model contribution as predicted in [78] to explain the proton radius puzzle is included in the theoretical prediction. Obviously, our measurement disfavors this extension of the standard model. In such a way, we demonstrate based on an example, how the muonic helium results can be used to infer information on, and constrain, the proton radius puzzle.

The blue bar represents the position (its width being the $\pm 1 \sigma$ uncertainty) of the transition frequency measured in $\mu^4\text{He}^+$ from a supposedly erroneous experiment [79]. The observed discrepancy between our measurement and the blue bar clearly confirms that the previous muonic helium measurement was wrong as already pointed out in [80].

The measured transition frequency in $\mu^4\text{He}^+$ (after accounting for minor systematic corrections) reads [76]

$$E_{(2P_{1/2}-2S_{1/2})}^{th} = 368.660 (17) \text{ THz (PRELIMINARY)} \quad (8)$$

$$E_{(2P_{3/2}-2S_{1/2})}^{th} = 333.352 (16) \text{ THz (PRELIMINARY)}, \quad (9)$$

with the uncertainty dominated by statistics. Similar values will be given for $\mu^3\text{He}^+$ when the analysis is concluded.

By comparing the measured transition frequencies with the corresponding theoretical predictions summarized in Eqs. (6) and (7) a new value of the alpha particle charge radius can be extracted [76]:

$$R_E^\alpha = 1.67829(53) \text{ fm (PRELIMINARY)}. \quad (10)$$

This value is more precise but compares well with the value extracted from electron-proton scattering of $R_E^\alpha = 1.681(4) \text{ fm}$ [77]. Similarly, a comparison between the transition frequencies in $\mu^3\text{He}^+$ with the corresponding theoretical prediction can be used to deduce the helion-charge radius. At this stage, we refrain from giving a value, as data analysis is still incomplete.

As can be seen from Eq. (10) the nuclear charge radii of the alpha particle will eventually be obtained from muonic helium spectroscopy with a relative precision of $3 \cdot 10^{-4}$ limited by the polarizability contribution. Similarly for the helion charge radius. These nuclear radii are interesting parameters for comparison with scattering and He spectroscopy results [77]. Even more interesting from the physical point of view is the comparison with the predictions from few-nucleon ab-initio calculations [81, 82, 83, 84, 85, 86, 87, 88]. Indeed these radii are benchmarks as important as the masses and the magnetic moments to test ab-initio nuclear theories. Conversely, they can be used to fix some low-energy constants describing the nuclear interaction in an effective approach.

These radii can be used also to improve on the absolute values of the ^6He and ^8He halo nuclei when combined with the corresponding isotopic shift measurements [81]. Moreover, the difference between the alpha-particle and helion-charge radii extracted from $\mu^4\text{He}^+$ and $\mu^3\text{He}^+$ respectively can be used to sort out the 4σ discrepancy that presently exists between two ^3He - ^4He isotopic shift measurements [89, 90]. When combined with measurements in regular helium and helium ions [50, 91, 92] our measurements also lead to enhanced bound-state QED tests for one- and two-electron systems.

Therefore, besides providing additional insight into the proton radius puzzle, the spectroscopy of muonic helium will provide benchmarks to understand the low-energy structure of the alpha particle and helion nucleus. In a nutshell these are the motivations and physics impacts of the laser development we have pursued in this thesis and described in the following chapters.

3. The muonic helium experiment

The principle of the μHe^+ 2S-2P experiment [50] is to form μHe^+ ions in the 2S state, to excite the 2S-2P transition with a pulsed laser, and then to detect the emission of an 8 keV X-ray from the deexcitation of the 2P state into the ground state as a signature of the successful laser transition. A resonance curve can be obtained by plotting the number of 8 keV X-rays versus the laser frequency. By comparing the measured resonance frequency with the corresponding theoretical prediction, the nuclear charge radius can be determined.

An intense negative pion beam from the HIPA facility of the Paul Scherrer Institute, Switzerland is used to produce a negative muon beam of few keV energy [1] that can be efficiently stopped in He gas at 3 mbar pressure and room temperature. The low energy muons replace one of the electrons in the He atoms to form muonic helium atoms in highly excited states with principal quantum number $n \approx 14$. The second electron is also released by an internal Auger transition, thus leaving an excited μHe^+ ion. From these excited states, various deexcitation processes take place as external Auger emissions and radiative decays accompanied by Stark mixing within levels of the same principal quantum number. These deexcitation processes (muonic cascade) feed the 2S state with a probability of 1.5(5) % [80, 93, 94], while the vast majority of the deexcitation process ends up directly in the ground state without passing through the 2S state as shown in Figure 5.

The lifetime of the 2S state is governed by three processes: the muon decay (the free muon lifetime is 2.2 μs), two-photon transition to the ground state ($\Gamma_{2\gamma} = 1.18 \cdot 10^5 \text{ s}^{-1}$), and quenching by collisions with neighboring He atoms ($\Gamma_{\text{quench}} = 2.7 (1.0) \cdot 10^3 /(\text{s mbar})$) [80, 93, 94]. At the chosen pressure of 3 mbar that is a trade-off between muon stopping efficiency in the He gas and collisional quenching of the 2S-state, the 2S-state lifetime is of about 1.7 μs .

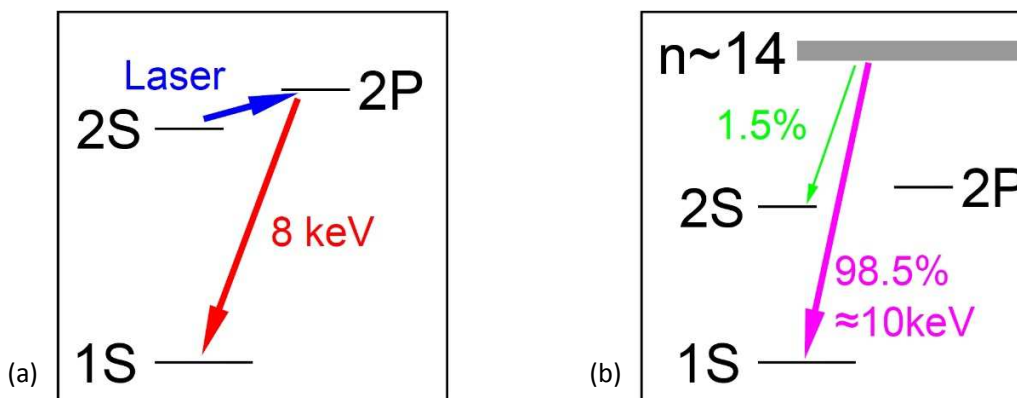


Figure 5: Principle of the muonic experiment. (a) Schematic of the laser experiment whose goal is the measurement of the 2S-2P transition. The on-resonance laser light excites the 2S-2P transition. The 2P state decays within a fraction of a ps to the ground state emitting an 8 keV X-ray. (b) Muonic atom cascade. The muonic atoms are formed in a highly excited state with the principal quantum number $n \approx 14$. The subsequent muonic cascade (deexcitation process) populates the 2S state with a probability of about 1.5%.

With a delay of about one microsecond after the muonic atom formation, a laser pulse of 5-10 mJ energy and a wavelength tunable between 800 and 970 nm arrives in the target region and is injected into the multi-pass cavity which allows a homogeneous illumination of the muon stop volume and an enhancement of the laser fluence. On-resonance light induces $2S \rightarrow 2P$ transitions with a probability of about 20 %. From the 2P state a rapid (within 1 ps) deexcitation to the ground state takes place with emission of an 8 keV X-ray as shown in Figure 5. The detection of the 8 keV X-rays in time coincidence with the laser light can be used as a signature of the occurred laser transition. In fact, the resonance given in Figure 4 shows the number of 8 keV X-rays in time coincidence with the laser light normalized to the number of prompt 8 keV X-rays produced during the muonic atom formation. This normalization accounts for the number of formed muonic atoms at a given laser frequency so that fluctuations of the muon beam intensity and variations of the measurement times are compensated.

The complex experimental setup we realized for this experiment can thus be divided into the following components:

- A low-energy beam line delivering 280/s negative muons with few keV energy. The muons arrive at randomly distributed times and are detected in a non-destructive way prior to their entrance into the He gas target.
- A He gas target containing the multi-pass cavity to enhance the laser light.
- A laser system that, on being triggered by the entering muon, delivers in a short time ($< 1 \mu\text{s}$) a pulse to drive the 2S-2P transition.
- A detector system for the detection of the 8 keV X-rays from the 2P-1S transitions and the electrons from muon decay.
- A data acquisition and trigger system.

Some of these components will be discussed in more detail in the following.

3.1. The low-energy muon beam line

A schematic view of the low-energy muon beam line is shown in Figure 6. The main components are a cyclotron trap (CT), a toroidal magnetic field acting as a momentum filter (MEC), and a solenoid (PSC) where the gas target, the optical multi-pass cavity, and the detectors are placed. The CT consists of two super-conducting coils creating a magnetic field similar to a “magnetic bottle” which acts as a trap for the muons. Pions with a momentum of 100 MeV/c from the πE5 beam line at PSI, Switzerland, are tangentially injected into the CT and degraded at the periphery of the trap. After crossing the degrader, the pions are confined and brought into an orbit that passes close to the trap center. With a lifetime of 26 ns the pions decay into muons. 30 % of these remain trapped in the CT due to the confinement exerted by the magnetic field. A Formvar foil with a thickness of 200 nm is placed in the center of the trap. The trapped muons cross this foil several times and their initial kinetic energy that is in the MeV range is moderated down to a kinetic energy in the keV range. A nickel layer sputtered onto the Formvar foil is used to define the electrostatic potential at the center of the trap to -20 kV. When the muons are slow enough, this negative

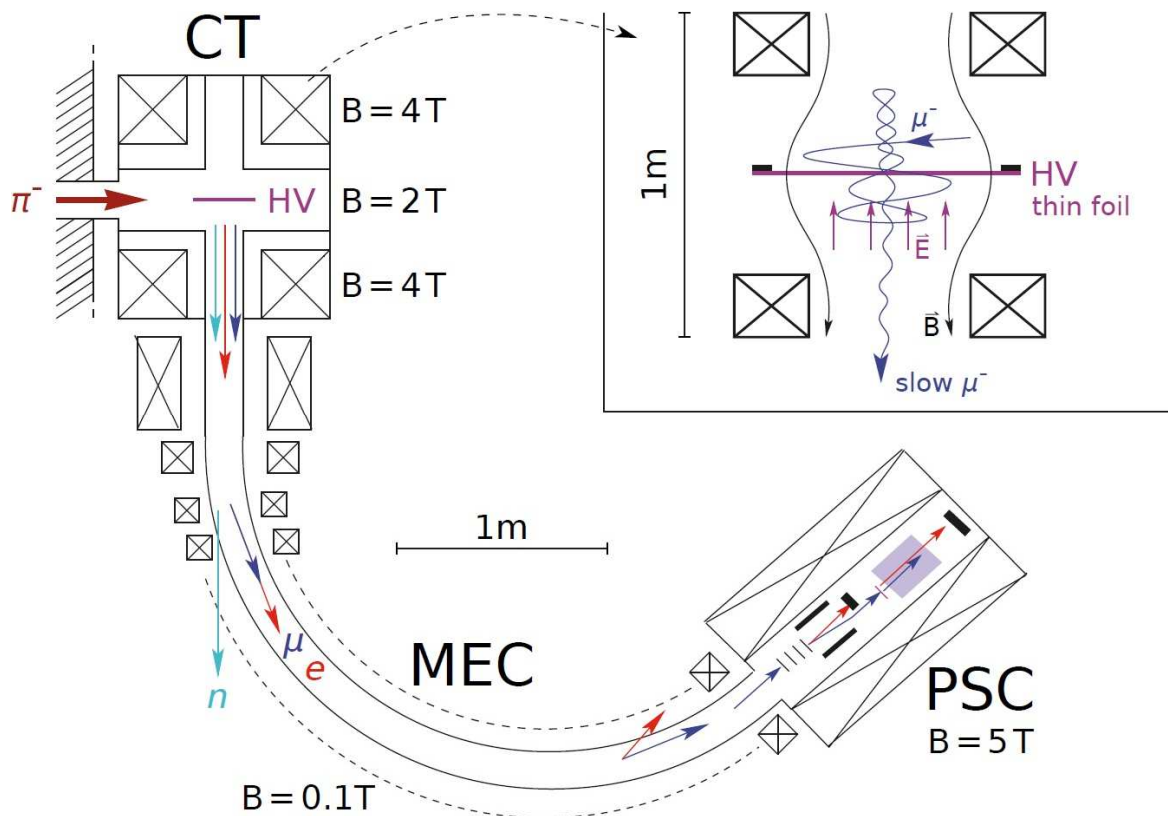


Figure 6: Schematic of the low energy muon beam line for the 2S-2P measurement in μHe^+ . Pions from the πE5 beam line are injected into the cyclotron trap (CT). In the trap, they decay in MeV energy muons that are slowed down with the help of a metallized foil placed in the center of the trap that is set at high voltage (HV). This potential is helpful to extract the muons with low transverse momentum from the trap. The ejected muons follow the toroidal magnetic field (MEC) and are then focused into the 5 T solenoid (PSC) where the experiment takes place. The insert is a zoom of the CT region showing also a schematic of a muon trajectory. (Reproduced from [50]).

potential applied to the Formvar foil provides an additional longitudinal momentum to the muons sufficient to overcome the magnetic confinement [95].

Hence, the negative muons are ejected axially from the cyclotron trap and guided to the so called muon extraction channel (MEC). The MEC is a segment of a toroidal magnetic field oriented in horizontal direction as shown in the Figure 6 with an average field strength of $B = 0.15$ T produced with 17 identical coils. The muons exiting the CT are guided through the toroidal field of the MEC to the fringe field of the 5 T solenoid (PSC). In such a way, the muons are transported from the high background region of the CT into the low background region of the PSC. Momentum selection is achieved in the MEC due to the inhomogeneity of the B field: the vertical position of the muons leaving the MEC field depends on its momentum, so that the placement of a suitable aperture can be used to select the desired momentum.

As detailed in Figure 7, before stopping in the He gas target the muons are detected in a non-destructive way using several carbon foils and an E x B filter. This detection works in the following way: a muon crosses several carbon foils having a thickness of 40 nm and set at various high voltages between -12 and -2 kV. In the foils the muons lose energy and additionally some electrons are emitted. The potential difference between foils accelerates the electrons so that each muon leaving Stack 1 is accompanied by some electrons. The following E x B filter separates the muon from the much faster electrons because the faster electrons drift much less than the muon and can be detected by the plastic scintillator S_1 . Its signal is used

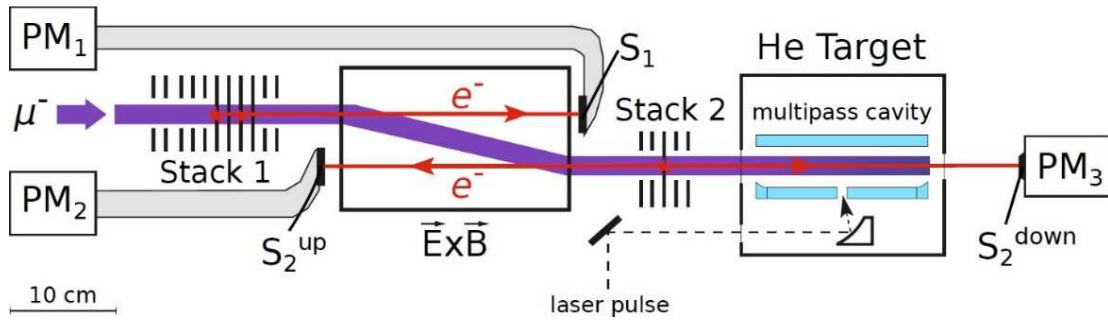


Figure 7: Schematic view of the apparatus within the 5 T solenoid where the He target is placed. Before stopping in the He gas target two stacks of carbon foils are used to detect the muons entering the setup. The non-destructive detection of the muons is achieved by detecting the electrons that are emitted in the foils when crossed by the muon. The electrons are observed by using plastic scintillators (S_1 , S_2^{up} and S_2^{down}) connected with long light-guides to photo-multipliers (PM_1 , PM_2 and PM_3). The muon stopping volume is surrounded by the multipass optical cavity to enhance the laser light. The laser pulse is coupled into the cavity through a small hole of 0.6 mm diameter about 1 μ s after the muonic helium formation. (Adopted from [50])

to generate the trigger for the data acquisition (DAQ) and for the laser system. The muon then crosses a second stack of carbon foils (Stack 2). The released electrons are again detected in both S_2^{up} and S_2^{down} . A delayed coincidence between the electron signals from S_1 and S_2 (S_2^{up} or S_2^{down}) with the correct time of flight corresponding to a muon with a kinetic energy of a few keV is used to trigger the laser and the DAQ systems. The stacks of carbon foils provide the non-destructive detection of single muons and reduce the energy of the muons from about 20 keV to few keV. These muons are efficiently stopped in our gas target.

3.2. The target region

After leaving the second stack of carbon foils the muons have to cross the 20 nm thick entrance window of the gas target made of Formvar [61] and having transverse dimensions of $19 \times 8 \text{ mm}^2$. The gas pressure of about 3 mbar as mentioned before was a trade-off accounting for the muon stopping efficiency and the collisional-induced quenching of the metastable $2S$ state. As a consequence of the low pressure, the muon stopping volume in the He gas is relatively large: its length is about 20 cm. This imposes hard requirements on the laser system because it has to provide sufficient pulse energy to efficiently drive the $2S$ - $2P$ transitions (having small matrix elements) over this large muon-stopping volume ($20 \times 8 \times 200 \text{ mm}^3$).

As shown in Figure 8, around the muon stop distribution there are two mirrors forming the multi-pass optical cavity to enhance the laser light. To detect the 8 keV X-rays two rows of 10 LAAPDs each, are placed above and below the muon stopping volume [96]. These LAAPDs also serve to detect the electron from muon decay, used to discriminate the good laser events from the background. This electron detection is complemented by means of four plastic scintillators placed around the target to detect the fraction of the electrons from muon decay spiraling in the magnetic field with large transverse momentum (relative to the Michel spectrum end-point of 53 MeV).

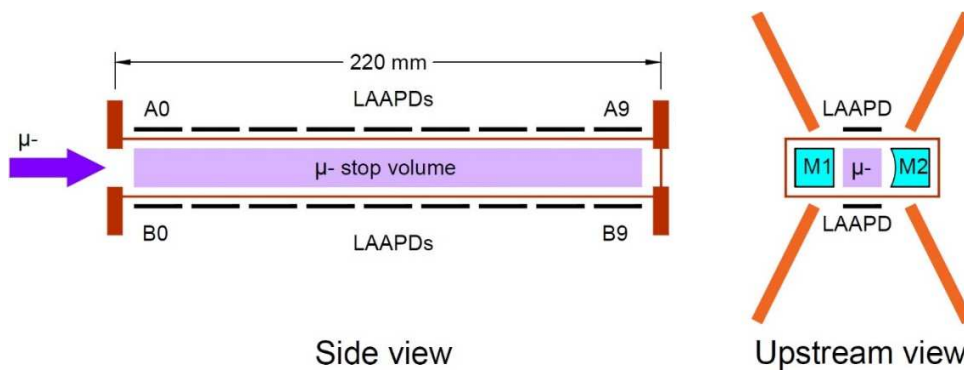


Figure 8: Side and upstream view of the target region showing the muon stop volume (purple), the X-rays detectors (LAAPDs), the mirrors of the laser cavity (M1 and M2), and the four scintillators (orange in the upstream view) for the detection of the electrons from the muon decay.

3.3. The laser system

A schematic view of the laser system developed for this experiment is shown in Figure 9. It is composed of a pulsed thin-disk laser operating at a wavelength of 1030 nm and pumped with two cw diode lasers operated at wavelengths of 940 nm and 969 nm. The frequency-doubled pulses of the thin-disk laser are then used to pump a Titanium-Sapphire (Ti:Sa) laser whose frequency is controlled by a cw single frequency Ti:Sa through an injection-locking mechanism. The pulses of the Ti:Sa laser which are in the wavelength region of 800-970 nm and have a bandwidth of < 100 MHz are then transmitted from the laser hut to the muon beam line and coupled into the multi-pass cavity surrounding the muon stop distribution.

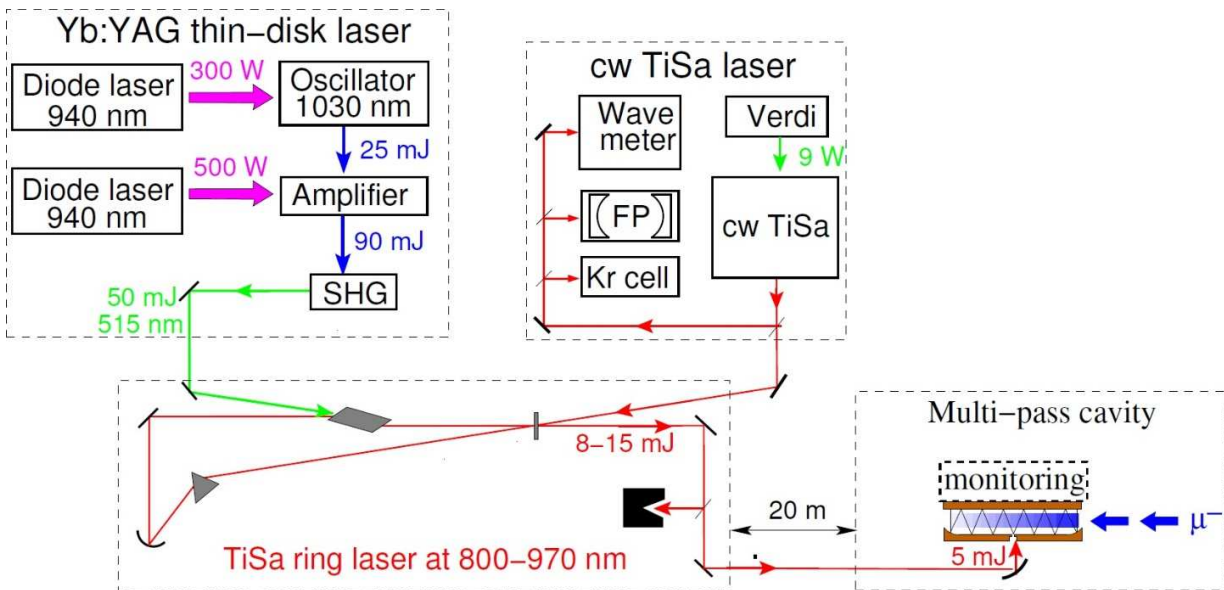


Figure 9: Schematic of the laser system for the μHe^+ 2S-2P experiment. Energies are given at running conditions during the beam times.

A muon entering the target region at random time triggers the laser system. More precisely, the coincidence within the correct time of flight of the muon detectors (S_1 , S_2^{up} and S_2^{down}) is used to trigger the Yb:YAG thin-disk laser which is composed of a Q-switched oscillator and a multi-pass amplifier (see Figure 9). A short delay between laser trigger and emission of the pulse is achieved by continuously pumping the active media of the thin-disk laser with 0.8 kW power so that the largest possible amount of energy is continuously available in the active medium. When the laser is triggered, this energy can thus be released in a short time to build up the pulse.

Moreover, the thin-disk oscillator is operated in pre-lasing mode to further shorten the latency time of the thin-disk oscillator down to 400 ns. The oscillator has been proven to deliver pulse energies of up to 110 mJ (before optical damage occurs) but during data-taking it was operated safely at 25 mJ of pulse energy, to ensure the needed stability, to cope with the stochastic trigger and the noisy environment of the experimental hall. More details are presented in Chapter 6.

The pulses with a duration of about 40 ns delivered by the oscillator are then transmitted through two optical isolators preventing optical feedback and are coupled into an 8-pass amplifier whose pulsed gain is about 3.6 (at 90 mJ of output energy from the amplifier). The amplifier is based on a non-standard configuration whose main peculiarity is its insensitivity to thermal-lens effects even for large beam widths. The amplifier has been tested up to a pulse energy of 145 mJ. To avoid damage of the active medium and some critical mirrors the amplifier has not been tested at higher pulse energies. More details about the multi-pass amplifier are presented in Chapter 7 while a picture of the thin-disk laser developed for the μHe^+ experiment is shown in Figure 10.

A frequency-doubling stage (SHG) is used to convert the wavelength of the disk-laser pulses from 1030 nm to 515 nm which is a suitable wavelength for the pumping of the Ti:Sa laser. During data-taking the Ti:Sa laser was pumped with pulses of about 50 mJ energy and delivered pulses with energies between 15 mJ at $\lambda = 840$ nm and 8 mJ at $\lambda = 970$ nm. The Ti:Sa laser is a single-frequency ring oscillator with a cavity length of about 1 m. While a prism performs a rough wavelength selection, the injection-seeding with cw laser light from an external single-frequency cw Ti:Sa guarantees single frequency operation. The cw Ti:Sa laser is stabilized on an external Fabry-Perot (FP) cavity which has been frequency calibrated using saturation spectroscopy of Cs and a wave-meter.

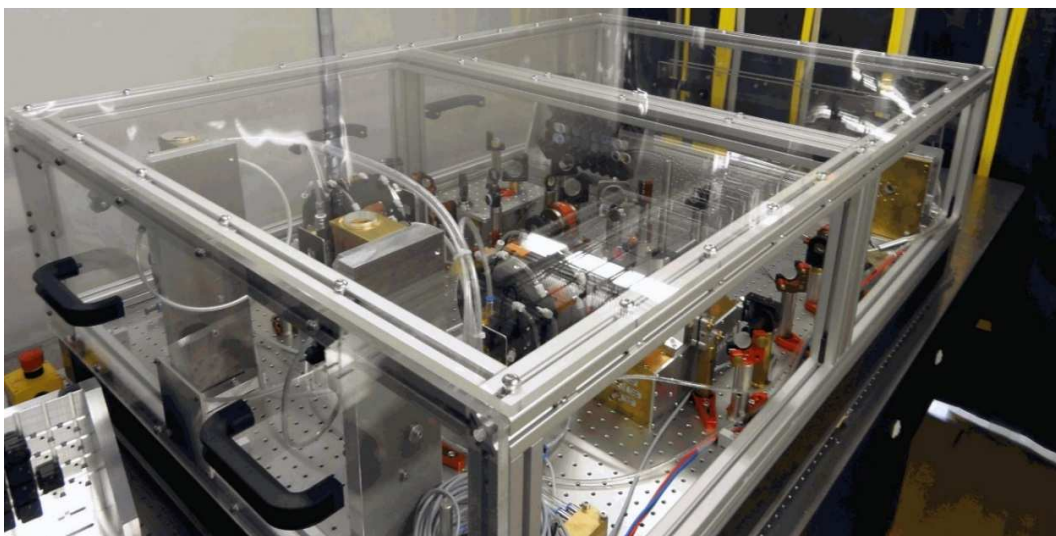


Figure 10: Picture of the thin-disk laser enclosed in a Plexiglas box. The box dimensions are 110 x 190 x 50 cm³.

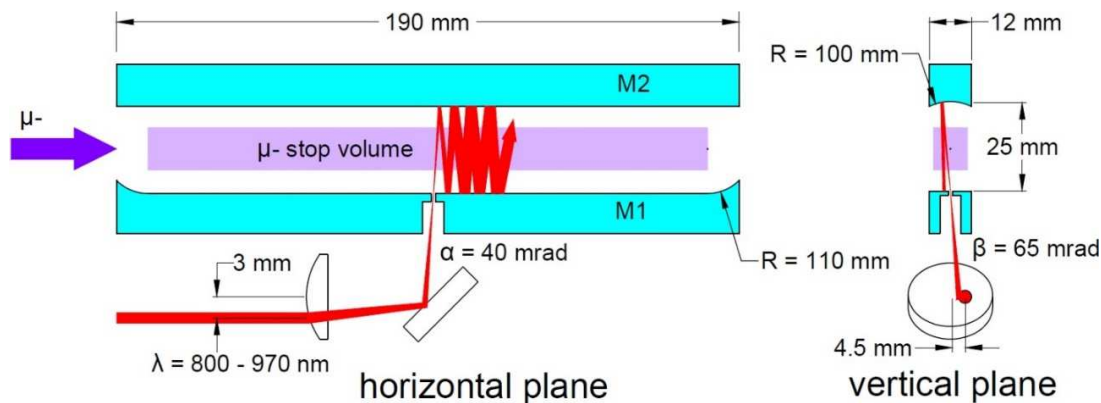


Figure 11: Scheme of the multi-pass cavity and its in-coupling as used in the beam time of 2014 to illuminate a large volume. The multi-pass cavity itself consists of two 190 mm long mirrors. A focusing optical element is used to inject the light through the 0.63 mm large hole in one of the mirrors. The cylindrical mirror (top) creates vertical confinement for the incoming laser beam while the end-parts of the flat mirror (bottom) create horizontal confinement. Injection under a finite angle in horizontal and vertical direction is used to illuminate the enclosed volume appropriately for the experiment. The muon stop volume is given in purple.

The length of about 70 ns of the output pulse was chosen as a trade-off accounting for optical damage of the enhancement cavity and the background rate in the observation time window of the 8 keV X-rays. Adjustment of the pulse length was obtained by variations of the pump energy and pump-energy density, the length of the optical cavity and the choice of the transmission of the out-coupler. These parameters were varied depending on the laser wavelength during data-taking.

As visible in Figure 9, injection seeding was performed through the output coupler. Besides providing the single-frequency operation, the seeding light also enforces the directionality of the light circulating in the ring cavity. In such a way, feedback from the oscillator into to cw Ti:Sa laser is eliminated. Most importantly we also protect the fibers used to transport the cw light from the cw Ti:Sa laser to the pulsed Ti:Sa laser from the backwards traveling pulse.

Frequency chirps occurring in the pulsed Ti:Sa [97] laser have been quantified in two ways: using a wave-meter apt for the measurement of pulses and by performing spectroscopy of a krypton-absorption line. A frequency shift of -60 (20) MHz has been measured for a Ti:Sa output pulse energy of 8 mJ. This shift is negligible compared with the statistical uncertainty of about 17 GHz of the frequencies of the measured 2S - 2P transitions in μHe .

The energy of the pulse emitted by the Ti:Sa laser is adjusted by means of a wave-plate and a polarizing cube. The pulses are propagated from the laser hut to the πE5 area, where they first enter the muon beam line, then the gas target. There they are coupled into the optical multi-pass cavity [55] surrounding the muon stop volume used to enhance the laser fluence seen by the muonic atoms. The laser pulses were reaching the target with a delay of about 900 ns with respect to the trigger time. A commercial beam pointing stabilization system by TEM-Messtechnik having two two-axis motorized mirrors and two quadrant detectors was used to minimize beam drifts at the entrance of the muon beam line. One quadrant detector was placed in the laser hut, at the Ti:Sa laser output, while the second one was mounted in the vicinity of the muon beam line.

The working principle of the multi-pass cavity [55] used to enhance the laser fluence is sketched in Figure 11. This cavity consists of two 190 mm long mirrors (M1 and M2) placed alongside the muon stop volume with a spacing of 25 mm. Mirror M2 is cylindrical with a curvature radius of $R = 100$ mm. This

mirror ensures confinement of the laser light in vertical direction. The other mirror, M1, is flat except for the upstream and downstream extremities where two cylindrical end-pieces with a radius $R = 110$ mm are mounted. These end-pieces, which are curved horizontally, ensure the confinement of the laser light in the horizontal direction.

The laser pulses are coupled with an efficiency (in terms of energy) of about 95 % into the cavity through a small hole with a diameter of 0.6 mm at the center of the flat mirror (M1) with an angle of 40 mrad and 65 mrad in horizontal and vertical direction, respectively. This tilt is achieved by shifting the laser beam off-axis with respect to the optical axis of the lens placed in front of the coupling hole as sketched in Figure 11. The shifts are 3 mm in horizontal direction and 4.5 mm in vertical direction. The purpose of this lens with a focal length of 75 mm is to focus the beam down to a waist of about 0.1 mm at the center of the coupling hole.

The in-coupled beam bounces successively between the two mirrors M1 and M2. The average number of reflections depends on the average reflectivity of the mirrors over their large surface. The mirrors have a nominal reflectivity of 99.98% between $\lambda = 800$ nm and $\lambda = 1000$ nm. However, several loss mechanisms reduce the efficiency: the non-specular scattering given by the surface roughness, the particulate contamination, the imperfections of the coating, the losses at the coupling hole and the losses at the transition regions between the flat mirror and the cylindrical end pieces. At best, a confinement time of 110 ns has been observed which corresponds to an average number of reflections of about 1300.

The tilt of the in-coupled laser beam, the divergence of the laser beam and the various parameters of the cavity have been chosen to achieve an almost homogeneous light distribution in a volume with transverse area of 190×8 mm². After in-coupling the laser light bounces between the two mirrors and spreads out in the cavity. An example of a measured light distribution for an aligned cavity is shown in Figure 12. A sufficiently homogeneous light distribution is observed. The “peak” close to the center is produced by the first bounces of the laser light immediately after in-coupling, i.e. at a time when the spreading of the laser pulse due to its divergence is still limited. In this measurement, the light is injected at a direction moving to the right. Contrarily, the light distribution on the left side of the coupling hole shows a much better homogeneity because this region is reached after a reflection at the right cylindrical termination of the flat mirror. This implies that many bounces occur between the two mirrors before the pulse reaches the left side of the cavity for the first time. The horizontal profile also shows two maxima at the end pieces where the light moving outwards is reflected back towards the center.

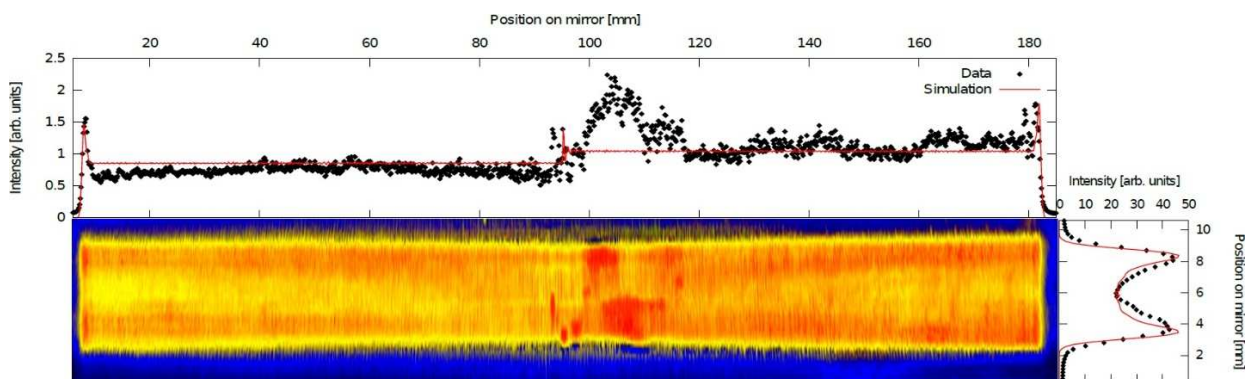


Figure 12: Distribution of the light fluence inside the cavity measured using a thin wire that is moved along the long “axis” of the cavity volume. The 2D plot shows the light distribution in the mid-plane in-between the two mirrors M1 and M2. The corresponding horizontal and vertical 1D projections are also shown. The light is injected in the center and moves initially to the right. (Reproduced from [55]).

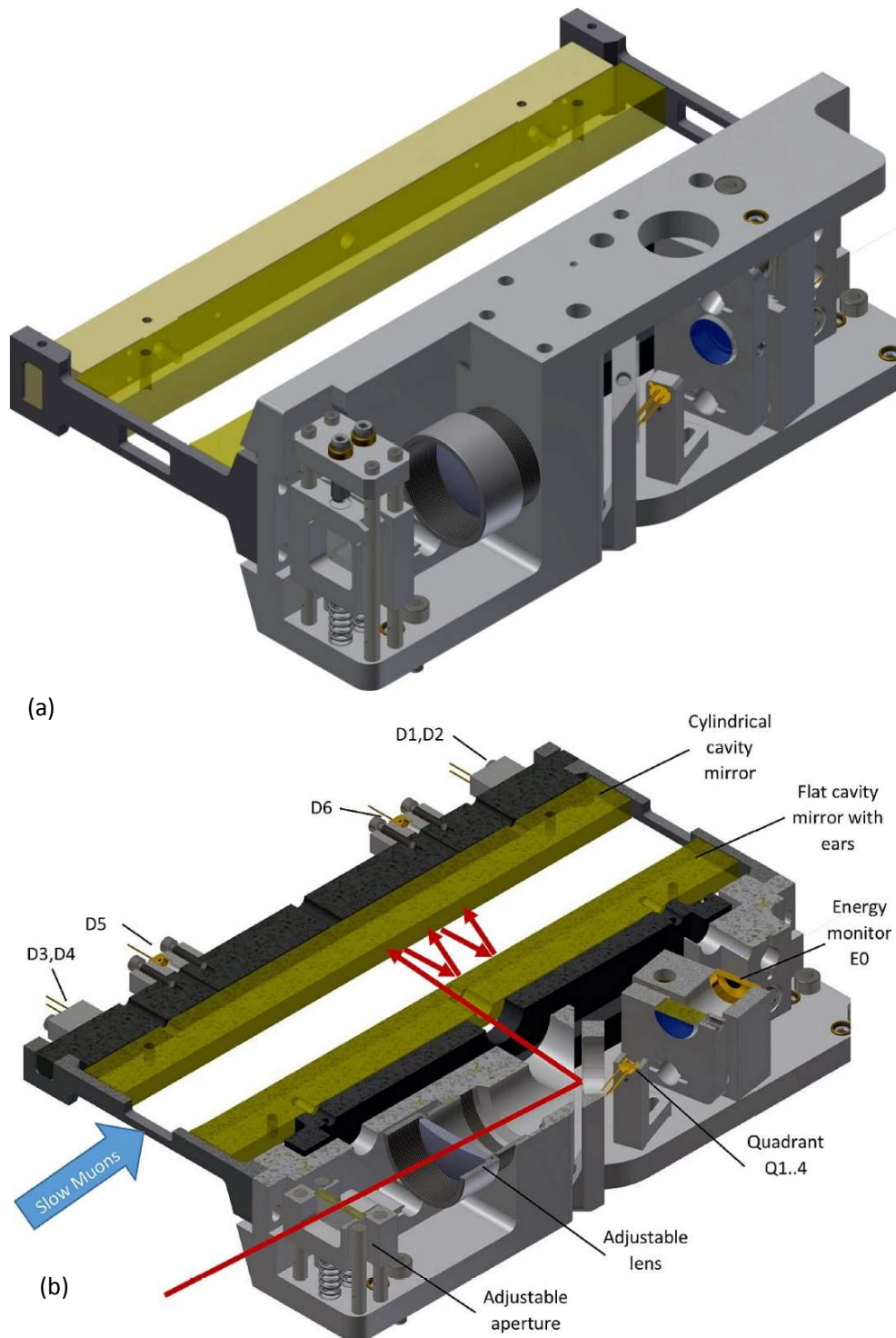


Figure 13: 3D drawing of the multi-pass enhancement cavity surrounding the muon stop distribution. The two mirrors are given in green while the path of the laser pulse just before and just after in-coupling is drawn in red. (a) Global view which shows the “monolithic” of the mechanics which cannot be accessed during data-taking. All adjustable components are accessible only from the top given the constraints from the target. (b) A cut of the 3D drawing of panel a) in the plane of the laser propagation. Various diodes (Q_i , E_0 , D_i) are installed to monitor the light in-coupling and distribution in the cavity.

To prevent damage to the substrate when a misaligned laser beam impacts the borders of the coupling hole we implemented a slit system (adjustable aperture) in front of the coupling lens (see Figure 13). In addition, the position of the laser beam at the cavity hole is monitored by imaging the beam leaking from the 45-degree mirror into a quadrant detector Q1.4 so that the quadrant position is equivalent to the position of the hole. A large diode E0 is used to measure the incoming pulse energy. Several photo-diodes D_i have been placed on the backside of the mirror M2 as visible in Figure 13 (b) to monitor the light distribution inside the cavity during data-taking. From this data, we extract the space-resolved intensity of the circulating light and its lifetime. Non-optimal in-coupling, misalignment and possible damage of the optical cavity were monitored in this way. The information from these diodes was recorded in the data acquisition (DAQ) system and is used in the final analysis to correct for fluctuations of the pulse energy and laser fluence on a pulse-to-pulse basis.

3.4. Requirements for the laser system

The muons reaching the He gas target have a stochastically distributed arrival time (cw muon beam) and an average intensity of about 280 /s. The average laser-trigger rate R_{laser} not only depends on the muon intensity, but also on the required minimal delay time (dead time of the laser system) t_{min} between two laser shots:

$$\frac{1}{R_{laser}} = t_{laser} = t_{muon} + t_{min} \quad (11)$$

where t_{muon} is the average time between two successive muons and t_{laser} the average time between two laser shots. Therefore, the dead time of the laser system has to be sufficiently short (<1.5 ms) to avoid a significant decrease of the laser-trigger rate relative to the average muon rate.

Table 1: 2S - 2P transition properties for $\mu^4\text{He}^+$ and $\mu^3\text{He}^+$. E differences, wavelengths, sub-level populations η and the laser fluences F_{sat} required to saturate the transition are given. For the wavelengths, we assumed here the predictions when we wrote the proposal.

Isotope	Transition	ΔE [meV]	λ [nm]	Pop. (η)	F_{sat} [J/cm ²]
$\mu^4\text{He}^+$	$2S_{1/2} - 2p_{3/2}$	1526	812	1	1.1
$\mu^4\text{He}^+$	$2S_{1/2} - 2p_{1/2}$	1380	898	1	2.2
$\mu^3\text{He}^+$	$2S_{1/2}^{F=0} - 2P_{1/2}^{F=1}$	1119	1108	$\frac{1}{4}$	2.1
$\mu^3\text{He}^+$	$2S_{1/2}^{F=0} - 2P_{3/2}^{F=1}$	1294	958	$\frac{1}{4}$	1.1
$\mu^3\text{He}^+$	$2S_{1/2}^{F=1} - 2P_{1/2}^{F=1}$	1286	964	$\frac{3}{4}$	3.2
$\mu^3\text{He}^+$	$2S_{1/2}^{F=1} - 2P_{1/2}^{F=0}$	1344	923	$\frac{3}{4}$	6.4
$\mu^3\text{He}^+$	$2S_{1/2}^{F=1} - 2P_{3/2}^{F=2}$	1436	863	$\frac{3}{4}$	1.3
$\mu^3\text{He}^+$	$2S_{1/2}^{F=1} - 2P_{3/2}^{F=1}$	1461	849	$\frac{3}{4}$	6.4

Table 2: Requirement for the laser system used in the muonic helium experiment.

Wavelength (tunability)	800-970 nm
Pulse energy (transition dependent)	8-15 mJ
Pulse-to-pulse energy fluctuation	< 5% rms
Bandwidth	< 1 GHz
Delay between trigger and pulse in the cavity	< 1 μ s
Average trigger rate	200 Hz
Trigger time structure	stochastic
Number of reflections in the enhancement cavity	1000
Uptime	> 90%

In the beam times of 2013 and 2014 we limited the minimal time between two laser shots to about $t_{min} = 1.5$ ms. Shorter t_{min} were leading to pulse-to-pulse instabilities of the Ti:Sa laser. Therefore, the laser system was triggered at an average repetition rate of about $R_{laser} \approx 200$ /s during data-taking.

The short lifetime of the 2S state (1.7 μ s at 3 mbar pressure) also poses a tough requirement to the laser system. Practically, the latency time of the laser system has to be smaller than 1 μ s to avoid significant losses of the 2S population prior to the arrival of the laser pulse which would result in a significant decrease in the event rate. Therefore, the laser system has to deliver its pulse within 1 μ s after being triggered by the muon entering our setup.

The laser system must also be tunable in the wavelength range from 800 to 970 nm. In fact, as summarized in Table 1, the expected wavelengths of all-possible E1 transitions but one lie within this range. All these transitions but the one at 1.1 μ m are accessible with a Ti:Sa laser. However, for several of these transitions the Ti:Sa laser has to be operated far away from its gain maximum which is at a wavelength of about 795 nm. This has to be compensated by increasing the pulse energy of the pump laser (the thin-disk laser).

The transition probability W that a μHe^+ atom is excited from the 2S state to the 2P state by the laser pulse is

$$W = \eta \epsilon_{2S} (1 - e^{-F/F_{sat}}), \quad (12)$$

where $\epsilon_{2S} = 1.5\%$ is the total 2S-state population at 3 mbar of pressure of the target gas, η is the fraction of population within the 2S sub-levels, F the laser fluence and F_{sat} the laser fluence needed to saturate the transition. Here we assume that the laser frequency is resonant with the transition. The values of F_{sat} and η are reported in Table 1 for each transition. Large laser fluences increase the event rate, but to avoid power broadening of the transition the scan of the resonance has to be performed at fluences $< F_{sat}/2$, so that at most 30% of the sub-level population is transferred to the 2P state by the laser pulse.

Even though we are dealing here with E1 transitions, the saturation fluence required to drive the 2S - 2P transitions in muonic helium is large because of the smallness of the muonic helium atom (small matrix element). The required laser pulse energy depends on the saturation fluences, scales linearly with the area of the cavity mirrors that needs to be illuminated, and scales inversely proportional to the enhancement factor of the cavity. For the specific cavity previously described, an in-coupled pulse of 10 mJ energy yields

a laser fluence of 0.8 J/cm^2 . This value has to be compared with the values of F_{sat} reported in Table 1. When accounting for non-negligible beam losses occurring between the Ti:Sa laser and the enhancement cavity we see that the Ti:Sa laser has to deliver pulses with energies between 8 mJ and 15 mJ.

The goal of the experiment is to measure the 2S-2P transition frequencies with a precision of about 50 ppm. The transition frequencies must thus be determined with a precision of approximately 15 GHz, which corresponds to $\Gamma/20$ where $\Gamma = 320 \text{ GHz}$ is the natural line width of the 2S-2P transition. Therefore, only moderate requirements for the laser bandwidth exist: it must be smaller than a few GHz, so that it does not significantly affect the precision of the measured transition.

The various requirements for the laser system are summarized in Table 2. The pulse-to-pulse stability of the laser is a relevant issue as variations of the pulse energy could result in a systematic distortion of the line shape. An asymmetry of the average pulse energy between measurements on the left and on the right side of the resonance (red and blue detuned, respectively) causes a shift of the line center of the measured resonance. For this reason, we are recording the intensity of the laser light inside the cavity to be used offline to correct for this effect. To keep these corrections small, long-term stability and small pulse-to-pulse-fluctuations are advantageous.

The laser system has to operate continuously and with an uptime larger than 90 % over several months. This is related to the low event rate of about 5 events/hour on resonance (1 background event per hour) and to the large scanning range where the lines had to be searched due to the uncertainty of the nuclear effect and the possibility of physics beyond the standard model.

4. The active medium of the thin disk

The thin-disk laser [98, 99, 100, 101] is a diode-pumped solid-state laser of high average power capability, excellent beam quality and a high wall-plug efficiency. It represents one of the workhorses in the high-power industrial sector and in research for continuous wave operation (CW), nanosecond pulse operation (ns) and mode-locked (fs) operational modes. The power scalability of the thin-disk laser is related to the geometry of the active medium and its pump and cooling schemes. In this chapter, we first introduce the working principle of the thin-disk laser with an emphasis on the design of the active medium, its power scalability and its limitations. Then we concentrate on the thermal lens effects of the active medium. In more detail:

- **Section 4.1: Principle of the thin-disk laser**
The thin-disk laser concept and its power scalability are presented. This includes the geometry of the active medium and an introduction to the typically used pump scheme.
- **Section 4.2: Amplified spontaneous emission**
The amplified spontaneous emission (ASE) represents a limitation for power and energy scaling. Various active medium designs mitigating this limitation are discussed.
- **Section 4.3: Thermal lens**
In this section, three different effects contributing to the residual thermal lens of the active medium are discussed. Spherical and aspherical components are scrutinized. Results of simulations based on finite element methods are also presented.
- **Section 4.4: Analytical model of the bending of the thin disk**
A simple analytical model of the main thermal lens effect related to the bending of the assembly of thin disk and heat sink is presented. It allows fast evaluation of the thermal lens effect. The results are compared with finite element method (FEM) calculations.

This chapter is thus mainly devoted to the characterization of the thin disk: from the gain profile, to thermal lens and aspherical optical phase distortions (OPD). The gain profile together with the aspherical components give rise to aperture effects that are discussed further in Chapter 5. These aperture effects have a significant impact on the design of resonators and multi-pass amplifiers. Consideration of these aperture effects becomes mandatory, for example, for the multi-pass resonator architecture presented in Chapter 8 apt for energy scaling of thin-disk mode-locked oscillators. The thermal lens effects presented in this chapter are also at the core of a new scaling limitation disclosed for the first time in Chapter 9 given by a self-driven growth of misalignment.

4.1. Principle of the thin-disk laser

The thin-disk laser is a solid-state laser with the ability to generate high average power, high pulse energies, with good beam quality and high efficiency [102, 103, 104, 105]. The active medium of a thin-disk laser is a crystal (e.g. Yb:YAG) shaped as a disk typically with several mm in diameter and a thickness of between 100 and 400 μm . The diameter is dictated by the output power and pulse energy, while the thickness depends on the active material, its doping concentration and the mode of operation. The active medium is pumped optically using high-power diode lasers of low beam quality.

The geometry of the active medium of the thin disk optimizes the thermal management of the heat produced by the pumping process to minimize the thermal stress that may lead to fracture and birefringence, and to minimize the gain losses due to the increase in temperature. This is especially important for Yb:YAG as it is characterized by a strong thermal overlap between the ground state and the lower laser energy level (for this reason Yb:YAG is often referred to as a quasi three-level system).

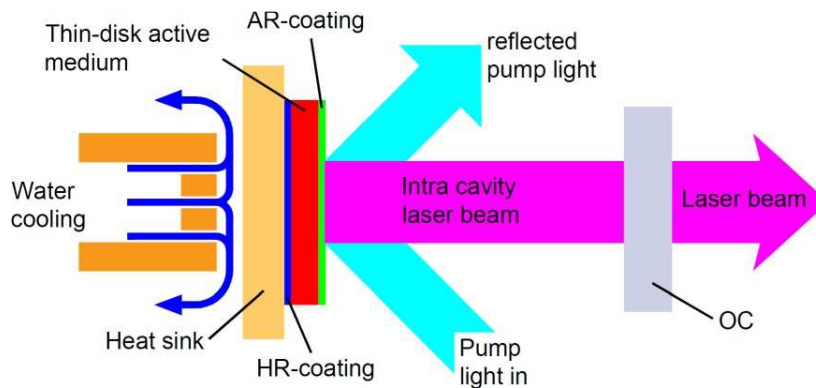


Figure 14: Principle of the thin-disk laser. The laser resonator is formed by the HR-coating on the backside of the active medium, the active medium and the out-coupling (OC) mirror. The active mirror is contacted with a water-cooled heat sink. HR = high-reflectivity coating, AR = anti-reflective coating.

A scheme of the working principle of thin-disk laser with an emphasis on the assembly of the thin disk and the heat sink is depicted in Figure 14. A face of the cylindrically shaped thin disk is thermally contacted with a water-cooled heat sink. The contacted face is coated with a high-reflective (HR) stack that serves as a mirror for both the laser ($\lambda = 1030 \text{ nm}$) and the pump ($\lambda = 940 \text{ nm}$) wavelengths. A laser beam impinging on the thin disk is thus amplified, back reflected and again amplified. By placing a mirror (out-coupler) in front of the thin disk, a simple laser oscillator can be formed composed of the HR mirror, the active medium, and the out-coupler. The pump radiation is brought to the thin disk in a quasi end-pumped configuration.

To understand the superiority of the heat management in a thin-disk laser consider Figure 15. It compares the temperature distributions of a pumped active medium for a rod laser (left panels) and for a thin-disk laser (right panels). The rod is pumped and cooled radially. Therefore, for rods, the heat transport occurs in radial direction, i.e. perpendicular to the laser direction. The radial heat removal brings about a radial temperature profile with a maximum on the rod axis. The maximal temperature increases with the square of the diameter of the rod (assuming constant and homogeneous heat generation in the rod volume) while the minimum is at the rod surface which is typically water-cooled (see Figure 15 (c)). Hence, the maximal temperature of the rod increases linearly with the output power (energy) whose scaling to avoid optical

damage calls for an increase of the laser eigenmode (beam) width, and thus an increase of the rod diameter to avoid optical damage. The parabolic temperature profile in the transverse direction gives rise to a strong thermal lens effect because of the temperature dependence of the refractive index (dn/dT) [106].

Contrarily, the thin disk is pumped in a quasi end-pumped configuration, and the heat flow occurs along the disk axis that corresponds to the laser axis. As the temperature gradient is mainly along the laser axis, the thermal lens effects related with the temperature dependence of the refraction index is strongly mitigated. Still, as will be detailed later, thermal lens effects do exist and represent the most severe limitation in power scaling of thin-disk lasers, given the large width of the eigenmode needed for high-power lasers.

While heat removal from the central rod region is hindered by the necessity to cross a distance of several mm comparable to the rod radius, heat removal in the thin disk is very efficient as heat transport occurs over a distance of only about 100 μm comparable to the thickness of the thin disk. Cooling of the thin disk is thus effective, given the short distance the heat has to flow, and the large cooling surface relative to the volume where the heat is produced (high surface-to-volume ratio).

Thin-disk lasers are considered power and energy scalable because the thermal lens effect and the temperature within the active medium do not depend on the pump power but only on the pump power

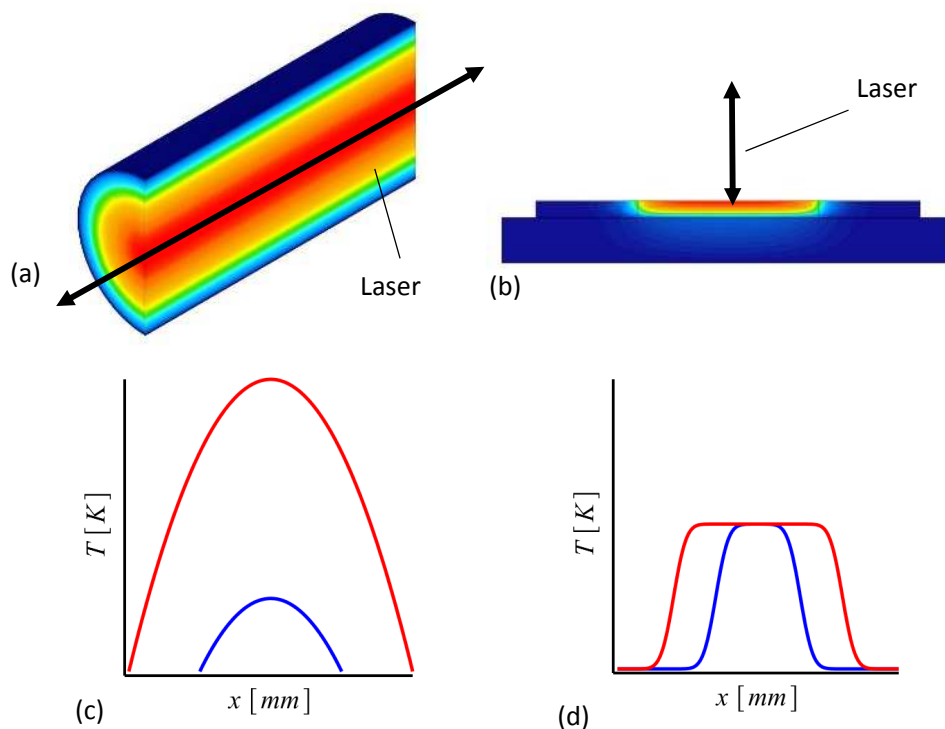


Figure 15: Temperature distributions in the active medium of a rod (left panels) and a thin disk (right panels). (a) 3D temperature distribution in a homogeneously pumped and transversely cooled rod having a maximum in the rod center. The heat flow is in radial direction. (b) 3D temperature distribution in its thin disk. The heat flow is in axial direction. (c) 1D temperature profiles of the rod (for a direction transverse to the rod axis) for two pump spot diameters. The maximal temperature scales with the square of the diameter of the pumped region (rod) assuming constant pump power density. (d) 1D temperature distributions at the surface of the thin disk in transverse direction (perpendicular to the thin-disk axis) for two pump spot diameters assuming a constant pump power density. The temperature in the central region does not depend on the pump diameter and the pump power but only on the pump power density.

density (see Figure 15 (d)). Thus, energy and power scaling can be obtained in principle “simply” by increasing the pump spot and the eigenmode sizes while keeping a constant pump power density.

Moreover, the efficient cooling allows pumping in the kW power range and the use of quasi-three-level system materials [107] having a low quantum defect and high gain. To date, the material of choice, especially in industrial applications, is Yb:YAG. However, the community is searching and optimizing new materials showing greater thermal conductivity, for higher output power and having larger bandwidths for ultrashort pulse generation and tunable lasers [108, 109, 110, 111, 101].

The small thickness of the thin disk provides outstanding cooling and power scaling. Yet, in a single pass through the active medium (the thin disk), only a small fraction of the pump light is absorbed. By making the backside of the thin disk reflective also for the pump wavelength, a double pass in the active material can be realized. Still, the absorption in this double pass is not sufficient. This shortcoming related to the minor absorption of the pump radiation due to the small thickness of the thin disk can be compensated using a multi-pass scheme for the pump light [112, 113, 53].

The working principle of this multi-pass pump scheme, which is used to redirect the (not absorbed) pump light to the active material several times, is depicted in Figure 16. The light produced by a high-power diode laser is first homogenized in either a multi-mode fiber or a rod homogenizer [100]. The output surface of this optical element is then imaged into the thin disk with a suitable magnification. The light not absorbed by the disk in the double-pass propagation through the active material is then redirected to the disk after a 4f-propagation, which is realized using a system of prisms and a large parabolic mirror [100, 53]. Iterating this scheme allows the realization of multiple passes. The numbering given in Figure 16 (b) describes the sequence of the pump beam positions at the parabolic mirror for the various passes. Starting from position 1 the pump beam is moving towards the disk. At the disk, the light is back reflected to position 2. From there the light is redirected to the system of prisms which retro-reflects the pump light at position 3. From there the light reaches position 4 after a second reflection at the disk. Iterating this scheme of reflections between thin disk, parabolic mirror and prisms, several passes at the active medium can be realized. In the particular case depicted in Figure 16 (b) when the beam reaches the spot 14, it is back reflected by the system of prisms so that the beam travels back the same path but in opposite direction, doubling the number of passes at the thin disk.

From the optical point of view, the propagation of the pump beam follows the scheme: 4f-imaging, disk, 4f-imaging, disk... and so on. The imaging properties of the 4f-scheme reproduce the beam spot profile and its divergence from pass to pass (neglecting phase-front distortions occurring at the disk). Therefore, this multi-pass scheme can be used to generate a flattop profile, that is, a pump profile with sharp boundaries. This is achieved because the light profile at the output face of the homogenizer typically has a flattop profile. Imaging this profile into the disk and realizing the multi-pass propagation of the pump light using a 4f-relay imaging results in a flattop pump profile. A well-defined pump region with sharp boundaries is important particularly for three-level-system materials due to the high lasing threshold. By contrast, a Gaussian pump profile would lead to a lower laser efficiency.

The multi-pass arrangement guarantees an efficient absorption in the order of 80 % of the pump beam. Together with the use of Yb:YAG as an active material, a quasi three-level material, with large gain and small quantum defect (laser wavelength at $\lambda = 1030$ nm, and pump wavelength at $\lambda = 940$ nm or $\lambda = 976$ nm), this guarantees an overall optical-to-optical efficiency of up to 72 % [105] for the thin-disk laser.

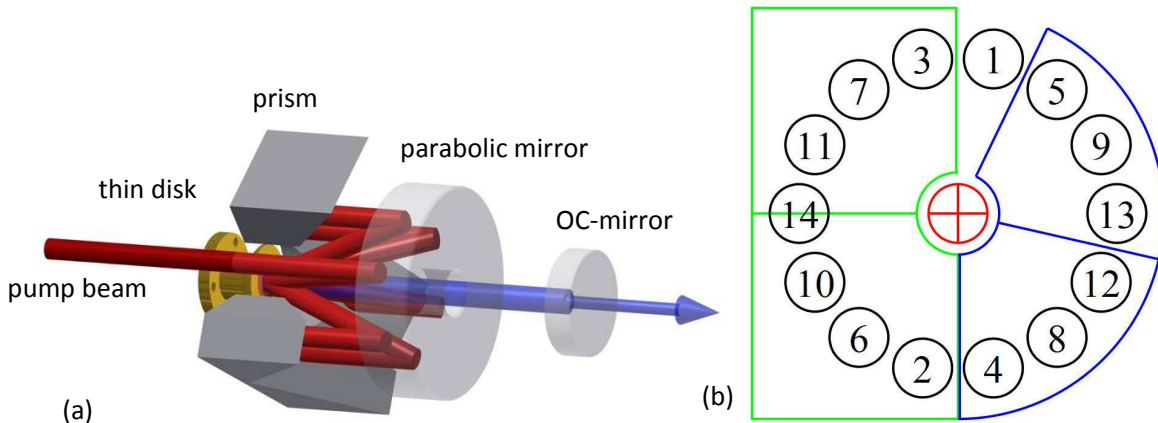


Figure 16: Pump optic arrangement for thin-disk laser. (a) 3D scheme showing the various passes of the pump beam at the disk based on an imaging scheme formed by a parabolic mirror and a system of prisms. The pump beam is in red, the laser beam in blue. (b) Schematic of the beam routing at the parabolic mirror position. The projections of the disk (red cross) and prisms (blue and green) are also shown. Using this configuration, the pump light is redirected to the thin disk 14 times. See [53] for more details.

Summarizing, the temperature gradient in the thin disk is mainly along the thin-disk axis, which is parallel to the laser beam axis. Together with the efficient cooling, due to the large surface-to-volume ratio, this leads to a significant suppression of the thermal lens effect. An additional consequence of the geometry of thin disk and heat sink is that the temperature in the pumped region only depends on the pump power density (assuming pump diameters larger than few times the disk thickness). This feature underlies the power scalability of thin-disk lasers because larger output power and energy can be reached “simply” by scaling the pump and the laser beam sizes while keeping the same pump power density and laser intensity.

However, the increase of the laser mode needed for energy and power scaling results in an increased sensitivity to the residual thermal lens effects which eventually limit the achievable scaling [100, 114, 115, 116]. Even though thermal lens effects are strongly suppressed in the thin disk, nowadays they still represent the major limitation in power scaling due to the large laser beam width involved at the high power (energy) frontier. This thesis focuses on the design and realization of resonators and multi-pass amplifiers that minimize the sensitivity to thermal lens variations opening the way to energy and power scaling.

4.2. Amplified spontaneous emission (ASE)

In this section, we briefly introduce an important limitation in power and energy scaling of thin-disk lasers: the amplified spontaneous emission (ASE) [117, 118, 119, 120]. It is the large aspect ratio between the transverse size (5 to 10 mm) of the pumped region and the thickness of the active region (100 μm) that gives rise to strong ASE effects in thin-disk lasers [121, 122]. In fact, as shown in Figure 17 (a), a laser beam that is reflecting on the thin disk experiences a small gain, proportional to the thickness d_{AM} of the active medium. Contrarily a photon that is emitted spontaneously in transverse direction as shown in Figure 17 (b) is traveling a much larger (two orders of magnitude) path in the pumped region of the active medium

experiencing a correspondingly larger gain. The amplification of the spontaneously emitted photon is thus large and leads to a reduction of the population inversion with consequent decrease of the gain for the laser light.

The amplification of the spontaneously emitted photon is further increased by the fact that a considerable part of the spontaneously emitted light is trapped in the thin disk due to total internal reflection [123, 117, 121] as shown in Figure 18. Because of the total internal reflection, the ASE photons have a long path in the pumped region and are redirected several times from the disk periphery to the pumped region. This feedback to the pumped region significantly enhances the amplification process of the spontaneously emitted photons. It may even happen that gallery modes start to lase within the active medium causing a dramatic decrease of the thin-disk gain [124].

As ASE increases with increasing pump spot diameter, it represents a serious limitation to energy scaling. For laser operation in the CW operational mode, this effect is mitigated because the circulating laser intensity stimulates the coherent emission of photons into the laser beam. Oppositely, for so-called fluorescence operation, where the laser is pulsed at low repetition rates, ASE limitations are severe because prior to the formation of the laser pulse there is no circulating laser power. Thus, the large majority of the pump power (we assume continuous pumping) is converted into ASE.

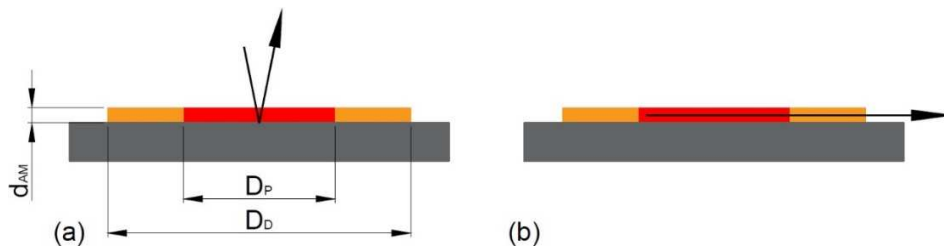


Figure 17: Comparison between the path lengths in the active medium travelled by a laser photon circulating in the thin-disk laser resonator (a) and a photon spontaneously emitted in transversal direction (b). The gain for the laser light is considerably smaller than the gain for the spontaneously emitted photon given the fact that for typical applications $d_{AM} = 100 \mu\text{m}$ and the pump diameter $D_P = 5 \text{ mm}$. The pumped region of the disk is marked in red; the unpumped region of the doped thin disk is displayed in orange, and the heat sink is given in grey.

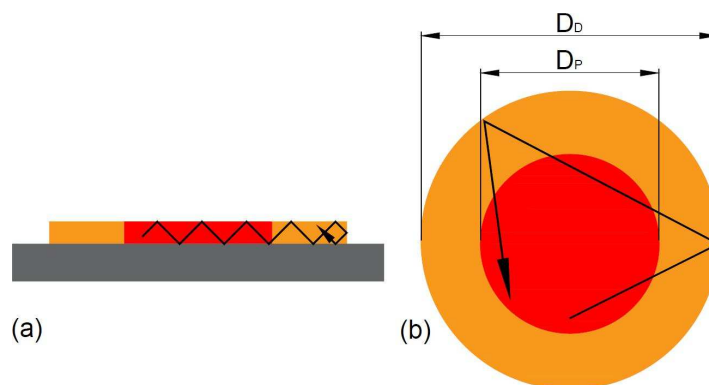


Figure 18: The total internal reflection occurring at the active medium boundaries increases the path length of the spontaneously emitted photons in the pumped region yielding a larger ASE effect. The pumped region of the disk is in red, the unpumped region of the doped thin disk in orange, and the heat sink in grey. The arrows represent the path of a spontaneously generated photon. For large values of the D_P/D_D , parasitic lasing may occur in the form of whispering gallery modes [125].

ASE has to be minimized because it decreases the gain and the energy stored in the active medium. This can be achieved by optimizing the thin-disk geometry, by beveling the disk border, by the correct choice of the HR coating, and the correct choice of the heat-sink material.

4.2.1. Reduction of the total internal reflection

Even though the front side of the thin disk is coated with an anti-reflective (AR) layer, the spontaneously emitted photon with an angle larger than a material-dependent critical angle (with respect to the normal of the surface) will undergo total internal reflection. For the front side of the thin disk, the critical angle only depends on the refraction index of the active medium and the refraction index of air [117, 121]. Hence, this angle can only be influenced by the choice of the active-medium host material (a reason to use fluoride crystals).

The backside of the disk, on the contrary, has a high reflective (HR) dielectric coating that is highly reflective for normal incidence but becomes transmissive at large angles relative to the normal of the surface. Approximatively, the HR coating of the backside becomes transmissive for angles where the front side becomes reflective due to total internal reflection. Differently from the front side of the disk, to understand the fate of the photon that is transmitted by the HR layer, we also need to consider the contacting of the active medium with the heat sink and the heat sink itself.

Consider first the thin disk design where the active medium is soldered into a metallic heat sink as shown in Figure 19 (a). Even though the HR coating for large angles is transmissive, the metallization reflects back the fluorescent light into the active medium. The ASE light is confined at the rear side of the disk by the reflectivity of the metallic heat sink.

By placing an absorptive layer in between the HR coating and the metallization, the back reflection from the heat sink into the active region could be eliminated or strongly reduced. Yet, this absorptive layer that automatically occurs when the metallic layer contains chromium as bonding agent, increases heat generation, reducing the optical damage threshold of the thin disk. Thin disks based on this design were tested and showed an overall reduced performance compared with active material glued onto diamond heat sinks [126].

In fact, the state-of-the-art thin-disk technology is based on the active medium being glued onto a diamond heat sink as shown in Figure 19 (b). Here the disk is contacted with a diamond heat sink using an optically transparent glue of high refractive index. Because of the large refractive indices of the glue ($n = 1.5$ [127])

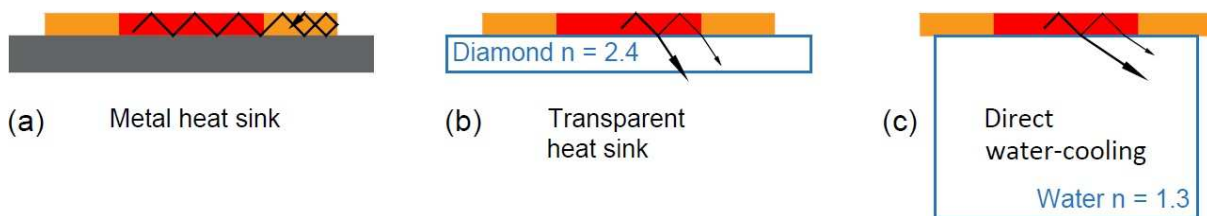


Figure 19: The reflection of the ASE light at the rear face of the thin disk can be reduced by suitable choice of the heat sink and its contacting with the active material. In (a) the active material is soldered to a metallic heat sink which reflects back the ASE light into the active material. In (b) the disk is contacted with a diamond heat sink using an optically transparent glue of high refractive index. In (c) the water directly cools the HR coating of the active medium. The larger refractive index of the water compared to air leads to a partial reduction of the total internal reflection. The red areas indicate the pumped region, the orange ones the active material and the metallic heat sink is shown in grey. The arrows represent the paths of spontaneously generated photons.

and the diamond ($n = 2.4$), the ASE photons escape from the active material and are dispersed in the diamond, reducing ASE effects. An optimized coating design accounting for the requirements of laser bandwidth and pump incident angle (see e.g. [128]) in combination with the use of a high-refractive index glue may significantly reduce the ASE effect and thus increase the gain of thin-disk lasers. Moreover, the use of diamond as heat-sink material is very advantageous: its superior heat conductivity and stiffness compared with metallic-based heat sink yields smaller thermal lens effects. The resulting lower temperature reduces self-absorption and thus increases gain.

Another possibility to suppress ASE is shown in Figure 19 (c) where the active material is in direct contact with the cooling water. In such a way, the critical angle above which total internal reflection occurs is increased by the fact that water has a refractive index of $n = 1.3$. In this way, a considerable fraction of the light is transmitted into the water and leaves the thin disk. RoFin-Sinar Laser GmbH introduced this design for high power thin-disk lasers in 1999 [129]; however due to the pronounced thermal lens of this design the laser design was limited to multi-mode lasers.

4.2.2. Beveling of the thin disk

The total internal reflection of the ASE radiation occurring at the disk borders redirects the ASE photons into the pumped region as shown in Figure 20 (a) leading to a further amplification of the ASE. In order to reduce this back-reflection from the disk periphery to the pumped region the disks may be beveled [117] as shown in Figure 20 (b). Photons that were transported via total internal reflection to the periphery of the disk experience an angle relative to the new normal of the disk surface that is smaller than the critical angle. Therefore, they are transmitted and escape from the disk. For photons still impinging on the slanted disk surface with an angle larger than the critical angle, total internal reflection occurs. However, the beveled surface reduces the incidence angle of the photon at next arrival to the surface, so that photon escape may occur.

Initially, beveling considerations were restricted to a single reflection at the edge of the thin disk. This resulted in the idea that the optimal angle relative to the thin-disk surface was 66° [123]. However, it was known that radiation absorbers usually made use of a grazing incidence as this increases losses [130, 131, 132]. Indeed, three-dimensional considerations showed that the photon escape efficiency increases with decreasing angle [117, 133]. The only drawback associated with the small angle is the reduction of the useful active region.

Another possibility to reduce the feedback from the periphery of the disk to the pumped region as shown in Figure 20 (c) is to roughen the surface of the disk periphery [133] so that photons arriving in this region may face angles smaller than the critical angle. The escape efficiency however is smaller in this case.

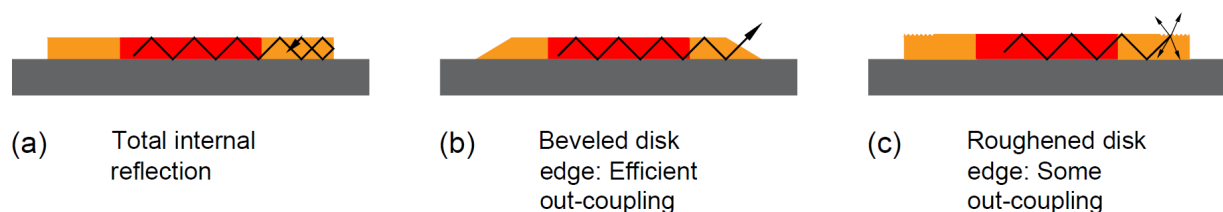


Figure 20: Beveling and roughening of the periphery of the thin disk reduce the feedback caused by total internal reflection from the disk border to the pumped region. (a) Feedback from the periphery to the pumped region caused by the total internal reflection at the disk periphery. (b) Beveling of the disk periphery leads to efficient extraction of the ASE photons. (c) Roughing of the disk periphery leads to partial out-coupling of the ASE light.

4.2.3. Thicker thin disk

Another way to mitigate the ASE problem is to reduce the ratio of axial to transversal dimension of the pumped region. This can be achieved by increasing the thickness d_{AM} of the thin disk as shown in Figure 21 (b). Therefore, the impinging laser beam experiences a longer path in the active region. As a consequence, the laser gain is increased relative to the ASE gain. However, this increase in thickness reduces the cooling efficiency and increases the temperature of the disk, which leads to a larger reabsorption of the laser light (quasi-three-level system) and thus to a lower gain. These effects can be partially attenuated by reducing the doping concentration that results in increased thermal conductivity [101].

The larger thickness of the disk gives rise; not only to an increased temperature but also to a larger deviation from a purely longitudinal heat flow causing stronger thermal lens and an increase of non-spherical contributions to the thermally induced optical phase delay OPD (see Sec. 4.3). Therefore, the optimization of the thickness of the thin disk d_{AM} is a trade-off between these various effects: ASE, thermal lens, deformation of the beam, reabsorption, optical damage and mechanical stress. For the muonic atoms experiments, a high gain and a large amount of stored energy are needed. For this reason we used disks with a thickness of 450 μm with a doping concentration of 5 % to be compared with the typical thickness of 140 μm and a doping concentration of 9 % used for CW or very high repetition rate operations [104, 134].

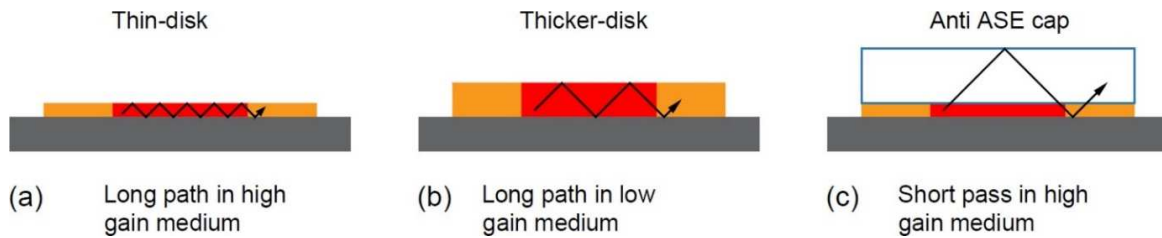


Figure 21: (a) Standard disk with a large ASE effect. (b) Thicker disk: the path length of the laser photons is increased compared to the path length of the ASE photons which remain the same as in (a). (c) Disk with an anti-ASE cap made by the same host material of the active medium but without doping. Heat deposition only occurs in the red region.

4.2.4. Anti-ASE cap

A decrease of the path travelled by the spontaneously emitted photons in the region with inversion population can be obtained by bonding a cap of undoped material to the front side of the thin disk. The anti-ASE cap only serves to dilute the spontaneously emitted photons so that they move in a region without doping and thus in a region with no gain. This is possible because the refractive index of the anti-ASE cap is similar to the refractive index of the doped material and therefore the total internal reflection is suppressed at the interface between active medium and cap [125]. The heat generation only occurs in the doped region, i.e. close to the heat sink [134, 135, 136]. Therefore, in this concept the temperature distribution, the gain and the heat flow in the doped region are similar to the ones occurring in a standard disk. Yet, the thermal lens effect in this type of thin disk is increased relative to a standard disk as the expansion of the undoped cap contributes to the mechanical bending of the disk. In addition, the aspherical components of the OPD are increased, due to a larger fraction of heat flow in radial direction. Moreover, there is also some heat deposition in the undoped cap, which increases the temperature of the front side of the disk.

Manufacturing this type of thin disk is more complex and more error-prone. The interface between doped region and undoped cap is exposed to high pump power and pulse energy. In addition, different thermal expansions of the two parts lead to mechanical stress. Adhesive-free bonding (optical contacting) is the method that can be used [137]. The reliability of the bonding process given the challenging requirements in terms of mechanical stress, optical and thermal properties is not yet to the level required for industrial applications, still very encouraging results have been observed as shown in Figure 22 and 23.

4.2.5. Our choice

In the initial phase of this project, we performed some studies of the gain profile for a disk having larger thickness (1 mm) and two disks each having an anti-ASE cap. We compared these measurements to a standard disk having a metallic heat sink. The results are summarized in Figure 22 and Figure 23. One of the two disks with anti-ASE cap (labeled “bonded 2” in the figures) shows an improved gain as expected from the reduction of the ASE effects. The other (labeled “bonded 1”), due to manufacturing issues does not show any gain improvement: with increasing pump power density it even performed worse than the disk soldered on the metallic heat sink. This manufacturing problem becomes evident when considering the 2D gain profile (not reported in this thesis) which shows a large asymmetry within the pumped region growing with pump power. This can be attributed to a poor thermal contact. Thus, presently the risks associated with the manufacturing of the thin disk with an anti-ASE cap outbalance the possible benefits. Especially the optical damage in pulsed operation could become the weakest point of this design. This was the reason for us to reject this design for our applications.

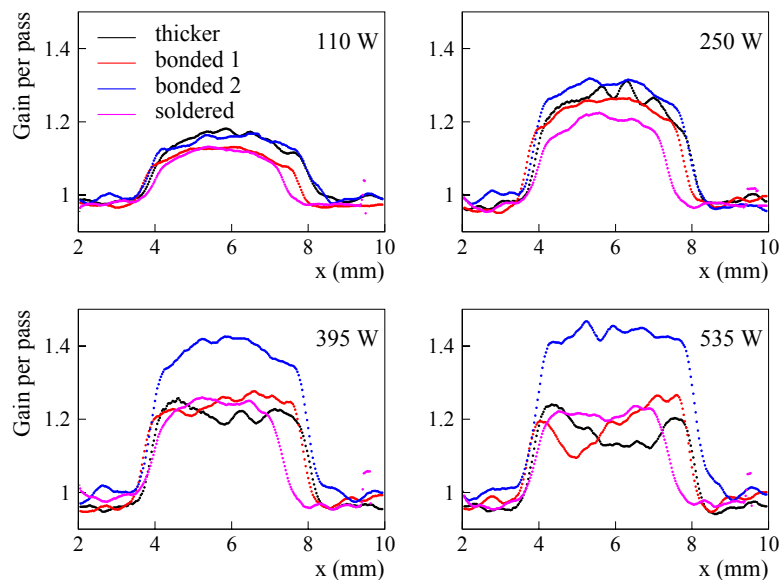


Figure 22: Space-resolved gain profiles measured for three different disk designs at various pump powers. “Thicker” denotes a disk of 1 mm thickness whose backside is directly water-cooled. “Bonded 1” and “bonded 2” denote disks having anti-ASE caps of 0.8 mm thickness. In these three cases, the active medium is directly cooled by the water, i.e. there is no additional support (in the form of a metallic heat sink or similar). “Soldered” denotes a standard thin disk soldered to a water-cooled metallic heat sink. The gain is given for the 1030 nm wavelength, the pump wavelength was at 940 nm, the total pump power is given in each panel. Details of the measurements are reported in Sec. 4.5.5 a summary of the thin-disk parameters is provided in Table 3.

The disk of 1 mm thickness (labeled “thicker” in the figures) for small pump power shows a slightly better gain. However, with increasing pump power (density) the issues related with the heat deposition outbalance the advantages related with the ASE reduction and therefore the performance decreases.

Thus, thicker disks do not show any gain increase, while the production of thin disks bonded to an anti-ASE cap is not yet a mature technology apt for the high-energy operation required for our experiments. On account of this preliminary study, which also includes interferometric measurements of the thin-disk thermal lens, we discarded unsupported thin disks (active medium directly cooled by the water), or disks with an anti-ASE cap. We opted to use thin disk glued onto a diamond heat sink. This choice is motivated by the reduction of ASE effects as explained above, but also by the reliability of the manufacturing process, the stiffness and the excellent thermal conductivity of the diamond heat sink that considerably reduce the thermal lens effect compared with conventional thin disk soldered onto metallic heat sinks. In this thesis, the thin disks glued onto diamond heat sinks were either delivered by TRUMPF or produced by our collaborators from IFSW, Stuttgart.

Table 3: Parameters of the disks used to measure the space-resolved gain of Figures 22 and 23.

Name	Thickness	Doping of Yb:YAG	Remarks
Thicker	1 mm	9%	Directly water-cooled Disk ideal for pulsed pumping
bonded 1	1 mm	9%	Directly water-cooled 200 μm doped; 800 μm undoped
bonded 2	1 mm	9%	Directly water-cooled 200 μm doped; 800 μm undoped
Soldered	0.2 mm	7%	Soldered to CuW

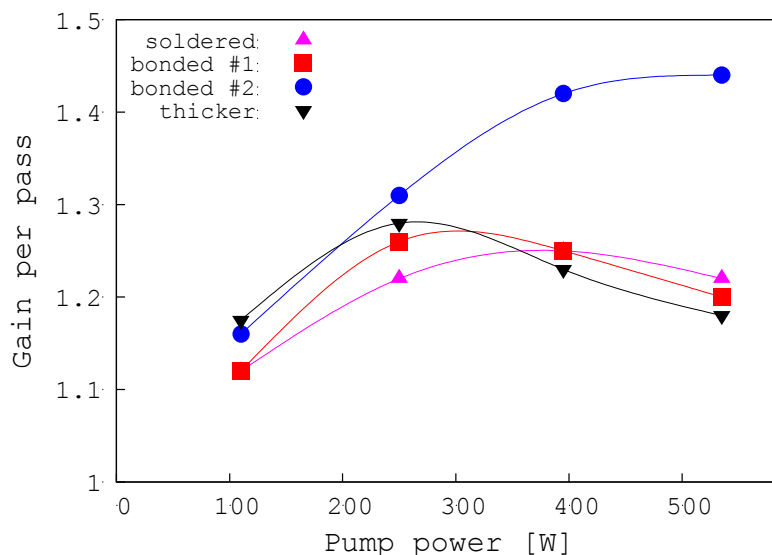


Figure 23: Laser gain for various thin-disk designs versus pump power. Plotted is the on-axis gain for the measurements shown in Figure 22.

4.3. Thermal lens

The thermal-lens effect is strongly suppressed in the thin disk because of the efficient cooling and the small temperature gradient in radial (perpendicular to the laser propagation) direction. Another consequence of the thin-disk geometry is that the temperature in the pumped region and therefore the thermal lens only depends on the pump power density (see Figure 15). These are the key properties underlying the power scalability of thin-disk lasers. However, power and energy scaling require an increase of the laser beam width resulting in increased sensitivity to the residual thermal-lens effects. In fact, the stability region for variations of the thermal lens decreases with the square of the laser eigenmode width. As will be demonstrated later, this increased sensitivity to thermal lens limits energy and power scaling [134, 138, 139] and calls for resonator and multi-pass amplifier designs having low sensitivity to thermal-lens variations.

In Sec. 4.3.1, we introduce the various contributions to the optical phase delay (OPD) at the thin disk. In Sec. 4.3.2, evaluations of the thermal lens effects using finite element methods (FEM) are presented while in Sec. 4.4 a simple analytical model describing the bending of the assembly of thin disk and heat sink is introduced. This bending, which is issued by the axial temperature gradient, gives rise to the largest component of the residual thermal lens. A comparison between the simple analytical model and the results from the FEM simulations is presented.

4.3.1. Thermal-induced OPD of the thin disk

Three main effects contribute to the thermal-induced OPD of the thin disk. These are summarized in Figure 24. The first and largest effect is related to the bending of the assembly of thin disk and heat sink caused by the axial temperature gradient; the second effect is given by the thermal expansion in axial (laser) direction; the third one is related to the temperature-dependence of the refractive index (dn/dT) of the active medium.

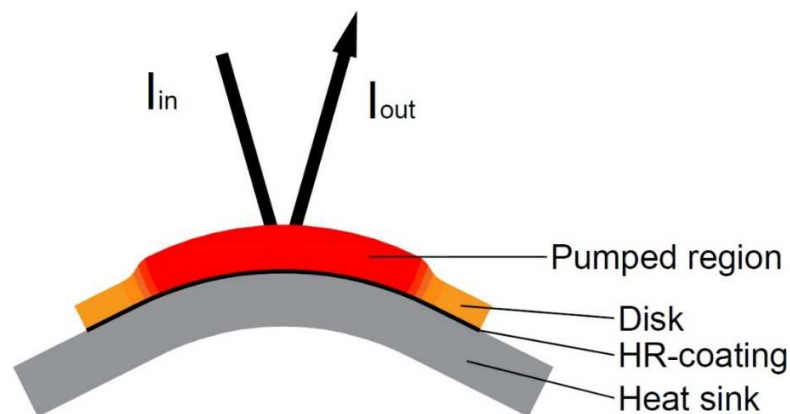


Figure 24: Thermal lens effect of the thin disk arising from the bending of the thin-disk assembly caused by the temperature gradient in axial direction similar to the effect in a bimetallic strip. The red region represents the pumped region, the unpumped region is given in orange. The temperature gradient in radial direction via the dn/dT and the expansion in axial direction yield an additional optical phase distortion. I_{in} and I_{out} represent the impinging and reflected laser beams, respectively.

A FEM simulation of the temperature distribution in the disk in pumped condition is shown in Figure 25. The backside of the heat sink is water-cooled down to 15 °C. The heat is generated in the pumped region of the active medium and is transported, basically in axial direction, to the water-cooled surface. Within the pumped region, the temperature distribution in radial direction is almost constant, as expected of a purely axial heat flow. At the periphery of the pump region there is an almost step-like change of the temperature (in radial direction).

The higher temperature in the pumped region leads to an expansion of the active material. The expansion in axial direction, i.e. in laser direction, gives rise to a longer optical path for the laser light being reflected at the “active” mirror. Hence, when only this effect is considered, the optical phase delay (OPD) experienced by the laser light is larger in the central region. Because of the homogeneous temperature distribution (in radial direction) within the pumped region, a laser beam experiences an OPD being basically constant in this region (when neglecting the bending of the thin disk which is treated separately). Contrarily, the abrupt change of the temperature in radial direction at the periphery of the pump region, combined with a non-zero dn/dT , gives rise to an abrupt change of the OPD in this transition region.

The expansion in radial direction leads to a bending of the disk. In fact, the inhomogeneous temperature distribution in axial direction gives rise to inhomogeneous thermal expansion. The rear side of the disk having a lower temperature expands less than the front side. The different expansions of front- and back-sides lead to a bending of the assembly of thin disk and heat sink similar to a bimetallic strip. The bending of the assembly of thin disk and heat sink induces a bending of the HR layer at the rear side of the active medium. An impinging laser beam being reflected at the disk is thus defocused due to the convex shape of the HR coating (see Figure 24).

An example of a simulated OPD that accounts for the three effects previously mentioned (bending, expansion in axial direction and dn/dT) using finite element methods (FEM) is shown in Figure 26. More details about this simulation will be given in Sec. 4.3.2. Within the homogeneously pumped area, the OPD can well be approximated by a parabolic profile given by the green curve. As the temperature in the central part is approximately homogeneous in radial direction, the temperature dependence of the refractive index ($dn/dT > 0$) and the thermal expansion in axial direction only cause a constant (x,y independent) change of the optical phase delay. This does not produce any thermal lens effect. Thus, within the pumped region the thermal lens effect can be well described by a spherical lens.

At the periphery of the pumped region, there is a quasi step-like variation of the temperature in transverse (x,y) direction. Over this small distance, the bending of the crystal exhibits no substantial change. Yet, here the OPD shows a deviation from the quadratic behavior because of the change of the refractive index versus temperature (dn/dT), and the change of the thermal expansion in axial direction. This deviation from the quadratic behavior is responsible for the excitation of higher-order beam components.

Outside the pump spot, the temperature of the active material is basically identical to the cooling-water temperature. In this region, the thermal lens is induced by the deformation arising in the pumped region combined with the mechanical constraints at the boundary. This may lead to significant aspherical deformations of the OPD.

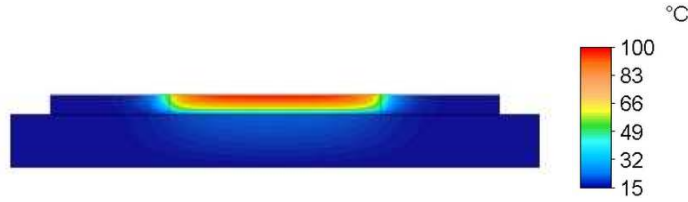


Figure 25: Finite element simulation using “Autodesk Simulation Mechanical 2015” of the temperature distribution in assembly of thin disk and heat sink as detailed in Sec. 4.3.2. The bottom surface of the heat sink is water cooled at 15 °C. The disk was pumped with a power density of 8 kW/cm², and we assumed a diamond heat sink of 1.5 mm thickness (the drawing is not to scale).

The optical phase difference relates the electric field of the laser beam before reflection $E_{in}(x, y)$, to the electric field of the laser beam after-reflection $E_{out}(x, y)$,

$$E_{out}(x, y) = E_{in}(x, y) g(x, y) e^{-i2\pi\frac{OPD(x,y)}{\lambda}}, \quad (13)$$

where $g(x, y)$ is the space-resolved gain, λ the laser wavelength and x, y the transverse coordinates. The one-dimensional OPD can be represented by a Taylor series

$$OPD(x) = a + bx + cx^2 + ho(x), \quad (14)$$

where a, b and c are constants and $ho(x)$ represents the higher-order contributions.

Typically, only the quadratic part (spherical lens) of the OPD given in Eq. (14) is considered. In fact, usually an OPD of the form $OPD(x) = cx^2$, is assumed so that the thin disk can be described by a lens with focal length of $f = 1/(2c)$. The constant term a only produces a global phase shift over the complete transverse dimension of the laser beam. This global phase delay simply corresponds to a change in the effective length of the resonator and is usually ignored. The linear term bx is also usually ignored because it simply describes the tilt of a flat optical component, which is implicitly accounted for in the alignment procedure

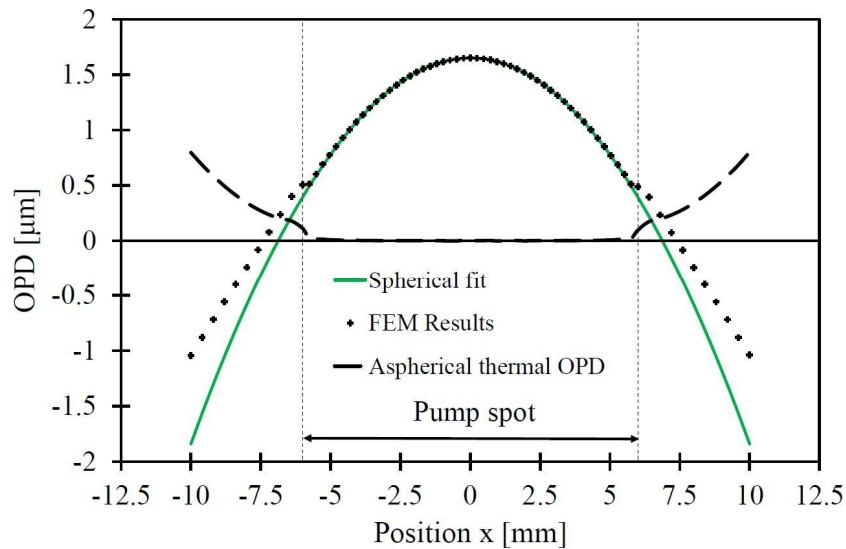


Figure 26: Space-resolved optical phase delay $OPD(x)$ experienced by a laser beam reflecting at the thin disk. The position x represents the distance from the disk axis. The crosses represent the results of the FEM simulations. The fit to the FEM simulation in the central region (for $|x| < 2.5$ mm) is given in green. The dashed line is the residual of the fit, showing that at the periphery of the pumped region there are higher-order thermally induced OPD components $ho(x) \neq 0$, while within the pumped region the OPD is well described by a thermally induced spherical lens.

of the laser resonator. This term however is playing a very important role, as detailed in Chapter 9, where a novel power scaling limitation related with the interplay of thermal lens and misalignment effects is presented. The higher-order contributions $ho(x)$ have been widely discussed in the literature [140, 141, 142, 143] because they produce and excite higher-order beam components beyond the TEM₀₀ Gaussian mode. An OPD with non-zero $ho(x)$ transforms an impinging Gaussian beam in the TEM₀₀ mode into a beam with a qualitatively different transverse structure (see Chapter 5 for more details).

4.3.2. Finite element method simulation of the OPD¹

The temperature distribution within the assembly of thin disk and heat sink can be computed using FEM simulations. We here perform full three-dimensional (3D) simulations unlike in [102, 144, 145] where radial-symmetric two-dimensional (2D) models are used. The computational effort related with the 3D modelling is higher and the resolution is lower. Yet, the 3D model allows us to capture the change of the thermal-induced OPD when there is a misalignment between the pump beam and the laser. As is detailed in Chapter 9, this change is at the core of the misalignment effect disclosed in [51] that represents a severe limitation in power scaling of thin-disk lasers.

In the FEM simulations presented in the following, we assume a setup of thin disk and heat sink as summarized in Figure 27. These material properties are summarized in Table 4. The setup is composed of a diamond heat sink with a thickness of 1.5 mm and a diameter of 25 mm and an active material made of Yb:YAG with a diameter of 20 mm and a thickness of 140 μm . The thin disk is pumped with a flattop profile with a diameter of 12 mm. Within the pump region of the active material, the pump process generates a heat load rate of 50 W/mm³. We assume the laser eigenmode to have a flattop profile with a diameter of 9.6 mm. We assume that within the laser eigenmode the heat deposition is reduced to 25 W/mm³. Our model does not consider the thermal barrier and the mechanical properties related with the HR coating and the glue used to contact the disk with the heat sink. In addition, we neglect the temperature-dependence of the heat production and the variation of the heat conductivity versus temperature.

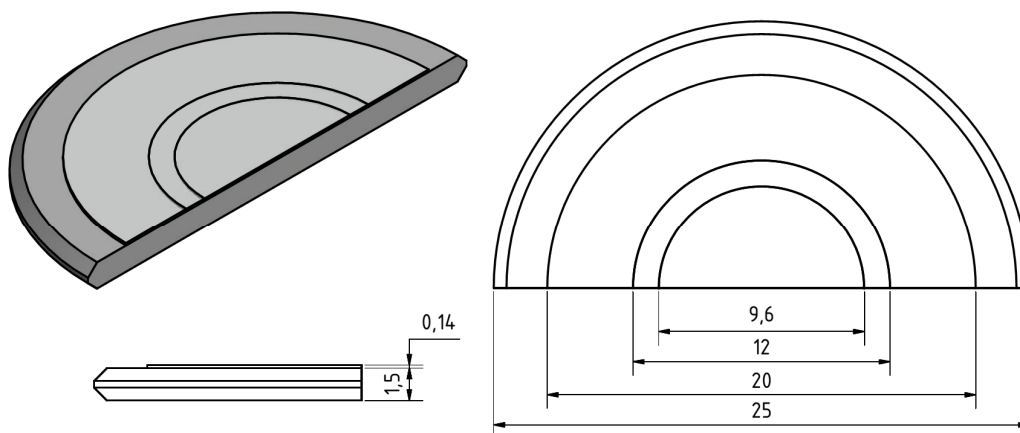


Figure 27: Thin-disk geometry used in the FEM simulations. The active medium of 140 μm thickness and 20 mm diameter is mounted onto a diamond heat sink of 1.5 mm thickness and a diameter of 25 mm. The pumped region is 12 mm in diameter while 9.6 mm is assumed for the laser mode (flattop profile). The beveled heat-sink edge diminishes boundary effects.

¹ Part of the text presented in this section is based on our publication [51].

Table 4: Parameters assumed in the FEM simulations to model the thermal lens of the disk contacted with the diamond heat sink as shown in Figure 27.

Yb:YAG (7%) thermal conductivity	7 W/mK
Yb:YAG Young's modulus	300 GPa
Yb:YAG avg. thermal expansion	$8 \cdot 10^{-6}$ 1/K
Yb:YAG refraction index change versus temperature (dn/dT)	$9 \cdot 10^{-6}$ 1/K
Thermal conductivity of diamond	1900 W/mK
Young's modulus of diamond	1100 GPa
Average thermal expansion of diamond	$9 \cdot 10^{-7}$ 1/K

Using this simplified model, which however captures the major features of the thermal-induced OPD, we have obtained the temperature distribution as shown in Figure 28. For this simulation we assumed the rear side of the diamond to be at a temperature of $T = 15$ °C given by the cooling water. The front surface of the thin disk reaches a temperature of about 100 °C. Due to the significantly higher thermal conductivity of the diamond compared with the Yb:YAG, there is a large temperature gradient in axial direction in the active material while the temperature of the heat sink is approximately constant. The simulation also shows that in the central region of the thin disk the temperature distribution in radial direction is approximately constant (independent of x, y). This is a consequence of the homogeneous pumping and the axial heat flow.

Laser operation changes the thermal load at the thin disk. In fact, laser operation reduces the heat deposition in the thin disk because it increases the radiative deexcitation of the upper laser levels at the expense of non-radiative deexcitation processes [51, 146, 147]. The reduction of the heat load due to laser operation depends on various parameters such as active medium material, pumping and lasing wavelengths [146, 147, 148, 149, 101]. In the simulations reported in the following, we assume that the heat load at the thin disk is reduced by a factor of two when there is laser operation [148]. The exact value of this factor at this stage is not important because here we are interested in conveying the qualitative changes of the thermal lens caused by the laser operation.



Figure 28: Temperature distribution of an assembly of thin disk and heat sink computed for no laser operation (fluorescence mode). The parameters of the thin disk parameters are given in the main text and in Table 4. The thermal load is 50 W/mm^3 in the pumped active region.

Figure 29 shows the effect of the laser operation on the temperature distribution in the thin disk for three cases. In (a) the thin disk is pumped but there is no laser operation. The laser is operated in the so called “fluorescence mode”. In (b) the thin disk is pumped with the same pump power density and pump spot profile as in (a) but in this case there is also laser operation. The laser mode is smaller than the pumped region (see Figure 27) and is aligned with the thin-disk pump-beam axis. The lasing process reduces the heat rate at the laser beam (eigenmode) position by a factor of two. (c) Similar to (b) but for a laser beam being 1 mm off-axis with respect to the pump and axis of the thin disk. The temperature decrease in the laser beam region caused by the laser operation is well visible when comparing Figure 29 (b) and (c) with Figure 29 (a) which represents the reference situation where the thin disk is in fluorescence operation. The asymmetric temperature distribution caused by the off-axis laser beam visible in Figure 29 (c) produces an asymmetric mechanical deformation of the assembly of thin disk and heat sink, which in a first approximation corresponds to a tilt of the assembly of thin disk and heat sink. As detailed in Chapter 9, this may give rise to a growing misalignment of the laser resonator, limiting power scaling of thin-disk laser oscillators.

Starting from the temperature distribution it is possible to compute the disk bending using a “second” FEM simulation. The red curve in Figure 30 represents an example of such a simulation. The simulations have been computed assuming that the active medium and the substrate of the heat sink are bonded together, i.e. that there is no slippage at their interface.

The green curve in Figure 30 shows the OPD changes only related to the change of the optical path length caused by the thermal expansion in laser direction and by the change of the refractive index versus temperature. The optical phase delay caused by these two effects can be computed using the following equation

$$OPD_{z\text{-expansion} \& \frac{dn}{dT}}(x, y) = 2 \int_0^{Z_0} n_{pump}(x, y, z) dz - 2 \int_0^{Z_0} n_0(x, y, z) dz, \quad (15)$$

where $n_{pump}(x, y, z)$ and $n_0(x, y, z)$ is the refractive index between the HR coating and the plane at $Z = Z_0$ as shown in Figure 31 for the pumped active medium and the unpumped active medium, respectively. The factor of two is required because the reflecting laser beam crosses the active medium twice. Note that space-resolved refractive index $n_{pump}(x, y, z)$ and the thermal expansion at each position (x, y, z) in the active medium are based on the temperature distribution computed in the first FEM simulation.

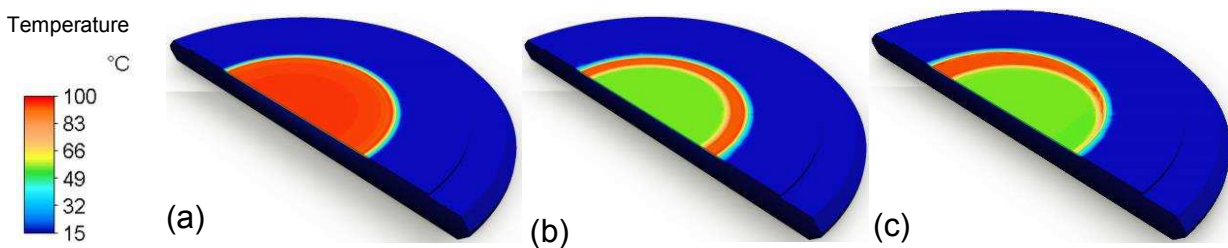


Figure 29: Temperature distributions of the assembly of thin disk and heat sink computed with FEM methods for three different conditions [51]. (a) In fluorescence operation, i.e. when the thin disk is pumped but there is no laser operation. The heat deposition in the pumped active region is 50 W/mm^3 . (b) In laser operation, showing the temperature decrease in the central region at the location of the laser beam where the heat load is assumed to be halved. (c) In laser operation similar to (b), but in this case the laser beam is 1 mm off axis.

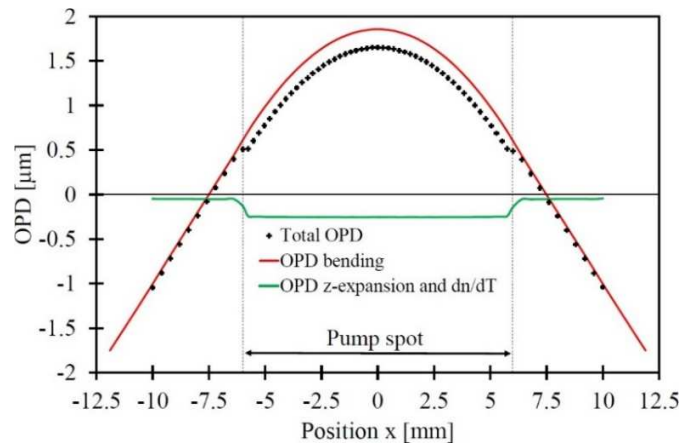


Figure 30: Optical phase delay (OPD) as a function of the distance from the axis of the thin disk obtained from FEM simulations. The total OPD (black) is dominated by the bending whose contribution is given in red. The OPD related with the expansion in axial direction and by a non-vanishing dn/dT are accounted for in the green curve.

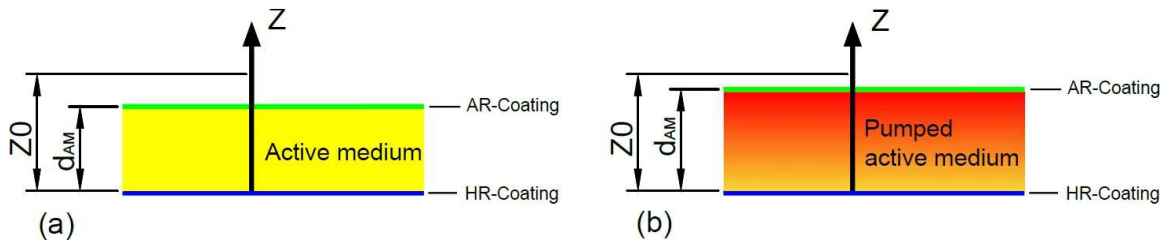


Figure 31: Scheme of the reference system used to compute the integral along the z -axis of Eq. (15) for an unpumped disk (a) and a pumped disk (b).

As a result of the almost homogeneous temperature distribution within the pumped region, the OPD related to these two effects has a step-like profile. Its constant value ($OPD(x, y) = const$) in the pumped region does not affect the properties of a (weak) laser beam impinging on the thin disk beside a global (position independent) phase shift provided the laser profile is smaller than the pump profile.

Figure 32 (a) and (b) show the OPD occurring at the thin disk in fluorescence mode computed in the “second” FEM calculation that accounts for mechanical deformations and is based on the temperature profile of Figure 29 (a) computed with the “first” FEM simulation. Figure 32 (c) and (d) show the OPD occurring at the thin disk in laser operation based on the temperature distribution of Figure 29 (b). In laser operation, the thin disk thermal lens is reduced because of the lower heat-rate deposition, but the complexity of the OPD increases.

These simulations include the three effects discussed above (bending, expansion in axial direction, dn/dT) and assumes the parameters summarized in Table 4 and Figure 27. The total OPD experienced by the laser beam (black crosses in Figure 32) in the central region is fitted with a parabolic profile. By subtracting this parabolic profile (the thermal lens) a residual OPD is obtained indicated by the dashed curves. The residuals are essentially flat in the central part of the thin disk. Here, the OPD behaves as a spherical lens. The deviations of the residual from this flat behavior that occur at the periphery of the pumped region give rise to a non-vanishing $ho(x)$ which results in the excitation of higher-order beam components beyond the Gaussian mode.

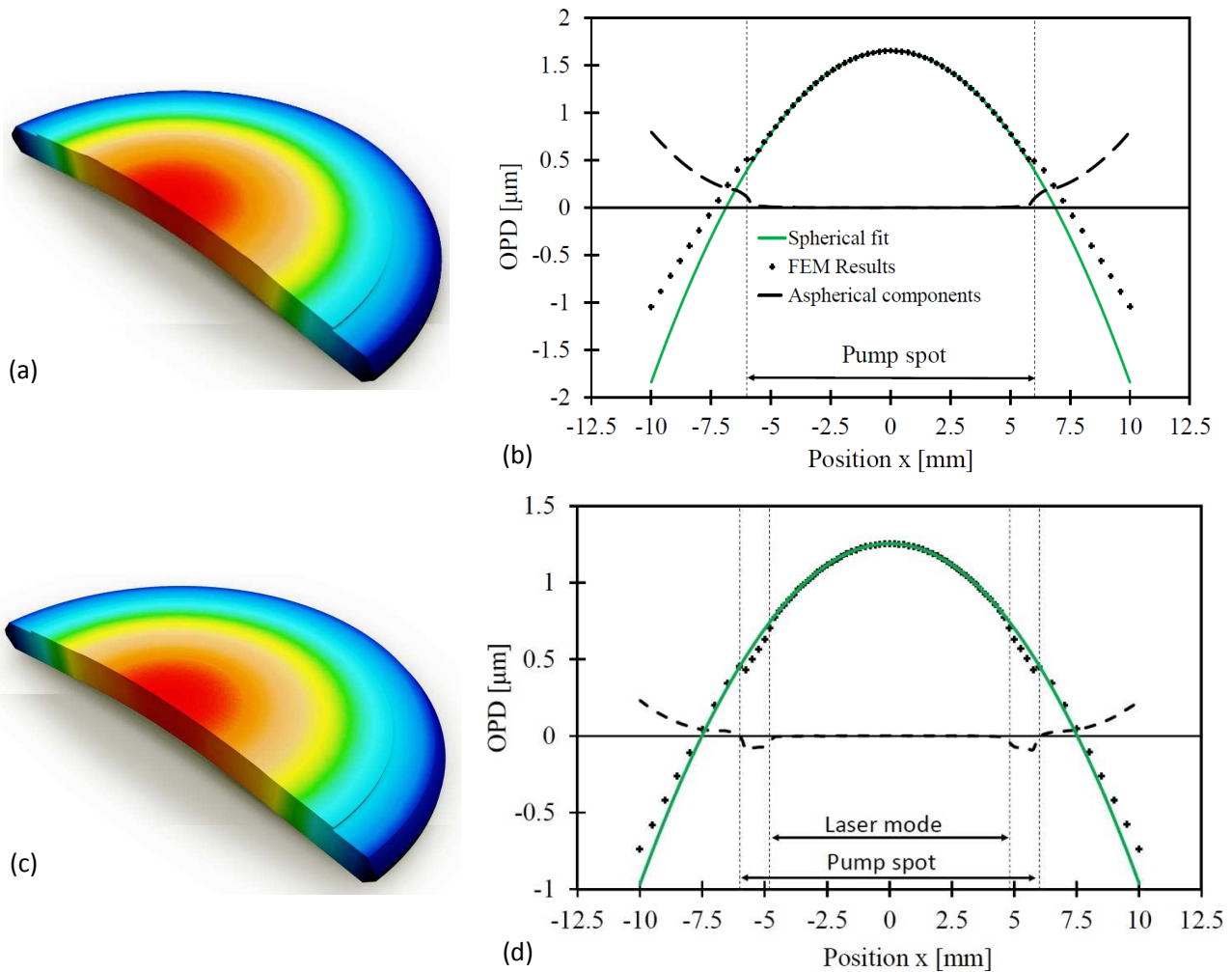


Figure 32: (a) Mechanical deformations of the assembly of thin disk and heat sink computed using FEM simulations based on the temperature profiles given in Figure 29 (a) for a thin disk operated in fluorescence mode (only pumping). The axial dimension has been magnified by a factor of 10 to visualize the deformation. The color-coding corresponds to the displacement in axial direction relative to the reference value defined for unpumped conditions. (b) Corresponding position-dependent total OPD (black crosses), its parabolic fit (green continuous line) and the residual between fit and FEM data (black dashed line). The total OPD has been fitted with a parabolic profile in the range $|x| < 2.5$ mm. The flatness of the residual in the central region demonstrates that the thermal lens effect in this region can be approximated with good precision with a spherical lens. Oppositely, at the periphery of the pumped region there are higher-order deviations. (c) Similar to (a) but for the temperature profile of Figure 29 (b), i.e. for laser operation. (d) Similar to (b) but for laser operation.

For Gaussian laser beams and Super-Gaussian pump profiles, the $h_0(x, y)$ are reduced given the smoother profiles compared to the flattop profiles that were assumed in the FEM simulations to better differentiate the various contributions.

In conclusion, FEM simulations demonstrate that to avoid distortions of the laser beam profile the width of the impinging laser beam has to be smaller than the pump profile. Larger beam widths could be advantageous as they reduce the issues related with optical damage. However, this would lead to greater losses and the excitation of higher-order beam components that may result in “hot spots” in the laser beam profile. These effects have to be considered when designing thin-disk resonators and multi-pass amplifiers (see Chapter 5).

4.4. Analytical model of the bending of the thin disk

In this section, we present a simple analytical model of the bending of the thin disk caused by the inhomogeneous temperature distribution in axial direction. An analytical expression for the radius of curvature of this bending and therefore of the spherical lens can be derived using this simple model. This analytical model, which captures the main contribution to the thermal lens effect, can be used for a quick optimization of the design of the assembly of thin disk and heat sink avoiding time-intensive FEM-based simulations.

Modelling of the bending starts from the knowledge of the temperature distribution. Then the temperature distribution is used to compute the free expansion of the assembly. In a third step, by constraining the position-dependent expansion so that the elastic potential energy in the assembly is minimal, the bending radius of the assembly is obtained. In the following, we will describe these three steps and conclude by presenting a comparison of the results obtained using this analytical model with the results from FEM simulations.

4.4.1. Temperature gradient in the assembly of thin disk and heat sink

In this simple stationary model (similar to [140]), we assume a homogeneous heat rate load over the whole volume of the active material and the diameters of the active material and the heat sink are identical. Therefore, the heat flux is purely in axial (z) direction toward the backside of the heat sink that is water-cooled. This heat flux gives rise to a temperature gradient in z -direction, while the temperature distribution in radial direction is constant $T(x, y, z) = T(z)$. As the occurring temperature range is between 293 K (temperature of cooling water) and 400 K (peak temperature at used power density) we do not have to consider the temperature-dependence of the heat conductivity so that we can make use of the simple linear model [150]. To deduce the temperature distribution $T(z)$ inside the assembly of thin disk and heat sink we make use of the relation between heat flux density $\phi_q(z)$, the temperature gradient dT/dz and the thermal conductivity λ given by

$$\phi_q(z) = -\lambda dT/dz. \quad (16)$$

The coordinate z is defined starting from the rear of the heat sink, which is in contact with the cooling water as shown in Figure 33. As summarized in this figure we further denote the thickness of the heat sink as d_{HS} and the thickness of the active material as d_{AM} .

As the heat deposition only occurs in the active material, the heat flux in the heat sink is constant, i.e. it does not depend on the z position. Moreover, because of symmetry, it is independent of the x and y coordinates. The heat-flux density (absolute value of the heat flux per unit area) expressed in W/m^2 in the heat sink is thus given by

$$\phi_q(z) = \varphi d_{AM} \quad \text{for } (0 < z < d_{HS}), \quad (17)$$

where φ represents the heat rate deposited in the active material per unit volume expressed in W/m^3 . The temperature gradient within the heat sink is thus constant and can be obtained simply by inverting Eq. (16) using the thermal conductivity of the heat sink λ_{HS} :

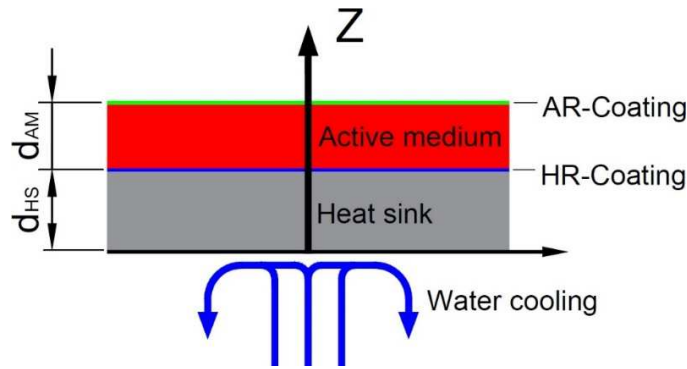


Figure 33: Scheme of the parameters of the thin disk and reference system used to describe the analytical model.

$$\frac{dT}{dz} = -\phi_q(z)/\lambda_{HS} . \quad (18)$$

Integrating this equation and inserting the heat flux density of Eq. (17), we obtain

$$T(z) = T(0) + \varphi d_{AM} z/\lambda_{HS} \quad \text{for } (0 < z < d_{HS}) , \quad (19)$$

where $T(0)$ is the temperature of the water-cooled surface at $z = 0$. We assume here that the temperature of the water-cooled surface of the heat sink does not depend on the thermal load.

To compute the temperature within the active material we proceed in a similar way. First, the heat flux density needs to be computed: the heat flux density is zero at the front side of the active material $\phi_q(z = d_{AM} + d_{HS}) = 0$, and it increases linearly with decreasing z until it reaches the value of $\phi_q(z = d_{HS}) = \varphi d_{AM}$ at the interface between the active material and the heat sink. Therefore, the heat flux density in the active medium takes the form

$$\phi_q(z) = \varphi (d_{HS} + d_{AM} - z) \quad \text{for } (d_{HS} < z < d_{HS} + d_{AM}) . \quad (20)$$

Integrating Eq. (18) adapted for the thermal conductivity of the active medium using the heat flux of Eq. (20) we find that the temperature in the active medium is

$$T(z) = T(0) + \frac{\varphi d_{AM} d_{HS}}{\lambda_{HS}} + \frac{\varphi}{2} \cdot \frac{d_{AM}^2 - (z - d_{HS} - d_{AM})^2}{\lambda_{AM}} (d_{AM} + d_{HS} - z) \quad (21)$$

$$\text{for } (d_{HS} < z < d_{HS} + d_{AM}) ,$$

where λ_{AM} is the thermal conductivity of the active medium.

Figure 34 shows a plot of the temperature distribution in the thin disk calculated from Eqs. (19) and (21). The temperature is plotted as a function of the axial distance z from the water-cooled surface. As the thermal conductivity of the heat sink is significantly higher than the one of the active material, there is a significantly lower temperature gradient in the heat sink as compared to the gradient in the active medium.

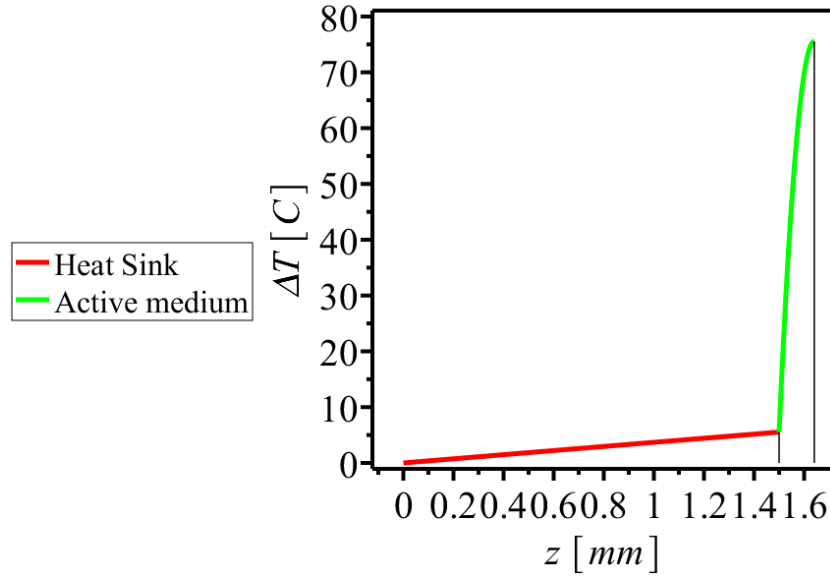


Figure 34: Temperature profile in the thin disk. Plotted is the temperature difference $\Delta T = T(z) - T(0)$ inside the active medium (green curve) and inside the diamond heat sink (red curve) relative to the water-cooled surface of the heat sink. Assumptions: $d_{HS} = 1.5$ mm, $d_{AM} = 140$ μm and $\varphi = 50$ W/mm^3 .

4.4.2. Free thermal expansion

The knowledge of the temperature distribution can be used to compute the thermal expansion of the assembly of thin disk and heat sink. We first consider the local (position-dependent) free thermal expansion [150] associated with the two materials composing the assembly. The one of the heat sink is

$$\frac{\Delta L}{L}(z) = \alpha_{HS} \frac{\varphi d_{AM}}{\lambda_{HS}} z \quad \text{for } (0 < z < d_{HS}), \quad (22)$$

where α_{HS} is the thermal expansion coefficient of the heat sink. Similarly, the local free thermal expansion of the active medium is

$$\frac{\Delta L}{L}(z) = \alpha_{AM} \left(\frac{\varphi d_{AM} d_{HS}}{\lambda_{HS}} + \frac{\varphi}{2} \frac{d_{AM}^2 - (z - d_{HS} - d_{AM})^2}{\lambda_{AM}} \right) \quad \text{for } (d_{HS} < z < d_{HS} + d_{AM}), \quad (23)$$

where α_{AM} is the thermal expansion coefficient of the active medium. A plot of this local thermal expansion as a function of the position along the z -axis is shown in Figure 35. The thermal expansion of the diamond heat sink is small compared with the thermal expansion of the active medium, for two reasons: small thermal expansion coefficient and small temperature differences $\Delta T = T(z) - T(0)$ between pumped and unpumped conditions.

The discontinuity at the interface between the active medium and the heat sink is given by the different thermal expansion coefficients of the two materials. In contrast, note that the temperature at the interface is continuous.

The thermal expansion $\Delta L/L$ occurs in the three dimensions: x , y and z . In z -direction this expansion is not restricted as in this direction each material layer with constant $z = z_0$ is simply displaced in z -direction by the integral expansion of all the layers beneath. Each layer with constant z can thus freely expand in z -direction given the absence of mechanical constraints.

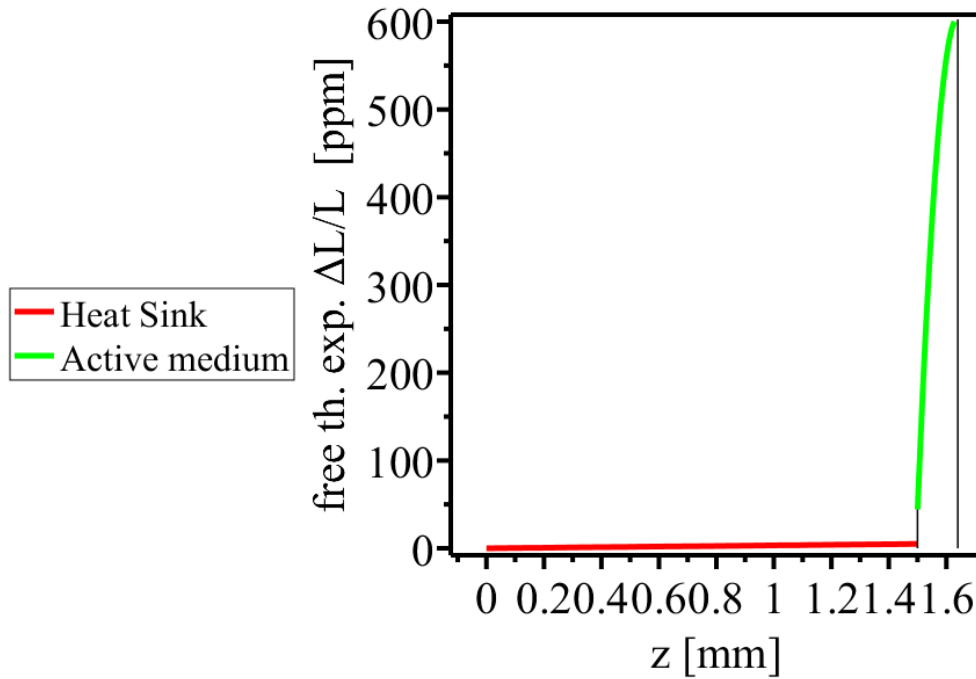


Figure 35: Local thermal expansion of the assembly of thin disk and heat sink for the temperature distribution of Figure 34 computed using Eqs. (22) and (23) $\alpha_{AM} = 8 \cdot 10^{-6} \text{ 1/K}$ and $\alpha_{HS} = 9 \cdot 10^{-7} \text{ 1/K}$. We assume that the expansion can occur freely (no boundary conditions) over the whole volume of the disk assembly.

Contrarily, in the transverse (x and y) directions the expansion cannot occur freely. On the one hand, the layers at z and $z + dz$ expand differently according to their temperature T and $T + dT$ and material properties. On the other hand, the two layers are mechanically connected so that slippage of two layers in transverse direction cannot occur. However, the thin disk can bend as sketched in Figure 36 to accommodate for the inhomogeneous thermal expansion and the requirement of mechanical continuity without slippage between the various layers.

4.4.3. Bending of the assembly of thin disk and heat sink

The aim of this section is to provide a modelling of the bending of the thin disk and to deduce the bending radius as a function of the various geometrical and material parameters of the assembly. Due to the homogeneous thermal load over the transverse direction, we assume a pure spherical bending of the assembly. Therefore, the volume of the assembly of thin disk and heat sink can be divided into identical “unit cells” as shown in Figure 36 so that the constrained thermal expansion in the transverse direction takes the simple form of a first-order polynomial

$$\left(\frac{\Delta L}{L}\right)(z) = A + B z, \quad (24)$$

where A and B are constants. Other functional shapes would lead to “unit cells” surfaces not matching to each other, which corresponds to a fracturing of the assembly.

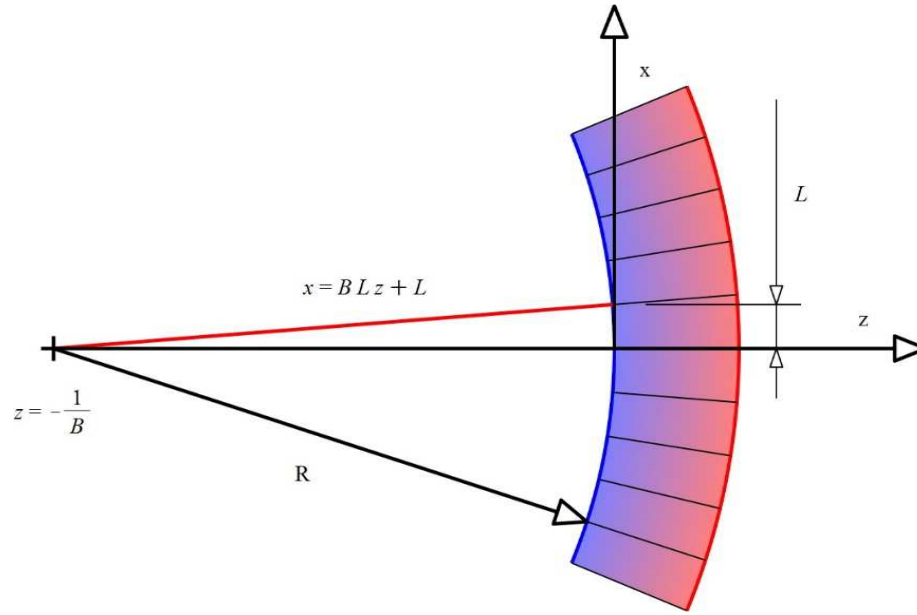


Figure 36: Sketch (not to scale) of the bending of the assembly of thin disk and heat sink due to the inhomogeneous temperature distribution, hot at the front side (red), cold at the rear side (blue). The black lines are used to indicate qualitatively the geometry of the “unit cells”. The bending of the assembly is not to scale; it has been increased by two orders of magnitude in order to make the effect visible. R is the bending radius.

Using trigonometric relations and assuming the transverse size of the thin disk to be much smaller than the bending radius R of the assembly, we find

$$R = -\frac{1}{B}. \quad (25)$$

The minus sign indicates that the thin disk acts as a defocusing optical element. Because the focal distance of a mirror is $R/2$, we obtain a focal strength of the thin disk V (in dioptric power) of

$$V = -2B. \quad (26)$$

The inhomogeneous thermal expansion produces a position-dependent internal stress (force per area) on the material, which causes a strain. For a linear material the elastic potential energy stored per unit volume is given by [150]

$$u_{pot} = \frac{1}{2} E \left(\frac{\Delta l}{l} \right)^2, \quad (27)$$

where E is the Young’s modulus and $(\Delta l/l)$ the strain. The radius of curvature of the assembly can be obtained by minimizing the total elastic energy stored in the assembly of active medium and heat sink [150]. The potential elastic energy arises from the difference in length expansion between the free thermal expansion $(\Delta L/L)_{free}$ and the resulting expansion after mechanical bending $(\Delta L/L)_{bending}$. The total potential elastic energy U_{pot} in the assembly is thus given by

$$U_{pot} = \frac{1}{2} \iiint E \left(\left(\frac{\Delta L}{L} \right)_{free} - \left(\frac{\Delta L}{L} \right)_{bending} \right)^2 dx dy dz, \quad (28)$$

where the integral runs over the whole volume of the assembly. Because of the homogeneity in transverse direction the x and y integrations can easily be performed so that the potential energy becomes

$$U_{pot} = \frac{F}{2} \int_0^{d_{HS}+d_{AM}} E(z) \left(\left(\frac{\Delta L}{L} \right)_{free} - (A + Bz) \right)^2 dz, \quad (29)$$

where F is the transverse surface of the assembly. Note that the Young's modulus $E = E(z)$ depends on the z -position because the assembly is composed of various materials. The parameters A and B have to be chosen so that the potential energy U_{pot} is minimized. This leads to the conditions $\partial U_{pot}/\partial A = 0$ and $\partial U_{pot}/\partial B = 0$. The derivative

$$\partial U_{pot}/\partial A = 0 \quad (30)$$

is equivalent to

$$0 = \int_0^{d_{HS}+d_{AM}} E(z) \left(\left(\frac{\Delta L}{L} \right)_{free} - (A + Bz) \right) dz. \quad (31)$$

Inserting the free thermal expansion of the active medium and of the heat sink given in Eqs. (22) and (23), and the Young's modulus of the heat sink E_{HS} and of the active medium E_{AM} , we obtain

$$0 = \int_0^{d_{HS}} E_{HS} \left(A + Bz - \alpha_{HS} \frac{\varphi d_{AM}}{\lambda_{HS}} z \right) dz + \int_0^{d_{AM}} E_{AM} \left(A + Bz - \alpha_{AM} \left(\frac{\varphi d_{AM} d_{HS}}{\lambda_{HS}} + \frac{\varphi d_{AM}^2 - (z - d_{HS} - d_{AM})^2}{2\lambda_{AM}} \right) \right) dz. \quad (32)$$

The solution of this integral then leads to the following equation for A and B :

$$0 = \varphi d_{AM} \left(\frac{E_{HS} \alpha_{HS} d_{HS}^2}{2\lambda_{HS}} + \frac{E_{AM} \alpha_{AM} d_{HS} d_{AM}}{\lambda_{HS}} + \frac{E_{AM} \alpha_{AM} d_{AM}^2}{3\lambda_{AM}} \right) - B \left(\frac{E_{HS} d_{HS}^2}{2} + E_{AM} d_{HS} d_{AM} + \frac{E_{AM} d_{AM}^2}{2} \right) - A (E_{HS} d_{HS} + E_{AM} d_{AM}). \quad (33)$$

In a similar way applying the condition $\partial U_{pot}/\partial B = 0$ to Eq. (29), we obtain

$$0 = \frac{\partial}{\partial B} \int_0^{d_{HS}+d_{AM}} E(z) \left(\left(\frac{\Delta L}{L} \right)_{free} - (A + Bz) \right)^2 dz. \quad (34)$$

After performing the derivative this equation transforms to

$$0 = \int_0^{d_{HS}+d_{AM}} z E(z) \left(\left(\frac{\Delta L}{L} \right)_{free} - (A + Bz) \right) dz. \quad (35)$$

Inserting the free thermal expansion of the active medium and of the heat sink given in Eqs. (22) and (23), and the Young's modulus for the heat sink E_{HS} and of the active medium E_{AM} , we obtain

$$0 = \int_0^{d_{HS}} z E_{HS} \left(A + Bz - \alpha_{HS} \frac{\varphi d_{AM}}{\lambda_{HS}} z \right) dz \quad (36)$$

$$+ \int_0^{d_{AM}} z E_{AM} \left(A + Bz - \alpha_{AM} \left(\frac{\varphi d_{AM} d_{HS}}{\lambda_{HS}} + \frac{\varphi}{2} \frac{d_{AM}^2 - (z - d_{HS} - d_{AM})^2}{\lambda_{AM}} \right) \right) dz .$$

The solution of this integral gives rise to another equation for parameters A and B :

$$0 = \varphi d_{AM} \left(\frac{E_{HS} \alpha_{HS} d_{HS}^3}{3\lambda_{HS}} + \frac{E_{AM} \alpha_{AM} d_{HS}^2 d_{AM}}{\lambda_{HS}} + \frac{E_{AM} \alpha_{AM} d_{HS} d_{AM}^2}{3\lambda_{AM}} + \frac{E_{AM} \alpha_{AM} d_{HS} d_{AM}^2}{2\lambda_{HS}} + \frac{5E_{AM} \alpha_{AM} d_{AM}^3}{24\lambda_{HS}} \right) - B \left(\frac{E_{HS} d_{HS}^3}{3} + E_{AM} d_{HS}^2 d_{AM} + E_{AM} d_{HS} d_{AM}^2 + \frac{E_{AM} d_{AM}^3}{3} \right) - A \left(\frac{E_{HS} d_{HS}^2}{2} + E_{AM} d_{HS} d_{AM} + \frac{E_{AM} d_{AM}^2}{2} \right). \quad (37)$$

By combining Eq. (33) with Eq. (37) the two parameters A and B can be deduced as a function of the geometrical and material properties of the assembly and the heat rate density deposited in the active medium. In this model, the dioptric power of the thin disk is given by

$$-V = \frac{\varphi d_{AM}}{\lambda_{HS} \lambda_{AM}} \cdot \frac{2E_{HS}^2 \alpha_{HS} d_{HS}^4 \lambda_{AM} - 4E_{HS} E_{AM} \alpha_{HS} d_{HS}^3 d_{AM} \lambda_{AM} - 6E_{HS} E_{AM} \alpha_{HS} d_{HS}^2 d_{AM}^2 \lambda_{AM} + 12E_{HS} E_{AM} \alpha_{HS} d_{HS} d_{AM}^3 \lambda_{AM}}{E_{HS}^2 d_{HS}^4 + 4E_{HS} E_{AM} d_{HS}^3 d_{AM} + 6E_{HS} E_{AM} d_{HS}^2 d_{AM}^2 + 4E_{HS} E_{AM} d_{HS} d_{AM}^3 + E_{AM}^2 d_{AM}^4} + \frac{\varphi d_{AM}}{\lambda_{HS} \lambda_{AM}} \cdot \frac{4E_{HS} E_{AM} \alpha_{AM} d_{HS}^2 d_{AM}^2 \lambda_{HS} + 12E_{HS} E_{AM} \alpha_{AM} d_{HS} d_{AM}^2 \lambda_{AM} - 5E_{HS} E_{AM} \alpha_{AM} d_{HS} d_{AM}^3 \lambda_{HS} + E_{AM}^2 \alpha_{AM} d_{AM}^4 \lambda_{HS}}{E_{HS}^2 d_{HS}^4 + 4E_{HS} E_{AM} d_{HS}^3 d_{AM} + 6E_{HS} E_{AM} d_{HS}^2 d_{AM}^2 + 4E_{HS} E_{AM} d_{HS} d_{AM}^3 + E_{AM}^2 d_{AM}^4}. \quad (38)$$

This equation allows the evaluation of the thermal lens that can be used for a fast optimization of the thin disk geometry and material composition. Indeed, this evaluation is significantly simpler and faster than the corresponding assessment with a FEM simulation.

4.4.4. Results from the analytical model and comparison to FEM simulations

In this section, Eq. (38) is used to evaluate the dioptric power of the thin-disk assembly for various heat-sink materials and thicknesses and the results are compared to various corresponding FEM simulations. This comparison serves, on the one hand, to validate our model and on the other hand, to quantify its precision.

Figure 37 shows the dioptric power of the thin disk as a function of the thickness of the heat sink in a double logarithmic plot for various promising heat sink materials. The active medium is Yb:YAG with a doping concentration of 7 % and a thickness of $d_{AM} = 140 \mu\text{m}$. The thermal and mechanical properties are summarized in Table 4. The thermal heat rate density within the active medium was assumed to be $\varphi = 50 \text{ W/mm}^3$. Note that in the analytical model it is assumed that the thin disk is homogeneously pumped (differently from the practical situation), to its periphery so that the pumped volume corresponds to the volume of the active medium. The inprecision related with this assumption will be discussed later.

For small thicknesses of the heat sink, the refractive power of the assembly is dominated by the thermal bending of the active medium. For large thicknesses of the heat sink, the focal strength of the assembly is dominated by the thermal bending of the heat sink. For thicknesses in the transition range both the Young's moduli of active medium and heat sink are of relevance, together with the difference between the thermal expansions of the active medium and the heat sink.

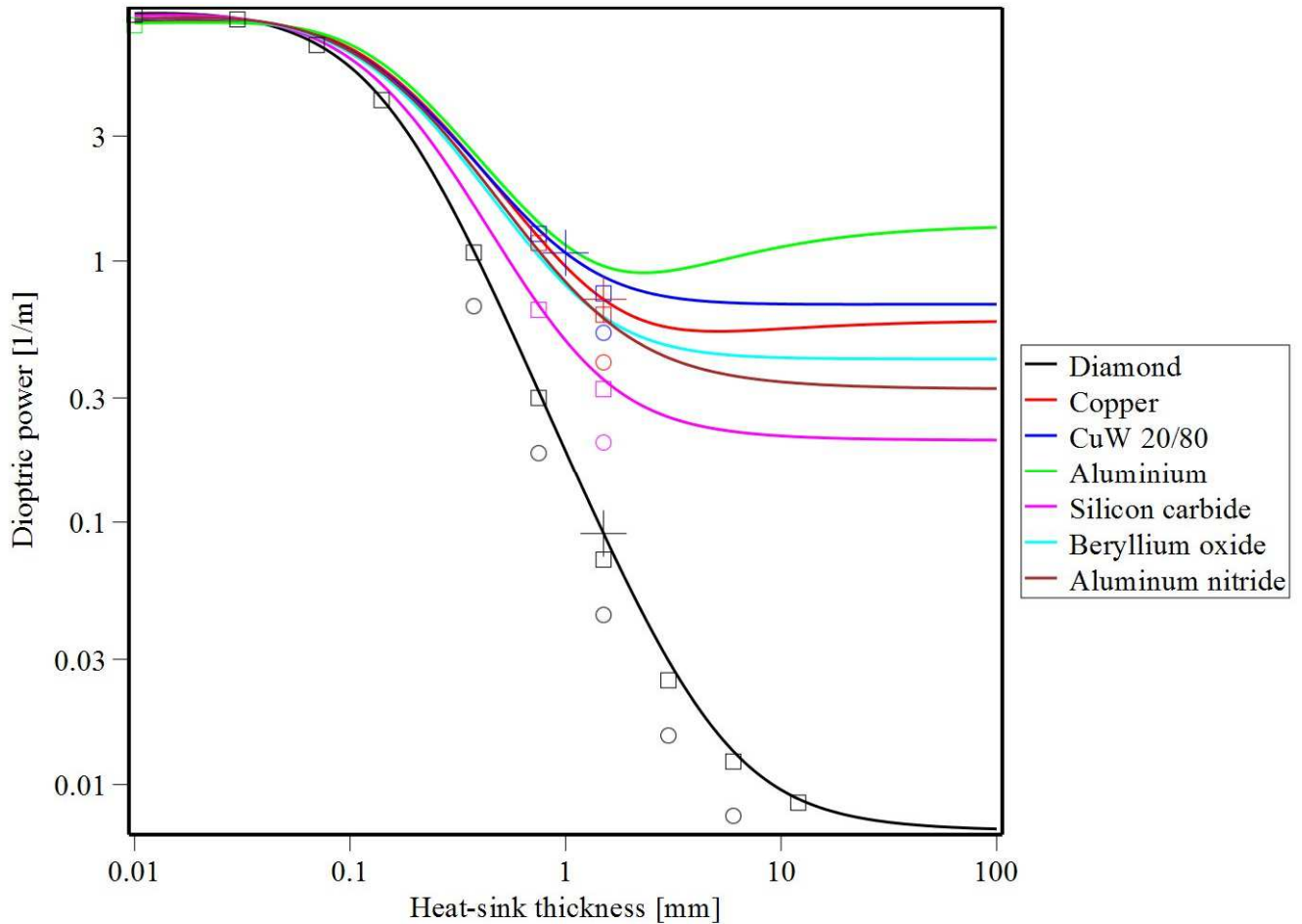


Figure 37: Dioptric power of the thin disk as a function of the thickness of the heat sink for various heat-sink materials. The continuous curves represent the results of the analytical model. The empty squares are the FEM results assuming that the thin disk is pumped homogeneously over the complete transverse area as shown in Figure 38 (a). The empty circles represent FEM evaluations where the diameter of the pumped area is by a factor of two smaller than the diameter of the thin disk (see Figure 38 (b)). The crosses indicate the three generations of thin disk designs (see text). We chose material properties summarized as in Table 5, $d_{AM} = 140 \mu\text{m}$, and a thermal load of 50 W/mm^3 .

As visible from Figure 37, with increasing thickness of the heat sink the focal strength of the assembly decreases. This is because the increased heat-sink thickness reduces the bending of the active material given the larger thermal conductivity of the heat-sink materials. However, in a real setup, an increased heat-sink thickness causes a higher thermal resistance and thus an increased temperature of the active material. Due to the extremely high thermal conductivity of diamond, the heat sink made from diamond virtually shows no saturation effect. In principle, the thickness of the diamond substrate could be much larger than the thickness of the other heat sinks, but in practice, its thickness is limited by price.

The green line represents the thermal lens obtained with a heat sink made of aluminium. Differently to the other heat-sink materials presented, the thermal expansion of aluminium is significantly larger than the one of the active medium. This difference leads to a bimetallic effect inverted compared to the bending which would arise for the two materials considered separately. This is the origin of the minimum of the green curve at a thickness of the heat sink of about 2 mm.

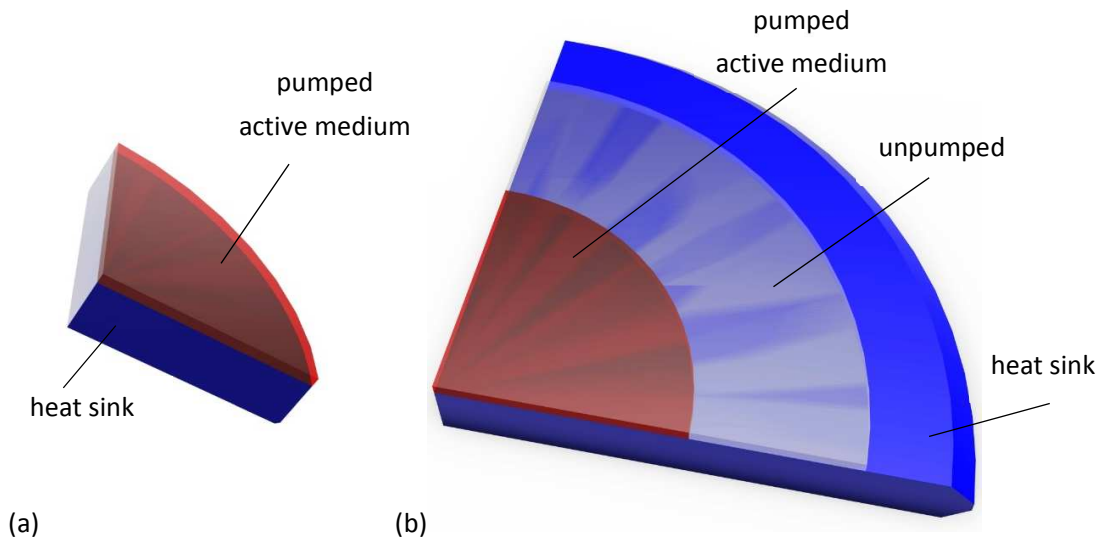


Figure 38: Sketch of the assembly of the pumped thin-disk crystal on the heat sink. (a) Simplified thin-disk geometry used to compute the empty squares of Figure 37 and 39. Here the thin disk is pumped homogeneously to its periphery. (b) Realistic thin-disk design used to compute the empty circles of Figure 37 and 39. The pumped region (red) diameter is by a factor of two smaller than the thin-disk diameter.

Table 5: Mechanical properties of the thin disk and possible heat-sink materials.

Material	Thermal conductivity (λ) [$\text{Wm}^{-1}\text{K}^{-1}$]	Young's modulus (E) [GPa]	Thermal expansion coefficient (α) [10^{-6}K^{-1}]
Yb:YAG 7%	7 [101]	300 [151]	≈ 8 [151]
CuW (20/80)	180 [152]	280 [152]	8.8 [152]
Diamond	1900 [153]	1100 [154]	0.9 [153]
SiC	305 [155]	700 [155]	4.5 [156]
AlN	200 [157]	350 [157]	4.63 [157]
BeO	265 [158]	345 [158]	8.0 [158]
Al	235 [159]	70 [159]	23.1 [160]
Cu	401 [161]	128 [161]	17 [160]

For comparison, in Figure 37 we highlighted the parameters of some historical and to-date typical thin-disk designs (crosses). In the first generation of thin disk, the laser crystal was soldered with indium to a copper heat sink with a thickness of $d_{HS} = 1.5$ mm (red cross). In the second generation, the crystal was soldered to a thermal-expansion-matched heat sink made of copper tungstate (CuW 20/80) with a thickness of $d_{HS} = 1$ mm using a gold-tin solder (AuSn 80/20) (blue cross). Due to the lower thermal conductivity of the copper-tungstate alloy, the thermal lens effect is slightly increased compared

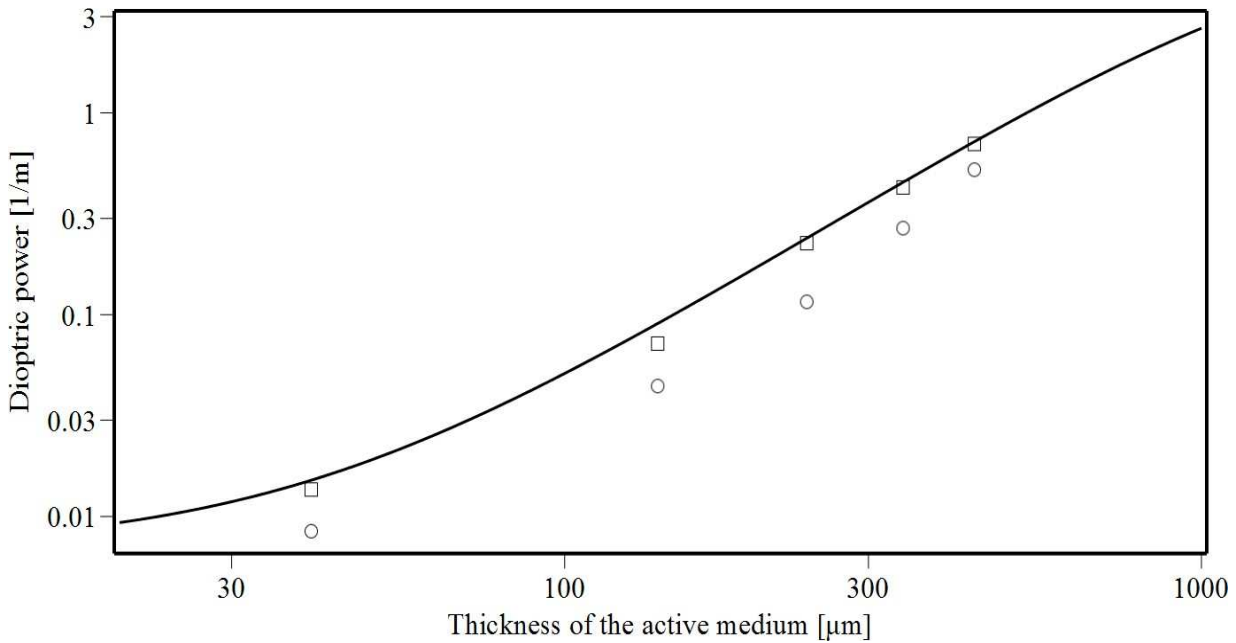


Figure 39: Thin-disk thermal lens for variations of the thickness of the active medium. The continuous curve represents the solution of Eq. (38). The squares represent the focal strength from FEM evaluations based on the simplified thin-disk design presented in Figure 38 (a). The circles represent the focal strength extracted from FEM evaluations based on the realistic thin-disk design presented in Figure 38 (b). Assumptions: active material is Yb:YAG with a doping concentration of 7%, the diamond heat sink with 1.5 mm thickness, and the heat load of $7 \text{ W}/\text{mm}^2$ is independent on active medium thickness. As a result, the volumetric thermal load varied from 15.9 to $175 \text{ W}/\text{mm}^3$.

to the one resulting from using pure copper. However, the design having expansion-matched materials diminishes the tensile stress resulting in higher power capabilities [162, 163]. Laser crystals glued to diamond heat sinks are used in the third generation of thin-disk lasers (black cross). In this case, the thermal lens is strongly reduced compared to other designs.

The position of the crosses along the various curves demonstrates that the choice of the heat-sink thickness in the various historical generations of thin-disk lasers was optimal. In fact, the thin-disk designs were chosen to have the minimal thickness that guarantees a small thermal-lens effect (just prior to saturation) while minimizing the thermal resistivity of the heat sink to minimize the temperature of the active material.

The empty squares represent the dioptric power computed using FEM methods assuming the material properties, pumping conditions and thin-disk geometry as shown in Table 5 and in Figure 38 (a) (similar to the assumptions used to derive equation Eq. (38)). In particular, as in the analytical model, also for this FEM computation it was assumed that the thin disks are pumped homogeneously over the complete transverse area. The focal strength of the thin disk based on the diamond heat sink was evaluated for 10 different thicknesses of the heat sink, from $10 \mu\text{m}$ to 12 mm . In addition, we evaluated the thermal lens for other heat-sink materials (CuW, Cu, SiC) for two thicknesses of the heat sink (0.75 mm and 1.5 m). The agreement between the results from the analytical model (curves) and the results from the FEM

simulations (empty squares) based on the same assumptions demonstrates the intrinsic correctness of the analytical model².

The empty circles represent the focal strength obtained with FEM computations based on the realistic thin-disk design presented in Figure 38 (b). In this case, the diameter of the heat sink is twice the diameter of the pumped area. The focal strength of the diamond-based heat sink was computed for five different thicknesses of the heat sink, from 375 μm to 6 mm. In addition, we evaluated the thermal lens for thin disks based on CuW, Cu and SiC for a thickness of 1.5 mm of the heat-sink material.

The focal strengths obtained from the FEM simulations computed for the realistic situations turn out to be systematically shifted to lower values by a constant factor of about 1.5 relative to the results from the analytical model. This factor decreases when the pumped-area diameter approaches the diameter of the thin disk. In principle, a study of this systematic shift can be undertaken in order to be able, in a second step, to correct the result of the analytical model. In such a way we estimate that using the analytical model and a small correction to it, it is possible to estimate the thermal lens of the thin disk at accuracies of about 10-20 %.

In Figure 39 the focal strength of the thermal lens is shown for variations of the active medium thickness. The focal strengths have been computed with the analytical model (curve), with FEM simulations assuming that the pumped area coincides with the total transverse area of the disk (empty squares), and with FEM simulations assuming that the diameter of the pumped area of the thin disk (empty circles). Here deviations of the FEM simulations from the analytical model are visible similar to Figure 37.

In conclusion, we have demonstrated that the one-dimensional model presented in this section represents a fast method to evaluate thermally-induced lens effects arising from the bending of the thin disk, which can reach an uncertainty of 10 - 20 %. Note also that this model could be extended to include additional layers as coating, glue, etc.

² The small deviations visible for heat sink thicknesses of 1.5 mm, 3 mm and 6 mm are mainly caused by the limited size of the mesh used in the FEM simulation compared to the relevant geometrical sizes.

5. Impact of apertures on laser design

Aperture effects are usually neglected when designing laser resonators and multi-pass amplifiers. However, it will become evident in the following chapters that aperture effects do play an important role. This chapter starts by describing the transmission of a laser beam through an aperture. We show that aperture effects guarantee laser operation in the TEM₀₀ mode. At the same time, aperture effects cause beam distortions that can be interpreted as scattering to beam components beyond the TEM₀₀ mode. Various types of aperture are compared.

The central part of this chapter explains how to implement Gaussian apertures into the ABCD-matrix formalism. This allows fast (analytical) computations of the laser propagation in an optical segment and the eigenmodes in a resonator comprising apertures. In summary, this chapter is divided into several sections:

- **Section 5.1: Motivation**
The motivation of the importance of apertures is provided, together with some examples of their influence on laser beam propagation.
- **Section 5.2: Transmissivity of apertures**
The effect of an aperture is to partially absorb and partially transmit an impinging laser beam. The transmitted fraction can be expanded in various Gaussian-Laguerre transverse components. Here we present a mathematical description of these two processes.
- **Section 5.3: Diffraction at apertures**
Here we quantify the fraction of the power transmitted via an aperture and diffracted into higher-order beam components.
- **Section 5.4: Gaussian, Super-Gaussian and flattop apertures**
Gaussian, Super-Gaussian and hard apertures are compared. This comparison allows defining in an approximate way the size of the Gaussian aperture to be used to describe a Super-Gaussian aperture.
- **Section 5.5: ABCD-matrix formalism and Gaussian apertures**
Gaussian apertures can be implemented in the ABCD-matrix formalism. A detailed derivation of this implementation is given. Two new ABCD-matrices are needed: one describing the evolution of the complex q -parameter of the Gaussian beam, the other one describing the excursion and tilt of the Gaussian beam axis from the optical axis.
- **Section 5.6: Losses at apertures**
Simple formulas to compute transmission losses for the TEM₀₀ mode through a Gaussian aperture are given for two cases: the laser beam is aligned or misaligned with the aperture.
- **Section 5.7: Multi-pass amplifiers with apertures**
A mismatched (offset, tilt, beam size, divergence) laser beam injected into a periodic optical system propagates with a non-zero excursion from the optical axis and shows an evolution of the beam width. It is demonstrated how aperture effects damp these excursions and irregularities.

- **Section 5.8: Resonators with apertures**

The evaluation of the resonator Gaussian eigenmode is derived for resonators containing apertures through the “expanded” ABCD-matrix formalism. The impact of aperture effects on the stability properties and losses is discussed.

5.1. Motivation

In Sec. 4.3 and Sec. 4.5 it has been shown that the profile of the optical phase delay OPD experienced by a laser beam reflecting at the thin disk has a central region well described by a thermal lens, while at the periphery of the pumped region it shows deviations from the parabolic shape. For a thin-disk laser, these phase distortions may produce effective aperture losses significantly larger than the losses associated with gain and absorption guiding [164, 162, 165]. In fact, for thin-disk lasers the gain (absorption) difference between the central region and the periphery of the disk is smaller than 20%.

When the aperture and the Gaussian eigenmode have similar sizes, the apertures ensure laser operation in this mode, as higher-order transversal modes experience significantly higher losses. By contrast, when the pump spot is much larger than the TEM00 mode, several transverse higher-order modes may oscillate in the resonator.

It is tempting to increase the beam or mode size at the position of the active medium in order to diminish the risk of optical damage and to make use of “all” the energy stored in the active medium. However, with increasing beam diameter at constant pump size, the losses inflicted on the beam strongly increase due to larger absorption and diffraction effects at the periphery of the pumped region. These effects thus reduce the laser efficiency and the quality of the extracted and circulating beams.

Collins propagations [166] can be used to describe the evolution of a coherent laser beam and its deformations caused by a position-dependent OPD. In this Chapter, however, we make use of the fact that Gauss-Laguerre wave functions [167] constitute an infinite set (basis) of independent solutions of the wave equation [168, 169]. We assume the Gauss-Laguerre modes to have a common wavelength and initially to have a fixed phase relation given the coherence of the amplified beam. As a result, the beam profile is the interference pattern of the various Gauss-Laguerre components of different amplitude and phase. Thus, not only the size but also the shape of the deformed laser beam evolves along the propagation because of the difference in phase delays (Gouy phase shifts [170, 171]) accumulated by the different Gauss-Laguerre components while propagating along the z-direction as

$$\Delta\alpha = (1 + 2p + n) \cdot \arctan\left(\frac{z}{z_R}\right). \quad (39)$$

where z_R is the Rayleigh range, n and p the number of the azimuthal and radial nodal lines of the Gauss-Laguerre beams.

For the multi-pass amplifier, which we developed in 2006-2008 to measure the proton radius, we have chosen large beam widths at the position of the thin disk in order to avoid optical damage [117]. In fact, at that time there was a shortage of thin disks with a high damage threshold. For this reason, we needed

to develop a multi-pass amplifier able to deal with higher-order transverse beam components. The Gaussian mode was no longer sufficient to describe the propagation. Thus, we developed a numerical code based on Collins propagations able to deal with the phase distortions and with the position-dependent gain and absorption profiles occurring at the active medium [117, 172].

Optimization of the amplifier layout and its in-coupling was challenging and time consuming in both the simulations and the practical implementations given the measured gain and OPD profiles. In Figure 40 we present the laser beam profiles at the position of the thin disk for the 12-pass amplifier developed for the measurement of the proton radius, which were simulated using the Collins integrals. The layout of the amplifier was adapted to the measured OPD and gain profiles to obtain the regular pattern. The beam propagation was exhibiting an alternating succession of Gaussian-like profiles and quasi-donut-like profiles. The quasi-donut-like profiles exhibit small radial “tails” and are free of hot spots, implying large gains and an increased optical damage threshold. Special care was applied when selecting the thin disk and optimizing the amplifier layout to avoid profiles having large peaks (“hot spots”) in the beam center (around $x = 0$) which would reduce the optical damage threshold.

Good agreement was observed between simulated and measured profiles as visible by comparing Figure 40 with Figure 41. However, due to the uncertainties of the measured position-dependent gain and OPD profiles, as well as the parameters of the in-coupled beams, a time-consuming optimization of the multi-pass amplifier layout was necessary to reach stable beam propagation with optimal profiles and gains in all passes. Due to this lengthy and complex optimization, in the multi-pass amplifier described in Chapter 7 we opted for smaller laser beams.

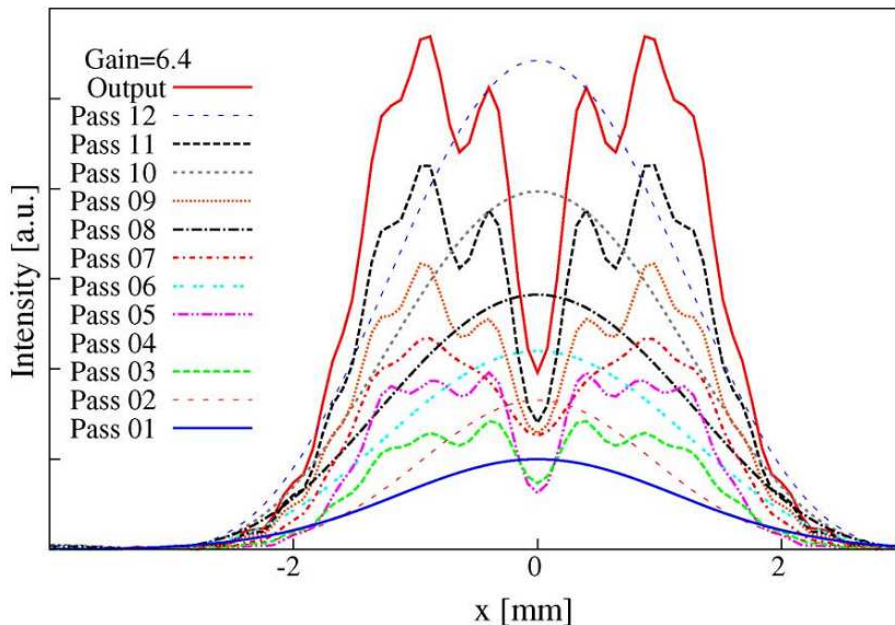


Figure 40: Simulated beam profiles at the various passages at the thin disk in the 12-pass amplifier realized for the measurement of the proton radius. The simulations are based on Collins propagations, which require the knowledge of the OPD and gain profiles at the thin disk. The laser beam alternates between Gaussian-like profiles for even passes, and quasi-donut-like profiles for odd passes. At the same time, amplification occurs as indicated by the increasing amplitude with increasing pass number. This propagation is obtained for laser beam widths exceeding the rule of thumb condition of Eq. (40). The figure is reproduced from [117].

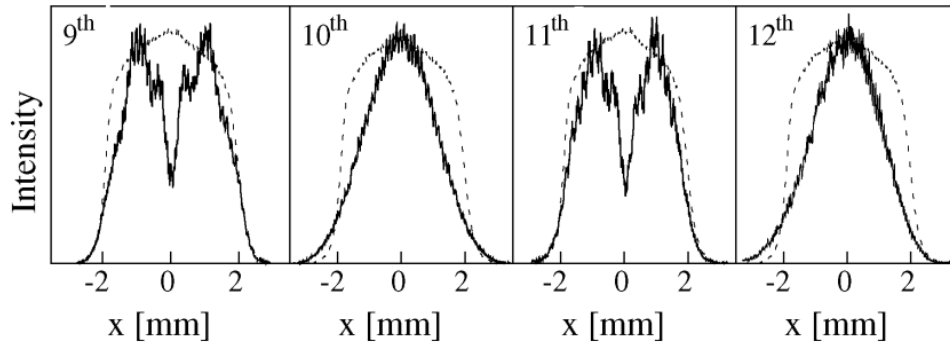


Figure 41: Beam profiles (continuous) measured at various passes in the multi-pass amplifier realized for the measurement of the proton radius. The laser beam alternates between Gaussian-like and a quasi-donut-like profiles. The pump profile (dashed) is also shown for reference. This figure is reproduced from [117].

It would be beyond the scope of this chapter to describe in detail the working principle of the multi-pass amplifier and the propagation of the corresponding higher-order transverse beam components. The interested reader is referred to [117, 166, 173]. What we would like to emphasize here, is that for large laser beams and OPDs of the thin disks with large higher-order $ho(x, y)$ distortions, a vast variety of transverse beam profiles can be obtained. Some examples of measured 2D and 1D profiles are given in Figure 42 and Figure 43, respectively. These laser profiles have been measured at the odd passes of a multi-pass amplifier based on a concatenation of identical segments [54, 117] for various thin disks (OPD profiles) and various segment layouts. They result from complex interference patterns between the various transverse components that have been excited at the thin disk. A similar behavior was observed in unstable resonators [173, 174, 175, 176]. At each successive pass through the thin disk, the various transverse components are partially mixed (scattering process), partially suppressed (absorption) and new ones generated (diffraction).

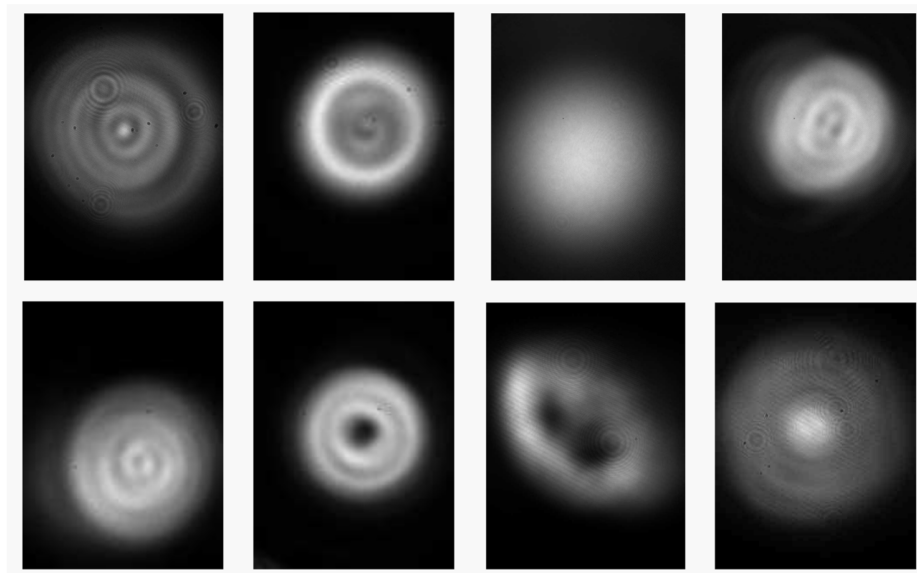


Figure 42: Beam profiles measured at the odd passes in a multi-pass amplifier formed by a concatenation of nearly identical stable segments [117]. Each picture has been taken for different thin disks or segment layouts. A considerable excitation of high-order transverse beam components is observed when the laser beam widths w is exceeding the rule of thumb condition of Eq. (40) and the thin disks soldered onto metallic heat sinks were used.

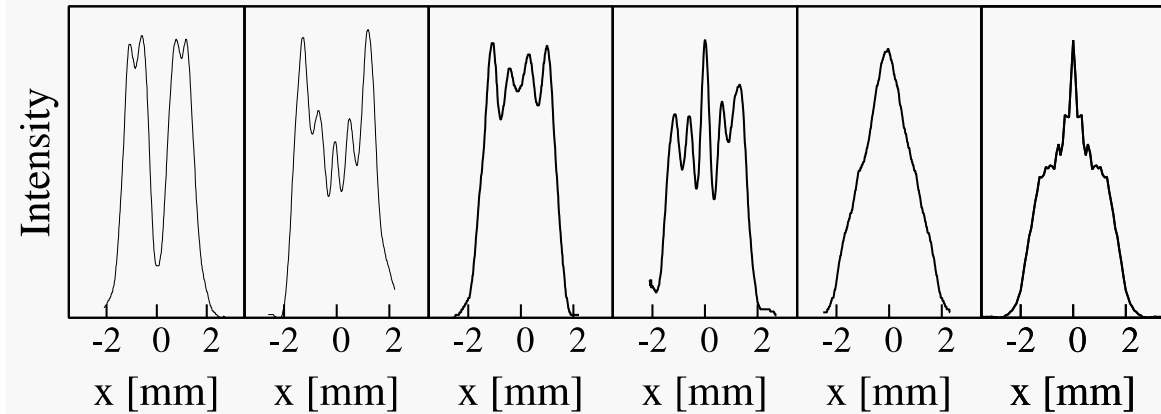


Figure 43: Similar to Figure 42 but only in one dimension. The segment layout and thin disk giving rise to the first profile were used for the measurement of the proton radius. Profiles as in the last panel are disadvantageous as they bring about a decreased optical damage threshold due to the presence of hot-spots at the center. This figure has been reproduced from [117].

In the thin-disk laser community, typically the Gaussian mode to be amplified is chosen to fulfill the condition

$$w \approx 0.35 D_p, \quad (40)$$

where w is the Gaussian beam width at the position of the thin disk, and D_p the diameter of the Super-Gauss profile of the pumped region at FWHM. This rule of thumb results from a trade-off between optical damage, gain, scattering into and absorption of higher-order transverse beam components.

As mentioned before, smaller laser beam widths increase the risk of optical damage and reduce the efficiency of the laser because of the smaller overlap with the pumped region. A resonator design having a TEM₀₀ mode width much smaller than in Eq. (40) results in multi-mode (transversal) operation affecting laser quality and stability. On the other hand, laser beams with large widths at the aperture suffer from increased absorption and increased scattering into higher-order transverse beam components that have larger propagation losses.

Typically, the propagation of a Gaussian beam in an optical system is described using the ABCD-matrix formalism. This formalism also provides a simple analytical method to compute the TEM₀₀ eigenmode of the resonator [177, 178, 179]. However, in standard optical simulations based on the ABCD-matrix formalism aperture effects are neglected.

In fact, aperture effects considerably complicate the laser beam propagation because of the excitation of higher-order transverse beam components, and the reduction of the width of the TEM₀₀ mode at the aperture. Yet as will be detailed later, Gaussian apertures can be easily implemented in the ABCD-matrix formalism as lenses with imaginary values [180, 181, 182, 170]. Thus, it is possible to analytically describe the beam propagation in an optical system containing apertures. The effect of an aperture on a laser beam will be the subject of Sec. 5.2 and Sec. 5.3 while the implementation of aperture effects in the ABCD-matrix formalism is covered in Sec. 5.4.

Aperture effects in several applications modify only slightly the predictions computed using standard ABCD-matrix formalism. However, there are situations where aperture effects lead to fundamental differences. One of such examples is presented in Chapter 8.

5.2. Transmissivity of apertures

When the size of the pump spot is large compared to the width of the TEM₀₀ mode, the laser operates in several transverse modes. By reducing the size of the pump spot, operation in the fundamental transversal mode is enforced as higher-order modes experience less gain. In this section, we describe this selection process. To do so, the finite-size pump spot is represented as a superposition of an infinite pump spot (providing a homogeneous gain) and an aperture with finite size. Therefore, in this section we investigate the transmission of a laser beam through an aperture with rotational symmetry.

Let us assume a laser beam propagating in positive z-direction and impinging on an aperture which can be positioned at $z = 0$ without loss of generality. We only consider rotational symmetric apertures and beams. Due to the symmetry of the problem the amplitude \vec{E} of the electric field of the freely propagating laser beam can be expanded in terms of Gauss-Laguerre laser functions [167]

$$\vec{E}_{p,m}(r, \varphi) = \vec{e}_{pol} \sqrt{\frac{\mu_0}{\epsilon_0}} \sqrt{2P} \Psi_{p,m}(r, \varphi), \quad (41)$$

where P is the laser power, \vec{e}_{pol} is the polarization vector, μ_0 the vacuum permeability and ϵ_0 the vacuum permittivity. $\Psi_{p,m}(r, \varphi)$ are the normalized Gauss-Laguerre wave functions defined as [150]

$$\Psi_{p,m}(r, \varphi) = \begin{cases} \sqrt{\frac{2}{\pi}} \frac{1}{w} e^{-\frac{r^2}{w^2}} L_{p,0} \left(2 \frac{r^2}{w^2} \right) & m = 0 \\ \sqrt{\frac{p!}{\pi \cdot (m+p)!}} \frac{2}{w} \left(\frac{r\sqrt{2}}{w} \right)^m e^{-\frac{r^2}{w^2}} L_{p,m} \left(2 \frac{r^2}{w^2} \right) \sin(m\varphi) & m > 0 \end{cases}, \quad (42)$$

where r represents the radial distance from the optical axis, φ the azimuthal angle, w the beam width at the aperture position, $L_{p,m}$ the Laguerre polynomials specified by the two integer numbers m and p . $\Psi_{p,m}$ represents the wave amplitude fulfilling the Helmholtz electromagnetic wave equation. The phase factors are neglected here since we simply consider only the wave at a fixed position in z (at the aperture position).

The wave functions of Eq. (42) form a complete basis and are normalized so that

$$\int_0^{\infty} 2\pi \Psi_{p,m}^2 r dr = 1. \quad (43)$$

As a result, the intensity is proportional to $\Psi_{p,m}^2(r)$ and the laser power is

$$P = \int_0^{\infty} 2\pi \sqrt{\frac{\epsilon_0}{\mu_0}} |\vec{E}|^2 r dr. \quad (44)$$

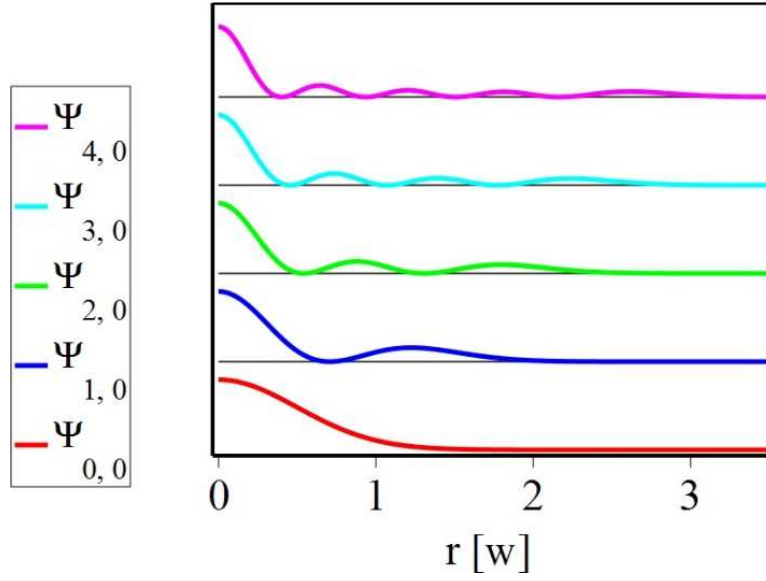


Figure 44: Gauss-Laguerre laser beam wave functions $\Psi_{p,m}(r)$ for $m = 0$ as a function of the distance r from the symmetry axis expressed in units of width w of the laser beam.

The radial distribution of some Gauss-Laguerre laser beam modes for $\Psi_{p,0}$ ($m = 0$) is plotted in Figure 44. The most important mode is the fundamental (TEM00) mode given by [183]

$$\Psi_{0,0}(r, \varphi) = \sqrt{\frac{2}{\pi}} \frac{1}{w} e^{-\frac{r^2}{w^2}}. \quad (45)$$

Both the input and the transmitted wave can be described using the basis given in Eq. (42). The transmitted beam has a reduced intensity and a radial distribution different from the ingoing beam due to the reduction of the width and the diffraction at the aperture. As a result, the outgoing wave (the wave leaving the aperture) is not simply given by the incoming wave attenuated by a factor.

To compute the Gauss-Laguerre expansion of the transmitted mode we first have to know the transmission of an aperture. For example a classical hard aperture blocking the laser beam for $r > R_0$ and having 100 % transmission for $r < R_0$ is defined as

$$\phi(r) = \begin{cases} 1 & r \leq R_0 \\ 0 & r > R_0 \end{cases}. \quad (46)$$

In this chapter, we define $\phi(r)$ to be the transmission for the amplitude of the optical wave.

The scattering amplitude $A_{p,m,q,n}$ from one input beam component $\Psi_{q,n}$ to another outgoing beam component $\Psi_{p,m}$ can be simply computed as

$$A_{p,m,q,n} = \langle \Psi_{p,m} | \phi | \Psi_{q,n} \rangle \quad (47)$$

$$A_{p,m,q,n} = \int_0^{2\pi} \sin \varphi d\varphi \int_0^\infty r \phi(r, \varphi) \Psi_{p,m}(w, r, \varphi) \Psi_{q,n}(w, r, \varphi) dr. \quad (48)$$

In Eqs. (46) and (48) we assumed that the aperture does not modify the wave-front curvature or the phase delay of the laser beam. Equation (48) can also be used to determine the transmissivity of a resonator

eigenmode through the aperture. In this case only the coupling term of the laser mode with itself is of interest i.e. for $p = q$ and $m = n$ ³.

Due to the assumed rotational symmetry typically only laser beam components with $m = 0$ need to be considered. Thus, we define the scattering amplitude $A_{p,q}$ as

$$A_{p,q} = \langle \Psi_{p,0} | \phi | \Psi_{q,0} \rangle. \quad (49)$$

The fraction of the power that is transmitted (diffracted) from an incoming beam component $\Psi_{q,0}$ into a transmitted beam component $\Psi_{p,0}$ is thus simply

$$I_{p,q} = |A_{p,q}|^2 = \left(\int_0^\infty 2\pi r \phi(r) \Psi_{p,0}(w, r) \Psi_{q,0}(w, r) dr \right)^2. \quad (50)$$

Given an incoming laser mode or beam component $\Psi_{q,0}$ its total transmissivity T_q through the aperture is expressed by

$$T_q = 2\pi \int_0^\infty r \phi^2(r) \Psi_{q,0}^2(w, r) dr. \quad (51)$$

The transmissivity T_q accounts for all possible beam components (Gauss-Laguerre wave functions $\Psi_{k,0}$) of the transmitted beam, so that it can be written as

$$T_q = \sum_k I_{k,q}. \quad (52)$$

A plot of the transmissivity T_q for input modes $\Psi_{q,0}$ at the hard aperture described by Eq. (52) is shown in Figure 45. As expected, for vanishing aperture radius R_0 the transmissivity vanishes; for an increasing R_0 the transmissivity becomes larger and asymptotically approaches 100%.

Even more relevant for the suppression of laser operation in higher-order modes is the fraction of the laser power transmitted through the aperture that remains in the same mode, i.e. $\Psi_{p,0}(r, w) \rightarrow \Psi_{p,0}(r, w)$:

$$I_{p,p} = |A_{p,p}|^2. \quad (53)$$

Figure 46 shows the transmissivity $I_{0,0}, I_{1,1}, I_{2,2}, I_{3,3}, \dots$ from Gauss-Laguerre wave functions $\Psi_{p,0}$ before the aperture into the same Gauss-Laguerre wave functions $\Psi_{p,0}$ after the aperture. Thus, in a laser cavity the quantity $1 - I_{p,p}$ represents the aperture losses of the $\Psi_{p,0}$ resonator eigenmode. In fact, the coupling to different beam components $\Psi_{p,0}(r, w) \rightarrow \Psi_{q,0}(r, w)$ with $p \neq q$ adds to the absorptive losses caused by the aperture. In a resonator the transmissivity $I_{p,p}$ is the relevant quantity needed to determine the roundtrip losses of the cavity eigenmode.

³ Here we have assumed that the eigenmodes of the resonator are approximatively given by the Gauss-Laguerre wave functions $\Psi_{p,m}$ as in this section (and generally in this thesis) we consider only apertures causing small distortions. This is related to the low thin-disk gain, which would not sustain laser operation when large aperture losses (large distortions) are involved. Furthermore, we do not consider phase masks as presented, for example, in reference [287], used to generate a fundamental mode having a super-Gaussian profile.

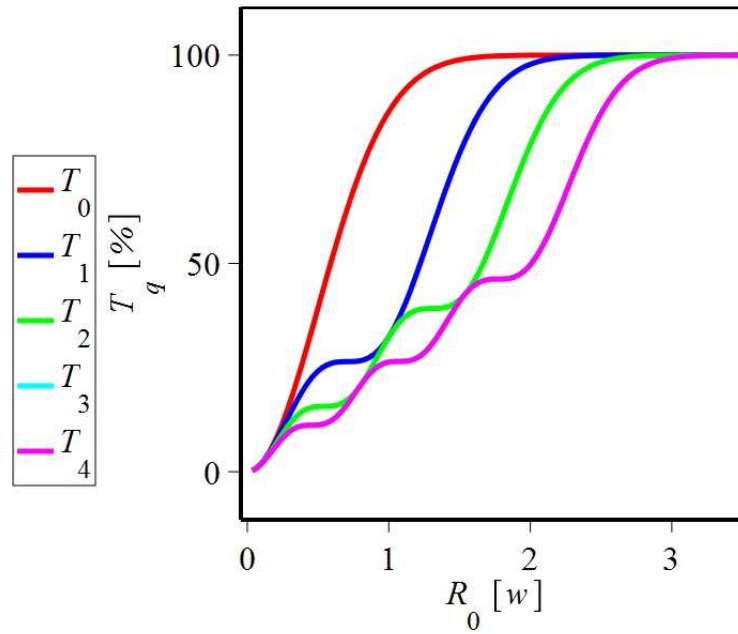


Figure 45: Total transmissivity T_q given by Eq. (52) for various Gauss-Laguerre wave functions $\psi_{q,0}$ as a function of the aperture radius R_0 normalized to the input beam width w . T_q represents the fraction of the total transmitted power for each wave function $\psi_{q,0}$, regardless of the deformation of the transmitted laser mode.

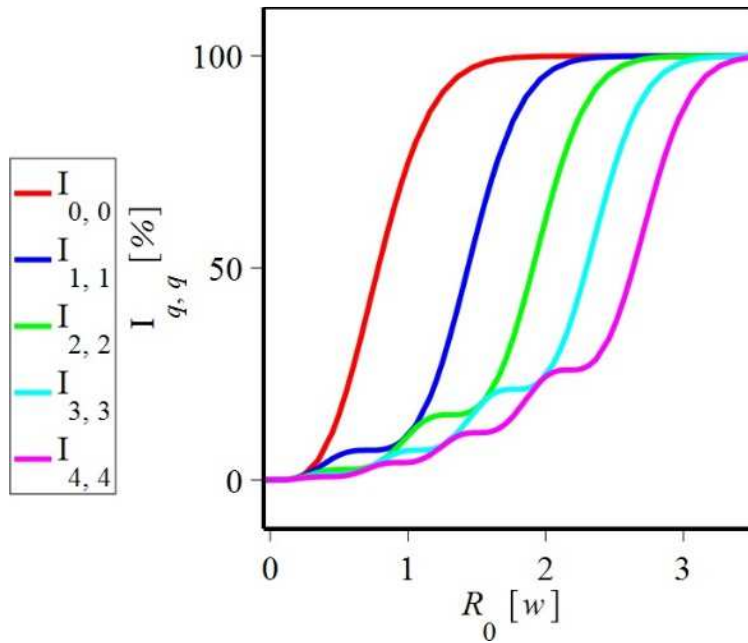


Figure 46: Transmissivity $I_{q,q}$ for the modes $\psi_{q,0}(r, w) \rightarrow \psi_{q,0}(r, w)$ via the flattop aperture given in Eq. (45) as a function of the radius of the aperture R_0 .

5.3. Diffraction at apertures

In the previous section, we quantified the aperture losses assuming that the resonator eigenmodes were given by Gauss-Laguerre wave functions $\Psi_{p,0}$. Yet, the transmitted laser mode, being deformed, has to be expressed as a sum of Gauss-Laguerre wave functions to account for the diffraction from $\Psi_{p,0}(r,w) \rightarrow \Psi_{q,0}(r,w)$ with $p \neq q$. In this section, we evaluate the fraction of power that is refracted into higher-order beam components when a Gaussian beam ($\Psi_{0,0}$) impinges on the aperture. This information is then used to extract the pump spot diameter that provides sufficient mode selectivity while minimizing beam distortions.

The fraction of the beam power, which is diffracted by the aperture from the Gaussian mode into higher-order beam components, is defined by the difference of the total transmission and the transmission of the Gaussian mode component into itself:

$$T_0 - |A_{0,0}|^2 = \sum_{k \neq 0} |A_{k,0}|^2 \quad (54)$$

This fraction is implicitly normalized to the input power. Similarly, it is interesting to consider the fraction of high-order beam components that have been excited by the aperture relative to the total power transmitted through the aperture

$$S = \frac{T_0 - |A_{0,0}|^2}{T_0} = \frac{\int 2\pi r \phi^2(r) \Psi_{0,0}^2(r) dr - \left(\int 2\pi r \phi(r) \Psi_{0,0}^2(r) dr \right)^2}{\int 2\pi r \phi^2(r) \Psi_{0,0}^2(r) dr} \quad (55)$$

In Eqs. (50) and (55) we assumed that the same Gauss-Laguerre wave functions are used to express the input and the output beams. Thus, we implicitly assumed that the beam width at the input (w_{in}) equals the beam width at the output (w_{out}). As, the size of the beam is reduced by passing an aperture, it is more suitable to express the transmitted wave as a sum of Gauss-Laguerre wave functions having a width w_{out} smaller than the input width w_{in} . The width of the transmitted beam for the Gaussian mode component is simply given by the expression

$$w_{out} = \frac{\int_{r=0}^{\infty} r^2 \phi^2 \Psi_{0,0}^2 dr}{\int_{r=0}^{\infty} r \phi^2 \Psi_{0,0}^2 dr} \quad (56)$$

When using w_{out} from Eq. (56) as the width parameter to describe the outgoing beam in terms of Gauss-Laguerre wave functions, we find that the power fraction of the higher-order components of the transmitted beam relative to the transmitted total power is

$$S' = \frac{\int 2\pi r \cdot \phi^2(r) \Psi_{0,0}^2(r, w_{in}) dr - \left(\int 2\pi r \phi(r) \Psi_{0,0}(r, w_{in}) \Psi_{0,0}(r, w_{out}) dr \right)^2}{\int 2\pi r \phi^2(r) \Psi_{0,0}^2(r, w_{in}) dr} \quad (57)$$

The fractions of the transmitted power which have been excited into higher-order components given by the quantity S and S' are shown in Figure 47 together with the total transmitted intensity T_0 . The total transmission increases with increasing aperture diameter R_0 . At the same time the excitation of higher-order components S and S' decreases. Note that S' is considerably smaller than S because a Gaussian wave function with w_{out} better fits the transmitted beam.

The scattering losses can be reduced significantly by using soft apertures instead of the hard flattop aperture of Eq. (46). In Sec. 5.4, it is shown that for Gaussian apertures the fraction of higher-order components generated by the aperture is exactly zero if the reduction of the beam width caused by the aperture is considered.

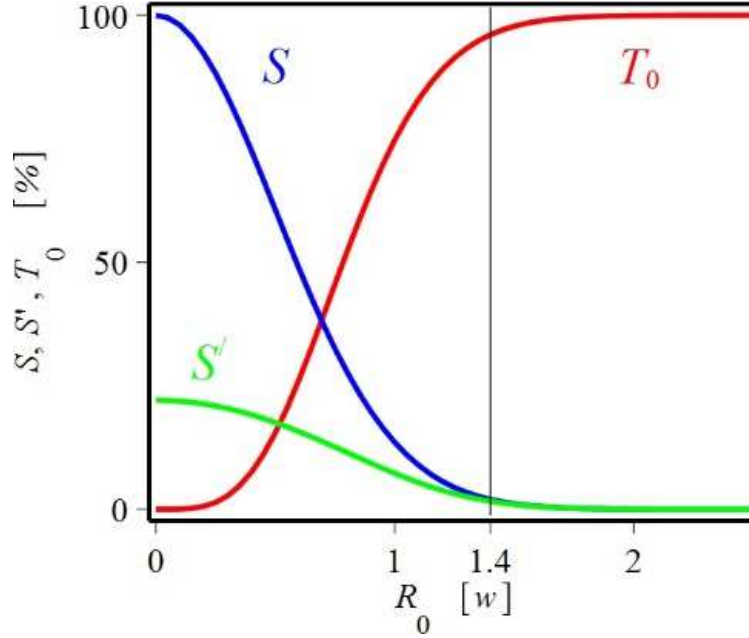


Figure 47: Fractions of transmitted power (S and S') that is scattered into higher-order components versus the aperture radius R_0 for the flattop aperture of Eq. (46). In comparison, the total power transmission T_0 is shown.

5.4. Gaussian, Super-Gaussian and flattop apertures

In Figure 48 the quantities T_q , $I_{q,q}$, S and S' are compared for three aperture types: flattop, Super-Gaussian, and Gaussian. These apertures are distinguished by the sharpness of their transmission curves. The flattop profile is identical to the classical hard aperture considered in the previous sections

$$\phi(r) = \begin{cases} 1 & r \leq R_0 \\ 0 & r > R_0 \end{cases} \quad (58)$$

A soft aperture having a homogeneous transmission at the center and a smooth fall-off can better describe the gain profile of the active medium and the losses caused by higher-order distortions of the OPD of the thin disk. Super-Gaussian apertures [184], as

$$\phi(r) = e^{-\frac{1}{2}\left(\frac{r}{R_0}\right)^6} \quad (59)$$

have a transmission close to 1 over a large range at the center, and a smooth fall-off at $r \approx R_0$. Gaussian apertures given by

$$\phi(r) = e^{-\left(\frac{r}{w}\right)^2} \quad (60)$$

can easily be treated analytically and integrated into the ABCD-matrix formalism. For clarity, we remind here that the aperture functions $\phi(r)$ are acting on the input wave Ψ so that the transmitted power normalized to the input power is

$$T = \int \phi^2(r) \Psi^2(r) 2\pi r dr . \quad (61)$$

As mentioned before, apertures could be used to enforce laser operation in the TEM00 mode. For example, consider the transmission curves T_q for a flattop aperture as shown in Figure 48 b1). The power transmission through an aperture with radius $R_0 = 1.4 w$ for the fundamental mode $\Psi_{0,0}$ is 98%, while for the $\Psi_{1,0}$ mode it is only 68%. For higher-order modes, the transmission decreases further. Therefore, the use of a flattop aperture with radius $R_0 = 1.4 w$ leads to a good selectivity between the fundamental and higher-order modes.

For a Super-Gaussian aperture, the selectivity between modes according to the total power transmission is still high as shown in Figure 48 b2), but the TEM00 mode suffers from a slightly smaller transmission at the reference value $R_0 = 1.4 w$ relative to the transmission for a flattop aperture. Gaussian apertures further decrease the power transmission and the selectivity (relative transmission of the various modes) as shown in Figure 48 b3). These three plots (b1, b2 and b3) demonstrate that independently of the choice of the aperture type, higher-order modes (and equally beam components) suffer from larger transmission losses and that the selectivity improves for apertures with a sharper fall-off.

The quantity $I_{q,q} = |A_{q,q}|^2$ shown in Figure 48 c1), c2) and c3) represents the intensity transmission for the $\Psi_{q,0} \rightarrow \Psi_{q,0}$ diffraction process, where the final and initial modes are identical. This quantity is more relevant than the total transmitted power that accounts for all possible final beam components. $I_{q,q}$ can be used to compute the losses of the mode $\Psi_{q,0}$ circulating in the optical system. Usually the fundamental mode $\Psi_{0,0}$ is of relevance. As can be seen from the plots, $I_{q,q}$ shows an even better mode selectivity compared with the total power transmission T_q .

As already mentioned previously, the beam width is changed when passing through the aperture so that the beam parameter w at the output of the aperture w_{out} differs from the parameter w at its input w_{in} . Hence the transmitted wave should be expanded in terms of Gauss-Laguerre components with $w = w_{out}$. The quantity $I'_{q,q} = |A'_{q,q}|^2$ describing the power transmission for the process $\Psi_{q,0}(r, w_{in}) \rightarrow \Psi_{p,0}(r, w_{out})$ would be the most appropriate quantity to compute the losses for the mode circulating in the system. The relevant case for applications is represented by the $\Psi_{0,0}(w_{in}) \rightarrow \Psi_{0,0}(w_{out})$ scattering.

The scattering processes $\Psi_{0,0}(w_{in}) \rightarrow \Psi_{0,0}(w_{in})$ and $\Psi_{0,0}(w_{in}) \rightarrow \Psi_{0,0}(w_{out})$ can be quantified from the parameters S and S' given in Figure 48 d1), d2) and d3). S and S' can be used to compute the power fraction of intensity which is scattered away from the TEM00 mode propagating in the optical system. It represents the diffraction losses normalized to the transmitted power for an input beam in the TEM00 mode. By comparing Figure 48 d1), d2) and d3) it is evident that the scattering losses in higher-order components decrease with smoother fall-off of the aperture transmission curve, reducing the selectivity for the TEM00 mode. The extreme case is given by the Gaussian aperture where $S' = 0$. This means that a Gaussian aperture does not scatter the input TEM00 mode into higher-order components provided that the basis functions used to describe the transmitted wave account for the decrease in beam width according to Eq. (56). Thus the transmitted wave Ψ^{out} for an input mode $\Psi_{0,0}(w_{in})$ reads

$$\Psi^{out} = T_0 \Psi_{0,0}(w_{out}). \tag{62}$$

As we will see later (see Eq. (109)) the transmitted power T_0 for Gaussian apertures takes a very simple form which only depends on w_{in} and the size W of the Gaussian aperture.

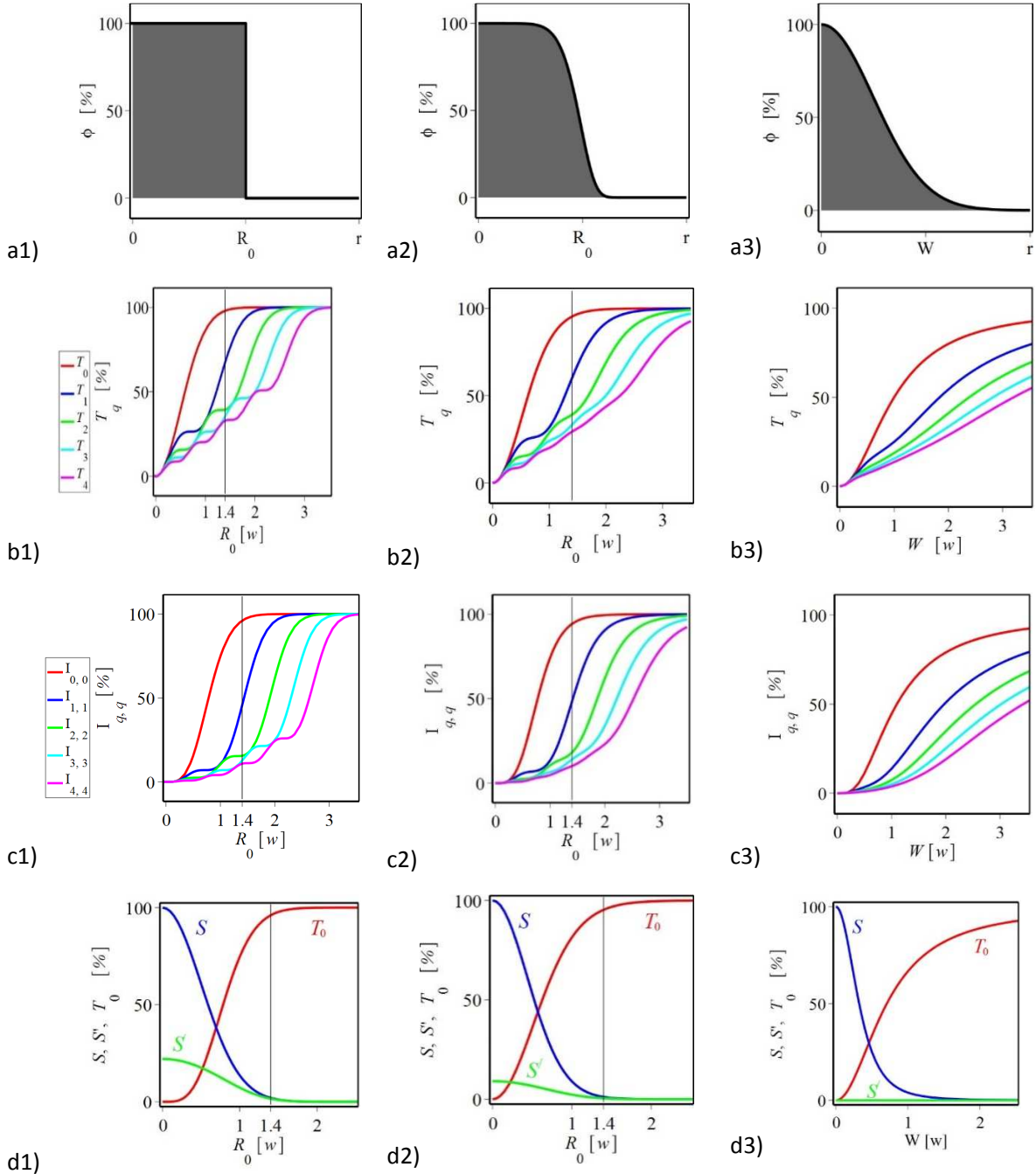


Figure 48: Aperture effects for three types of aperture: flattop (left column), Super-Gaussian (middle column) and Gaussian (right column). The a) row shows the transmission curves $\phi(r)$ via the apertures and the b) row the total transmittivity T_q for a given input mode $\Psi_{q,0}$. The c) row shows the transmittivity $I_{q,q} = |A_{q,q}|^2$ for the processes $\Psi_{q,0} \rightarrow \Psi_{q,0}$ and (d) indicates the fraction S and S' of the transmitted power which is scattered into higher-order components for an input wave in the Gaussian mode $\Psi_{0,0}$.

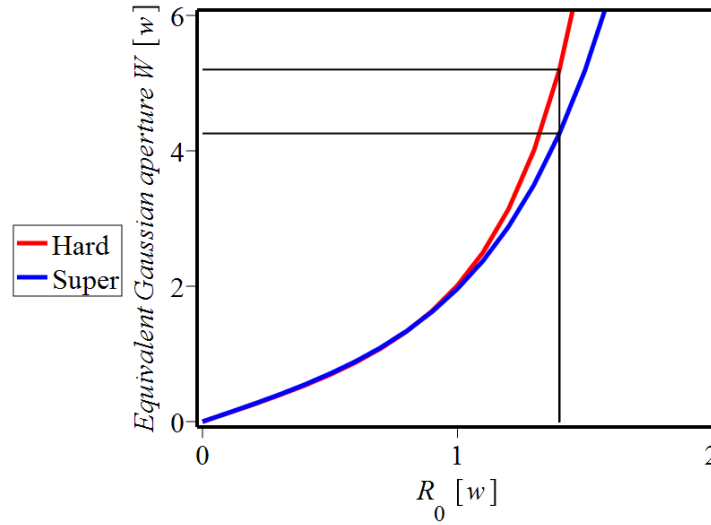


Figure 49: The aperture width W of a Gaussian aperture having the same transmission as a hard aperture for a radius of R_0 is given in red. The width W of a Gaussian aperture having the same transmission as a super-Gaussian aperture R_0 is given in blue. According to a rule of thumb, for optimal performance the pump radius R_0 has to be 1.4 times larger than the beam width w the value marked in the black line. The Gaussian aperture to be used to simulate the aperture effect in the thin disk is in this case $W \approx 4.2 w$, or equivalent to $W \approx 3 R_0$.

5.4.1. Equivalent Gaussian aperture

As will be detailed in Sec. 5.4, Gaussian apertures can be implemented in the ABCD-matrix formalism. Conversely, the aperture effects at the thin disk have a Super-Gaussian profile, as a consequence of the gain profile and the OPD profile that shows deviations from a spherical thermal lens at the periphery of the pump profile. Yet, super-Gaussian apertures cannot be implemented directly in the ABCD-matrix formalism. Therefore, we need to define equivalent Gaussian apertures to account for the effects of the Super-Gaussian apertures. In other words, we need to find a relation between the R_0 given in Eq. (59) and W given in Eq. (60). Applying this relation, we can deduce the size W and use it to simulate the aperture at the thin disk. R_0 is known as it corresponds to the radius of the pump profile at FWHM.

The aim of this subsection is to define an equivalent Gaussian aperture having similar power transmission $I_{0,0}$ and similar output beam width (w_{out}) to what is obtained with a Super-Gaussian aperture. By comparing the power transmission $I_{0,0}$ of a TEM₀₀ mode via a Gaussian aperture and a Super-Gaussian aperture

$$I_{0,0}^{Gauss}(W, w) = I_{0,0}^{SuperGauss}(R_0, w), \quad (63)$$

we obtain a relation between the size of the Gaussian aperture W and the radius R_0 of the Super-Gaussian aperture. This relation is plotted in Figure 49.

As mentioned before, the rule of thumb applied in the thin-disk laser community is to have the following relation between the laser mode width w at the thin disk and the radius R_0 of the pump profile (Super-Gaussian aperture)

$$\frac{R_0}{w} \approx 1.4 \leftrightarrow w \approx 0.35 D_p, \quad (64)$$

where we have used the fact that the pump diameter is $D_p = 2 R_0$. As can be extracted graphically from Figure 49, the size W of the Gaussian aperture has to fulfill the relation

$$\frac{W}{w} \approx 4.2 \quad (65)$$

to have the same losses. Therefore, when equating the transmission $I_{0,0}$, we find that the equivalent Gaussian aperture size W is

$$W \approx 3.0 R_0. \quad (66)$$

For comparison, Figure 49 also shows the equivalent Gaussian aperture W having the same transmission $I_{0,0}$ as a flattop aperture of radius R_0 . In this case, the equivalent Gaussian aperture size is $W \approx 3.6 R_0$. This serves to give a feeling for the sensitivity of the results to variations of the sharpness of the aperture fall-off.

In a similar way, by equating the width w_{out} for a Gaussian aperture and a Super-Gaussian aperture

$$w_{0,0 out}^{Gauss}(W, w_{in}) = w_{0,0 out}^{SuperGauss}(R_0, w_{in}), \quad (67)$$

we obtain a relation between the size of the Gaussian aperture W and the radius R_0 of the Super-Gaussian aperture. This relation is plotted in Figure 50. As can be extracted graphically from this figure, the equivalent Gaussian size W for a Super-Gaussian aperture of radius $R_0 \approx 1.4 w$ is

$$\frac{W}{w} \approx 3.0. \quad (68)$$

Therefore, when equating the transmitted width w_{out} we find that the equivalent Gaussian aperture size W is

$$W \approx 2.1 R_0. \quad (69)$$

By comparing Eq. (69) with Eq. (66) it is found that both conditions, similar transmitted in power $I_{0,0}$ and similar output width w_{out} , can be fulfilled approximately by choosing

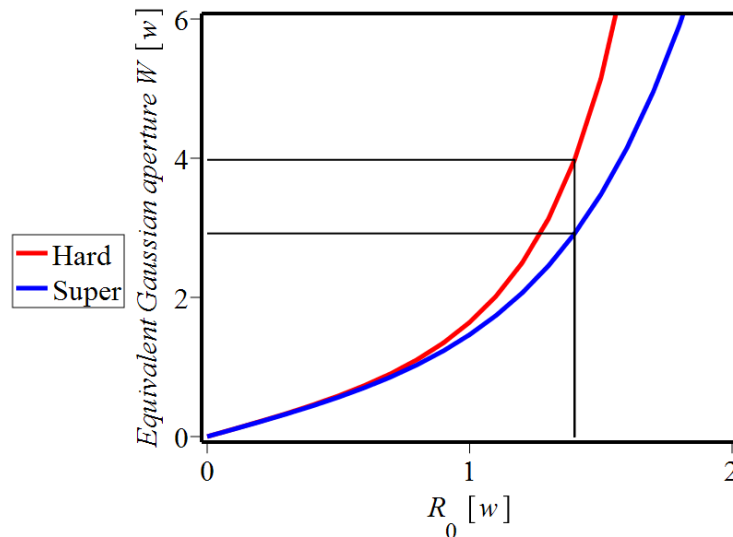


Figure 50: The aperture width W of a Gaussian aperture having the same reduction of the beam width as a hard aperture for a radius of R_0 is shown in red. The aperture width W of a Gaussian having the same reduction of the beam width as a super-Gaussian aperture R_0 is given in blue. According to a rule of thumb, for optimal performance the pump radius R_0 has to be 1.4 times larger than the beam width w . The Gaussian aperture to be used to simulate the aperture effect in the thin disk is in this case $W \approx 3.9 w$, or equivalently, $W \approx 2.1 R_0$.

$$W \approx 2.6 R_0 . \quad (70)$$

Thus, throughout this thesis, we assumed apertures fulfilling the condition

$$W \approx 4 w_{in} \quad (71)$$

for the simulations of the aperture effect. Note that this relation holds when the pump radius R_0 and the laser mode width w at the aperture fulfill the condition $R_0 \approx 1.4 w$, which is a rule of thumb derived from the practical application where the optical-to-optical efficiency of the laser was optimized. It represents a trade-off between aperture losses and overlap with the pumped region.

5.5. ABCD-Matrix formalism and Gaussian apertures

In this section we describe a method of implementing Gaussian apertures in the ABCD-matrix formalism. Two types of ABCD-matrix are needed to describe the aperture effects on a Gaussian beam: one ABCD-matrix has to be used when computing the complex q -parameter of the Gaussian beam and another one to compute the evolution of the Gaussian beam excursion and tilt from the optical axis.

5.5.1. ABCD-matrix for geometrical rays

We start with a brief review of the ABCD-matrix formalism [185]. Originally, this formalism was developed for calculating the propagation of a geometric ray that is defined by a transverse excursion x and a tilt of θ from the optical axis (z-axis):

$$\text{Ray} = \begin{bmatrix} x \\ \theta \end{bmatrix}. \quad (72)$$

The position x' and the tilt θ' of the ray after propagation in an optical element (lens, mirror, free propagation etc.) are given by

$$\begin{bmatrix} x' \\ \theta' \end{bmatrix} = \begin{bmatrix} A & B \\ C & D \end{bmatrix} \begin{bmatrix} x \\ \theta \end{bmatrix}, \quad (73)$$

where $\begin{bmatrix} x \\ \theta \end{bmatrix}$ represents the ray at the input transverse plane, $\begin{bmatrix} x' \\ \theta' \end{bmatrix}$ the ray at the output plane of the optical element, and the ABCD-matrix is a 2x2 matrix specific of the optical element. The basic optical elements [185] are free propagations described by

$$M_{free} = \begin{bmatrix} 1 & L \\ 0 & 1 \end{bmatrix}, \quad (74)$$

where L represents the propagation distance along the z-axis, lenses described by

$$M_{lens} = \begin{bmatrix} 1 & 0 \\ -\frac{1}{f} & 1 \end{bmatrix}, \quad (75)$$

where f represents the focal length of the lens, flat mirrors described by

$$M_{flat\ mirror} = \begin{bmatrix} 1 & 0 \\ 0 & 1 \end{bmatrix} \quad (76)$$

and curved mirrors described by

$$M_{curved\ mirror} = \begin{bmatrix} 1 & 0 \\ -\frac{2}{R_m} & 1 \end{bmatrix}, \quad (77)$$

where R_m is the radius of curvature.

The output ray transverse excursion and tilt after transmission through a succession of N optical elements is thus represented by

$$\begin{bmatrix} x' \\ \theta' \end{bmatrix} = \begin{bmatrix} A_N & B_N \\ C_N & D_N \end{bmatrix} \cdots \cdots \begin{bmatrix} A_2 & B_2 \\ C_2 & D_2 \end{bmatrix} \begin{bmatrix} A_1 & B_1 \\ C_1 & D_1 \end{bmatrix} \begin{bmatrix} x \\ \theta \end{bmatrix}. \quad (78)$$

5.5.2. ABCD-matrix formalism for Gaussian beams

The same ABCD-matrices can be used to describe the evolution of a Gaussian beam [185] (fundamental mode or a higher-order mode) through an optical system. TEM₀₀ beams are represented by the complex beam parameter q given by

$$\frac{1}{q} = \frac{1}{R} - i \frac{\lambda}{\pi w^2}, \quad (79)$$

where λ is the wavelength, w the beam width and R the wave-front curvature. The parameters $q = q(z)$, $R = R(z)$ and $w = w(z)$ are dependent on the z -position. Equation (79) can be written equivalently as

$$q = (z - z_0) + i z_R, \quad (80)$$

where z_0 represents the focus position and z_R the Rayleigh length of the beam. The distance from the focus is thus given by the real part of q ,

$$(z - z_0) = \text{Re}(q), \quad (81)$$

while the square root of the complex part represents the beam waist at the focus position

$$w_0 = \sqrt{\frac{\lambda \text{Im}(q)}{\pi}}. \quad (82)$$

The beam width at any position z is obtained from

$$w(z) = \sqrt{\frac{\lambda}{\pi \text{Im}\left(\frac{1}{q(z)}\right)}}. \quad (83)$$

The complex beam parameter q can be propagated along an optical element using the same ABCD-matrices is applied to propagate the geometrical rays using following expression [185]

$$\begin{bmatrix} q' \\ 1 \end{bmatrix} = k \begin{bmatrix} A & B \\ C & D \end{bmatrix} \begin{bmatrix} q \\ 1 \end{bmatrix}, \quad (84)$$

where q' is the complex beam parameter after propagation in the optical system, q the beam parameter at the input of the optical system and k a normalization factor. This system of two equations can be solved. From the second equation, the normalization k can be deduced. From the first equation and the normalization we obtain

$$q' = \frac{Aq + B}{Cq + D}. \quad (85)$$

Equation (85) can be applied to any ABCD-matrix, even to matrices with imaginary components and to matrices that are the result of a multiplication of matrices

$$\begin{bmatrix} A & B \\ C & D \end{bmatrix} = \begin{bmatrix} A_N & B_N \\ C_N & D_N \end{bmatrix} \cdots \cdots \begin{bmatrix} A_2 & B_2 \\ C_2 & D_2 \end{bmatrix} \begin{bmatrix} A_1 & B_1 \\ C_1 & D_1 \end{bmatrix} \quad (86)$$

describing the propagation in a succession of N optical elements.

5.5.3. Transmission of the TEM₀₀ mode through a Gaussian aperture

Consider a Gaussian beam which propagates in z -direction having an offset (excursion) x_{in} in x -direction relative to the optical axis (z -axis). The transverse part of its amplitude is

$$\Psi_{0,0}(x, y) = \sqrt{\frac{2}{\pi}} \cdot \frac{1}{w} \cdot e^{-\frac{(x+x_{in})^2 + y^2}{w^2}} \quad (87)$$

where x, y are the transverse coordinates and w is the beam width. The mode is normalized so that

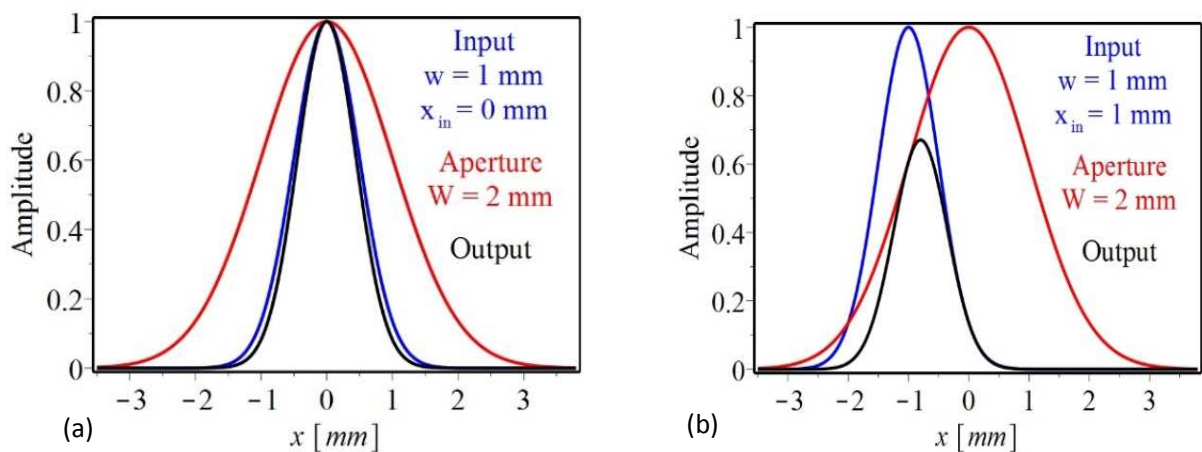


Figure 51: Amplitude of the transmitted beam $\Psi_{0,0}^{out}(x)$ (black) shown for two cases. (a) The impinging beam given in blue $\Psi_{0,0}^{in}(x)$ is aligned (on-axis) with the Gaussian aperture given in red. (b) Similar to a) but here the impinging beam is 1 mm off-axis.

$$\iint_{-\infty}^{\infty} \Psi_{0,0}^2(x, y) dx dy = 1. \quad (88)$$

This laser mode impinges on a Gaussian aperture centered to the optical axis whose amplitude transmission curve is

$$\phi(x, y) = e^{-\frac{x^2+y^2}{W^2}}. \quad (89)$$

The amplitude of the outgoing (transmitted) beam Ψ^{out} is related to the input beam Ψ^{in} as

$$\xi \Psi^{out}(x, y) = \phi(x, y) \Psi^{in}(x, y) \quad (90)$$

where ξ is a normalization constant. It can be shown that a Gaussian aperture transforms a Gaussian beam into another Gaussian beam with different width and beam excursion. Therefore, no higher-order-mode components are generated, provided that the transmitted Gaussian beam is expressed using w_{out} from Eq. (56) (see also S' in Figure 48 d3). The width and excursion of the output beam can thus be obtained starting from the assumption that

$$\xi \Psi^{out} = \xi \Psi_{0,0}(x, y, w_{out}) = \phi(x, y) \cdot \Psi_{0,0}(x, y, w_{in}). \quad (91)$$

This equation can be written using the explicit expression for the input and output Gaussian beams as

$$\xi \Psi^{out} = \xi \sqrt{\frac{2}{\pi}} \frac{1}{w_{out}} e^{-\frac{(x+x_{out})^2+y^2}{w_{out}^2}} = \sqrt{\frac{2}{\pi}} \frac{1}{w_{in}} e^{-\frac{(x+x_{in})^2+y^2}{w_{in}^2}} e^{-\frac{x^2+y^2}{W^2}}, \quad (92)$$

where w_{in} and w_{out} are the widths of the input and output beams, and x_{out} , x_{in} are the offsets (excursions) of the input and output beams, respectively. A comparison between the left side and the right side of this equation can be used to find the width of the output beam

$$\frac{1}{w_{out}^2} = \frac{1}{w_{in}^2} + \frac{1}{W^2}, \quad (93)$$

the offset of the transmitted beam

$$x_{out} = x_{in} \frac{W^2}{w_{in}^2 + W^2}, \quad (94)$$

and the normalization factor

$$\xi = e^{-\frac{x_{in}^2}{w_{in}^2 + W^2}}. \quad (95)$$

Two examples of transmitted amplitudes are given in Figure 51 for the case that the impinging laser beam is centered with the aperture axis ($x_{in} = 0$), and for the case that the laser beam axis has an excursion ($x_{in} \neq 0$) relative to the symmetry axis of the aperture.

As visible from Figure 51 (b) and from the Eqs. (92) to (95) the transmitted beam still has a pure Gaussian shape also for the case that the incident laser beam has an excursion relative to the axis of the aperture. The width of the transmitted laser beam w_{out} does not depend on the beam excursion so that the q -parameter of the Gaussian beam can be propagated neglecting misalignments. By crossing the aperture, however, the offset of the beam is reduced according to Eq. (94). In summary, the transmitted (amplitude)

is a Gaussian mode with a width given by Eq. (93), an offset from the optical axis as expressed by Eq. (94), and an amplitude at a maximum of $\sqrt{\frac{2}{\pi}} \frac{1}{w_{in}} e^{-\frac{x_{in}^2}{w_{in}^2 + W^2}}$.

5.5.4. Gaussian apertures in the ABCD-matrix formalism

With the knowledge won in Sec 5.4.3 the implementation of Gaussian apertures in the ABCD-matrix formalism for Gaussian beams is surprisingly simple [170]. First, we rewrite Eq. (79)

$$\frac{1}{w^2} = i \frac{\pi}{\lambda} \left(\frac{1}{q} - \frac{1}{R} \right). \quad (96)$$

For an aperture, the incoming and outgoing beams have different widths $w_{out} \neq w_{in}$, but the phase front curvature R remains unchanged $R_{in} = R_{out} = R$. Combining Eq. (96) with Eq. (93) assuming $R_{in} = R_{out} = R$, we find

$$i \frac{\pi}{\lambda} \left(\frac{1}{q_{out}} - \frac{1}{R} \right) = i \frac{\pi}{\lambda} \left(\frac{1}{q_{in}} - \frac{1}{R} \right) + \frac{1}{W^2}, \quad (97)$$

where q_{in} and q_{out} are the complex beam parameters before and after the aperture, respectively. This equation can be expressed as

$$\frac{1}{q_{out}} = \frac{1}{q_{in}} - i \frac{\lambda}{\pi W^2} \quad (98)$$

$$q_{out} = \frac{1}{\frac{1}{q_{in}} - i \frac{\lambda}{\pi W^2}} \quad (99)$$

$$q_{out} = \frac{q_{in}}{1 - q_{in} \cdot i \frac{\lambda}{\pi W^2}}. \quad (100)$$

By comparing this equation, with Eq. (84), the four components of the ABCD-matrix describing the aperture can be deduced: $A = 1$, $B = 0$, $C = -i \frac{\lambda}{\pi W^2}$ and $D = 1$. Thus, the ABCD-matrix for a Gaussian aperture of width W takes the form

$$M_{aperture} = \begin{bmatrix} 1 & 0 \\ -i \frac{\lambda}{\pi W^2} & 1 \end{bmatrix}. \quad (101)$$

This matrix corresponds to a matrix for a thin lens, but with an imaginary focal length.

The ABCD-matrix of the thin disk that exhibits both a lens effect (with a focal strength f) and an aperture effect (with size W) can be obtained by multiplying the ABCD-matrix for a thin lens given in Eq. (75) by the ABCD-matrix for an aperture shown in Eq. (101) to yield

$$M_{disk} = \begin{bmatrix} 1 & 0 \\ -\frac{1}{f} - i \frac{\lambda}{\pi W^2} & 1 \end{bmatrix}. \quad (102)$$

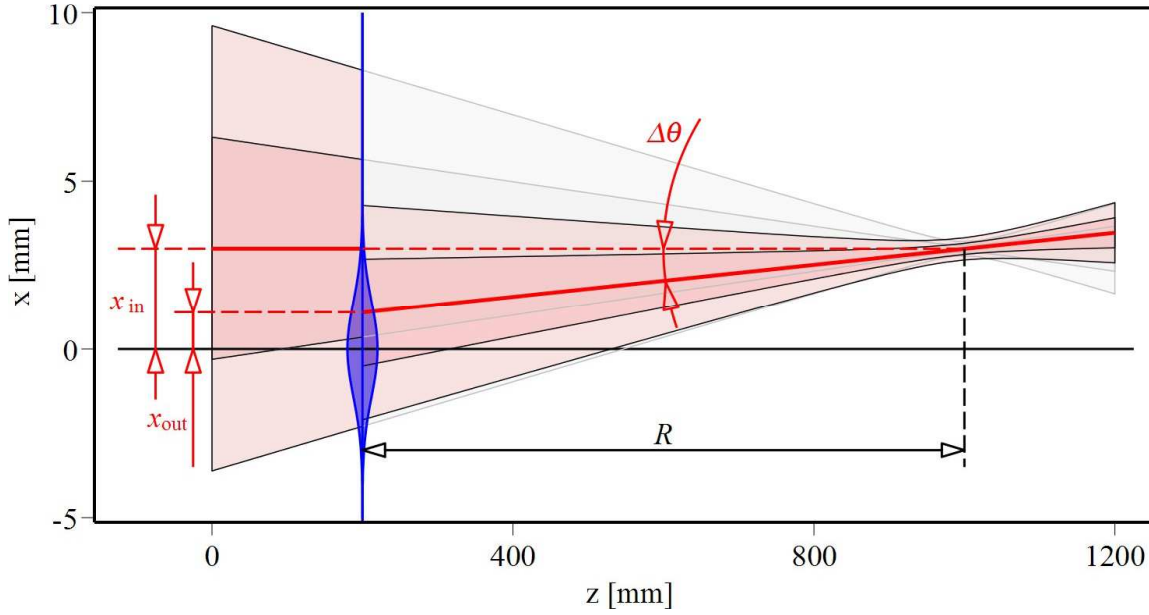


Figure 52: Change of the beam offset and beam tilt when passing through an aperture whose transmission is indicated in blue. The Gaussian input beam travels parallel to the optical axis ($\theta_{in} = 0$) with an excursion of $x_{in} \neq 0$. The darker and lighter shaded red areas indicate the $\pm w$ and the $\pm 2w$ range of the beam, respectively. After transmission through the aperture, the offset is reduced to x_{out} and the beam acquires a tilt $\theta_{out} \neq 0$ because the aperture selects only part of the beam. The aperture does not affect the focus of the beam that remains at the same position as the phase-front curvature. Geometrical considerations can be used to deduce that $\Delta\theta = \theta_{out} - \theta_{in} = (x_{out} - x_{in})/R$.

5.5.5. Tilts and excursion from the optical axis

As detailed in Sec. 5.4.1 the evolution of a geometrical ray from the input face to the output face of an optical element or system is given by

$$\begin{bmatrix} x' \\ \theta' \end{bmatrix} = \begin{bmatrix} A & B \\ C & D \end{bmatrix} \begin{bmatrix} x \\ \theta \end{bmatrix}. \quad (103)$$

The axis of a Gaussian beam described by an offset (excursion) and a tilt relative to the optical axis follows the same evolution as a geometrical ray for all standard optical elements as free propagation, lenses, mirrors etc. except for apertures. In this section, we aim to derive the ABCD-matrix describing the change of the offset and tilt for a Gaussian beam at an aperture. In fact, for the propagation of the geometrical rays the complex ABCD-matrix of Eq. (101) cannot be used. A new ABCD-matrix has to be derived for this purpose. Such a matrix can then be used to evaluate for example the sensitivity to misalignment of an optical system comprising apertures.

To do so we can make use of some special properties of Gaussian apertures applied to Gaussian beams. We have seen previously that the width of the transmitted Gaussian mode is unaffected by the beam excursion. This means that the width evolution of the beam (eigenmode) along the optical system can be evaluated neglecting the offset (excursion) of the beam from the optical axis.

On the other hand, the Gaussian aperture not only causes a reduction of the beam excursion according to Eq. (94), but also a change of the tilt angle of the Gaussian beam as

$$\theta_{out} = \theta_{in} - x_{in} \frac{w_{in}^2}{w_{in}^2 + W^2} \frac{1}{R}. \quad (104)$$

This equation can be derived by considering the geometry presented in Figure 52. The ABCD-matrix of a Gaussian aperture for the axis of a Gaussian beam can be obtained combining Eqs. (94) and (104)

$$M_{aperture}^{geometrical} = \begin{bmatrix} \frac{W^2}{w_{in}^2 + W^2} & 0 \\ -\frac{w_{in}^2}{w_{in}^2 + W^2} \frac{1}{R} & 1 \end{bmatrix}, \quad (105)$$

where W is the aperture size (see Eq. 60), w_{in} the beam width at the input face of the aperture, R the wavefront curvature of the beam at the aperture.

Note that this ABCD-matrix depends on parameters w_{in} and R of the impinging Gaussian beam. Thus, it can only be calculated after the evolution of the Gaussian mode along the optical system has been computed with the ABCD-matrix formalism neglecting misalignment of the beam from the optical axis. Unlike standard propagation matrices, the determinant of this matrix is smaller than one, because of the reduction of the offset that occurs in the aperture. The ABCD-matrix obtained can be used to evaluate misalignments (excursions and tilts) for a Gaussian beam propagating in an optical system similar to classic ray propagation.

5.6. Losses at apertures

The intensity transmitted through a Gaussian aperture of size W for an impinging $\psi_{0,0}$ beam as given in Eq. (86) with width w_{in} and excursion x_{in} can be computed analytically using the transmittivity

$$T_{tot} = \frac{P_{out}}{P_{in}} = \frac{\iint dx dy \frac{2\xi^2}{\pi w_{in}^2} e^{-2\frac{(x-x_{out})^2+y^2}{w_{out}^2}}}{\iint dx dy \frac{2}{\pi w_{in}^2} e^{-2\frac{(x-x_{in})^2+y^2}{w_{in}^2}}} = \xi^2 \left(\frac{w_{out}}{w_{in}}\right)^2 = \xi^2 \frac{W^2}{w_{in}^2 + W^2}, \quad (106)$$

where P_{out} and P_{in} are the transmitted and the input powers of the beam, respectively. For a Gaussian beam aligned with the aperture ($x_{in} = 0$) $\xi = 1$, while $\xi < 1$ when the aperture axis and the laser beam are misaligned. Thus, the losses at the aperture can be factorized as a product of two terms: one alignment-independent T_W , one alignment-dependent $T_{alignment}$, so that

$$T_{tot} = T_W T_{alignment}, \quad (107)$$

where

$$T_{alignment} = \xi^2 = e^{-2\frac{x_{in}^2}{w_{in}^2 + W^2}} \quad (108)$$

and

$$T_W = \frac{W^2}{w_{in}^2 + W^2} . \quad (109)$$

The total transmission in an optical system T_{OS} through the various apertures is the product of the various transmissions T_{tot} at the various apertures:

$$T_{OS} = \prod_k (T_{tot})_k . \quad (110)$$

Therefore, the total transmission in an optical system can be factorized in an alignment-independent $(T_W)_{OS}$ and an alignment-dependent $(T_{alignment})_{OS}$ part:

$$T_{OS} = (T_W)_{OS} \cdot (T_{alignment})_{OS} = \prod_k (T_W)_k \cdot \prod_k (T_{alignment})_k . \quad (111)$$

When a Gaussian laser beam is misaligned ($x_{in} \neq 0$) relative to the axis of the aperture, the losses at the aperture are increased. Yet, the output-beam width w_{out} does not depend on the misalignment, i.e., w_{out} does not depend on x_{in} as visible in Eq. (93). This fact allows us to first evaluate the evolution of the beam width $w(z)$ along the optical system independently of the misalignment effects. To compute it for an optical system comprising apertures, the complex ABCD-matrix given by Eq. (101) has to be used.

In a second step, misalignment effects can be treated. The misalignment evolution of the axis of a Gaussian beam described with an excursion $x(z)$ and tilt $\theta(z)$ from the optical axis can be computed using standard ABCD-matrix formalism complemented by the ABCD-matrix for apertures given in Eq. (105). Note that for apertures, contrarily to all standard elements, the ABCD-matrix for computing the width evolution differs from the ABCD-matrix for computing the misalignment evolution.

In a third step, the losses caused by the apertures can be computed using Eqs. (105) to (110). To compute the losses (transmission) in an optical system where the Gaussian beam is perfectly aligned with the apertures, only the knowledge of the width evolution $w(z)$ along the optical system is needed together with the size of the apertures. When misalignments are present, the computation of the losses requires, in addition, the knowledge of the excursion evolution $x(z)$ along the optical system.

5.7. Multi-pass amplifiers with apertures

In previous sections we developed the formalism to compute the beam width evolution $w(z)$ and the excursion evolution $x(z)$ along an optical system containing Gaussian apertures. In this section, we illustrate the effect of the soft apertures arising in the pumped medium on $w(z)$ and $x(z)$, considering the specific case of a multi-pass amplifier.

5.7.1. Evolution of the beam width along the multi-pass amplifier

We consider a multi-pass amplifier (see Chapter 7 and [54] for more details) as a succession of identical optical segments, each of them containing two passes at the active medium. An example of a segment

together with the propagation of a Gaussian mode in this segment is given in Figure 53. By concatenating four of these segments, the 8-pass amplifier shown in Figure 54 can be realized.

This regular beam evolution in the multi-pass amplifier occurs only when the input laser beam is correctly matched to the “eigenmode” of the underlying segment. When the input laser beam is not correctly matched, an irregular beam propagation occurs as demonstrated in Figure 55. Also in this figure, the aperture effects at the thin disk are neglected. By contrast, in the simulations presented in Figure 56 the aperture effects are considered. The comparison between Figure 55 and 56 demonstrates that the apertures damp the irregular oscillations of the beam width around the layout value. The aperture thus leads to a damping of the irregular width oscillations, so that at the amplifier output the beam width approaches the layout value. This effect, already described in [186], is regularly observed in regenerative laser amplifiers.

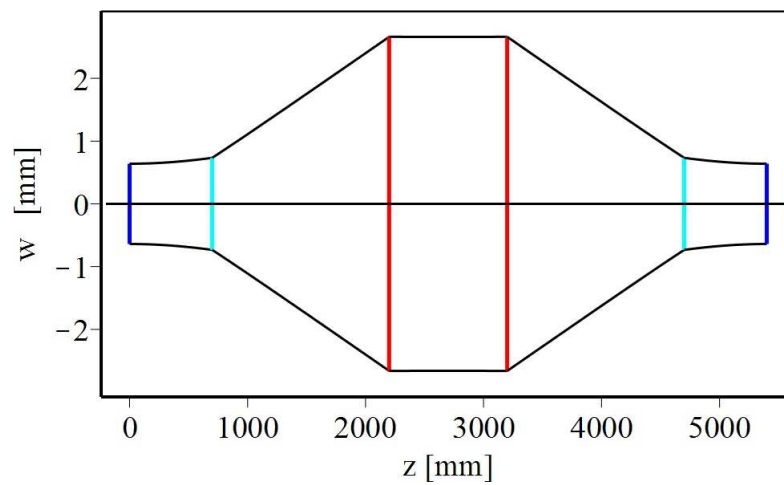


Figure 53: Scheme of an optical segment. The vertical lines represent the position of the optical elements: the thin disks are indicated in red, which also act as focusing elements, the flat mirrors are given in blue, and the convex mirrors are represented in cyan. The segment is symmetric. A propagation for a mode-matched Gaussian beam is shown in black. Soft apertures are neglected.

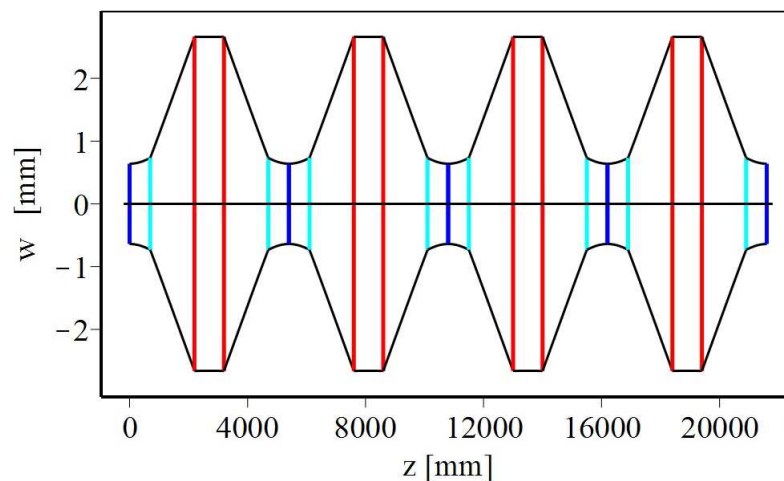


Figure 54: Multi-pass amplifier formed by the concatenation of four segments of Figure 53. The corresponding Gaussian beam evolution along the multi-pass amplifier is shown. In addition, in this case we assume that the in-coupled beam is mode-matched to the amplifier so that a regular beam evolution occurs (same width at all the positions of the thin disk). Soft aperture effects are neglected.

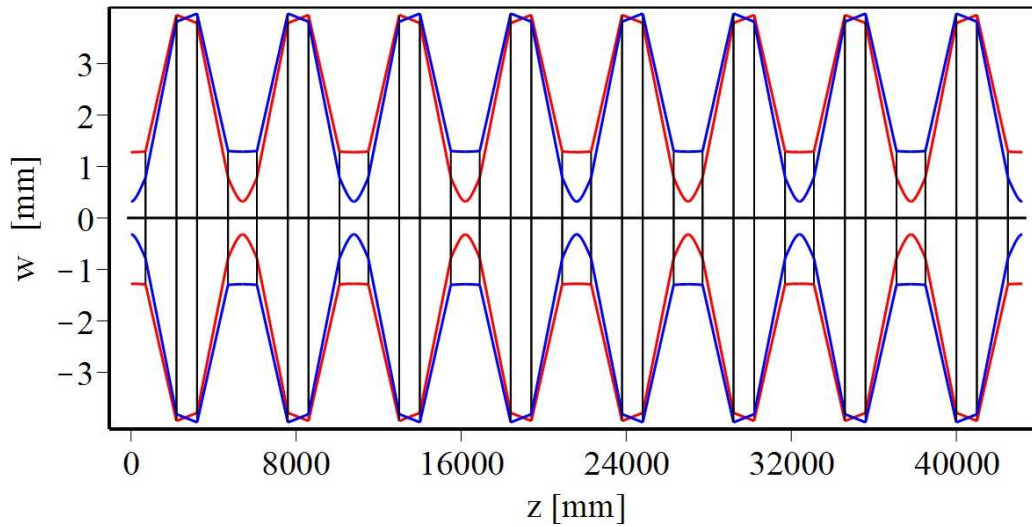


Figure 55: Beam width evolution along the multi-pass amplifier for two in-coupled laser beams. In both cases, the in-coupled laser beams do not match the amplifier layout. Therefore, irregular evolutions of the beam widths take place. Soft aperture effects are neglected.

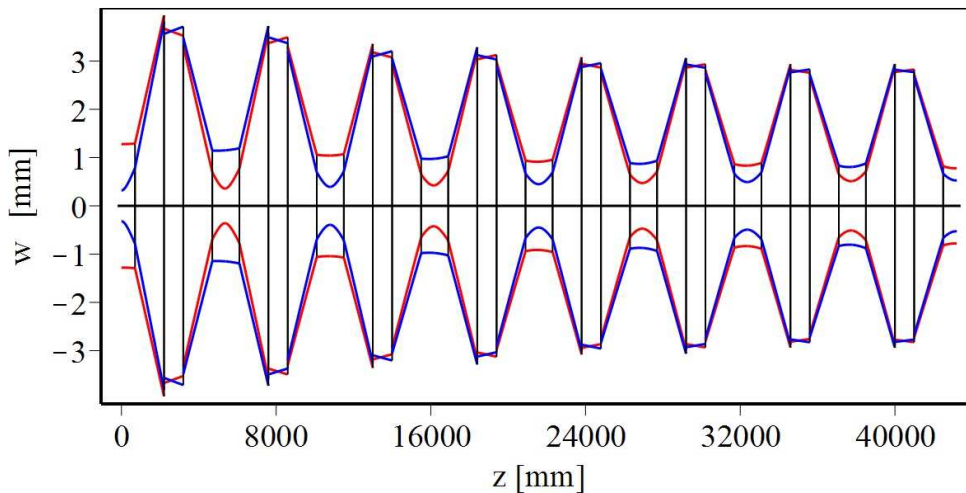


Figure 56: Similar to Figure 55 but in this case, aperture effects are considered. An aperture size of $W = 10$ mm was assumed at each position of the thin disk, while the layout width (for mode-matched in-coupling) of the beam at the thin disk is $w = 2.7$ mm.

This irregular beam propagation gives rise to variations of the beam size at the positions of the thin disk that lead either to large transmission losses or to optical breakdown. In Figure 57 the simulated transmission through the 16-pass amplifier of Figure 56 is presented as a function of the in-coupled beam width. As expected, there is an optimal value (mode-matched value) which corresponds to the layout value where a regular beam propagation having the same widths at all passes at the thin disk occurs. The transmission has been computed using Eqs. (106)-(111) which require the knowledge of the beam widths w at the various passes at the thin disk. We assumed here that the Gaussian beam axis is aligned with the optical axis, i.e. we assume $x(z) = 0$ for all z , so that there are no losses caused by misalignment. The plot shows a roundtrip transmission of $T_w = 32\%$ for ideal in-coupling. This is equivalent to a transmission of 93.1% for each pass on the active medium. Taking into account an effective gain of 22% for a reflection on the thin disk (see Chapter 7) the gain on the axis of the thin disk can be assumed to be $22\% + 6.9\% = 29\%$.

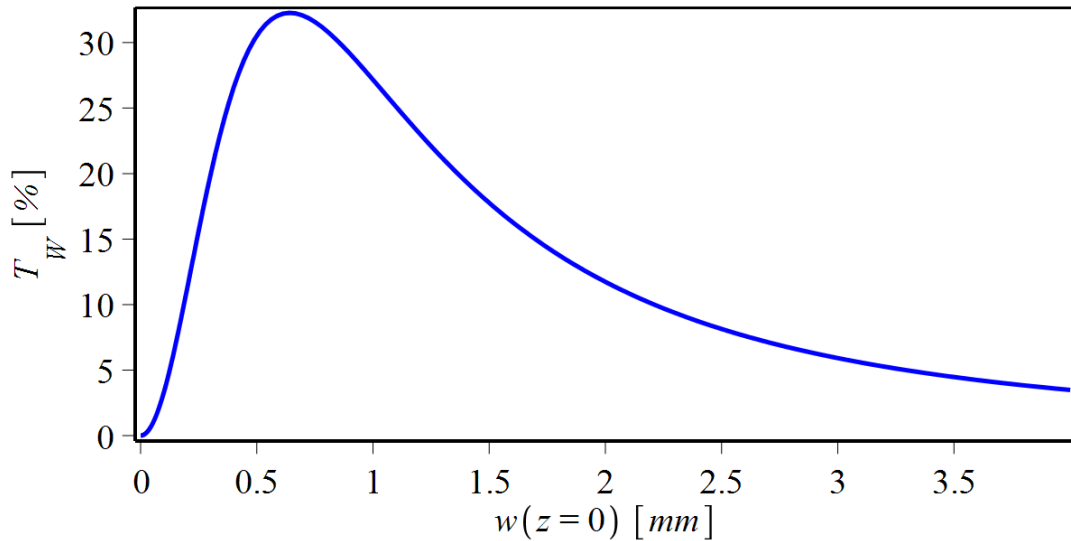


Figure 57: Transmission of the laser power through the 16-pass amplifier of Figure 56 for variations of the in-coupled beam width w at $z=0$. The transmission is maximal when mode-matching occurs. An aperture size of $W = 10$ mm was assumed at each thin disk position.

5.7.2. Evolution of the beam excursion along the multi-pass amplifier

When the laser beam propagates along the axis of the optical system, per definition the beam excursion $x(z)$ vanishes, i.e., $x(z) = 0$ for all values of z . This trivial solution represents the ideal case. However, it is interesting to consider the properties of the multi-pass amplifier for misalignments between the optical axis and the laser beam. In Sec. 5.4.5 we developed the mathematical formalism to trace the evolution of the Gaussian beam axis along the optical system. The propagation of the Gaussian beam axis (excursion and tilt) is almost identical to the standard ABCD-matrix propagation of a geometrical ray. The only difference is given by the additional ABCD-matrix (see Eq. (105)) that needs to be included to describe the apertures.

An example of the evolution of the beam excursion $x(z)$ along the amplifier of Figure 55 (without aperture effects) is given in Figure 58. Here two cases are handled: the in-coupled beam is mode-matched but enters the multi-pass amplifier with an excursion $x(z=0) \neq 0$ from the optical axis; the in-coupled beam is mode-matched but enters the multi-pass amplifier with a tilt $\theta(z=0) \neq 0$ from the optical axis. By contrast, the simulations of Figure 59 show the beam width evolution when aperture effects are considered. The apertures lead to a damping of the initial misalignment $x(z=0) \neq 0$ and $\theta(z=0) \neq 0$, while the beam propagates in z -direction. At the amplifier output, the Gaussian beam axis has approached the optical axis. Here we have assumed that the multi-pass oscillator is perfectly aligned.

Using Eqs. (108)-(111), it is possible to evaluate the additional losses at the apertures caused by the misalignment. Figure 60 presents the losses inflicted by the multi-pass amplifier arising from the misalignment. It is assumed here that the multi-pass amplifier is perfectly aligned, but the in-coupled laser beam may have an offset $x(z=0) \neq 0$ from the optical axis. For a matched in-coupling $x(z=0) = 0$, we have $x(z) = 0$ for all z . The transmission is thus 100 %, i.e. there are (per definition) no additional losses. For $x(z=0) \neq 0$, the Gaussian beam axis evolves in the amplifier as shown by the blue curve in Figure 59. At the positions of the thin disk, the non-vanishing excursion of the Gaussian beam axis from the optical axis causes additional aperture losses. Therefore, the transmission for $x(z=0) \neq 0$ decreases.

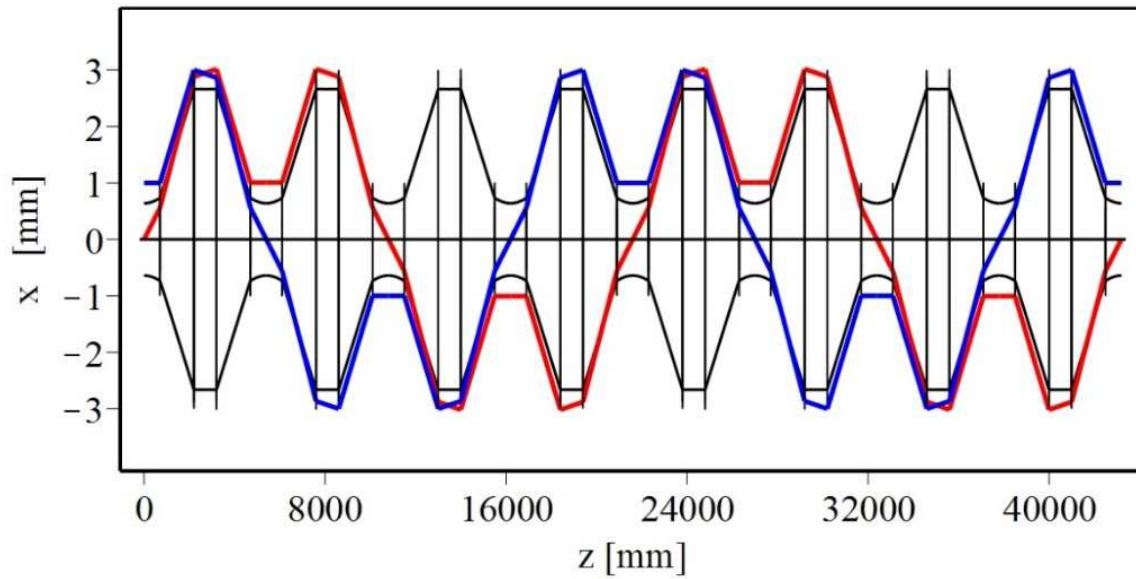


Figure 58: Beam excursion $x(z)$ evolution along the multi-pass amplifier for two misaligned in-coupled beams: (blue) the input beam has an excursion of $x(z=0) = 1$ mm, (red) the input beam has a tilt of $\theta(z=0) = 41.3$ arcsec. In this simulation, aperture effects have been neglected. The multi-pass amplifier has been assumed to be perfectly aligned. For comparison, the beam width evolution along the optical system is also shown (black curve).

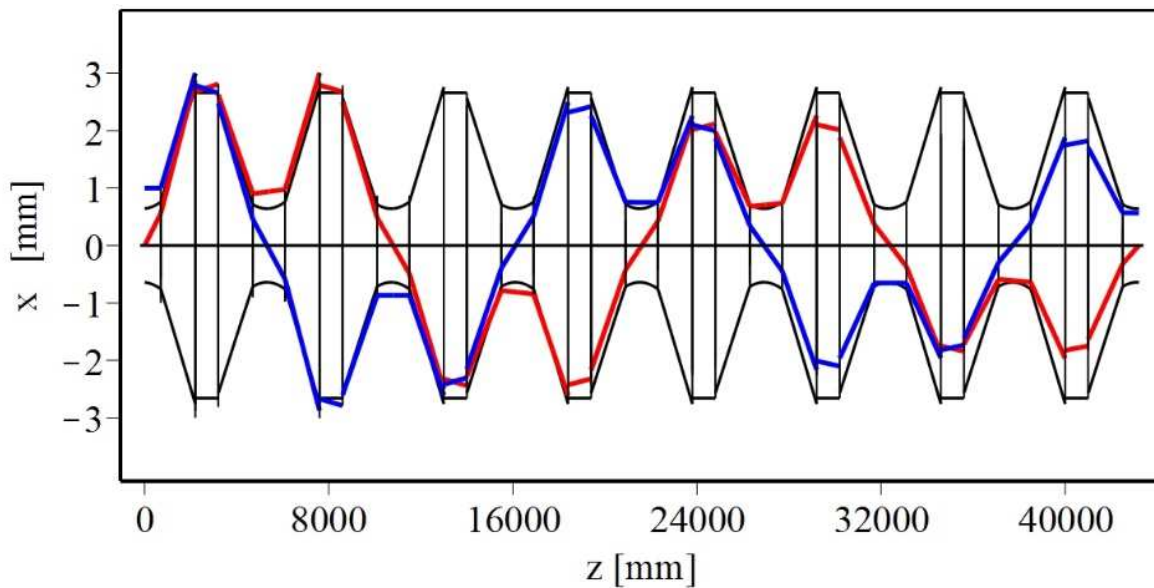


Figure 59: Similar to Figure 58 but including aperture effects. An aperture size of $W = 10$ mm was assumed at each thin-disk position, while the layout width (for mode-matched in-coupling) of the beam at the thin disk is $w = 2.7$ mm.

Because of the multiplicative structure of Eq. (111), the total transmission T_{Os} in the multi-pass amplifier for an in-coupled beam of width $w(z=0)$ entering the amplifier with an excursion $x(z=0) \neq 0$ from the optical axis, is simply given by multiplication of the corresponding transmission curves of Figure 57 and Figure 60.

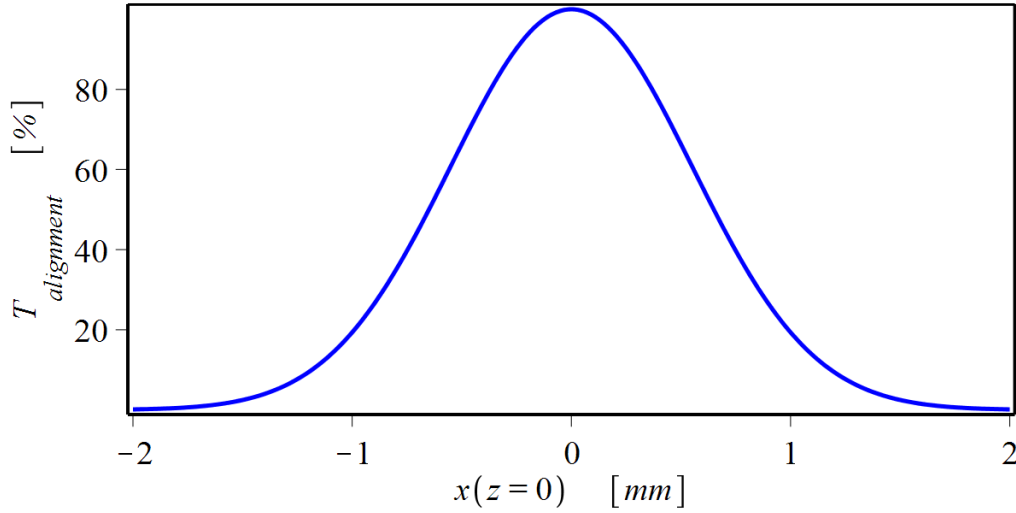


Figure 60: Misalignment-related transmission $T_{alignment}$ of the laser power through the 16-pass amplifier of Figure 59 as a function of the in-coupled beams initial excursion $x(z=0)$. The transmission is 100 % when the in-coupled beam is on the optical axis. We assumed that the multi-pass amplifier is perfectly aligned and the input beam mode-matched. An aperture size of $W = 10$ mm was assumed at each position of the thin disk, while the layout width (for mode-matched in-coupling) of the beam at the thin disk is $w = 2.7$ mm.

5.8. Resonator design with apertures

The TEM₀₀ eigenmodes of a resonator are usually determined by evaluating the ABCD-matrix for a roundtrip propagation. This evaluation can be realized starting from an arbitrary position within the laser resonator. Consider the complex Gaussian beam parameter $q(z)$ at an arbitrary position z_0 in the resonator. After a roundtrip propagation in the resonator described by the ABCD-matrix the complex beam parameter is transformed as

$$q'(z_0) = \frac{A q(z_0) + B}{C q(z_0) + D}. \quad (112)$$

In a stable resonator, the laser mode has to reproduce itself after a roundtrip. Therefore, the eigenmode of the resonator must fulfill the condition

$$q'(z_0) = q(z_0). \quad (113)$$

Combining Eq. (112) and Eq. (113) we obtain, assuming that the ABCD-matrix elements are all real, that [185]

$$q(z_0) = \frac{A - D}{2C} \pm \sqrt{\frac{(A + D)^2 - 4}{4C^2}}. \quad (114)$$

Since the eigenmode width is related to the imaginary part of q through the equation

$$w(z_0) = \sqrt{\frac{\lambda}{\pi \operatorname{Im}\left(\frac{1}{q(z_0)}\right)}}, \quad (115)$$

physical solutions generally only exist when the imaginary part of q is larger than zero:

$$\text{Im}(q) > 0. \quad (116)$$

For real ABCD-matrix elements, this condition is equivalent to

$$|A + D| < 2. \quad (117)$$

In this case, the solution with the positive sign in Eq. (114) is the physical one. All resonator layouts fulfilling the condition $|A + D| < 2$ represent stable resonators sustaining a finite eigenmode. In this range, the eigenvalues for the beam parameter q are complex as required for physically meaningful laser beams (see e.g. Eq. (115)). The range for which a resonator parameter (e.g. thermal lens) can be varied while the condition $|A + D| < 2$ is fulfilled is commonly referred to as the “stability region”.

For the case $|A + D| \geq 2$, there are no solutions, i.e. the resonator does not sustain any eigenmodes, because the eigenvalue q is real (see e.g. Eq. (115)) and the related beam is a spherical wave of radius q (diverging with positive q and converging with negative q). This violates the paraxial beam assumption and the requirement for laser beam confinement. This description does not account for aperture effects that are essential in the field of unstable resonators [173, 174, 175, 176]. Still the parameter q can be used to describe approximatively the phase front curvature of the truncated beam. In fact, due to the insufficient focusing present in the unstable resonator, an initial circulating laser beam expands until limitations caused by an aperture (e.g. a mirror edges) prevents its further growth. When the gain at the active medium can compensate for the great losses (cut-off) occurring at this aperture, stable (in time and mode structure) laser operation can occur in a well-defined laser eigenmode that can be highly structured [173, 174, 175, 176].

In this thesis, we only consider Gaussian apertures as they can be described in the ABCD-matrix formalism using Eq. (101). The presence of Gaussian apertures in a resonator gives rise to ABCD-matrix elements with complex values, i.e. having imaginary components. In this case, the solution of Eq. (113) does not take the simple form of Eq. (114) but must be evaluated for each given resonator layout. However, generally speaking, a resonator containing apertures always sustains an eigenmode. This result is fundamentally different from the standard approach (for stable resonators), which neglects aperture effects. In other words, by including Gaussian apertures in the resonator design, we treat every resonator as an “unstable resonator”. This means that eigenmodes exist for any resonator layout. However, to evaluate whether laser operation is possible, aperture losses have to be smaller than the gain. Thus, it is of utmost importance for resonators containing apertures to evaluate the power transmission in a roundtrip.

5.8.1. Stability properties and aperture losses of a simple resonator

Figure 61 shows a resonator layout and the corresponding TEM₀₀ eigenmode for two cases: (a) without aperture effects at the thin disk, (b) with aperture effects. The aperture at the thin disk causes a reduction of the transmitted beam width so that the forward propagating beam mode differs from the backward propagating mode.

When designing resonators, it is customary to study the dependence of the beam width at a given position in the resonator on variations of a resonator parameter such as the distances between mirrors, or the focal strengths of lenses, mirrors, etc. A plot of the eigenmode for variations of one of these parameters can be used to expose the stability of the resonator. In this thesis, we call “stability plots” the plots showing variations of the eigenmode width for variations of the thermal lens of the thin disk. This should not be

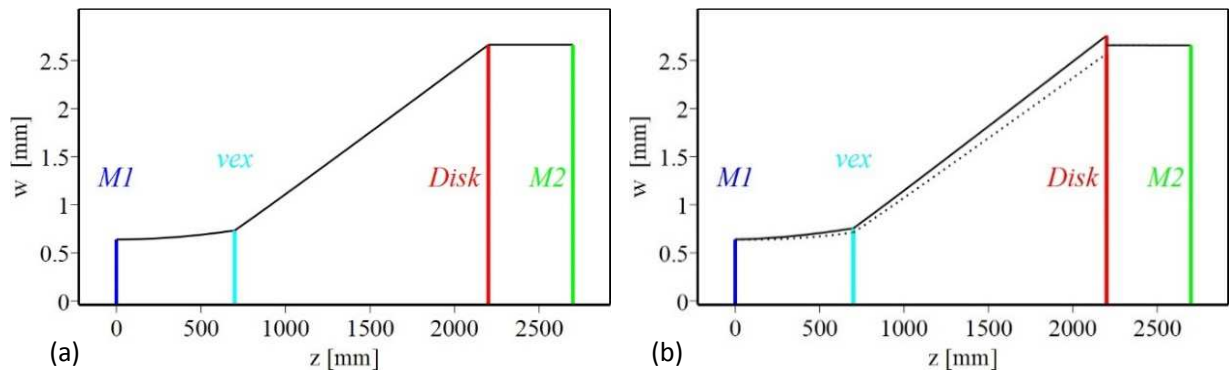


Figure 61: Simple resonator layout with the corresponding TEM₀₀ eigenmode evolution. The vertical lines give the position of the various optical elements: the thin disk with focusing effects is shown in red, the defocusing mirrors (or lenses) in cyan. The end mirrors M1 and M2 are flat. In (a), the aperture effects at the thin disk are neglected, while in (b) they are accounted for. An aperture size of $W = 10$ mm was assumed to be compared with the layout beam width at the thin disk of $w = 2.7$ mm. When aperture effects are present, the forward (black continuous) and backward (black dashed) propagating modes differ.

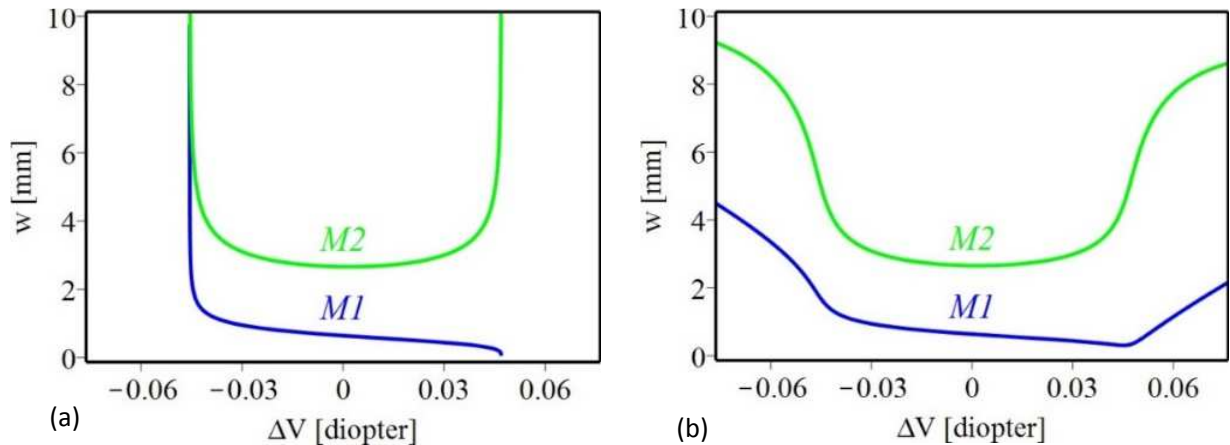


Figure 62: Stability plots for the resonators of Figure 61 with (a) and without (b) aperture effects. Plotted are the eigenmode widths at the M1 and M2 mirror positions.

confused with the stability diagram presented in [177] for example. An example of this kind of plots is given in Figure 62 for the resonator of Figure 61. It shows the eigenmode widths at the mirror M1 and mirror M2 positions for variation of the dioptric power of the thin disk. These widths are plotted for two cases: neglecting (a) and considering (b) the aperture effects at the thin disk.

An optimal resonator layout is achieved when the eigenmode width at a given position along the resonator is insensitive to variations of the dioptric power of the thin disk ΔV . Figure 62 (a) which has been computed neglecting aperture effects demonstrates that the layout of Figure 61 (a) is optimal. In fact, in both cases the beam width at the mirror M2 position is essentially constant for a large range of dioptric power variations around the layout value ($\Delta V = 0$).

With increasing deviation from this layout value, the eigenmode size becomes increasingly dependent on ΔV . At a given value (in this case $\Delta V \approx \pm 0.05$ diopters) the eigenmode size at the end mirrors becomes either zero or infinite. The stability region is defined as the range of ΔV variations where a finite value of waist exists. For even larger variations of ΔV ($|\Delta V| > 0.05$ diopters) no solutions exist. Therefore, no laser operation can be achieved in this region.

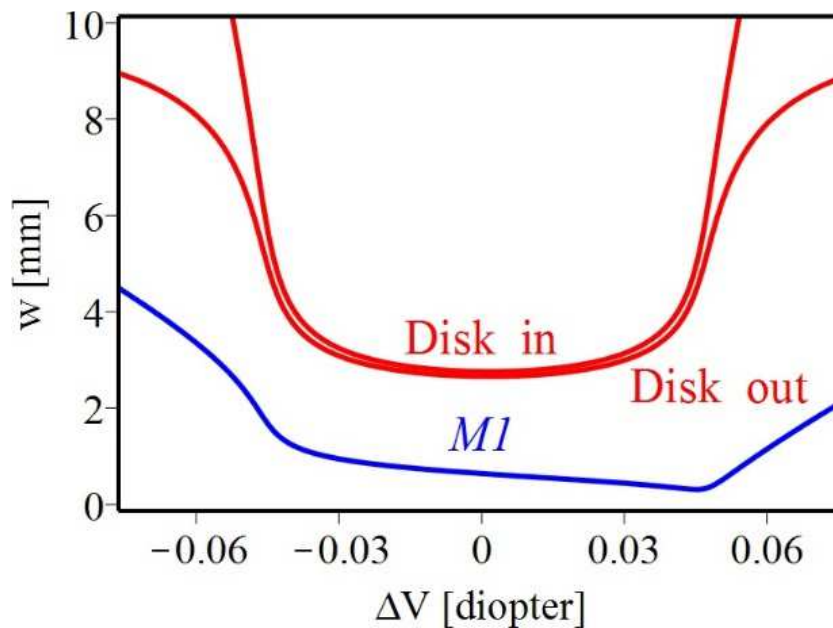


Figure 63: Stability plots of the optical resonator presented in Figure 61(b) with aperture effects. Plotted are the eigenmode widths at the position of the thin disk and the mirror M1 position for variations of the dioptric power of the thin disk ΔV . At the thin disk both input and output beam widths are given for the case of forward propagation. An aperture size of $W = 10$ mm was assumed at the position of the thin disk.

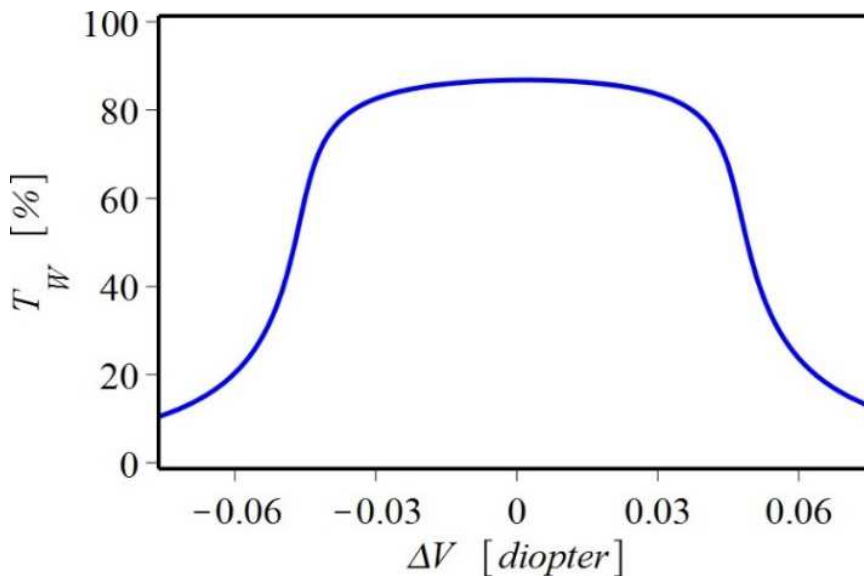


Figure 64: Roundtrip transmission (T_w) in the laser cavity presented in Figure 61 b), as a function of the dioptric power variation of the thin disk from the layout value. An aperture size of $W = 10$ mm was assumed at the position of the thin disk, to be compared with the eigenmode width of $w = 2.7$ mm at the thin disk for the layout value.

By comparing Figure 62 (a) with Figure 62 (b) we observe that the inclusion of aperture effects does not significantly change the width of the eigenmode, provided that the variations of the thin-disk lasers ΔV are small and around the layout value. At the center of the stability region (which is computed without accounting for the aperture effect) the impact of the apertures on the eigenmode properties is thus negligible. Because of this, standard resonator designs neglect aperture effects. However, for increasing deviation of $|\Delta V|$ from the layout value, the prediction that includes aperture effects increasingly deviates

from the prediction computed without aperture effects. It even turns out that aperture effects guarantee the existence of an eigenmode even outside the stability region (computed neglecting aperture effects). In spite of that, in this region the aperture losses are so elevated that this region is not suited for practical applications.

Thus, for the practical application, it seems that the aperture effects do not significantly affect the resonator design. For this reason, aperture effects have gained only limited attention in the community. However, they may be of central importance in resonator design as presented in Sec. 5.7.2 and in Chapter 8.

Figure 63 shows the eigenmode width w at the mirror M1 and at the thin disk. As the beam width is reduced when an aperture is crossed, at the position of the thin disk we observe two widths: an input width w_{in} and one output width w_{out} . It is clearly visible that outside the stability region the aperture dramatically reduces the width of the transmitted beam, so that significant aperture losses have to be expected (relative to the input beam width).

Laser operation can only occur when the roundtrip gain at the active medium or media exceeds the roundtrip losses. To estimate the roundtrip losses related with apertures, first the beam width of the eigenmode along the resonator, and particularly at the aperture positions, has to be determined. For the thin disk, the ABCD-matrix given in Eq. (102) has to be used. The beam width at the input w_{in} and at the output w_{out} of the aperture is determined from the q , evaluated using the ABCD-matrix formalism. The knowledge of these widths allows computing the aperture transmission (assuming no misalignment, i.e. $\xi = 1$) at each aperture using Eq. (109). By multiplying the transmission of all apertures encountered in a roundtrip, the total transmission in the resonator can be computed.

The roundtrip transmission T_w for the resonator with aperture presented in Figure 61 b) is shown in Figure 64 for variations of the dioptric power ΔV of the thin disk. By comparing this figure with Figure 62 we see that the transmission dramatically decreases for $|\Delta V|$ values at the periphery or outside the stability region (computed without aperture effects). Thus, at the periphery or outside the stability region the losses caused by the aperture are so large that laser operation is prevented or highly inefficient.

In conclusion, the stability plots that are commonly used to design laser resonators [177, 178], for resonators having aperture effects, must be complemented by plots of the roundtrip transmission for variation of the resonator parameters.

5.8.2. Stability properties and aperture losses of a multi-pass resonator

In this section, we present a resonator design that shows high sensitivity to aperture effects. It constitutes the basis for understanding the multi-pass resonator architecture presented in Chapter 8. Simulating this resonator, neglecting aperture effects leads to fundamentally different results than when accounting for them.

Consider the resonator presented in Figure 66 (a). It consists of a flat mirror M2, a focusing thin disk (given in red) a convex mirror (vex), a flat mirror M1, a convex mirror (vex), a focusing thin disk and an end mirror M2'. We further assume that the resonator is symmetric with respect to the mirror M1 and we neglect aperture effects. This resonator corresponds to a multi-pass oscillator with four reflections at the thin disk in a roundtrip. The corresponding stability is shown in Figure 66 (b).

In Figure 66 (c) the same resonator is presented as in Figure 66 (a). In addition, in this case aperture effects are neglected. However, there is a small asymmetry between the right and the left part of the resonator. In fact, distance d_L is slightly different (on the 1 % level) from distance d_R . Even though the asymmetry is very small, it significantly modifies the eigenmode of the resonator and the stability region. As can be seen in Figure 66 (d) the “original” stability region is split into two separate regions, i.e. a gap is generated within the stability region obtained for the perfectly symmetric layout. In and around this gap the laser operation is disrupted.

In Figure 66 (e) the same resonator layout is presented as in Figure 66 (c), i.e. the resonator has a small asymmetry. However, in this case the simulations also account for aperture effects at the thin disk. The corresponding stability plot shown in Figure 66 (f) reveals a fundamental difference compared with the stability plot of Figure 66 (d). The aperture effects eliminate the gap in the stability region so that the same stability region and eigenmode properties as for a perfectly symmetric resonator are obtained (compare with Figure 66 (b)). The roundtrip transmissions in the multi-pass resonators of Figure 66 (c) and (e) are compared in Figure 65 for variations of the dioptric power ΔV of the thin disk. When aperture effects are neglected, the roundtrip transmission is 100 %. Note that the transmission is only defined in the stability region where an eigenmode exists. The small gap around $\Delta V = 0$ is caused by the small asymmetry in the resonator. When aperture effects are considered, the eigenmode is defined for any value of the dioptric power of the thin disk. The gap disappears and at its previous position a minor fluctuation of the roundtrip transmission is visible. This small fluctuation does not significantly affect laser operation. Therefore, when aperture effects are included the multi-pass resonator having small asymmetries virtually behaves like the corresponding perfectly symmetric layout.

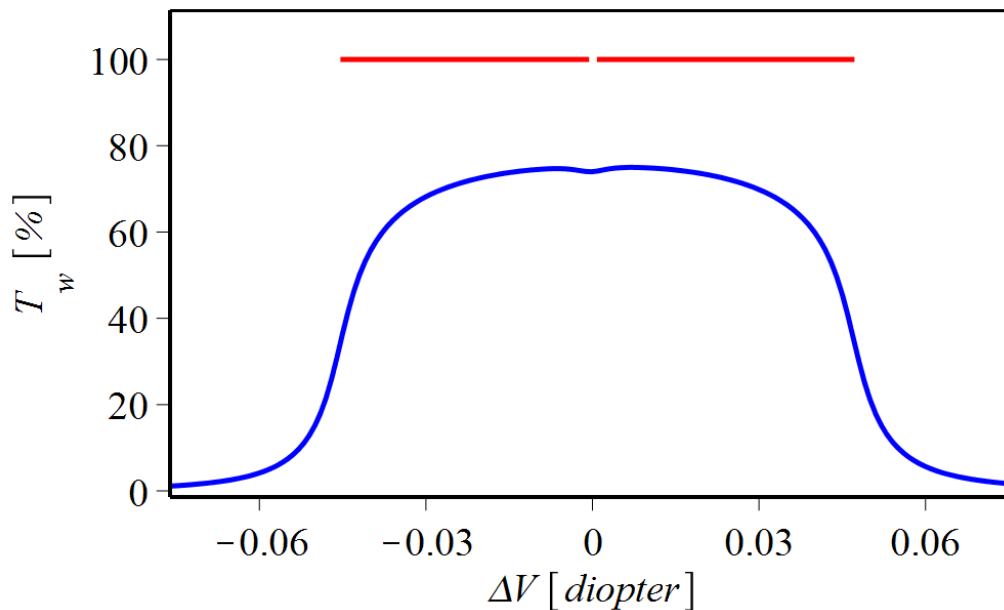


Figure 65: Roundtrip transmission T_w for the laser eigenmode in the multi-pass resonator for variation of the dioptric power of the thin disk ΔV . The blue transmission curve is for the resonator of Figure 66 (e) considering the aperture effects generated in all four reflections on the thin disk per roundtrip. Note that we ignore laser gain and other losses of the resonator. In contrast, the transmission curve given in red is for the resonator shown in Figure 66 (c) which is free of aperture effects. As the losses are not considered, the roundtrip transmission is in this case 100 %. However, the laser eigenmode is only defined within the laser’s stability region.

In the practical realization of a multi-pass resonator, small asymmetries as shown in Figure 66 (c) are unavoidable because of small variations of propagation lengths, incident angles and mirror curvatures. These asymmetries, when neglecting aperture effects, split the “original” stability region, i.e. the stability region computed assuming a perfectly symmetric layout. The situation becomes even worse for the multi-pass resonator shown in Figure 67. Segment-to-segment asymmetries fragment the “original” stability plot into various regions as demonstrated for a particular case in Figure 68 (a). Therefore, it seems that in practical application, where segment-to-segment asymmetries are unavoidable, these layouts have to be discarded. However, this conclusion is erroneous. In fact, including in the simulations the soft aperture effects that naturally occur in the pumped thin disk, we find that the “original” stability region and eigenmode properties computed for identical and symmetric segments are restored (see Figure 68 (b)). It is important to stress that this general behavior of the stability regions does not critically depend on the exact value of the assumed size W of the aperture. The amplitude of the small fluctuations in the stability plots for a multi-pass resonator with segment-to-segment asymmetries and aperture effects depends on the size W of the aperture and the magnitude of the asymmetries.

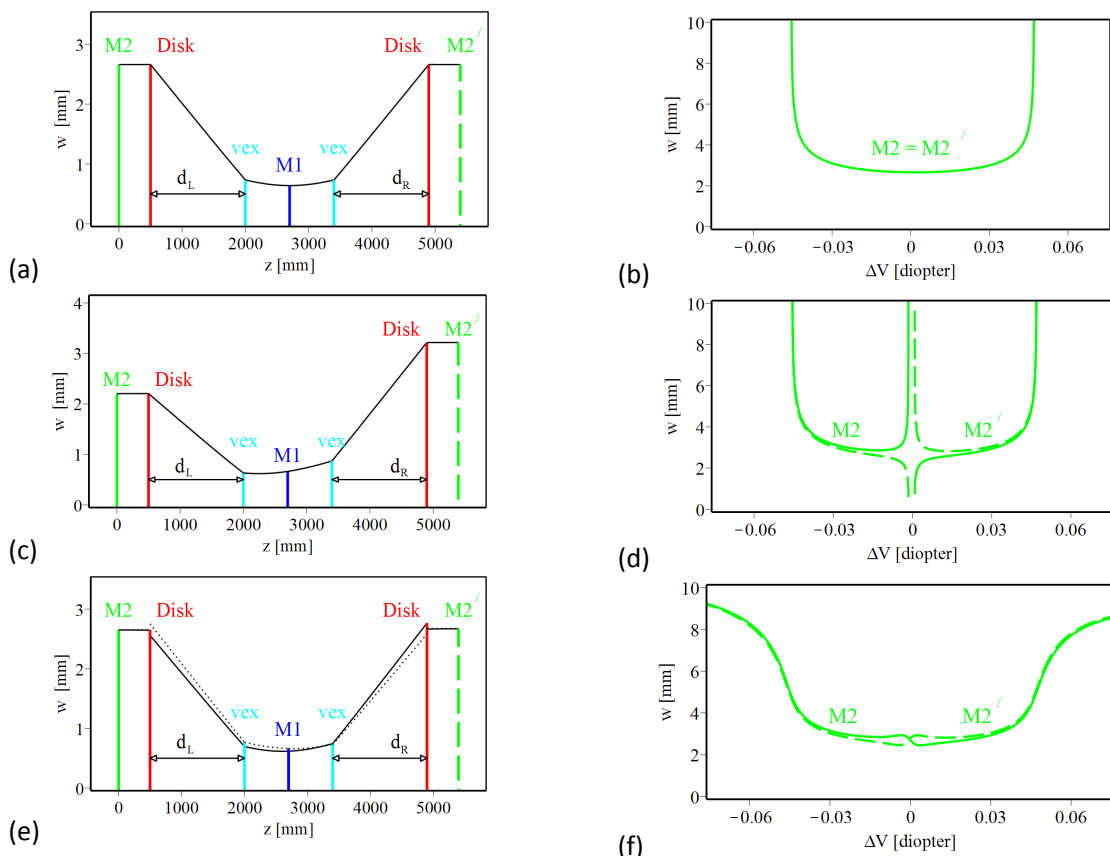


Figure 66: Multi-pass resonator with eigenmode evolution and corresponding stability plots. (a) Perfectly symmetric resonator without aperture effects. The vertical lines indicate the position of the various optical components: the thin disks also acts as focusing elements M1, M2 and M2' are flat mirrors. The evolution of the TEM₀₀ eigenmode along the multi-pass resonator is also shown (black curve). (b) Corresponding stability plot. Plotted are the eigenmode waists at the mirror M2 and M2' positions for variations of the dioptric power of the thin disk ΔV . (c) Similar to (a) but in this case there is a minor asymmetry, given by a minor difference between the two propagation lengths d_L and d_R . The corresponding stability plot is given in (d). (e) Similar to (c) but in this case aperture effects at the positions of the thin disk are included ($W = 10$ mm). The corresponding stability plot is shown in (f).

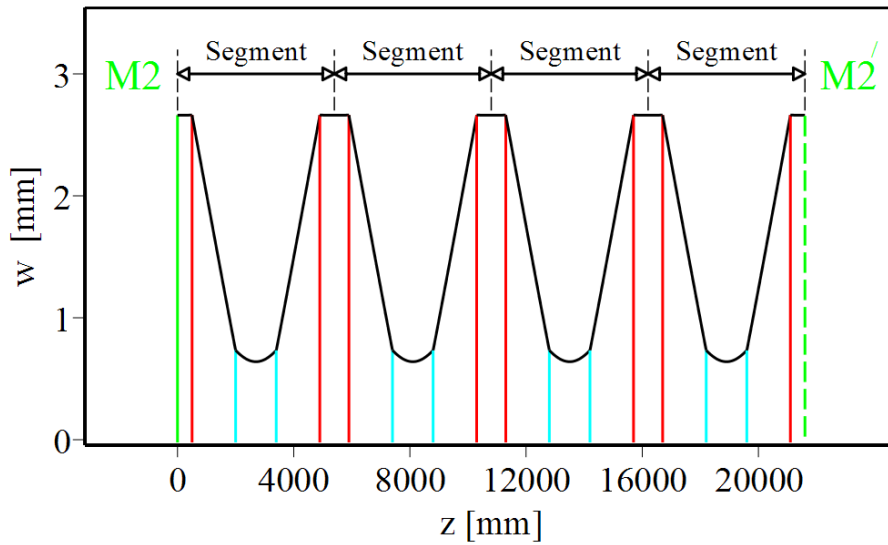


Figure 67: Multi-pass oscillator formed by concatenating multiple optical segments based on the resonator of Figure 66 (a). The corresponding eigenmode is also illustrated (black curve). Asymmetries and aperture effects are neglected when computing the eigenmode. The vertical lines indicate the position of the various optical elements.

Briefly, soft aperture effects need to be included when designing laser resonators and amplifiers to avoid erroneous conclusions. In addition, when treating optical resonators it is always helpful to complement the stability plots with roundtrip transmissions in order to evaluate the impact of apertures on laser efficiency.

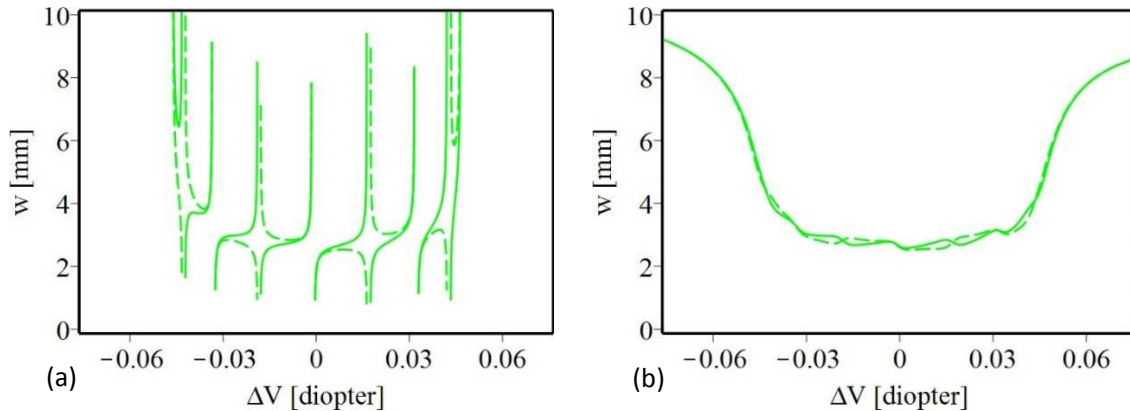


Figure 68: Stability plots of the multi-pass resonator given in Figure 67. Here we include minor asymmetries similar to Figure 66. Plotted is the eigenmode waist at the mirrors M2 and M2' versus variations of the dioptic power of the thin disk ΔV . In (a) the eigenmode has been computed neglecting aperture effects. In (b) the aperture effects have been included.

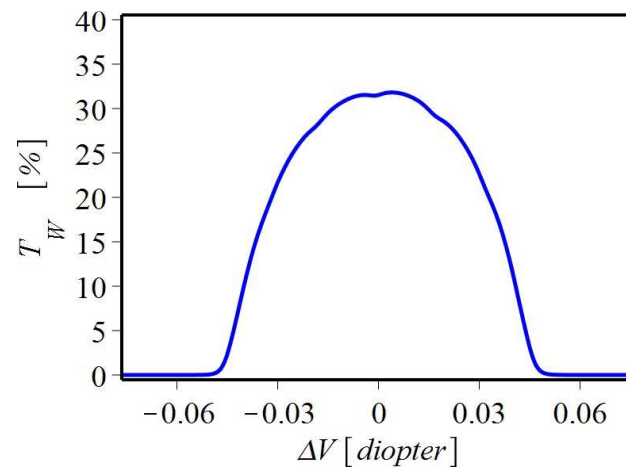


Figure 69: Roundtrip transmission for the eigenmode in the resonator shown in Figure 67 including small asymmetries and aperture effects at the thin disk (compare with the stability plot presented in Figure 68 (b)).

6. Q-switched thin-disk oscillator

The thin-disk laser for the muonic helium 2S-2P experiment has to fulfill the following requirements:

- pulse energy of about 100 mJ at 1030 nm,
- latency time (delay time between trigger and emission of the pulse) < 500 ns,
- stochastic trigger with minimal delay time between two successive pulses < 2 ms,
- continuous and stable operation over several months,
- good transverse beam quality (TEM₀₀-mode) for efficient SHG doubling,
- pulse length < 50 ns (given by the build-up time in the Ti:Sa).

To cope with these various requirements, we realized an Yb:YAG thin-disk laser based on an oscillator-amplifier scheme as shown in Figure 70. Both the oscillator and the amplifier are continuously pumped with high-power diode lasers operating in continuous wave. It is the continuous pumping and the long lifetime (in the 1 ms range depending on operational conditions) [187, 117] of the upper state population of Yb:YAG that guarantee a steady and substantial inversion population of the active medium. Hence, when the thin-disk laser is triggered, the pulse can immediately build up, resulting in a very short latency time as demanded by the muonic experiment.

Commercially available lasers delivering similar pulse energies have much longer latency times. For example flashlight pumped Nd:YAG lasers have latency times in the ms range. The longer latency time originates from the time needed to transfer the energy from the electrical capacitors through the flashlight into the laser active medium. As the flashlight can only sustain a limited peak intensity, a non-negligible time is needed for this pumping process.

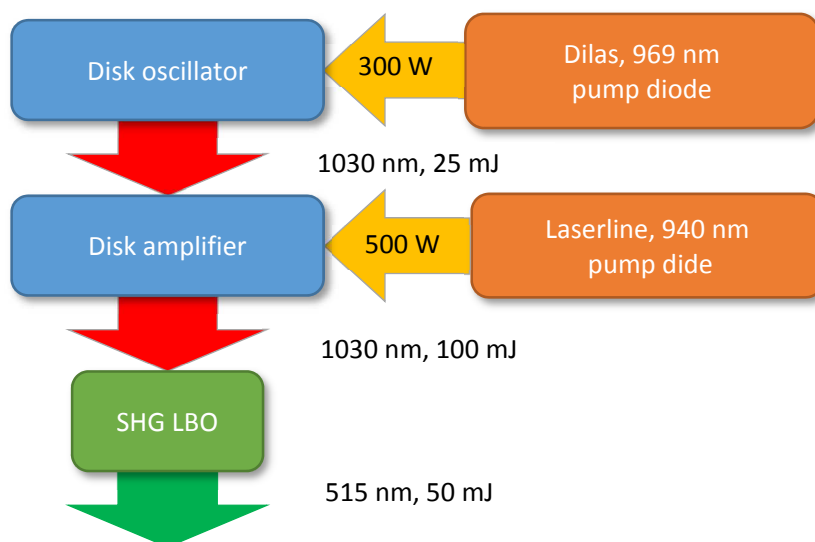


Figure 70: Schematic of the thin-disk laser developed for the muonic helium experiment composed of an oscillator and a multi-pass amplifier followed by a second harmonic generation (SHG) stage. The numbers refer to the performance during data taking.

In standard applications, the lasers are triggered at a fixed repetition rate using a clock. Conversely, in our experiment the muons enter the setup at random times so that no pre-synchronization of the laser system to the muon beam is viable. This is the origin of the short latency time requirement. Moreover, the stochastic trigger increases the challenges of the laser system also because the thermal lens at the active medium depends on the time elapsed from the previous pulse. Therefore, the laser system has to cope with fluctuations of the thermal lens from pulse to pulse, i.e. it has to be insensitive to variations of the thermal lens. For these reasons, we had to develop a peculiar thin-disk laser system with 100 mJ scaled energy capabilities, able to deliver a pulse within a short delay (500 ns) after being triggered and with a performance which does not depend on the time from pulse to pulse (down to a minimum of about 1 ms).

6.1. The oscillator dynamics

For the muonic experiment, we realized a Q-switched thin-disk oscillator as sketched in Figure 71. It consists of a 2 m long cavity including a telescope formed by the concave thin disk and a convex mirror. The thin disk is intersected twice in a roundtrip and it is pumped continuously using a diode laser generating 300 W at a wavelength of 969 nm. A Pockels cell (PC), a $\lambda/4$ wave-plate and a thin-film polarizer (TFP) are used to control the out-coupling of the resonator, i.e. to control the Q-switch dynamics. The TFP is a mirror whose reflectivity depends on the polarization of the impinging light. The PC and the $\lambda/4$ wave-plate act on the polarization of the circulating light. Hence, the interplay of these three elements can be used to realize an out-coupler whose reflectivity can be adjusted from 0 % to 100 %. The oscillator is operated in pre-lasing mode (also called self-seeding [135]), so that prior to the laser trigger there is a considerable circulating power. In this way, the pulse buildup does not have to start from spontaneously emitted photons. The dynamics of the complete Q-switch cycle work as follows:

- (a) Prior to triggering, the thin disk is continuously pumped, and the resonator is operating in cw pre-lasing mode close to laser threshold. The oscillator is waiting for a laser trigger with an amount of energy given by the pump power and the upper state lifetime of the active medium stored in the thin disk. The intensity of the circulating power is stabilized by a feedback loop (see Figure 71) that acts on the PC to adjust the resonator losses.
- (b) When the laser is triggered, the PC rotates the polarization of the circulating light so that the TFP acts as a 100% mirror. Therefore, the cavity is closed.
- (c) With closed cavity, the gain dominates over the losses so that a fast pulse buildup occurs.
- (d) After a given time, the PC is switched again so that the transmission through the TFP is increased. The cavity is (partially) opened. The circulating power is extracted from the resonator, giving rise to a laser pulse.
- (e) After the pulse extraction, some time is needed until the inversion population reaches its steady-state value. In the meantime, the PC voltages are adjusted back so that pre-lasing can restart. The oscillator is ready to accept the next trigger.

Figure 72 shows the laser intensity measured with two photo-diodes during pulse formation: one photo-diode (D_{int} in Figure 71) observes the circulating intensity (red curve) by measuring the light leaking through a cavity mirror, the other photo-diode (D_{out} in Figure 71) measures the intensity of the light transmitted

through the TFP (blue curve). In region (i) the laser is operated in pre-lasing mode, with both the transmitted and the circulating intensities being different from zero. At time (ii) the oscillator cavity is closed by switching the PC so that the TFP becomes a mirror with 100% reflectivity. Thus, the transmitted intensity drops to zero, while the circulating intensity experiences an exponential growth. This exponential growth continues until (iii), when the cavity is opened. The circulating power is extracted at time (iv) leading to the emission of a laser pulse. Because the cavity transmission does not drop to zero but only to about 70%, the pulse is extracted while amplification still occurs. In this way, a pulse is obtained with an exponential fall-off and a length exceeding the roundtrip time. Summarizing, the rising edge of about 15 ns of the extracted pulse is defined by the switching time of the PC while the falling edge has an exponential shape given by the interplay between pulse extraction (transmission through the TFP) and the amplification process, which decreases with time due to the depletion of the upper-state population.

At our running conditions, the pulse is extracted from the resonator before the thin disk is exposed to the saturation fluence of the active medium (see the exponential growth of the red curve). In this way, the optical-to-optical efficiency is not optimized but minimal pulse buildup time is reached. Extraction prior to saturation is also beneficial in terms of optical damage to the various components.

The laser gain per roundtrip is about 1.3, thus rather low compared to other laser types [188, 189]. To shorten the pulse formation, prior to pulsing we operate the laser in cw mode with a small (relative to the pump power of 300 W) output power of about 1 W. The gain in the active medium is thus basically unaffected by the pre-lasing operation. The pre-lasing enables the pulse formation to be initiated starting from a significantly higher circulating power compared to the power related to the spontaneous emission. We observed a reduction of the pulse buildup time by a factor of about two, down to 400 ns (for output energies of 35 mJ) when the laser is operated in pre-lasing mode.

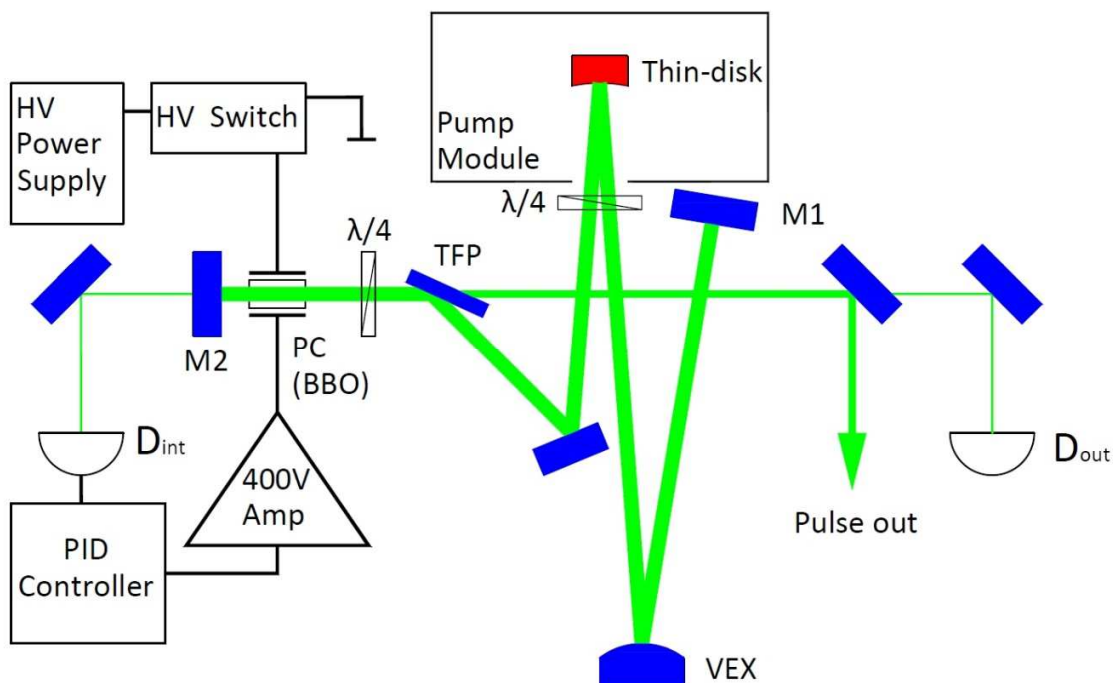


Figure 71: Scheme of the Q-switched thin-disk oscillator with feedback loop to stabilize the circulating power during the pre-lasing operation. M1 and M2 are the resonator end-mirrors, PC is the Pockels cell and TFP is the thin-film polarizer. The quarter wave-plate placed in front of the thin disk provides twisted mode operation of the laser (see Sec. 6.4). D_{int} and D_{out} are two photo-diodes measuring the circulating and extracted power, respectively.

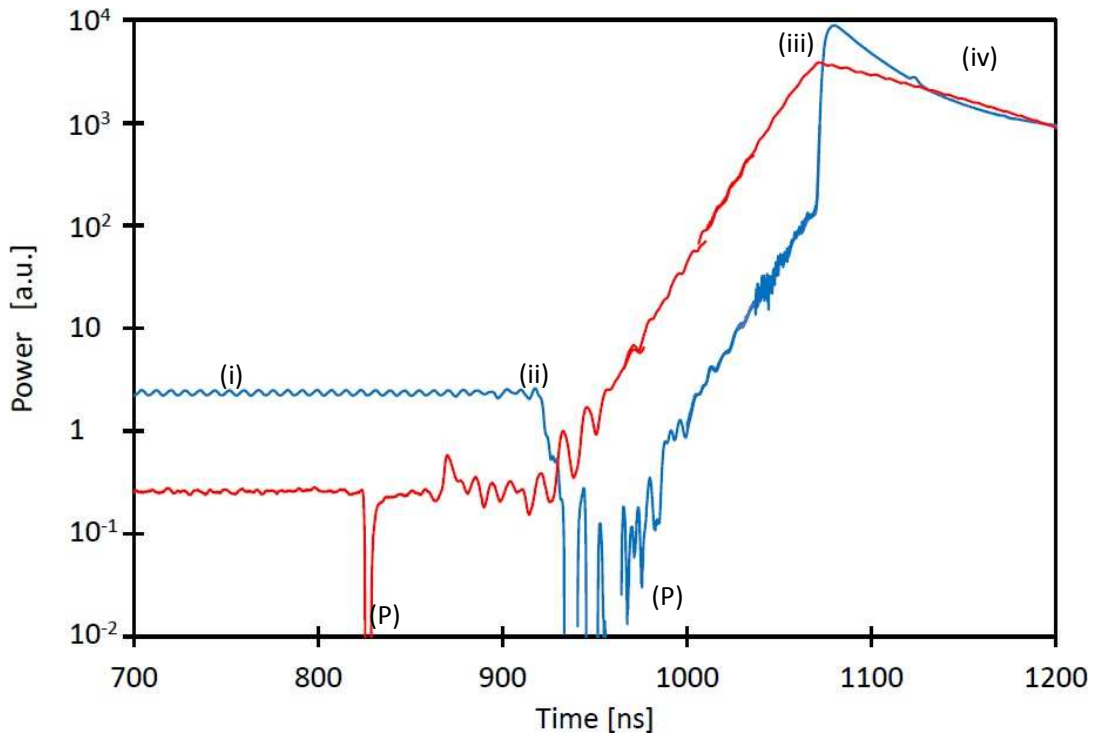


Figure 72: Circulating power (red) during the pulse formation measured with the photo-diode D_{int} placed behind the cavity mirror M2, and transmitted power through the TFP (blue) measured with the photo-diode D_{out} (see Figure 71). The pulse formation can be divided into the following steps: (i) pre-lasing operation, (ii) closing of the cavity followed by the amplification of the circulating power, (iii) opening of the cavity with subsequent extraction (iv) of the pulse. For low laser powers the electrical pickup (P) caused by the switching noise of the Pockels cell is visible in the logarithmic plot.

At the same time, the pre-lasing operation allows a reduction of the laser bandwidth and improvement of the transverse beam quality. Typically, Q-switch lasers start from spontaneously emitted photons (noise) in several longitudinal and transverse cavity eigenmodes. During pulse buildup, mode cleaning occurs ruled by the active medium aperture effects and gain profile [101]. However, in the short pulse buildup time the mode cleaning is limited [170]. Contrarily, in our case the significantly longer time of the pre-lasing operation allows for a more effective mode cleaning, which leads to single transverse mode operation. In pre-lasing operation, the laser bandwidth is reduced to single frequency operation limited by mechanical stability (the Schawlow-Townes limit is several orders of magnitude smaller [190]). Several lasers used the pre-lasing operation to take advantage of this bandwidth narrowing [135, 191, 192].

Because the pre-lasing occurs near laser threshold, it is extremely sensitive to vibrations, fluctuations of the laser gain and losses, and to relaxation oscillations. Therefore, to reduce the related instabilities, an active control of the circulating power during the pre-lasing operation is needed. Figure 73 shows the circulating power of the oscillator for two cases: (a) the pre-lasing operation is free running, and (b) the pre-lasing operation is actively intensity-stabilized. For the active stabilization, the feedback loop shown in Figure 71 is used. Figure 73 shows the laser dynamics as in Figure 72, but on a larger time scale (ms instead of μs), and zooming in the low-power range. In region (A) the oscillator runs in pre-lasing mode and is ready to accept a trigger. In (B) the laser is triggered and within a short time, it emits a pulse of low energy. In the power and time ranges of the plots, the pulse is reduced to a vertical line. After the pulse emission, the laser switches off (C), because the laser pulse has depleted the population of the upper

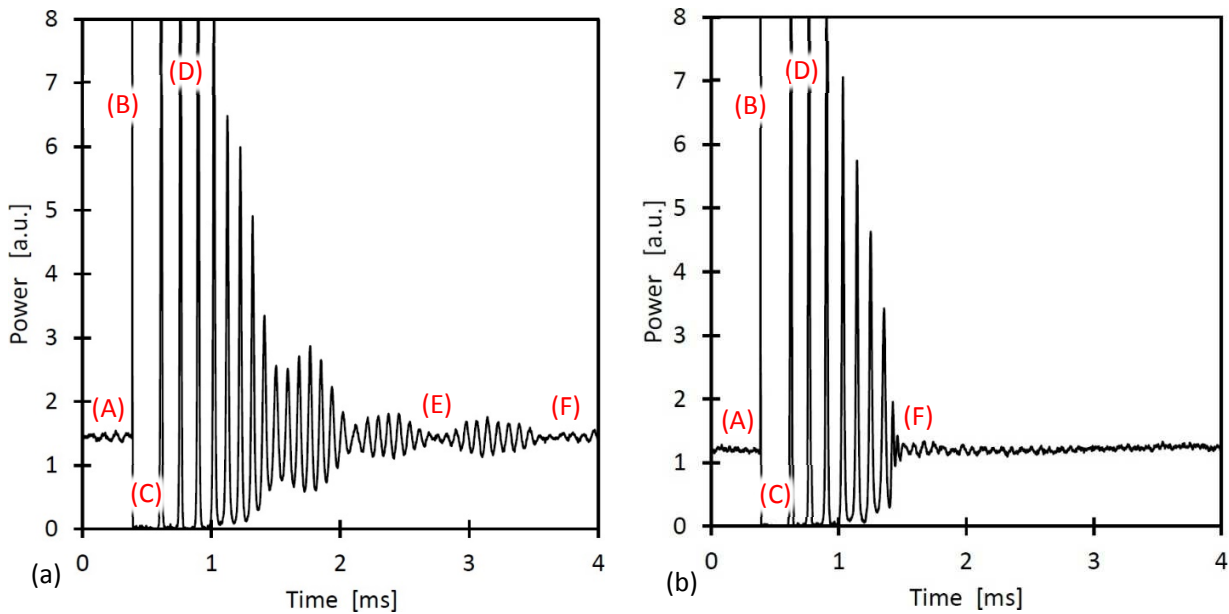


Figure 73: Circulating power in a Q-switch cycle on the ms time scale for free-running pre-lasing operation (a), and for active power-stabilized pre-lasing (b). The following stages characterize the Q-switch cycle: (A) pre-lasing; (B) trigger, pulse formation and pulse emission; (C) the laser switches off after extraction of some energy from the disk; (D) the laser starts to lase again but in an unstable way; (E) relaxation oscillation; (F) the laser again is ready to accept a laser trigger. In both cases, the extracted pulses have a low energy ($< 10 \mu\text{J}$) so that the laser is off only for a minor time (compare with Figure 74 where the extracted energy is much larger). The feedback loop is inhibited for a time span of about 1 ms after pulse extraction.

state so that the laser is below threshold. The laser power thus drops to zero. Soon afterwards, the oscillator again starts to lase because in the meantime the inversion population is being recovered due to the continuous pump process. However, initially the laser operation is unstable (D). Before approaching steady-state conditions (F), the laser first exhibits pronounced spiking (D) and then relaxation oscillation (E). The damping of this process is slow since the upper-state lifetime is much longer than the photon lifetime in the cavity. For an OC transmission of 30 % and a 2 m long cavity the photon lifetime in the cavity is $\tau_{\text{photon}} = \tau_{\text{roundtrip}} 1/\ln(R_{\text{OC}}) \approx 30 \text{ ns}$, to be compared with the effective (shortened by ASE effects) lifetime of 0.3 ms of the upper-state in Yb:YAG with a doping concentration of 5 % [117].

This leads to minimal damping of the relaxation oscillations as described in [117, 193] and [194]. As becomes visible when comparing Figure 73 (a) with Figure 73 (b), the active intensity stabilization of the pre-lasing process helps to shorten the damping time of these instabilities. For reasons that will be explained below, the active stabilization is switched off for about 1 ms after the pulse emission. Thereafter, it is switched on and within 0.2 ms the laser is ready to accept another trigger because the circulating power has reached its steady-state value (prior to trigger).

Figure 74 shows a plot similar to Figure 73 (b), but for the extraction of a pulse of much larger energy. Because of the larger pulse energy, the laser is off for a much longer time due to the greater depletion of the upper-state population that requires a much longer time to be restored. In addition, in this case, the active stabilization is turned off for 1 ms after the pulse extraction and the value of the integral component is buffered in this time. The integral part of the feedback loop would drift away from its steady-state value if the feedback loop was on while the laser is off. This would cause instabilities when the laser turns on again.

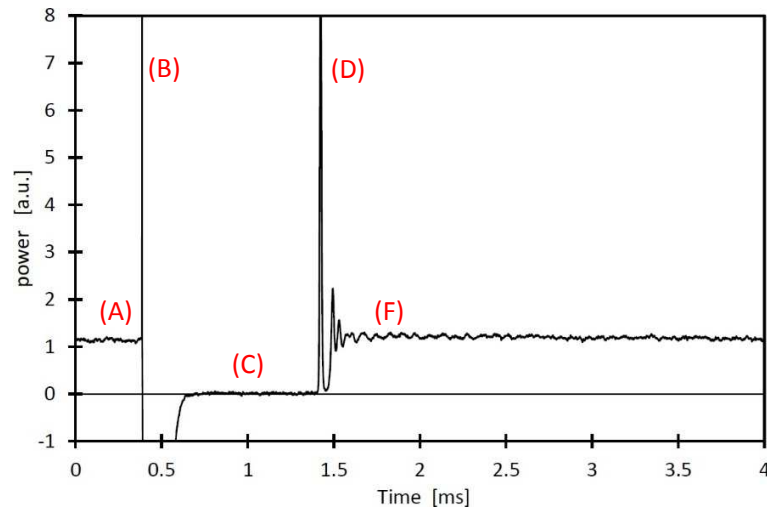


Figure 74: Similar to Figure 73 (b) but for a pulse energy of ≈ 30 mJ and repetition rates of 100 Hz. The negative power values after (B) are related to the saturation of the photo-diode.

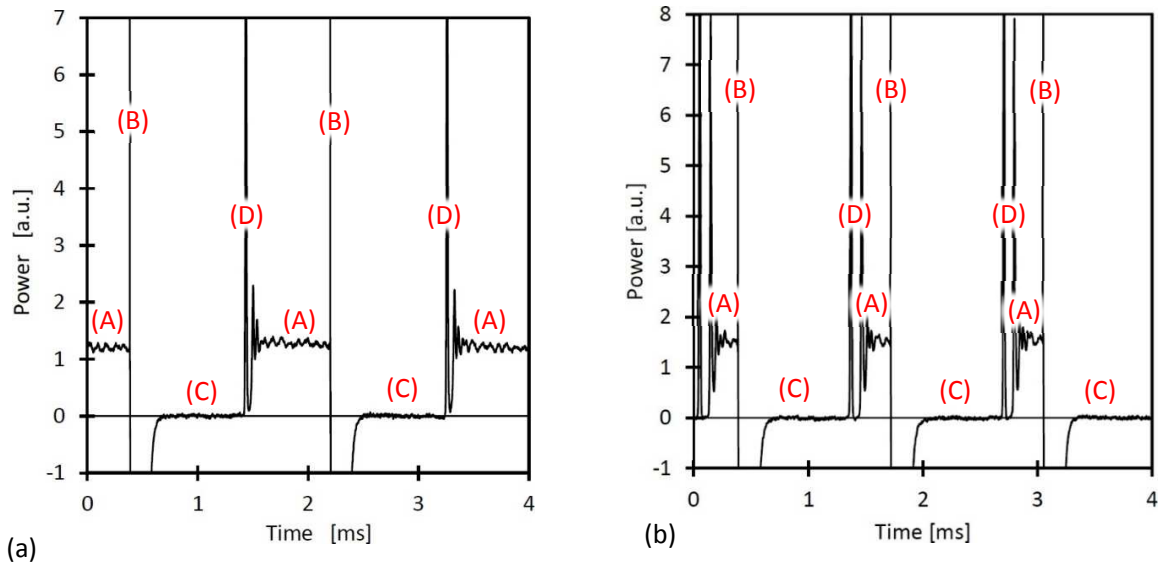


Figure 75: Similar to Figure 74 except for larger repetition rates: 550 Hz in (a), 750 Hz in (b).

The energy of the output pulses linearly depends on the pre-lasing power because the pulses are extracted prior to saturation of the laser gain. Hence, fluctuations of the pre-lasing power lead to fluctuations of the emitted pulse energies. These fluctuations increase in the successive laser stages (SHG, Ti:Sa) diminishing the average performance of the laser system as it cannot be appropriately optimized (optical damage issues). The circulating power time evolution of the circulating power when the laser is triggered at larger repetition rates (500 Hz and 800 Hz, respectively) is shown in Figure 75. Hence, in summary, the active stabilization brings along two advantages: pulse-to-pulse stability and higher repetition rates.

6.2. The oscillator eigenmode and cavity layout

The oscillator cavity was designed to have a pump spot with a diameter of 7 mm and, following the rule of thumb presented in Eq. (64) relating the optimal beam width with the pump diameter, a laser eigenmode width at the position of the active medium of $w = 2.5$ mm. As visible in Figure 71 the thin disk is used as a folding mirror and not as an end-mirror. In this way, the gain per roundtrip in the cavity is doubled resulting in a shortening of the buildup time of the pulse. A short buildup time however is only obtained provided the cavity length is short. Eigenmodes with large transverse sizes can be obtained in a short cavity using a telescope within the resonator. To further shorten the cavity length, we decided to use a concave thin disk, so that the thin disk is also the first mirror of the telescope. Given these premises, there are two possibilities, as shown in Figure 76, to realize a laser resonator consisting of a plane end-mirror M1, a convex mirror, the thin disk with a concave curvature, and a plane end-mirror M2: of type I (in zone I) and of type II (in zone II) [178].

As “long branch”, we define the right side, w.r.t. the thin disk of the resonator of Figure 76 which contains the telescope. Similarly, we define the left side, w.r.t. the thin disk as the “short branch”. “Long” and “short” here refer to effective propagation lengths given by the ratio A/B , where A and B are the first and second elements of the ABCD matrix of the two branches. For both types of resonator, the “long branch” shows a stronger variation of the eigenmode width compared to the “short branch” for variations of the thermal lens of the thin disk. One of the main differences between the two resonator types is that type I resonators have a strong focus in the “short branch”. Oppositely, in type II resonators the beam remains large and approximately constant. Hence, even though resonators of type I have better stability properties w.r.t. misalignment and thermal lens effects, we design our resonator to operate in the stability zone II.

The resonator layout of Figure 76 (b) yields a large and collimated eigenmode in the “short branch” the ideal location to place the PC. The “long branch” provides the resonator stability and defines the width of the eigenmode. At the position of the convex mirror (vex, cyan) and the end-mirror M1, the eigenmode width is small and strongly affected by variations of the thermal lens of the thin disk. As a result, these optical elements are critical from the optical damage point of view. Only laser mirrors with very high damage threshold of up to 100 J/cm^2 [195] can be used at these positions.

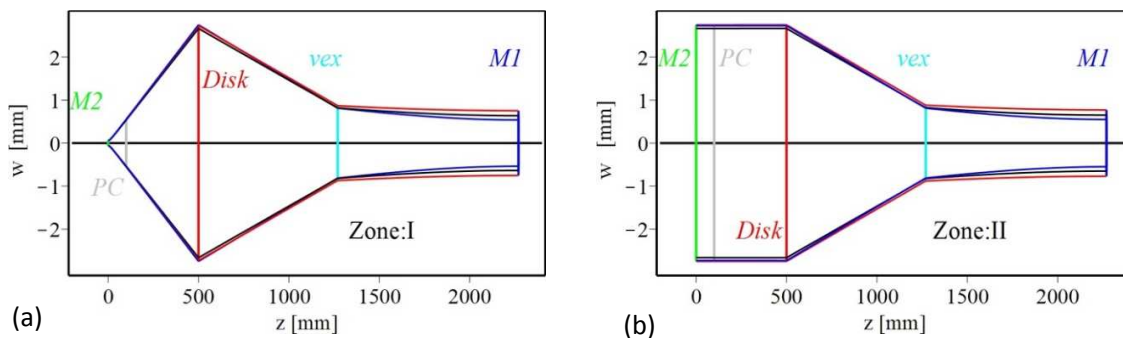


Figure 76: Type I (a) and type II (b) resonators formed by the active medium (disk), a telescope composed of the disk and a convex mirror (vex), and two flat end-mirrors M1 and M2. The radius of curvature of the disk is 2 m, of the convex mirror, -1 m. The position of the Pockels cell (PC) is also indicated, even though the PC does not affect the evolution of the beam width. The vertical lines give the position of the optical elements, while the other curves represent the width of the eigenmode along the resonators for three different values of the thermal lens of the thin disk (0 and ± 0.015 diopters). For the muonic experiment we realized the resonator in (b) corresponding to Figure 71.

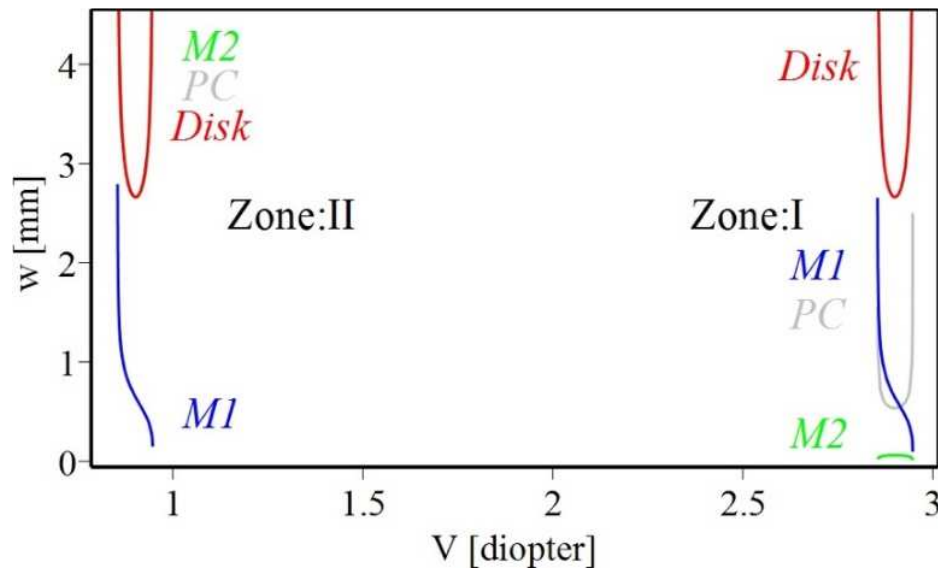


Figure 77: Stability plot of the two resonators shown in Figure 76. Plotted is the eigenmode width w at the various optical elements for variations of the dioptric power of the thin disk V .

We used a thin disk with a heatsink made from diamond with 2 m of nominal curvature (the interferometric measurement gave a value of 2.18 m for the unpumped operation). This value is altered by the thermal lens effect when the thin disk is pumped as detailed in Chapter 4. This rather small radius of curvature allows the realization of a short Galilei telescope, i.e. when combined with a convex mirror with a radius of curvature of $R = -1$ m.

The stability plots [178] for the two resonator types of Figure 76 are shown in Figure 77. Plotted is the eigenmode width w at the positions of the thin disk, Pockels cell, and end-mirrors for variations of the thermal lens of the thin disk. Only in the region where the width w is finite is the resonator stable, i.e. an eigenmode exists.

Because in our case only resonators of type II are of interest, in the following we only concentrate on them. A zoom of the stability plot in zone II is given in Figure 78 (a). The eigenmode width w in the center of the stability region can be adjusted by varying the distance between the convex mirror and the end-mirror M1. Similarly, the position of the stability region can be shifted by varying the distance between the thin disk and the convex mirror. Therefore, an adjustment of the eigenmode width and of the position of the stability region can be obtained almost independently by adjusting these two distances. Thin disk, PC, TFP and $\lambda/4$ plates are all placed in a region where the eigenmode is large and independent of variations of the dioptric power of the thin disk, as these elements have a lower optical damage threshold compared to high-power mirrors.

The stability plot of Figure 78 (a) has been computed assuming no aperture effects in the active medium. Conversely, in (b) aperture effects have been accounted for, as described in Chapter 5. The aperture effects, as detailed previously, extend the region of stability where an eigenmode exists to infinity. Yet, outside of the classic stability region computed neglecting aperture effects, the losses at the aperture are so large that laser operation in this region is strongly disfavored. Conversely, within the classic stability region, the aperture effects have a minimal impact on the resonator properties. For these reasons, aperture effects are usually neglected.

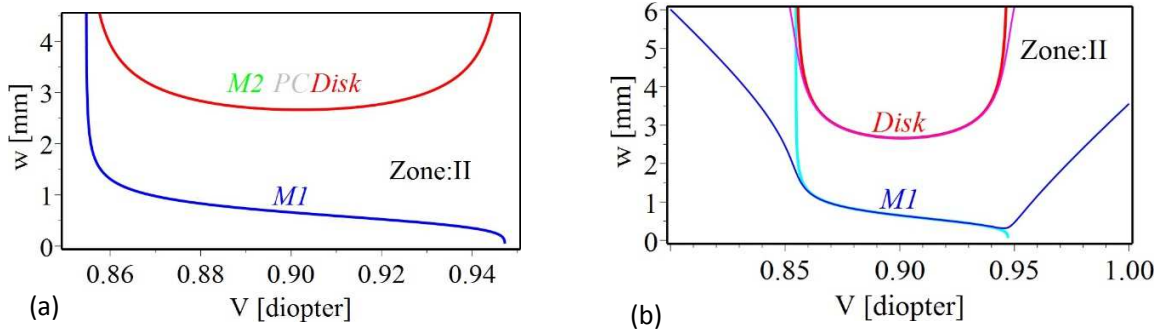


Figure 78: Stability plot for the type II resonator of Figure 76. In (a) the aperture effects occurring at the active medium have been neglected. In (b) a Gaussian aperture with $W = 10$ mm has been assumed. Plotted are the eigenmode widths at the various optical elements for variations of the dioptric power of the thin disk V .

6.3. The Pockels cell

The output coupling of our oscillator was controlled by the interplay of a PC, a $\lambda/4$ wave-plate and a TFP [196, 197, 198]. Besides being used to control the Q-switching, our PC was used, contrarily to standard designs, to stabilize the pre-lasing operation. Because of this, a customized PC had to be developed.

The $\lambda/4$ wave-plate is adjusted to guarantee laser operation close to threshold (pre-lasing) prior to trigger. Given the gain per pass on the thin disk of about 15 %, the required out-coupling in pre-lasing operation is about 30 %. The PC in the pre-lasing mode is operated at low voltage: a feedback loop delivering maximally -400 V acts on one of the PC electrodes to control the losses stabilizing the circulating power. When triggered, the cavity is closed by switching one electrode of the PC to high voltage. The high voltage is chosen so that the resonator transmission drops to about 0 %. Pulse extraction occurs when the cavity transmission is switched back to 30 %. In principle higher out-coupling could be chosen, resulting in shorter pulses. Yet, this is disadvantageous from the optical damage point of view; not only for the thin-disk oscillator, but also for the multi-pass amplifier and the Ti:Sa laser. Therefore, for our purpose the dynamic range of the resonator transmission that must be reached with the PC is moderate: it lies between 0 % and 30 %.

In Sec. 6.3.1, we describe by means of Jones matrices the interplay of the three elements controlling the out-coupling: PC, quarter wave-plate and TFP. We also demonstrate that PC voltages below the quarter-wave voltage are sufficient to cover the out-coupling variations needed. This is a non-trivial result given the fundamentally different action on the light polarization of the wave-plate and the Pockels cell. In Sec. 6.3.2 and 6.3.3, we present the electrical and mechanical design of the Pockels cell, respectively.

6.3.1. Jones matrix formulation of the Pockels cells

The evolution of the polarization in an optical system can be described using Jones matrices [199] where the light polarization is described by a two-component vector: $(0,1)$ and $(1,0)$ represent linearly polarized

beams in the horizontal and vertical directions, respectively. The evolution of the polarization in the oscillator shown in Figure 79 follows this sequence:

- The beam is reflected at the TFP which defines the polarization to be (1,0) as only the vertical component is reflected while the horizontal component is transmitted.
- The beam moves from the TFP to the $\lambda/4$ wave-plate. While propagating in this free space (air) the polarization vector is conserved. This is valid for any free propagation or propagation in non-birefringent materials. All the following free propagations are thus neglected in the discussion.
- The beam crosses the $\lambda/4$ wave-plate. The optical axis of the crystal lies in transverse plane oriented at an angle α w.r.t the horizontal direction.
- The beam passes the PC whose optical axis is also in the transverse plane at 45° w.r.t the horizontal direction.
- The beam is back reflected at the cavity end-mirror M2. This does not change the polarization vector.
- The beam passes the PC a second time.
- The beam passes the $\lambda/4$ wave-plate a second time.
- The beam reaches the TFP that reflects the vertical polarization and transmits the horizontal one.
- The vertical polarization propagates to the disk, where it is backreflected. The polarization is maintained in this propagation.

The polarization amplitude of the laser beam leaving the TFP and moving towards the mirror M2 is (1,0). After propagation through the $\lambda/4$ wave-plate, PC, back-reflection at M2, PC and $\lambda/4$ wave-plate the laser beam reaches again the TFP. Its polarization amplitude P before the TFP can be computed by multiplying the Jones matrices corresponding to the various (polarization-dependent) optical elements:

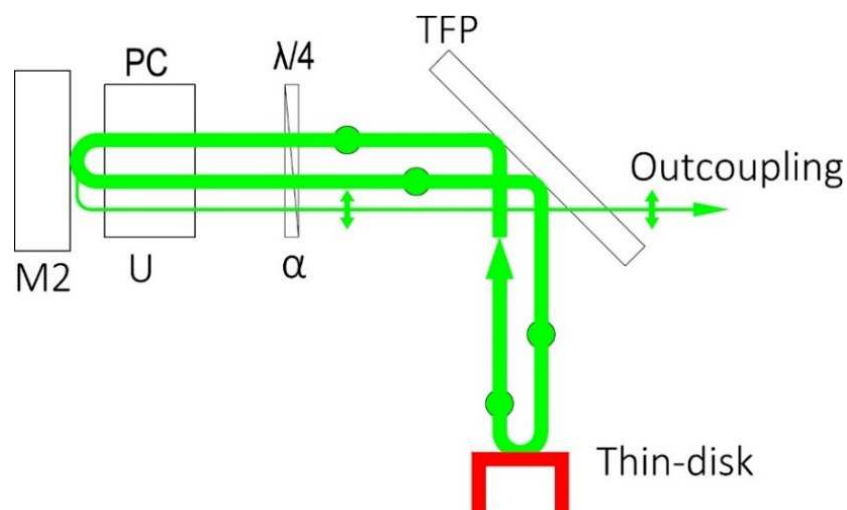


Figure 79: Simplified schemes of the oscillator illustrating the working principle of the polarization-dependent elements. The TFP transmits the horizontal polarization and reflects the vertical polarization. The green full circles stand for vertical polarization, the green double-head arrows for horizontal polarization. See main text for more detail.

$$P = M_{\alpha} M_{\lambda/4} M_{-\alpha} \cdot M_{45^{\circ}} M_{PC} M_{-45^{\circ}} \cdot M_{45^{\circ}} M_{PC} M_{-45^{\circ}} \cdot M_{\alpha} M_{\lambda/4} M_{-\alpha} \begin{bmatrix} 1 \\ 0 \end{bmatrix}, \quad (118)$$

where the matrix

$$M_{\lambda/4} = \begin{bmatrix} e^{i\frac{\pi}{4}} & 0 \\ 0 & e^{-i\frac{\pi}{4}} \end{bmatrix} \quad (119)$$

represents the Jones matrix for the $\lambda/4$ wave-plate, and

$$M_{PC} = \begin{bmatrix} e^{\pi i \frac{U}{U_{\lambda}}} & 0 \\ 0 & e^{-\pi i \frac{U}{U_{\lambda}}} \end{bmatrix} \quad (120)$$

the Jones matrix for the PC whose retardation depends on the applied voltage U with U_{λ} being the voltage needed (which depends on the geometry and material of the electro-optic crystal) to induce a retardation of λ . The matrix

$$M_{\alpha} = \begin{bmatrix} \cos(\alpha) & \sin(\alpha) \\ -\sin(\alpha) & \cos(\alpha) \end{bmatrix} \quad (121)$$

represents a rotation in the transverse plane by an angle α w.r.t. the horizontal. These rotational matrices are used because the Jones matrix of Eq. (119) is defined assuming that the optical axis is at a given angle α w.r.t the horizontal direction, while Eq. (120) is defined assuming that the optical axis of the PC crystal is at 45° w.r.t the horizontal direction. Note that an optical component with a matrix $M_{element}$ whose optical axis is at an angle β w.r.t. the horizontal, in the horizontal-vertical basis has to be described by $M_{\beta} M_{element} M_{-\beta}$.

To compute the fraction of the intensity reflected at the TFP we have to take the first component of the polarization vector P_1

$$P_1(U, \alpha) = i \cdot \cos(2\alpha) \cdot \cos\left(\frac{\pi U}{2 U_{\lambda/2}}\right) - (1 + i \cdot \cos(2\alpha)) \cdot \sin(2\alpha) \cdot \sin\left(\frac{\pi U}{2 U_{\lambda/2}}\right) \quad (122)$$

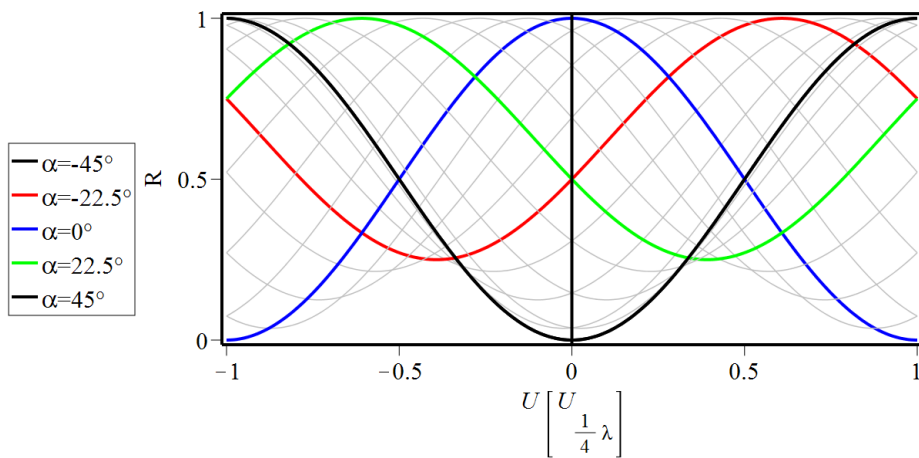


Figure 80: The effective reflectivity R of the TFP- $\lambda/4$ -PC system given as a function of the voltage difference U applied to the PC electrodes. The various lines represent the behavior for various orientations α of the wave-plate.

and square it to go from amplitude to intensity. The effective reflectivity R of the resonator out-coupler (TFP) depends on the voltage U applied at the PC and the angle α of the $\lambda/4$ wave-plate as

$$R = [P_1(U, \alpha)]^2. \quad (123)$$

The effective reflectivity R is a double periodic function with period of 90° for α , and period $U_{\lambda/2}$ for U . The reflectivity is plotted as a function of U in Figure 80 for various values of α . As visible from the figure, for large R , variations of α produce similar results to variations of U , so that a change of α is equivalent to a voltage offset.

For our PC crystal (BBO, $15 \times 15 \times 30 \text{ mm}^3$) $U_{\lambda/4} = 11.5 \text{ kV}$ [200]. Therefore, to switch from $R = 100\%$ to $R = 0\%$ a voltage difference of 11.5 kV is needed. However, prior to laser trigger the oscillator is operated in pre-lasing mode close to the laser threshold with a cavity reflectivity of about $R = 70\%$. The effective reflectivity R is then increased to 100% when the oscillator is triggered. The resonator is thus closed and remains closed until the PC is steered to yield an effective reflectivity of about $R = 70\%$. The needed dynamic range of the PC is thus only approximately $0.3 U_{\lambda/4}$.

Figure 81 illustrates the just-described time evolution of the effective reflectivity R during a Q-switch cycle. In pre-lasing operation, the PC voltage difference $U = U_1 - U_2$ is close to zero (red region). It is not exactly zero because a small voltage ($U_1 \neq 0, U_2 = 0$) is applied to the PC to stabilize the power of the circulating light. This stabilization is realized by a feedback loop (see Figure 71 and Figure 82) which delivers a voltage of between -400 V and 0 V . When triggered, the cavity is closed by applying a positive voltage of $U = U_1 = 3.2 \text{ kV}$. To extract the pulse from the cavity, the PC voltage is set to zero by switching the second electrode to the same voltage $U_1 = U_2 = 3.2 \text{ kV}$. The pre-lasing operation is off for 1 ms after pulse extraction. Thereafter, it switches on and the oscillator is ready to accept a new trigger.

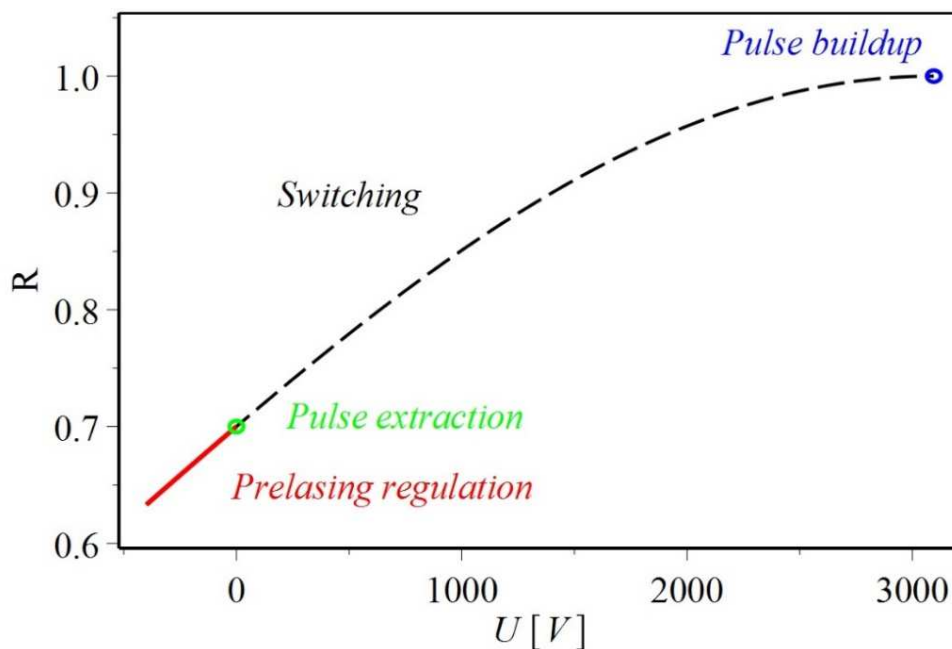


Figure 81: Time evolution of the effective reflectivity R during a Q-switch cycle. The behavior of R vs. $U = U_1 - U_2$ follows one line of Figure 80 obtained with $\alpha = 16.6^\circ$. During pre-lasing operation (red region), U is negative. After a trigger, the voltage U is switched to 2.3 kV and the effective reflectivity becomes $R = 1$. Pulse buildup occurs until the Pockels-cell voltage difference is switched to $U = 0$ to extract the pulse. The PC voltage is thus at $U = 0$ during pulse extraction. 1 ms after pulse extraction the pre-lasing regulation is switched on again.

6.3.2. The electric design

Our Pockels cell was optimized for:

- *Controlling the Q-switching dynamics:* The Q-switching requires a voltage jump of about 3 kV. The purchased high-voltage switches are capable of switching 16 kV within 15 ns [201].
- *Intra-cavity power stabilization of the pre-lasing:* This analog regulation relies on a continuous variation of the effective reflectivity R via a feedback loop acting on the PC with a variable voltage between of -400 V and 0 V.

For these purposes, to drive the PC electrodes we developed the electrical circuit of Figure 82. The central element of the PC is the electro-optic crystal that produces a phase retardation of the transmitted beam that depends on the electric field. The electric field that is applied transversely to the laser beam axis is defined by the potential at the two electrodes contacted with the crystal as shown in the central part of the figure.

In pre-lasing operation, the electric field in the PC crystal is adjusted to stabilize the power of the circulating light. This stabilization works in the following way. A photo-diode D_{int} , measuring the light leaking from the mirror M2 is used to monitor the circulating power. As shown in the bottom left part of the figure the amplitude of the photo-diode signal is fed into a PID controller. The error signal generated by the difference between the amplitude of the photo-diode and a set-point value is then fed to an analog amplifier delivering a voltage of between -400 V and 0 V. Through resistors R9, R6 and R5 this voltage is applied to the left electrode of the PC crystal. Variations of this voltage (U_1) can thus be used to adjust the cavity losses to stabilize the circulating power. The two switches SW1 and SW2 are open during the pre-lasing operation. Consequently, the right electrode is at zero voltage ($U_2 = 0$), while the voltage of the left electrode is only given by the just-described feedback loop ($U_1 \neq 0$).

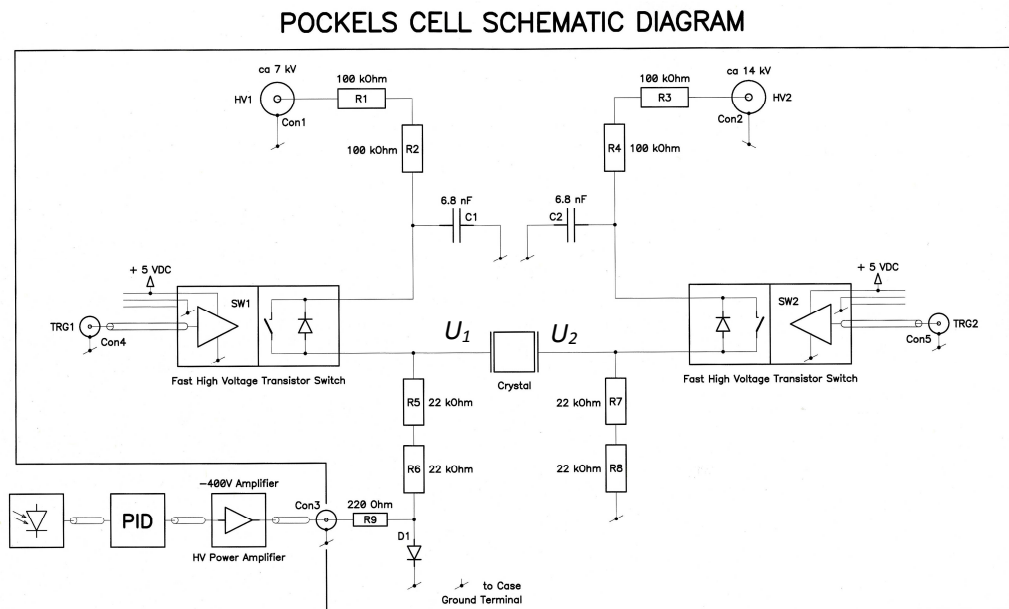


Figure 82: Electronic scheme used to drive the PC. Two switches SW1 and SW2 and a feedback loop controller steer the voltages at the crystal electrodes. Two customized Behlke HTS 160-01 switches [201] capable of switching 16 kV with 15 A and a rise time of 15 ns are used with an increased on-time of 2 μ s.

When the laser is triggered, the switch SW1 is closed. Within 15 ns, the left electrode of the PC is set to the voltage $U_1 = HV1$ given by an external voltage source. The right electrode remains at zero voltage ($U_2 = 0$) so that a strong electric field is created in the PC crystal. The cavity is closed and pulse buildup starts.

After a given time (that can be adjusted) also the switch SW2 is closed. Within 15 ns the right electrode is thus set to $U_2 = HV2$; since in our case $HV1 = HV2$, after this switching operation the electric field in the PC crystal drops to zero (or near zero). The effective reflectivity of the TFP returns to approximately 70 %, i.e. approximately to the value it had prior to laser trigger given by the orientation of the $\lambda/4$ wave plate. The pulse is emitted from the resonator.

The two switches of the PC have a 2 μ s on-time. This means that 2 μ s after the switch has been closed, the switch is reopened again. With open switches, the high voltages at the electrodes decay with a time constant of about 100 μ s given amongst other effects by the crystal capacitance, by R5, R6, R7 and R8. This means that both electrode voltages, which have been set at the same value, slowly decay back to zero. As the decay constants for the left and right electrodes are the same, the voltages at the two electrodes decay in a similar way. Thus, during this discharging process the electric field in the crystal remains nearly zero. After a few hundred microseconds both electrodes are at zero voltage and the two switches are open. With a delay of 1 ms after pulse extraction, the feedback loop that was inhibited during the pulse formation is switched on again. The laser returns to operate in pre-lasing mode.

During high-voltage switching, the -400 V amplifier of the feedback loop has to be protected because the switches generate spikes significantly higher than the amplifier limit. Diode D1 shown in the bottom left part of Figure 82 is used to protect the amplifier. When the left electrode (U_1) is at high positive voltage, a current is flowing through resistor R5, resistor R6 and diode D1, but no current flows back into the -400 V amplifier, as diode D1 opens to ground.

During the pre-lasing operation, diode D1 is closed as the amplifier has a negative voltage. In such a way, the voltage of the feedback loop amplifier can be applied to the left electrode (U_1) of the crystal. This motivated the choice of a negative voltage for stabilizing the pre-lasing and a positive voltage for the switching. We realized the PC using modified Behlke HTS 160-01 switches [201] capable of switching 16 kV with 15 A and a rise time of 15 ns, and a customized on-time of 2 μ s. The triggers of the switches were realized using TTL signals and coaxial cables with internal 50 Ω terminations to minimize possible pick-up noise that could produce false triggers.

The PC was designed so that for the majority of the time the electrodes of the crystal are at, or close to, zero voltage to reduce the probability that electrostatically charged dust is attracted to the crystal. For most of the time, also the electric field is at, or close to zero, so that photo-refractive effects related with the free electrons induced by multi-photon absorption are reduced [202]. To keep the PC at zero voltage during pre-lasing, the orientation of the $\lambda/4$ wave-plate has to be adjusted correspondingly to provide a rotation of the polarization corresponding to an effective reflectivity of about $R = 70$ %.

Barium-beta-borate (BBO) was chosen as PC crystal for its high damage threshold, low residual absorption and low hygroscopicity. BBO requires considerably higher $U_{\lambda/4}$ voltage due to the low non-linear coefficient (2.7 pm/V [200]) compared, for example, with Lithium Niobate having (34.4 pm/V [203]). However, the switching voltage is of lower concern for our PC design, given the availability of fast switches up to 30 kV. Still, a large $U_{\lambda/4}$ increases the complexity of the PC realization.

6.3.3. The practical realization

We used a BBO crystal with an aperture of $15 \times 15 \text{ mm}^2$ and a length of 20 mm. The transverse size of the crystal is thus 6 times larger than the eigenmode width at the PC location. Two lateral sides of the crystal are metallized to define a homogeneous electric field perpendicular to the laser propagation. The front and back surfaces have a high-power anti-reflex coating for our wavelength of $\lambda = 1030 \text{ nm}$ which simultaneously serves as a barrier to reduce the hygroscopic absorption of moisture.

The mechanical setup was optimized to fit into the optical system of the laser resonator. The basic mechanical requirements were:

- A beam height of $h = 125 \text{ mm}$,
- Crystal accessibility for inspection,
- Large optical aperture to avoid optical damage and diffraction losses,
- Short optical length to minimize cavity length,
- Clean separation between electronic part and optical setup to realize a dust-free environment,
- No polymer components close to the beam to reduce laser-induced dust generation in case of misalignment,
- Adjustable mechanics for crystal alignment is not required,
- Capable of operating at voltages up to $U = 10 \text{ kV}$.

Figure 83 shows a picture of the realized PC. The BBO crystal is placed in between the two brass electrodes (top part of the figure) mounted on an acrylic-glass plate. The height of the beam (crystal) is $h = 125 \text{ mm}$ from the optical breadboard, as in the rest of the thin-disk laser. All electronic components (switches, capacitors etc.) are below the beam height separated by the acrylic-glass plate to have “clean-room” condition in the optical region where the BBO crystal is placed. In fact, the electronic parts are the largest source of dirt and outgassing within the laser system.

Each electrode is being fixed to the acrylic-glass plate using a screw and two cylindrical dowel pins, providing a precise position and angle. The plate is 25 mm below the laser beam axis and shows a nearly perfect



Figure 83: Picture of the Pockels cell without lateral walls and protective cap for the optical region. The optical region (top) is separated by an acrylic glass from the region containing the electronics (switches, capacitors etc.). 3D wiring minimizes the breakdown issues.

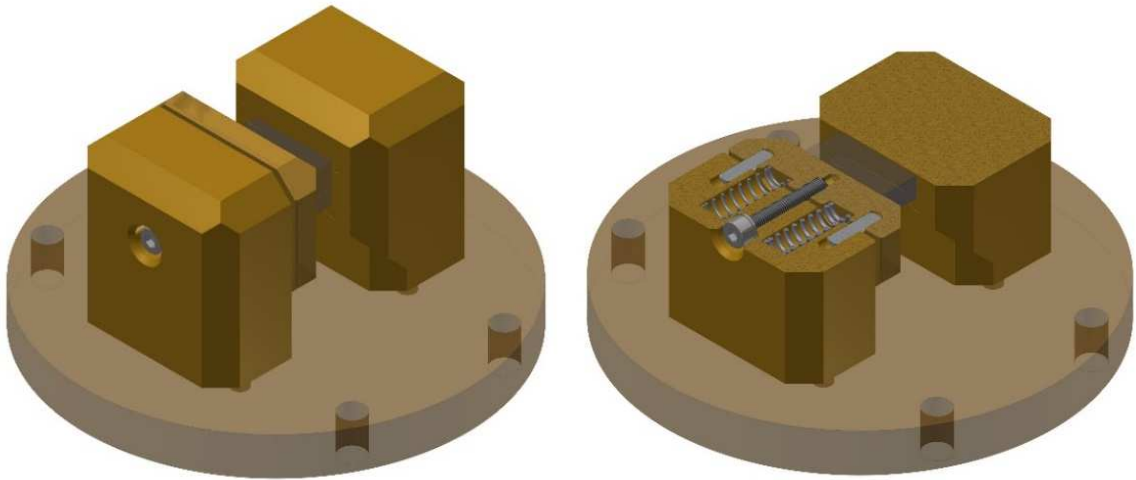


Figure 84: Optical region with the Brass Pockels cell electrodes clamping the BBO crystal mounted on an acrylic-glass plate. (a) Full 3D drawing. (b) Half-cut through the 3D drawing.

transmission for the laser wavelength so that even for significant amounts of light scattering at the electrodes or at the edge of the crystal the intensity is expected to be far below the threshold that could induce material damage. Unlike machined polymers, the surface of the acrylic glass is flat and smooth, making it ideal to clean with isopropanol. The use of a polymer base plate seems risky as polymers exhibit some creeps that could result in laser misalignment. However, note that the angular acceptance of the PC is several orders of magnitude larger than for laser mirrors.

The crystal is mounted between the two brass electrodes as shown in Figure 84. Inspection of possible crystal damage may take place without dismounting the crystal, thus without losing the laser alignment. This differs from standard PC designs, where inspection of the crystal requires dismounting from its holder. Compared to standard designs the space adjacent to the crystal does not contain any component made from plastics. This strongly reduces the contamination of the optical surface that would occur if a misaligned laser beam impinged on the polymers. However, to prevent electrical breakdown the spacing between the various elements set at different potential has to be increased to compensate for the lower isolation properties of air compared to plastic materials.

One electrode is split into two parts that are pulled apart by two springs. In this way, the electrode surface in contact with the BBO crystal is movable to allow for crystal replacement. The other electrode is stationary and acts as a position reference. The BBO is held in position in a gentle way only by the pressure exerted by the springs. The correct centering of the crystal can be achieved using the milled notch at the front surfaces of the electrodes. The electric field increase arising at the edges of the notch is minimized given small depth of the notch of only 0.1 mm. To prevent discharges (from electrode to electrode, or from electrode to the metallic housing) the electrodes were produced with significant chamfers.

A metallic housing (not shown in Figure 83 and Figure 84) protects the optical region of the crystal and electrodes against dust. This housing also represents a safety protection for the operator against high voltages. This window-free (only holes) housing can be removed without misaligning the resonator and provides an effective shielding for electromagnetic interference (EMI). Commercial PCs use optical windows to protect the crystal region from dust. We omitted protective windows of the housing, as these increase cavity losses, and the number of components vulnerable to laser damage.

6.4. Results

The thin-disk oscillator was pumped with 300 W of pump power from a fiber-coupled diode module operating at a wavelength of $\lambda = 969.6$ nm. As the diameter of the pump spot was about 7 mm, the pump power density was of the order of 2 kW/cm^2 . This has to be compared with 8 kW/cm^2 as typically used in cw lasers. Our smaller pump power density accounts for gain saturation caused by ASE and the higher thermal load due to the use of thicker disks ($345 \mu\text{m}$ instead of $140 \mu\text{m}$) and the operation in fluorescence mode. In fact, because of the quasi-three-level structure of Yb:YAG, the increased thermal load and temperature of the active medium leads to a decrease (rollover) [204] in gain, with increasing pump power.

To minimize the thermal load, we opted to pump the Yb:YAG active medium at its zero-phonon line centered around 969.6 nm instead of the classically used pump wavelength at 940 nm. This choice alone reduces the thermal load in the disk by a factor $(1030 \text{ nm} - 969.6 \text{ nm}) / (1030 \text{ nm} - 940 \text{ nm}) = 0.67$. The drawback is that the zero-phonon line has a width of only 2.5 nm [101]. Thus, the pump diode has to be frequency-narrowed and stabilized. This is achieved using a volume Bragg grating (VBG) [205] as feedback mirror to the laser diodes. The pump light from the diode is transported to the pump optics using a fiber with $600 \mu\text{m}$ core diameter. As pump optic, the standard 6 prism (16 passes) laser-head of TRUMPF [112, 206] is used.

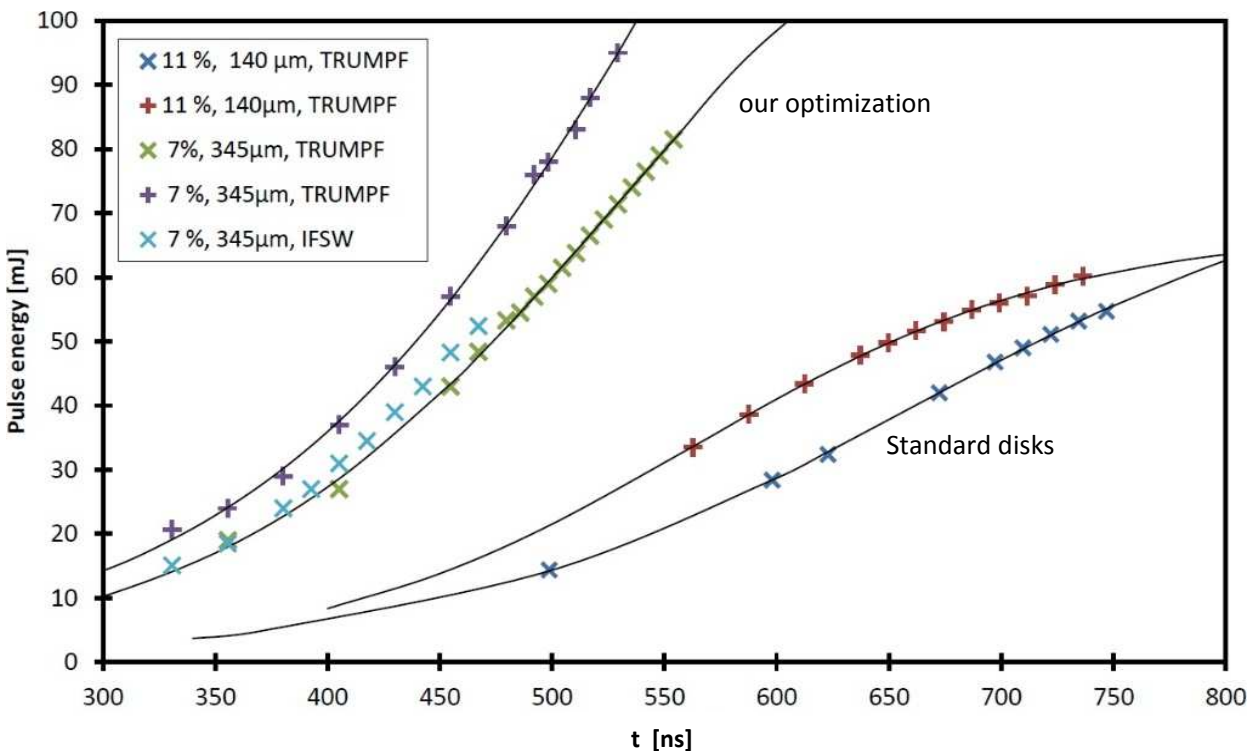


Figure 85: Oscillator pulse energy versus the oscillator enclosure time t . Two different types of thin disk with different thickness and doping concentration are used. The CVD-based disks are either from the IFSW [207] or from TRUMPF [208]. The various measurements are based on slightly different oscillator layouts but have similar eigenmodes and resonator lengths.

The eigenmode width at the active medium was designed to be $w = 2.5$ mm. As explained in Chapters 4 and 5, this choice is a tradeoff that accounts for several aspects. A smaller width would lead to lower damage thresholds and a smaller fraction of extractable energy. In addition, higher-order transverse modes could lase, leading to larger losses and a decrease of the beam quality. On the other hand, a larger eigenmode width [117] would cause strong aperture effects that decrease the gain and the beam quality.

The output energy of the oscillator can be adjusted by varying the time window in which the resonator is closed. As visible in Figure 85, an increase of this time window (delay between closing and opening of the cavity) leads to an increase in output pulse energy. The pulse energy was fitted using the function

$$E(t) = \frac{E_{max}}{1 - e^{G(t_{50\%}-t)}}, \quad (124)$$

where t is the enclosure time, E_{max} is the maximal extractable pulse energy, $t_{50\%}$ the time when $E = E_{max}/2$, and G is the small signal gain of the laser given by the small signal roundtrip gain g_0 and the roundtrip time τ_r as

$$G = \frac{g_0}{\tau_r}. \quad (125)$$

We derived Eq. (124) from the rate equation including gain saturation but neglecting intra-cavity losses. This is justified by the fact that the cavity is closed during pulse buildup. E_{max} is reached for the limiting case of an infinitely long pulse buildup time and no losses.

In the measurements of Figure 85, two types of disk have been used: one with 11 % doping concentration and a thickness of 140 μm suited for cw operation, the other one with a thickness of 345 μm and a doping of 7 % optimized for our conditions (fluorescence operation and large pulse energy). Both disks are based on a CVD heatsink. From the figure, it is clear that the optimization of the thin disk we have achieved in this thesis was significant. First of all, this optimization leads to a shorter delay (latency time) at a given output energy. Second, the thicker disk is capable of storing higher energy so that the inset of gain saturation occurs later (at a higher energy) compared to a thinner disk. This is also advantageous in terms of optical damage.

The use of the thin disk as a bending mirror in a linear cavity increases the effect of spatial-hole-burning [209]. Hence, several longitudinal modes can lase in the oscillator at the same time. The interference of the various modes produces mode beating [117, 210, 211] that generated large intensity fluctuations both in the pre lasing and in the pulse operation (see Figure 87 (a)). These fluctuations reduce the optical damage threshold in the thin-disk laser and in the following laser stages (SHG and Ti:Sa laser). It was described that the averaging effect of several passes in the active medium can be used to mitigate spatial-hole-burning [212]. However, this occurs only for mode-locked laser operation. For narrow-band laser operation an increase of the number of passes at the active medium enhances spatial-hole-burning.

In reference [210], mode beating was suppressed by inserting frequency-selective elements into the resonator so that only one mode can circulate in the cavity. On the contrary, in our laser system the cavity is too long to allow for efficient suppression of adjacent laser modes. However, as exposed in [213] so-called “twisted-mode” operation of the resonator can be implemented. The basic idea is to introduce a $\lambda/4$ wave-plate in front of the thin disk to suppress the interference between the first reflection and the

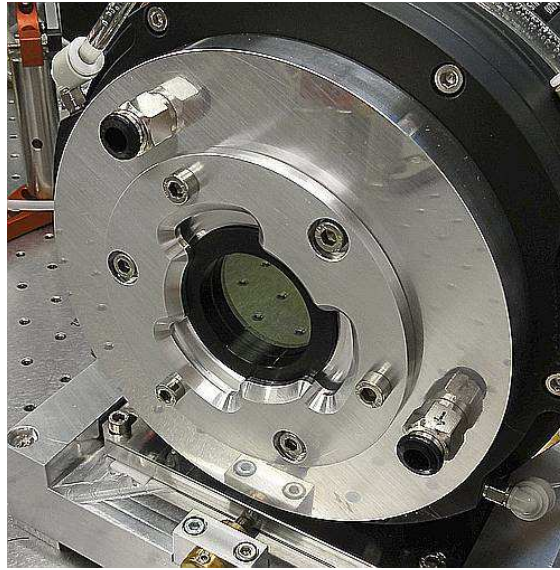


Figure 86: Picture of the modified TRUMPF laser-head [206]. It contains the pump optic and the thin disk and is closed with a rotatable 2-inch $\lambda/4$ wave-plate adjusted to suppress mode beating.

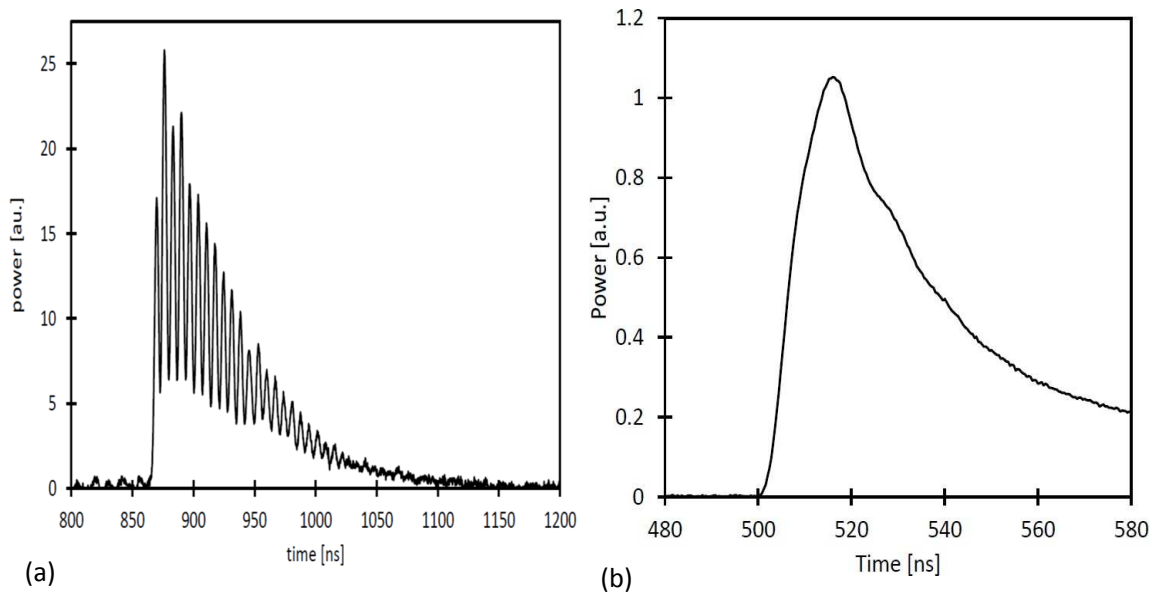


Figure 87 (a): Measured oscillator output pulse without (a) and with (b) the second (in front of the disk, see Figure 71) $\lambda/4$ wave-plate to suppress spatial-hole-burning and mode beating.

second reflection at the thin disk in a roundtrip. In our oscillator, we thus inserted a second $\lambda/4$ wave-plate as shown in Figure 71 in front of the thin disk. At the same time, this wave-plate as visible in Figure 86 was used as a window to close the pump module to prevent the dust to enter into the module, and to reduce the air turbulences leading to Schlieren effects [214]. The suppression of the mode beating by inserting the $\lambda/4$ wave-plate is well visible by comparing the two plots of Figure 87 [215, 216]. The mode-beating suppression results in a decrease of the intensity modulation of the pulse.

The FWHM length of the pulse in Figure 87 is approximately 50 ns. By increasing the output energy, the pulse length slightly decreases because the larger extracted energy more rapidly saturates the gain. Thus,

the oscillator goes more rapidly below threshold and the pulse is extracted with a lifetime given by the photon lifetime in the cavity.

In summary, the oscillator that we developed for the muonic helium experiment is capable of pulse energies up to 110 mJ, minimal delay time from pulse-to-pulse down to 1.2 ms, pulse-to-pulse fluctuation better than 1 % (with a 200 Hz trigger rate), short latency time of about 400 ns (for 25 mJ energy). A beams mode-quality of $M^2 = 1.01$ was measured in the pre-lasing operation. During data taking, however, the oscillator was safely operated to deliver “only” 25 mJ.

7. Thin-disk laser multi-pass amplifier⁴

In the context of the Lamb shift measurement in muonic helium [1, 2, 50, 217] we developed a thin-disk laser composed of a Q-switched oscillator and a multi-pass amplifier delivering pulses of 150 mJ at a pulse duration of 100 ns. Its peculiar requirements are stochastic trigger and short delay time (< 500 ns) between trigger and optical output [218]. The concept of the thin-disk laser allows for energy and power scaling at high efficiency. However, the single-pass gain is small (about 1.2). Hence, a multi-pass scheme with precise mode matching for large beam widths ($w = 2$ mm) is required.

Instead of using the standard 4f design, we have developed a multi-pass amplifier with a beam propagation insensitive to thermal lens effects and misalignments. The beam propagation is equivalent to multiple roundtrips in an optically stable resonator. To support the propagation we used an array of 2×8 individually adjustable plane mirrors. Astigmatism has been minimized by a compact mirror placement. For precise alignment, a kinematic array was realized using our own mirror mount design. A small signal gain of 5 for 8 passes at a pump power of 400 W was reached. The laser was running for more than 3 months without the need of realignment. Pointing stability studies are also reported here.

7.1. Introduction

A precise determination of proton and alpha particle charge radii can be achieved by laser spectroscopy of muonic hydrogen and muonic helium, respectively. Muonic hydrogen (μp) is an atom formed by a proton and a negative muon. Similarly, muonic helium is composed of a negative muon and a He nucleus. The muon is an elementary particle alike the electron but with a 207 times larger mass and a lifetime of $2.2 \mu\text{s}$. Because of the larger mass, the muon wave function significantly overlaps with the nucleus of the atom and therefore its energy levels strongly depends on the nuclear charge radius.

From a measurement of the 2S-2P transition in μp the CREMA collaboration has determined the proton charge radius 20 times more precisely [1, 2] than other determinations based on H spectroscopy and elastic electron-proton scattering. Yet the value obtained is, very surprisingly, seven standard deviations away from the world average. This discrepancy that was termed the “proton radius puzzle” has attracted great attention in atomic, nuclear and particle physics. Many investigations have been triggered [4], ranging from physics beyond the standard particle model to the proton structure (low energy QCD), to

⁴ This chapter is a reprint of [54]

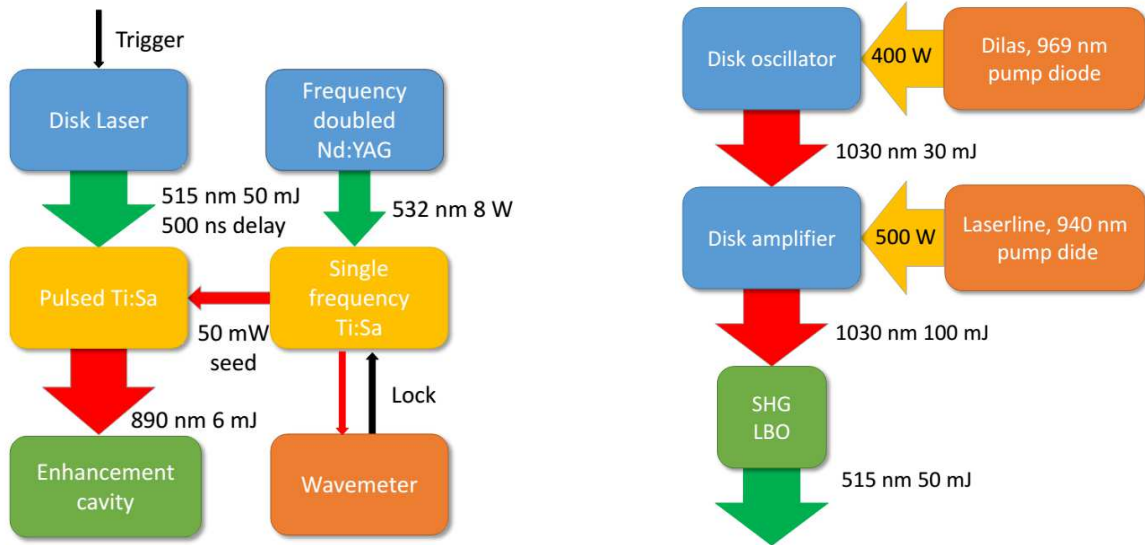


Figure 88: (Left) Scheme of the laser system. The frequency-doubled thin-disk laser is used to pump a frequency-locked Ti:Sa laser. This Ti:Sa is successively injected into an enhancement cavity to increase fluence [219]. (Right) Thin-disk laser scheme.

atomic energy levels (bound-state QED) and several experiments have been initiated in the fields of electron-proton scattering experiment and high-precision laser spectroscopy.

To contribute to a possible solution of the “proton radius puzzle” the CREMA collaboration performed spectroscopy of μHe^+ . The principle of the muonic He experiment is to stop muons in helium gas whereby muonic He is formed and then to measure the 2S-2P energy splitting by means of pulsed laser spectroscopy. A muon entrance detector provides a trigger signal for the laser system. About 2 μs after muonic helium formation the laser pulse illuminates the muonic atom to drive the 2S-2P transition (in resonance). A scheme of the total laser system is given in Figure 88 (left).

The muon detector triggers the continuously pumped thin-disk laser. Its pulses are frequency doubled (SHG) and used to pump a Ti:Sa laser, which is seeded by a stabilized continuous-wave Ti:Sa laser whose pulses are injected into a multi-pass cavity surrounding the helium gas target.

As the 2S-state lifetime is only 2 μs , the laser system needs to have a short delay time between trigger and pulse delivery. So we have developed a thin-disk laser in an oscillator-amplifier configuration (Figure 88 (Right)) with the following requirements:

- delay between electronic trigger and laser pulse < 500 ns,
- stochastic trigger,
- at least 100 mJ pulse energy,
- up to 500 Hz repetition rate.

In order to fulfill such a short delay no pulsed pumping scheme can be used. The energy needs to be stored in the laser crystal prior to trigger. We chose the thin-disk laser technology with Yb:YAG as active material. This crystal has a long upper state lifetime of about 1 ms and can be pumped with commercially available high-power diode lasers. The layout of the thin disk provides effective cooling and a small phase distortion [4]. This choice allows the extraction of pulses with large energies and high beam quality from a cw pumped active material within short time.

7.2. Amplifier concept

The basic property of an optical resonator is to reproduce the identical beam shape after one roundtrip. Our amplifier design is an unwinding of the beam propagation path inside a resonator. The top panel of Figure 89 is showing a schematic of the beam routing in our multi-pass amplifier. If correct coupling is achieved, it is equivalent to the resonator shown in the bottom panel. The amplifier thus inherits the stability properties of the resonator. Our aim was to design an amplifier insensitive to thermal lens effects. To do this we started with the design of a resonator with the desired beam width and stability.

In Figure 90 (left) the beam size along the resonator is given. The resonator consists of a flat end-mirror, the thin disk acting as a focusing mirror, a defocusing mirror and a flat end-mirror. The position of the thin disk within the resonator is represented by a vertical black line. The thin disk splits the resonator in two branches. A short branch with a plane parallel beam and a long branch including a Galilei telescope. Hence, the long branch is equivalent to an 11 m long free propagation. It thus provides stable operation for a large beam size ($w = 2.66$ mm). The black line represents the mode beam size at the cavity design values, the red and blue lines represent the beam size for variations of the dioptric power thin disk by ± 0.02 diopter.

Figure 90 (right) shows the corresponding stability plot for the resonator with design value. The blue line displays the beam waist at the thin disk and at the end-mirror of the short branch, while the black line shows the mode size at the end mirror of the long branch. This waist is the smallest inside the cavity, consequently the most critical for mirror damage.

The beam size at the position of the thin disk and at the short end of the cavity, which is displayed in Figure 90 as a blue line, does not change in first order with variation of thermal lens. A linear cavity containing a variable lens not as end-mirror always has two stability zones [178, 179]. However, due to the strong asymmetry of the resonator the second stability zone is at a focal strength of 2 diopters (not visible in the plot). The stability zone of a symmetric cavity has twice the width; still we chose an asymmetric layout because of our coupling scheme. The short side of the resonator is insensitive to variations of thermal lens and because of this; it is suitable for beam coupling.

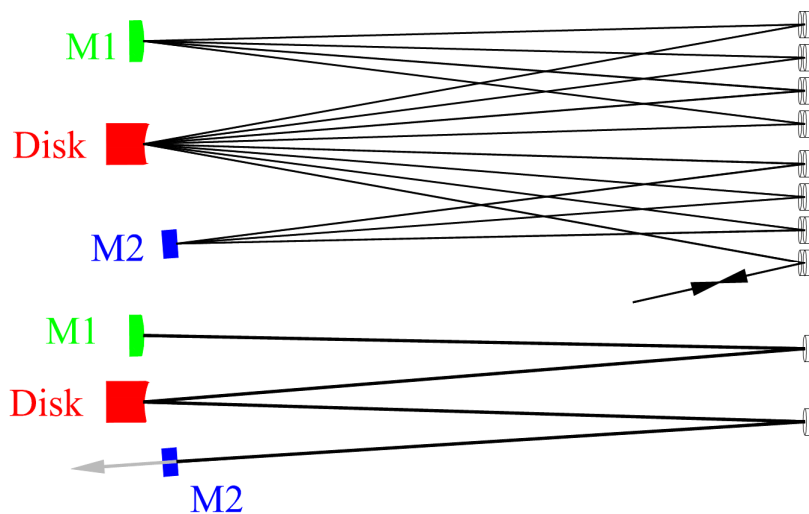


Figure 89: (Top) Scheme of the beam propagation in the amplifier. (Bottom) Scheme of the corresponding optical resonator.

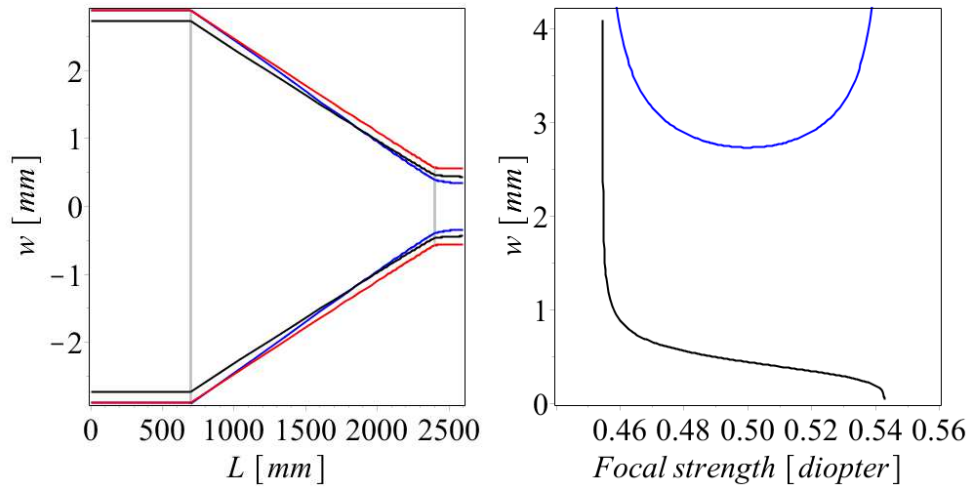


Figure 90: (left) Beam waist along the model resonator. The thin disk, whose position is given by the black vertical lines, has a curvature of 4 m equivalent to a focal strength of 0.5 diopters. The blue and red lines are the beam waists for 0.52 and 0.48 diopters, respectively. (right) Stability diagram. The curves are the beam size at the end-mirrors.

This resonator layout is used to generate an amplifier design with 8 reflections on the thin disk as shown in Figure 91. The laser amplifier starts with the optical system of resonator layout as in Figure 90 (Left). In order to realize a complete cavity roundtrip, an inverted version of this resonator is concatenated at the long branch of the resonator. In this way, a symmetric 2-reflection unit is generated, having a short branch on both extremities. This design provides convenient beam injection and extraction. In order to realize an 8-reflection design, 4 of these units are concatenated. The waist propagation at the design focal strength is displayed with a black line, the red and blue propagation represent higher and weaker dioptric power of the thin disk ± 0.02 diopter, respectively.

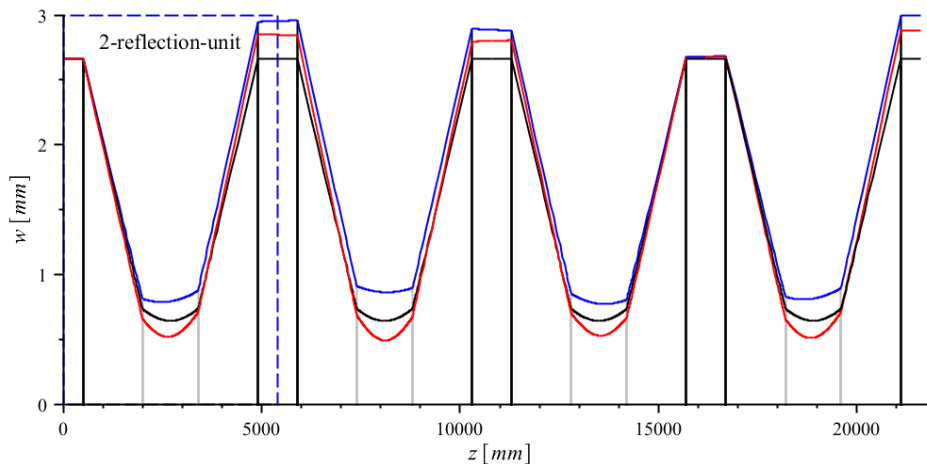


Figure 91: Beam propagation in the amplifier resulting from a concatenation of 8 optical segments equivalent to the resonator given in Figure 90.

7.3. Comparison to other concepts

Our propagation layout is similar to a regenerative amplifier [220, 221], as the pulse performs a limited number of roundtrips within the resonator. Within the multi-pass amplifier, each roundtrip has a dedicated beam path, resulting in a higher damage threshold at the cost of higher complexity of the propagation (larger number of optical elements). A multi-pass thin-disk amplifier provides amplification of pulse of arbitrary length (from ms to fs) and particularly, operation in burst mode [222].

Our design strongly differs from the 4f propagation most frequently used [223, 224]. The 4f propagation is usually used to image the beam at the active medium position from one path to the next one. However, the active medium (thin disk) produces amplitude and phase distortion of the beam. Due to the imaging properties of the 4f propagation, these distortions are accumulated 8 times at the same position. Hence, these deviations are adding up at each pass leading to a strong optical-phase distortion (OPD), and soft-aperture effects (see Figure 92) [225].

The collimated beam propagation used in several multi-pass designs [222, 226, 227, 228] can be seen as a special solution for the concatenation of nearly plane-parallel resonator. On the one hand, such propagation is very sensitive to thermal lens (see Figure 92 (left)) and pointing instabilities, while on the other hand the propagation has the potential to be very short even for large beam waists.

Waist and OPD of the output beam for different propagation layouts versus variations of the thermal lens are given in Figure 92, for beam waist of 2.66 mm at the position of the thin disk and 8 passes. The output beam characteristics of our multi-pass amplifier are insensitive to thermal lens variations over a range of 0.06 diopters, as visible in both plots. The 4f configuration shows a stable but reduced output beam waist (due to soft aperture), while the phase front curvature changes strongly with the thermal lens. The plane-parallel design is unstable in terms of both beam waist and OPD.

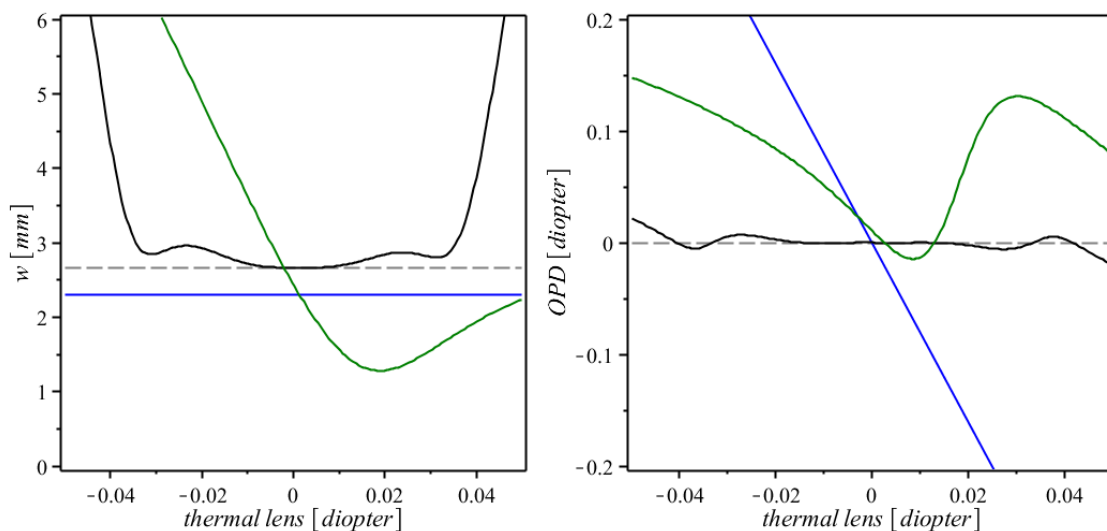


Figure 92: (Left) The exit-beam waist of the various amplifier concepts versus variation of the dioptric power of the thin disk. The dashed line represents the input beam. Our propagation (black), 4f propagation (blue) and the plane-parallel propagation (green). (Right) The corresponding plot for the phase front curvature.

The long-branch propagation between two passes at the thin disk acts as a Fourier transform. All higher-order disturbances are mapped into the beam halo. This halo is cut off on the next pass due to the soft aperture of the thin disk. The effect leads to an effective beam shaping as it takes place in a stable optical resonator. An amplifier designed for $M^2 = 1$ shows no degradation of beam quality.

The disk laser amplifier built for the measurement of muonic hydrogen [225] used soldered thin disks that produced higher diffraction artefacts. These effects reduced beam quality already in one pass. However, due to the beam-forming properties the beam quality stabilized at $M^2 = 1.4$. Similar effects are expected for glued thin disks at higher pumping power.

7.4. Realization of the multi-pass amplifier

The beam routing in the amplifier is realized using an array of mirrors as shown in Figure 93. An 8-reflection amplifier requires a 16-mirror array. The multi-pass propagation was designed to allow the use of the same end-mirrors (M1 and M2) for all passes, simplifying the layout. As all array mirrors are flat and only the radius of curvature and position of M1 and M2 have to be adapted to find the correct layout, cost and alignment effort are reduced.

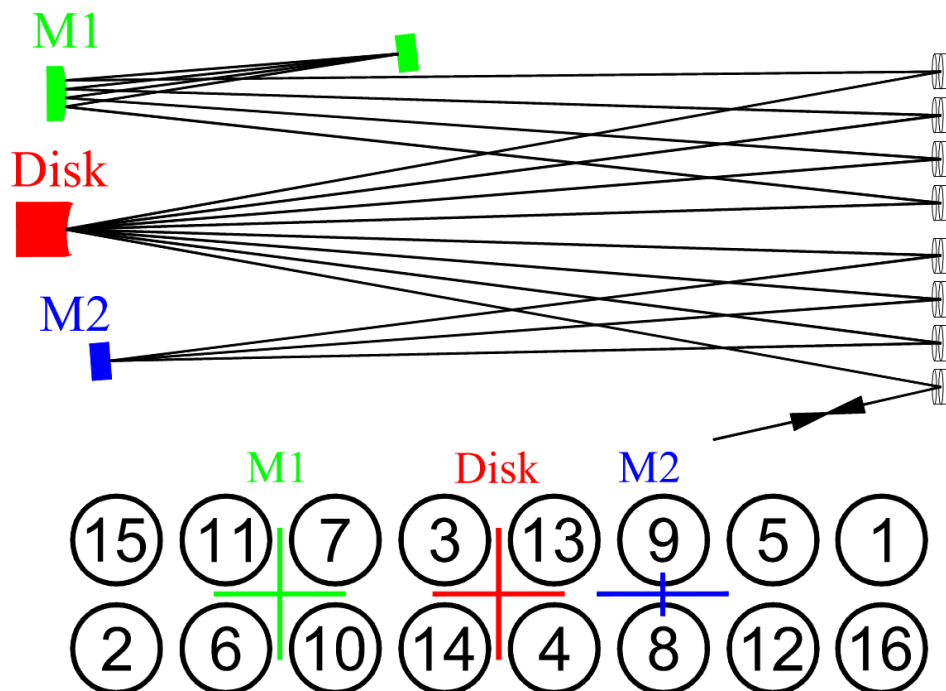


Figure 93: (Top) Scheme and propagation in the amplifier. (bottom) A front view on the mirror array, the mirrors A1 to A16 are numbered in the order of their use. The crosses mark the points where the axis of symmetry of mirrors and the thin disk hit the array plane. On the array plane, these points can be seen as point reflectors, leading to the given propagation. The beam entering the amplifier over the array mirror A1 is reflected on the thin disk to A2, from there over M1 to A3, over the thin disk to A4, over M2 to A5 and so on.

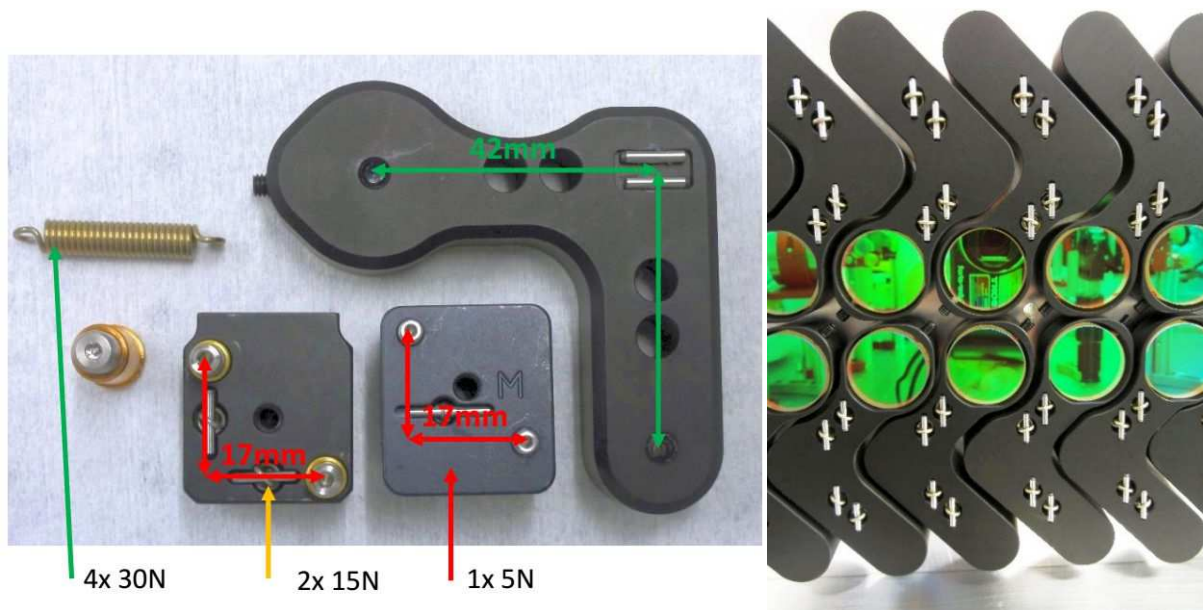


Figure 94: (left) L-shaped mirror mount compared to commercial solutions Newport 9771 and Thorlabs KSM mounts that provide similar mirror-to-mirror distance. (right) The mounted mirror array. The shape of the front plate was optimized for close placement. The interlaced array of L-shaped mirror mounts combines minimal placing of 31 mm and maximal stability. Figure 104:

In order to minimize the array size and, hence, the incident-angle related astigmatism, and at the same time maximize alignment stability of the individual mirrors, we developed L-shaped mirror holders (see Figure 94). The design provides mirror-to-mirror distances similar to commercial 1" compact mount solutions but it provides an alignment that is more precise and superior stability compared to high precision mounts. This is the consequence of a longer lever (37.7 mm compared to 42.4 mm), strong springs (4 x 12 N) and precise adjustment screws (1/4"-100) mounted on a 25 mm thick aluminum plate.

7.5. Measurement of laser operation

The beam quality of the system is excellent: the M^2 value was measured to be 1.00 (3) for all passes using a Thorlabs Beam Profiler. An output energy of 145 mJ was observed. To avoid optical damage during the 2 years of data taking, the system was operated at an output energy of about 90 mJ.

Figure 95 shows the amplifier gain as a function of the output energy. Figure 96 gives the output energy as a function of input energy taken 145 days apart without realignment of the amplifier. The gain of the amplifier remained basically unchanged over weeks of continuous operation as well as 3 months of shutdown including the air condition with room temperatures reaching values well above 30°C and several cooling water shutdowns. The minimal difference of the two plots shows the long-term stability of the amplifier.

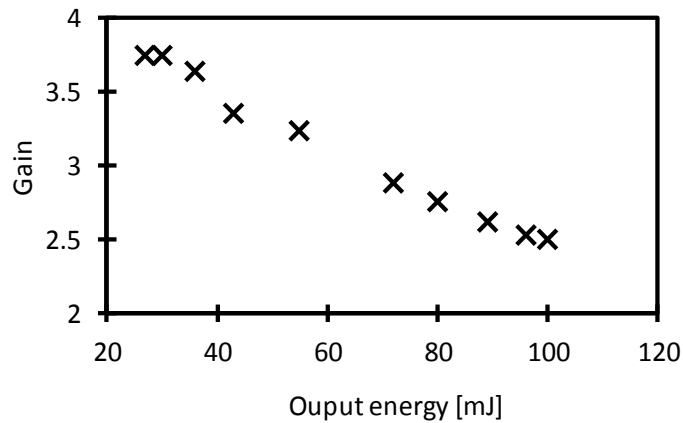


Figure 95: Amplifier gain versus output energy. The small signal gain is 5.1.

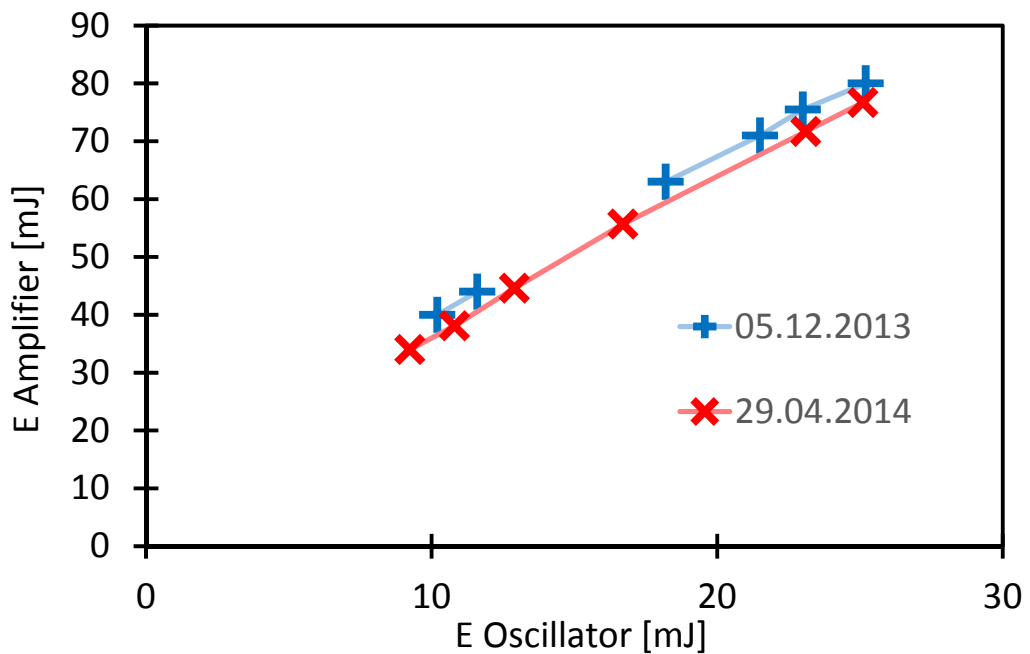


Figure 96: Output energy of the amplifier as a function of input energy.

7.6. Misalignment sensitivity

In this chapter, we present a theoretical study of misalignment and pointing instabilities for various multi-pass amplifiers. These results are then compared to measurements. Figure 97 is a misalignment plot, where the deviation of the beam from the optical axis is shown for a tilt of the in-coupled beam (blue) and for a tilt of the thin disk (red).

From the blue-line behavior, it can be inferred that the 2-reflection unit acts as Fourier transform optic. After 4 of these units the output beam has identical position and pointing to the input beam. A misalignment of the thin disk or of the end-mirrors compensates itself after 8 passes. Thus, excursion from the design position will be zero even if the input beam or the thin disk as tilted due to pointing fluctuations. In addition, the output beam angle after 8 passes is not affected by tilts of the thin disk.

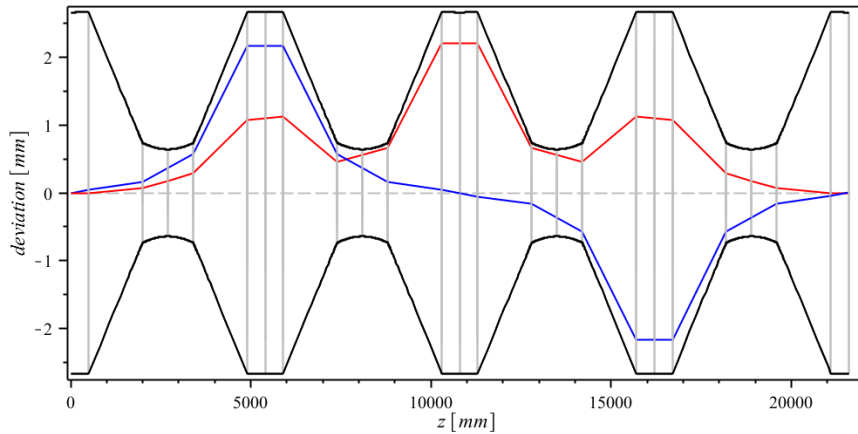


Figure 97: Misalignment plot. The deviation of the beam from the optical axis is indicated for a tilt of the in-coupled beam by 0.0025 mrad (blue) and for a tilt of the thin disk by 0.001 mrad (red). The width evolution of the Gaussian beam along the amplifier path is shown for comparison (black).

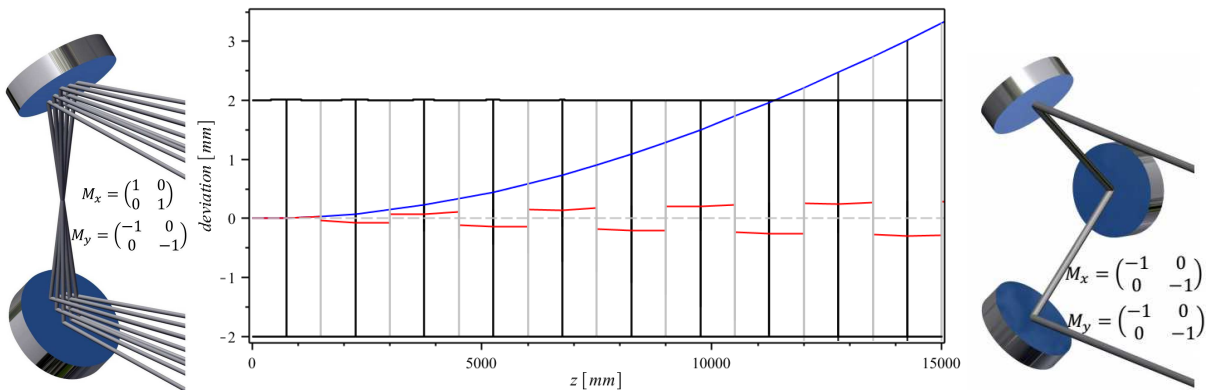


Figure 98: (Left) A pair of 45 ° mirrors used as M2 retro-reflector. M_x and M_y are the optical matrices describing the retro-reflection. (middle) Misalignment plot of the plane-parallel propagation used in [228]. Black vertical lines represent the positions of the thin disk. The thin disk has a misalignment of 0.025 m rad. The red line shows beam excursion at a plane end-mirror while the blue line represents the beam excursion if a pair of 45 ° mirrors is used. (right) Three-mirror corner-cube reflector. Using this reflector as M2 would provide stabilization in both directions.

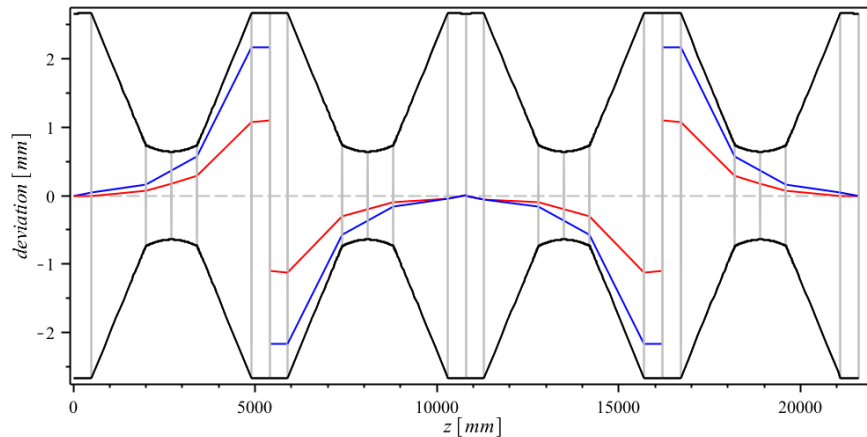


Figure 99: Misalignment plot of the modified version of our amplifier similar to Figure 97. Here M2 is replaced by a pair of mirrors as in Figure 98 (left).

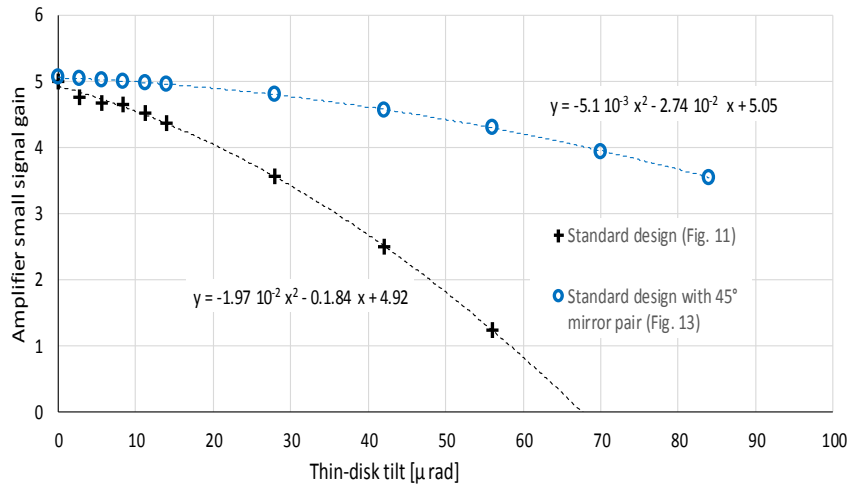


Figure 100: Amplifier gain versus thin disk tilt.

For comparison, we performed a simulation study for the multi-pass amplifier of [228] where an end-mirror was replaced by a pair of 45° mirrors. This retro-reflection is causing an inversion of angle and excursion in the yz -plane while the propagation in the xz -plane stays unaffected. This vertical retro-reflector significantly increases the pointing stability in vertical direction, especially for the nearly plane parallel setup of Figure 98 (middle). The use of a corner-cube reflector with 3 mirrors applied at an angle of 54° (Figure 98 (right)) would provide the same increase in stability for both directions (vertical and horizontal).

In order to determine the misalignment stability we conducted measurements at small signal operation. We used well-defined forces to realize controlled pitch misalignments of the thin disk. Tilts of $5.7 \mu\text{rad} / \text{N}$ have been measured.

As visible from Figure 100, the decrease of gain versus tilting shows a quadratic dependency. The value of the quadratic term is reproducible for different alignments. The quadratic term of the propagation using a 45° mirror pair is 4 times smaller than the value of our standard design corresponding to a misalignment sensitivity that is by a factor of two lower, as expected (see Figure 99).

7.7. Summary

We have developed a multi-pass amplifier with small sensitivity to thermal lens and pointing fluctuations. This amplifier has been used for months without the need for realignment. The introduction of a retro-reflector in the multi-pass amplifier reduced the effect of thin disk tilt by a factor of 4.

8. Multi-pass oscillator layout for high-energy mode-locked thin-disk lasers⁵

A novel optical layout for a multi-pass resonator is presented that paves the way for pulse energy scaling of mode-locked thin-disk lasers. The multi-pass resonator we are proposing consists of a concatenation of nearly identical optical segments. Each segment corresponds to a roundtrip in an optically stable cavity containing an active medium exhibiting soft aperture effects. This scheme is apt for energy and power scaling because the stability region of this multi-pass resonator, contrarily to the 4f-based schemes, does not shrink with the number of passes. Simulation of the eigenmode of this multi-segment resonator requires considering the aperture effects. This has been achieved by implementing effective Gaussian apertures in the ABCD-matrix formalism as lenses with imaginary focal length. We conclude by proposing a simple way to double the stability region of the state-of-the-art layouts used in industry achievable by minimal rearrangement of the optical components used.

8.1. Motivation

Ultra-short laser pulse sources [229, 230] enable a large variety of fundamental physics investigations to be performed, as well as technological and industrial applications. Many applications in industry and strong-field physics will tremendously benefit from an increase of the pulse energy into the mJ range at few -MHz repetition rates [231]. This will provide increased production throughput and provide processing for materials where non-linear multi-photon absorption is required. Similarly, the high average power will reduce measurement times and increased signal to noise for high field experiments providing new scientific possibilities.

Mode-locked thin-disk lasers [98, 232] are widely used in research laboratories and in industry because of their power scaling and high pulse-energy capabilities [227, 233, 234, 235, 236, 237, 238, 239, 240, 115] [241, 242]. The output pulse energy E of a mode-locked thin-disk laser can be increased, at a given average output power P_{avg} , by reducing the laser repetition rate f_{rep} , given the simple relation $E = P_{avg} = f_{rep}$ from energy conservation. Smaller repetition rates can be achieved simply by increasing the oscillator cavity length. One successful way to increment the resonator length was found by inserting into the cavity a Herriott-cell [243, 244]. However, the elevated intra-cavity pulse energy achieved in this way required operation of the oscillator in an evacuated environment to avoid detrimental non-linear effects in air [244].

⁵ This chapter is a reprint of [52].

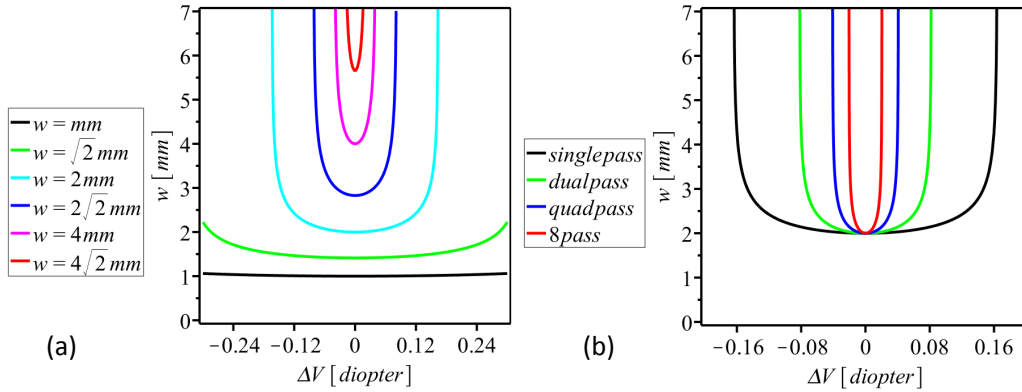


Figure 101: (a) The graph shows the stability plots for laser layouts with various beam waists on the thin disk in the center of stability. (b) The graph shows the stability plot for different 4f-based laser designs providing multiple passes on the thin disk. For both plots, a wavelength of 1030 nm was used. For a given eigenmode size, the stability plots do not depend on the specific layout of the resonator. Stability plots of multi-pass resonators based on 4f-imaging stages. Plotted are the cavity eigenmodes (TEM₀₀-mode) width w at the position of the thin disk for variations of the thermal lens thin disk from the layout value. The shrinking of the stability region with the number of passes per cavity roundtrip arising in 4f-based multi-pass resonators is demonstrated. We computed these diagrams using the ABCD-matrix formalism and by embedding the 4f stages at the position of the thin disk in the stable resonator. A wavelength of 1030 nm was used. For a given eigenmode size, the stability plots do not depend on the specific layout of the resonator.

The cavity length can be also increased by folding the laser beam on the active medium (thin disk) several times per roundtrip [234, 245]. The large gain per roundtrip attainable with such an active multi-pass cell enables large output coupling, which brings along a reduction of the intracavity power. Hence, this scheme providing a long cavity and decreased intra-cavity intensity is twofold advantageous and is qualified for industrial applications as it allows operation in air. Another important feature of a multi-pass resonator scheme is the reduction of Q-switching instabilities due to a linear decrease of the gain saturation fluence with the number of reflections at the thin disk [246, 247].

The multi-pass active cells realized to date [234, 245] are based on relay 4f imaging: 4f optical segments are used to image the thin disk from pass to pass so that the beam propagation in the active multi-pass cell proceeds following the scheme disk-4f-disk-4f-disk-4f The 4f propagation from the optical point of view corresponds to a zero effective length propagation and it does not provide stability for misalignment or variation of the focal strength of the thin disk. Hence, to realize a stable laser operation, the 4f multi-pass cell has to be embedded in a stable optical resonator [234]. The 4f multi-pass cell with N number of passes can be described as a single pass having a total optical length of $L_{\text{multi-pass}} = (N - 1)L$, a gain of $g_{\text{multi-pass}} = g^N$, and an active medium dioptric power of $V_{\text{multi-pass}} = N V$, where $L = 4 f$ represents the length of a single 4f-imaging stage, g the single-pass gain, and V the dioptric power of the thin disk. Due to these cumulative effects, the resonator stability zones [178] of an oscillator containing such a multi-pass 4f-based cell shrink linearly with the number of passes N as shown in Figure 101 for variations of the disk thermal lens [248]. This shrinking limits energy and power scaling [108]. In summary, the 4f-based multi-pass oscillators show a limited energy scaling (capitalizing only on the advantages related to the long cavity length and the reduction of the intracavity circulating intensity) but suffer from the shrinking of the stability region with the number of passes that reduces the maximally achievable output power. In this paper, a novel multi-pass resonator scheme is presented which overcomes the thermal-lens-related power and energy limitations of state-of-the-art multi-pass mode-locked laser oscillators. In Sec. 8.2, our multi-pass scheme is exposed whose stability regions do not shrink with the number of passes. This opens the

way for further energy and power scaling. A preliminary proof of principle of this new scheme is given in Sec. 8.3 while in Sec. 8.4 a design merging the to-date 4f-based industrial scheme with our scheme is presented.

8.2. New multi-pass resonator design

The multi-pass resonator we are proposing is based on a concatenation of identical (or nearly identical) segments. Each segment corresponds to a roundtrip in an optically stable resonator containing one pass (or more) on the same active medium, which exhibits soft-aperture effects.

Since the multi-pass oscillator is inheriting the eigenmode properties of the underlying segment, we design this segment to be stable and insensitive to thermal lens variations. An example of a stable resonator whose roundtrip propagation gives rise to a segment is shown in Figure 102. It is formed by a plane end-mirror M2, a thin disk acting as concave mirror, a convex mirror (Vex) and a flat end-mirror M1. The eigenmode width w evolution along this cavity is shown in Figure 103 (a). This cavity is widely used [178] because it provides an out-coupling mirror M2 with out-coupled beam waist (and divergence) insensitive to variations of the thermal lens of the thin disk as demonstrated by the blue continuous curve in Figure 103 (b) representing the eigenmode waist at the mirror M2 position for variations of the thermal lens of the thin disk. For comparison the beam waist at the other end-mirror M1 that features a larger dependency on the thermal lens variation is given as well (green dashed curve). This resonator layout is extensively used also because it allows for simple adjustments of the mode properties: the distance between thin disk and the convex mirror can be adapted to shift the stability region of the cavity, while the beam waist in the center of the stability region can be adjusted by adapting the distance between the M1 and the convex mirrors.

As already mentioned, the multi-pass resonator according to our scheme is obtained by concatenating multiple times the same optically stable segment: each segment corresponding to roundtrip propagation in a stable cavity. An example of such a concatenation is shown in Figure 104 where 8 segments based on the cavity shown in Figure 102 allow 16 reflections at the thin disk per roundtrip. The stability regions of this multi-pass resonator coincide with the stability regions of a single segment (given in Figure 103 (a)) provided all segments are identical. However, small differences between segments are unavoidable when practically realizing a multi-segment oscillator because of small variations of propagation lengths, incident angles and mirror curvatures.

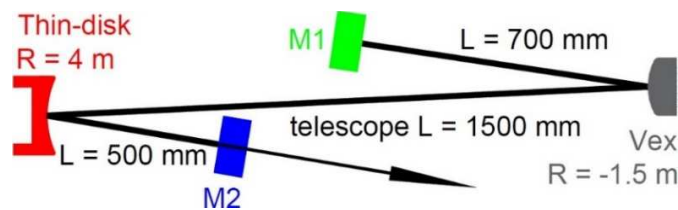


Figure 102: Standard thin-disk laser resonator layout given by a flat end-mirror M1, a convex mirror, a concave thin disk (red) and a flat end-mirror M2.

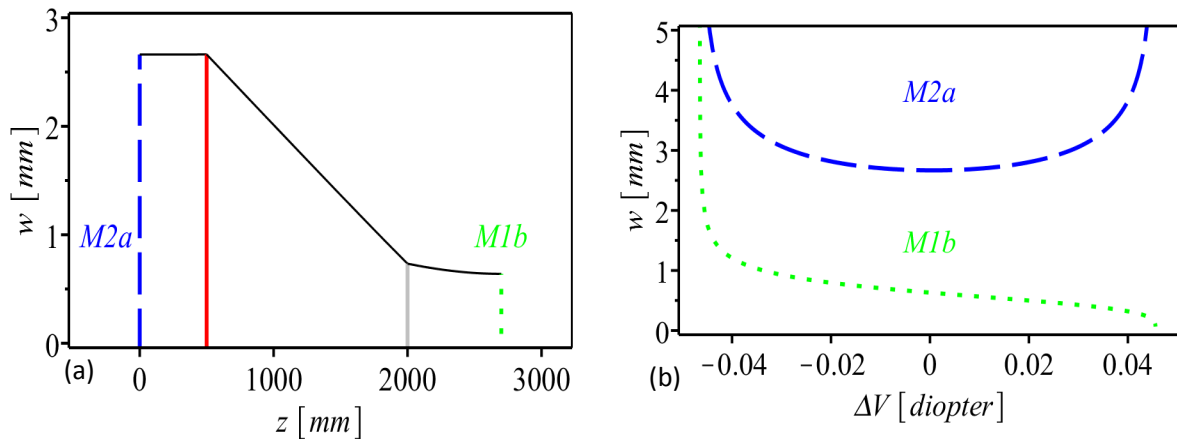


Figure 103: The classic stable cavity our oscillator and amplifier are based on. In a cavity roundtrip, the beam is reflected on the thin disk two times. In the scheme we want to introduce, this cavity is described as a single segment two-reflection cavity.

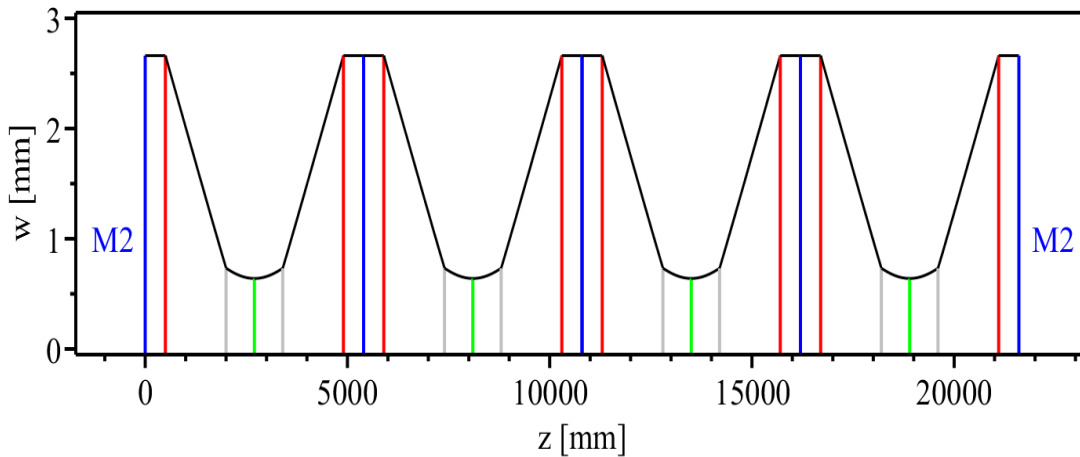


Figure 104: The 8-segment 16-reflection cavity based on the cavity given above. A laser design that was realized by introducing end-mirrors to our amplifier.

consideration of these segment-to-segment asymmetries is essential for the understanding of the new multi-pass resonator concept proposed here. In fact, the thin-disk laser community has discarded this design because apparently these asymmetries prompt the formation of gaps in the stability region. The gap size depends on the extent of the segment-to-segment asymmetry. The formation of these gaps as a consequence of small segment-to-segment differences is exemplified in Figure 105 for the particularly simple case that the multi-pass resonator is composed of only two segments. In the two-segment case, the gap arises in the center of the stability region. Similarly, for a multi-pass oscillator with several segments and various segment-to-segment deviations, a multitude of disruptions would apparently fragment and reduce the original stability region (of the single segment). It thus seems that the segment-to-segment asymmetries would undermine the usefulness of this scheme.

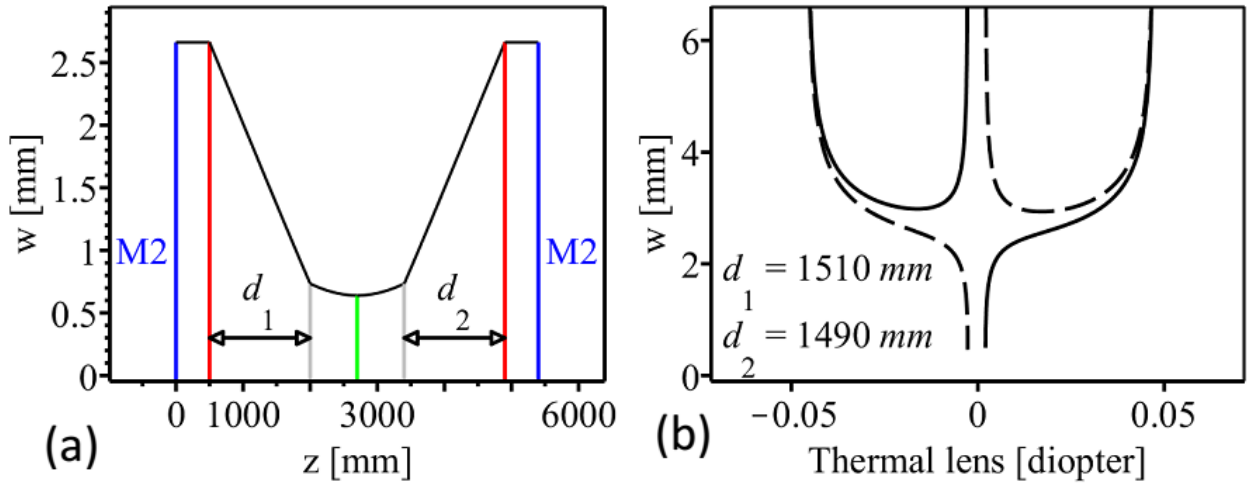


Figure 105: (a) Optical layout and eigenmode waist w of a two-segment resonator with 4 reflections at the thin disk per roundtrip. (b) Corresponding stability plot. Plotted is the eigenmode waist w at the two end-mirror positions M2 for variations of the thermal lens of the thin disk from the layout value. A small asymmetry has been introduced ($d_1 \neq d_2$) between the two segments which induces a discontinuity at the center of the stability region (cf. with Figure 103(b)).

The stability plots shown in Figure 101 - 114 have been computed using the ABCD-matrix formalism. This formalism is a powerful instrument to compute eigenmode and stability regions of resonators. However, as already noted in [249], it is mostly used for computing bare resonators neglecting the effect of the transversely varying gain in the active material. Aperture effects which naturally occur in a pumped active medium mainly due to gain (absorption) in the pumped (unpumped) regions and related diffraction (mainly outside the pumped spot) may significantly affect the eigenmode and stability properties of the resonator [250]. These effects can be described approximately by a Gaussian aperture at the active medium and included into the ABCD-matrix formalism as imaginary lens [177, 170, 251, 252]. The ABCD-matrix describing the thin disk can be thus written as

$$M_{thin-disk} = \begin{bmatrix} 1 & 0 \\ -\frac{1}{f} - i\frac{\lambda}{\pi W^2} & 1 \end{bmatrix} \quad (126)$$

where W represents the effective waist of the Gaussian aperture, λ the laser wavelength and f the focal length of the thin disk that also includes thermal lens effects.

Standard resonator designs do not include soft aperture effects because for a single-segment resonator (see Figure 106 (a)), the inclusion of aperture effects does not considerably alter the computed value of the eigenmode size for thermal lens variations of the thin disk within the “original” (computed without considering the soft aperture effect) stability region (see Figure 106 (b)). For dioptric power outside the “original” stability range, the inclusion of aperture effects results in eigenmodes with finite waist that implies an extension of the stability region [249, 253]. Therefore, the inclusion of aperture effects shows that in principle laser operation may occur also outside the “original” stability region. Yet this extension has no practical relevance because outside the “original” stability range the roundtrip losses caused by the aperture are increasing dramatically as demonstrated in Figure 106 (c) and [249, 254].

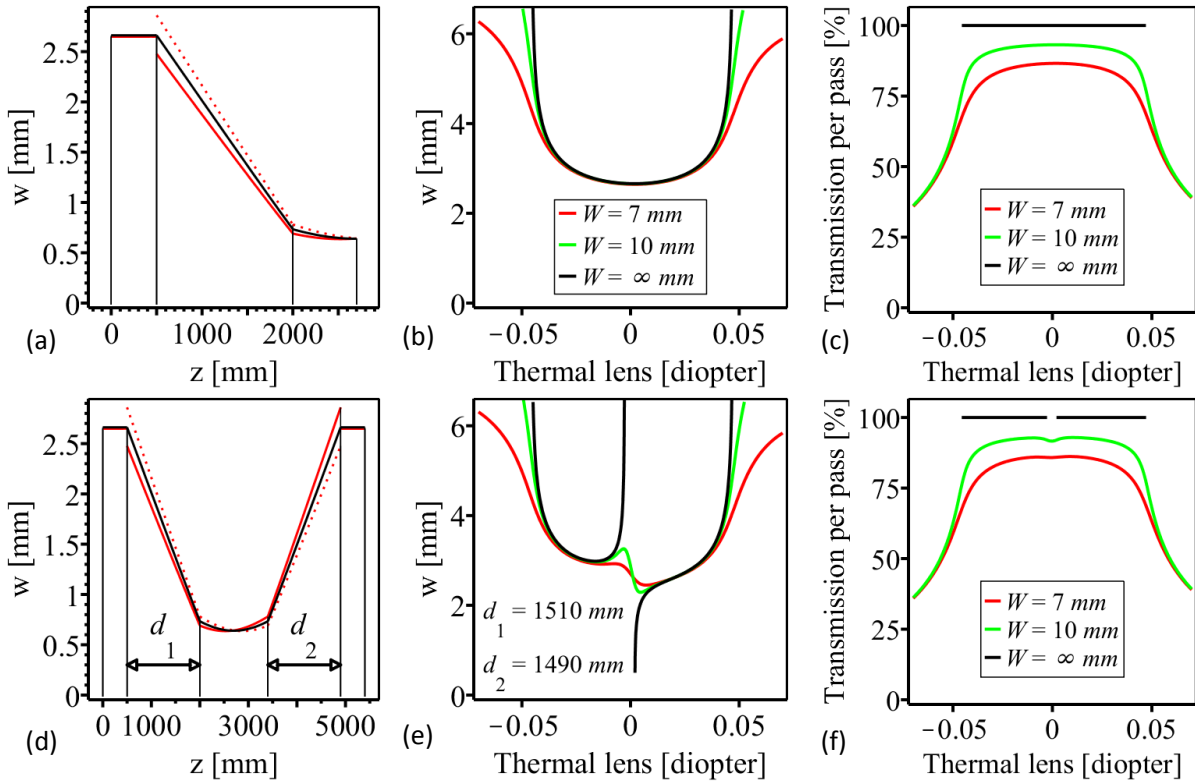


Figure 106: Influence of a Gaussian aperture at the active medium on the properties of single-segment (top row) and multi-segment (bottom row) resonators. (a) Optical layout and eigenmode waist w evolution of a single-segment resonator. The black curve has been computed without aperture effects. The two red curves represent the back (dotted) and forth (continuous) propagation when aperture effects are included. (b) Corresponding stability plot. Plotted is the waist at the left end-mirror position for variations of the thermal lens of the thin disk without aperture effects (black) and for two aperture waists W (green and red). (c) Average (over a roundtrip) transmission of the eigenmode through the Gaussian aperture for variations of the thermal lens. For an infinite sized aperture, the transmission (defined only within the stability region) is 100%. (d) Similar to (a) but for a two-segment resonator. (e) Similar to (b) but for a two-segment resonator where a small asymmetry between the two segments has been introduced. The aperture effects damp the instability and close the gap in the stability region. (f) Similar to (c) for the two-segment resonator with the above-specified small asymmetry. The increase of losses at the original gap position is minimal. All the curves have been computed using the ABCD-matrix formalism allowing for lenses with complex values.

Contrarily, aperture effects need to be included in the simulations of multi-segment resonators (e.g. Figure 106 (d)) having small segment-to-segment deviations. Simulating multi-segment resonators with small segment-to-segment deviations without accounting for soft aperture effects produces wrong results because it predicts the formation of gaps within the stability region that does not occur in reality. The inclusion of these soft apertures in the simulations suppresses these gaps as shown in Figure 106 (e) for the particular case of a two-segment resonator and leaves small residual fluctuations of the eigenmode waist. Hence, it is essential to compute the stability properties of the multi-pass resonator including soft aperture effects. However, it is important to stress that the general behavior of the stability regions does not critically depend on the exact value of the assumed aperture waist W as can be deduced by comparing the green with the red curves of Figure 106 (e).

In addition, the aperture-related losses per pass (averaged over a roundtrip) confirm that when including soft-aperture effects the multi-segment resonator with small asymmetries behaves similarly to the single-segment resonator. The residual waist fluctuations arising from the suppression of the gap give rise to a

negligible increase of losses per pass compared with the single-segment case as visible by comparing Figure 106 (f) with Figure 106 (c).

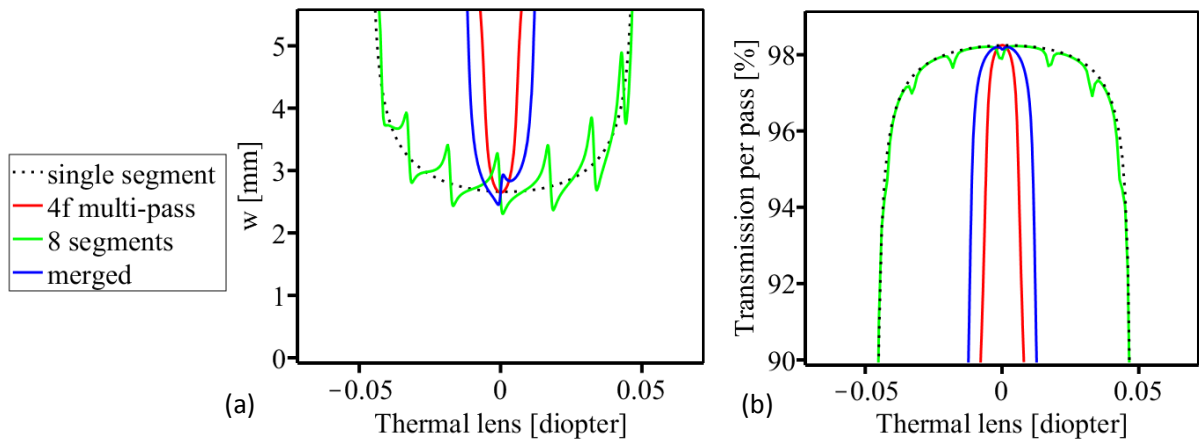


Figure 107: (a) Stability properties of three multi-pass resonator designs having same eigenmode waist w , 16 reflections (per roundtrip) at the active medium and a gain medium with a Gaussian aperture of $W = 20$ mm. The black dotted curve (1 segment containing two passes) represents the stability plot of the single-segment resonator of Figure 103(a). It serves as reference. The green curve (8 segments, each containing 2 passes) represents our design as a succession of nearly identical segments as given in Figure 104. The fluctuations arise from a small segment-to-segment asymmetry: the distance of disk to convex mirror in the first segment has been assumed to be 1518 mm i.e., 20 mm longer than in the other segments. Besides these fluctuations, the stability plot of the multi-segment resonator is identical to the stability plot of the single-segment resonator. The red curve (1 segment containing 16 passes) represents the stability plot for a 4f-based multi-pass resonator. Its stability region is 8 times smaller than the reference because it shrinks with the number of passes. The blue curve (2 segments, each containing 8 passes) represents a merged resonator concept (see Sec. 8.4) having two segments containing 4f-imaging stages. (b) Corresponding average (over a roundtrip) transmission through the Gaussian aperture at the thin disk for variations of the thermal lens of the thin disk.

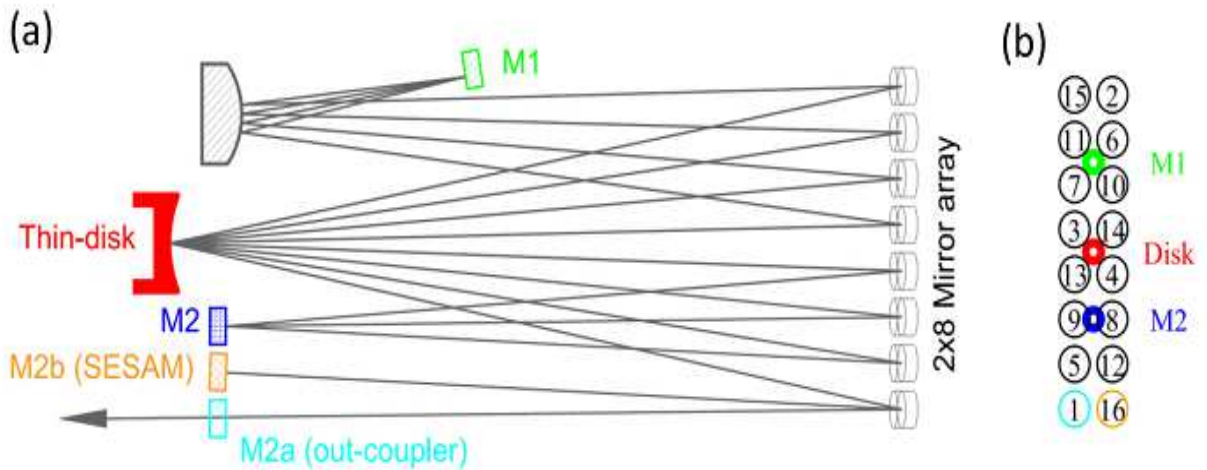


Figure 108 (a): Possible realization of a multi-pass oscillator with 16 reflections at the thin disk per roundtrip achieved by concatenating 8 identical segments. The beam routing requires a mirror array of 16 flat mirrors that can be adjusted individually. The two end-mirrors M2a and M2b could be used as out-coupler and as SESAM. (b) Mirror-array working principle. The beam routing at the mirror-array plane follows the given numbering and is achieved by successive reflections at the thin disk, mirror M1 and mirror(s) M2. The projection of these elements are indicated.

This behavior can be generalized to many segments: the stability region, mode waist and losses per pass (averaged over a roundtrip) for the 8-segment multi-pass resonator of Figure 104 with small segment-to-segment deviations turn out to be practically identical with the stability region, the mode waist and losses per pass of the underlying segment as demonstrated in Figure 107 (compare green solid with dashed black curves). The same figure for comparison also shows the smaller stability range featured by the multi-pass resonator based on 4f-imaging stages having the same number of passes and beam size at the active medium.

In summary, the soft aperture effects occurring naturally in the pumped active medium grant the realization of a multi-pass oscillator as a concatenation of several nearly identical optical segments. When considering aperture effects, the stability region and losses per pass of our multi-segment resonator are virtually identical to the stability region of the single-segment resonator. Therefore, contrarily to the 4f-based multi-pass resonator, the stability region of our multi-pass resonator does not shrink with the number of passes.

8.3. Proof of principle

For a proof of principle, we transformed the multi-pass amplifier [54, 117] that we developed for spectroscopy of muonic atoms [1, 2] into a multi-pass oscillator by adding two end-mirrors. This design schematically depicted in Figure 108 fulfills our requirements of sufficiently small segment-to-segment variations as it uses the same thin disk and the same convex mirror in all segments. Moreover, the mirror array that is used to fold the beam providing several passes on the same thin disk also guarantees similar path lengths and small incident angles.

The beam routing in this multi-pass oscillator obeys the following scheme. Starting from the out-coupler M2a the beam is reflected at the array-mirror 1 towards the thin disk. From here, it proceeds towards the array-mirror 2 and the convex mirror until it reaches M1. From M1 the beam travels back to the array at array-mirror 3, then to the thin disk and the array-mirror 4 until it reaches mirror M2. This scheme is iterated until the beam passes the array-mirror 16 and is back-reflected at the second end-mirror M2b. From here the beam propagates the same path backwards until it reaches again mirror M2a closing the roundtrip. The beam routing at the mirror-array position given by the numbering as shown in Figure 108 (b) can thus be understood as alternating point reflections at the thin disk, M1 and M2 mirror projections.

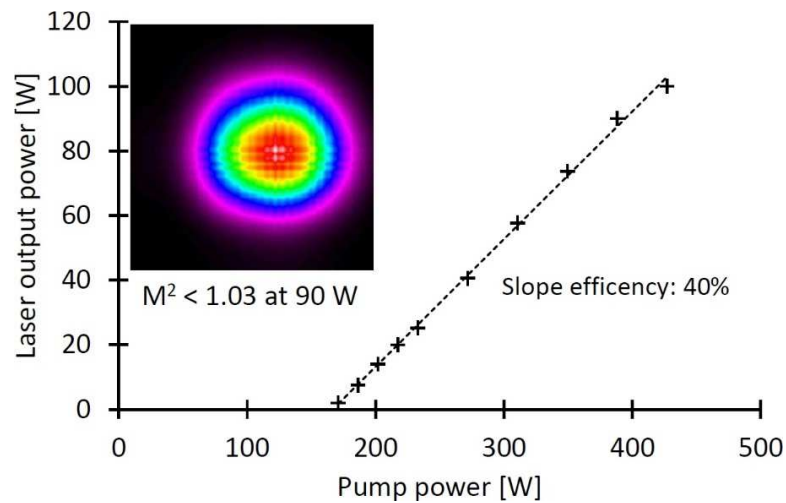


Figure 109: Input-output characteristics of the multi-pass resonator based on our design with 16 reflections per roundtrip. The measurements have been accomplished in a cw operation for a thin disk with a Yb:YAG crystal with a thickness of 345 μm , a 940 nm pump wavelength and an out-coupling mirror reflectivity of 50%. The inset shows the measured output beam.

The multi-pass oscillator (with 16 reflections at the thin disk per roundtrip) whose underlying segment specifications are given in Figure 102 has been tested in cw mode using a flat out-coupler with 50% transmission. As an active medium, a thin disk with a thickness of 345 μm made from Yb:YAG with 5% nominal doping concentration contacted by TRUMPF to a water-cooled CVD-diamond heat sink having a 4 m radius of curvature has been used. Even though the choice of the parameters of the thin disk was optimized for low repetition rate Q-switched operation, encouraging output powers and slope efficiency (40 % in TEM00 mode operation) have been observed as shown in Figure 109. This represents the first preliminary demonstration of the applicability of our multi-pass oscillator concept, in particular showing that the soft aperture effects naturally present in the pumped active medium are sufficient to suppress the instabilities related to the various segment-to-segment asymmetries associated with the practical realization of a multi-pass scheme.

8.4. A simple way to improve the multi-pass resonator based on 4f imaging

The multi-pass oscillators based on 4f-imaging stages show enhanced sensitivity to thermal lens effects as illustrated by the shrinking of the stability region with the number of passes in Figure 101. However, a major advantage of the 4f scheme is that a sequence of several 4f-imaging stages can be realized using only few optical elements as shown in Figure 110 (a) whose working principle is detailed in [53, 255, 256].

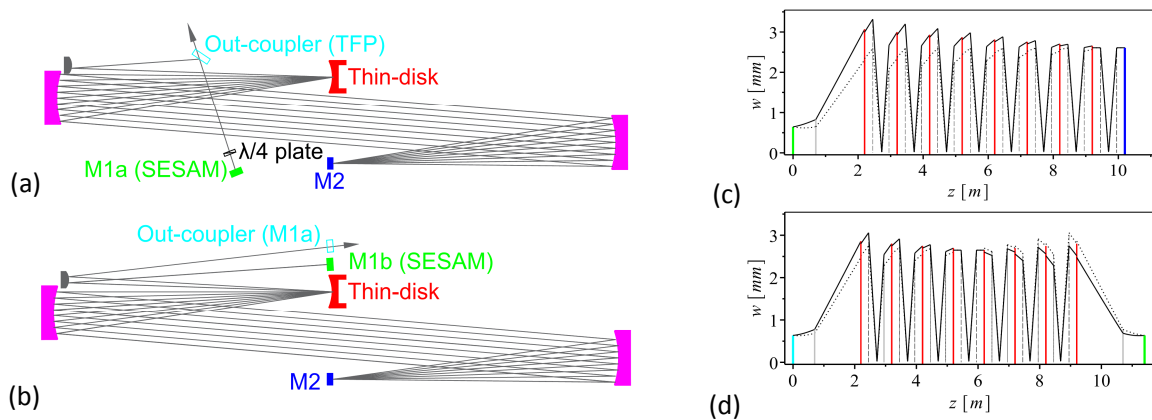


Figure 110: (a) Multi-pass oscillator based on 4f-imaging stages. Multiple 4f-imaging stages can be implemented using the same optical elements that simplifies the mechanical realization and decreases the production costs. TFP: thin-film polarizer. (c) Corresponding eigenmode waist evolution. Due to soft aperture effects the back (dotted line) and forth (continuous line) propagations have different waists. The vertical red lines represent the position of the thin disk. (b) Schematic of the merged concept with two segments, each containing half the number of reflections on the thin disk as in (a). (d) Corresponding eigenmode waist evolution.

On the other hand, our multi-pass oscillator concept has a superior stability for variations of the thermal lens, but it requires an array of mirrors resulting in increased mechanical complexity.

In Figure 110 (b), we present an optical layout that results from merging the two concepts. It consists of a concatenation of two optically stable segments (according to our scheme) each containing a multi-pass sequence based on 4f-imaging stages. As this merging can be achieved by a simple rearrangement of the optics used in the 4f-based system, it inherits a similar beam waist evolution (see Figure 110 (b) and (d)) and its simplicity, qualifying this scheme for industrial applications. At the same time, this merged layout shows improved stability because the stability region of our concept does not shrink with the number of segments. The resulting stability region of this merged scheme (two segments, each containing $N = 2$ 4f-propagations) is by a factor of two larger compared to the standard 4f-schemes (one segment with N 4f-propagations) as visible from the comparison of the blue and red curves in Figure 107, provided both multi-pass resonators have the same number of passes. Thus, with a simple rearrangement of the beam-path structure of the standard 4f design (but using the same optical elements) a by a factor of two larger stability region can be obtained opening the way to higher pump power density, beam waists and number of passes.

8.5. Conclusions

We have presented a multi-pass resonator scheme as a sequence of nearly identical optically stable segments, each segment containing the same active medium featuring soft-aperture effects. The stability region of such a multi-segment resonator does not decrease with the number of segments. Therefore, this concept solves the limitations of state-of-the-art multi-pass resonators based on 4f-imaging stages that feature a shrinking of the stability region with the number of passes on the active medium.

We have demonstrated that it is essential to include the soft aperture effects occurring in the active medium in the simulations. They suppress the formation of gaps within the stability region that would arise as a consequence of small segment-to-segment asymmetries associated with the practical realization of a multi-pass system. This has been achieved by implementing effective Gaussian apertures in the ABCD-matrix formalism as lenses with imaginary focal length.

The multi-pass resonator concept presented here requires small segment-to-segment asymmetries achievable using the same active medium in all passes. Larger segment-to-segment deviations would cause increased losses (decreased transmission through the aperture) which strongly reduce laser efficiency or even disrupt laser operation.

This multi-pass resonator layout is particularly suited for ultrafast lasers where the mode-locking mechanism is based on SESAM technologies [12]. The SESAM could be placed at the position of one of the resonator end-mirrors (e.g. mirror M2b in Figure 108) as at this position there is minimal intracavity intensity and the SESAM mirror would be intersected only once per roundtrip. This scheme having several passes on the active medium and large cavity lengths paves the way for energy and power scaling of mode-locked lasers expanding greatly the range of applications for ultrashort pulses delivered directly by a laser oscillator.

9. Thin-disk laser scaling limit due to thermal-lens induced misalignment instability⁶

We present a fundamental obstacle in power scaling of thin-disk lasers related with self-driven growth of misalignment due to thermal-lens effects. This self-driven growth arises from the changes of the optical phase difference at the disk caused by the excursion of the laser eigenmode from the optical axis. We found a criterion based on a simplified model of this phenomenon that can be applied to design laser resonators insensitive to this effect. Moreover, we propose several resonator architectures that are not affected by this effect.

9.1. Motivation

Thin-disk lasers (TDL) are well known for their power scalability that relates to the active medium geometry and its cooling technique [98, 99, 100]. The laser crystal is shaped as a thin disk with a diameter of typically several mm (depending on the output power/energy) and a thickness of 100 μm to 400 μm , depending on the laser active material, the doping concentration, the operation mode and the pump design. The backside of the disk is coated with dielectric layers acting as high reflector (HR) for the laser and the pump light, and it is contacted to a water-cooled heat sink [257] as shown in Figure 111.

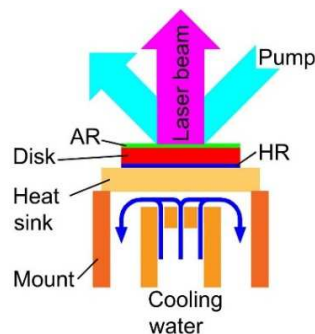


Figure 111: Scheme of the assembly of thin disk and heat sink (not to scale). The disk is thermally coupled to a water-cooled heat sink. Cooling and temperature gradients occur along the disk axis that corresponds to the laser axis. The back and the front sides of the disk are coated with a high reflective (HR) and an anti-reflex (AR) layer, respectively for both pump and laser wavelengths.

⁶ This chapter is a reprint of [51].

As cooling occurs along the symmetry axis of the thin disk and pumping in quasi-end-pumped configuration, the heat flow in the thin disk points along the disk axis which is also the laser axis [98, 162]. The temperature gradients inside the laser crystal are thus mainly parallel to the laser beam axis while in radial direction the temperature within the homogeneously pumped central area is nearly uniform. Thermal lens effects are thus strongly suppressed in TDL because of the efficient cooling (large surface to volume ratio) and the small temperature gradients in radial direction. Another consequence of the geometry of disk and heat sink is that the temperature in the pumped region and therefore the thermal lens depend only on the pump power density (assuming pump diameters larger than few times the disk thickness). This is one of the fundamental properties underlying the power scalability of TDL. However, power (energy) scaling calls for an increase of the beam waist resulting in an increased sensitivity to the residual thermal lens effects that eventually limits the achievable scaling [117, 102, 235, 236, 238, 248, 115]. When designing high-power (energy) lasers therefore it is essential to consider the stability properties of the resonator for variations of the disk thermal lens [102, 145]. These are usually represented in the form of so called “stability plots” [178] where the eigenmode size at an optical element in the resonator is plotted for variations of the disk dioptric power V .

The thermal-lens effect at the disk can be described using the position-dependent optical phase difference $OPD(x,y)$ experienced by the laser beam when reflecting on the disk. The outgoing (after reflection) laser field amplitude E_{out} is given by

$$E_{out}(x,y) = E_{in}(x,y) g(x,y) e^{-i\frac{2\pi}{\lambda}OPD(x,y)} \quad (127)$$

where E_{in} is the in-going (before reflection) laser field amplitude, $g(x,y)$ the space-resolved gain and λ the laser wavelength. A mathematically rigorous representation of the OPD can be accomplished using Zernike polynomials [258]. Simplifying, here we represent the one-dimensional OPD as a Taylor series

$$OPD(x) = a + bx + cx^2 + \dots \quad (128)$$

Standard resonator designs implicitly assume an OPD of the form $OPD = cx^2$, so that the disk can be described by a lens with a focal length of $f = 1/(2c)$. The linear term bx is normally ignored because it

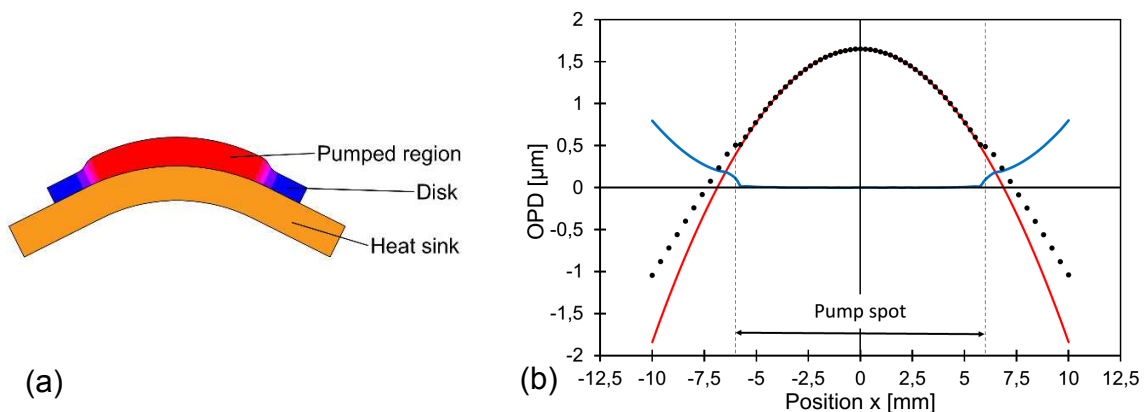


Figure 112: (a) Scheme (not to scale) of the bending of the assembly of thin disk and heat sink due to the axial temperature gradient. The “step-like” profile in laser direction is induced by the thermal expansion related to the warmer temperature within the pumped region compared with the unpumped region. (b) The dots represent the optical phase difference (OPD) at the disk computed with FEM methods for the parameters as detailed in the Appendix. Only the OPD caused by the pump process (fluorescence operation) is included here. The red curve is a parabolic function fitted to the data in the central region $x \in [-3;3]$ mm. The solid blue line gives the residual between the fit and the points.

simply describes the tilt of a flat optical component that is implicitly accounted for in the alignment process of the laser resonator. Similarly, the constant term a produces a global phase shift which corresponds to a change of the effective length of the resonator. The dots represent higher-order contributions that have been widely discussed in the literature [117, 235, 101] as they cause beam distortion and increased losses.

In this paper, we consider in more detail the interplay between the laser beam position at the active medium and the linear term bx . As detailed later, a laser beam impinging on the disk with a given deviation (excursion) from the disk-pumped-area axis induces a linear term bx in the OPD, i.e., a tilt of the disk. This tilt causes a resonator response that further modifies the position of the laser eigenmode at the disk. For certain resonator layouts a positive feedback between tilt and laser beam position may exist which leads to a continuous growth of the eigenmode excursion at the disk resulting in a disruption of the laser operation. For other resonator configurations, this interplay only leads to a finite increase of the initial excursion implying a reduced misalignment stability. A parameter will be defined to easily identify resonator designs unstable with respect to this effect, whose importance increases with the laser power.

9.2. Thermal lens at the disk

The rear side of the disk being at lower temperature expands (in radial direction) less than the front side causing a bending of the assembly of thin disk and heat sink as shown in Figure 112(a). We simulated OPD using finite element methods (FEM) to account for the bending of the dielectric mirror (HR) at the backside of the disk caused by this inhomogeneous radial expansion. These simulations also account for the thermal expansion of the disk in the laser direction and the variation of the disk refractive index versus temperature dn/dT .

A typical OPD simulation that includes all these effects computed using FEM as detailed in the Appendix is given in Figure 112(b). Within the homogeneously pumped area, the OPD can be well approximated by a parabolic profile, while at the periphery of the pumped region the OPD shows a deviation from the quadratic behavior that is responsible for the excitation of higher-order beam components.

The OPD of Figure 112 (b) considers pump effects but neglects thermal changes related to the laser operation. Indeed, laser operation reduces the heat deposition in the active material as it increases the radiative deexcitation of the upper laser levels at the expense of non-radiative processes [146, 147]. Other mechanisms as a change of the effective quantum defect between laser and fluorescence operation also contribute to this effect. The model we will display in the following sections uses the effective change of the thermal lens caused by the laser operation independently of its origin.

Figure 3 (a) shows the same FEM calculation as displayed in Figure 112(b) but now also taking into account the reduction of the thermal load by a factor of two [146, 147, 148] due to laser operation. In this FEM computation the laser beam (resonator eigenmode), the disk and the pumped area have a common axis. Within the laser eigenmode (which is smaller than the pumped area), the OPD shows a quadratic behavior.

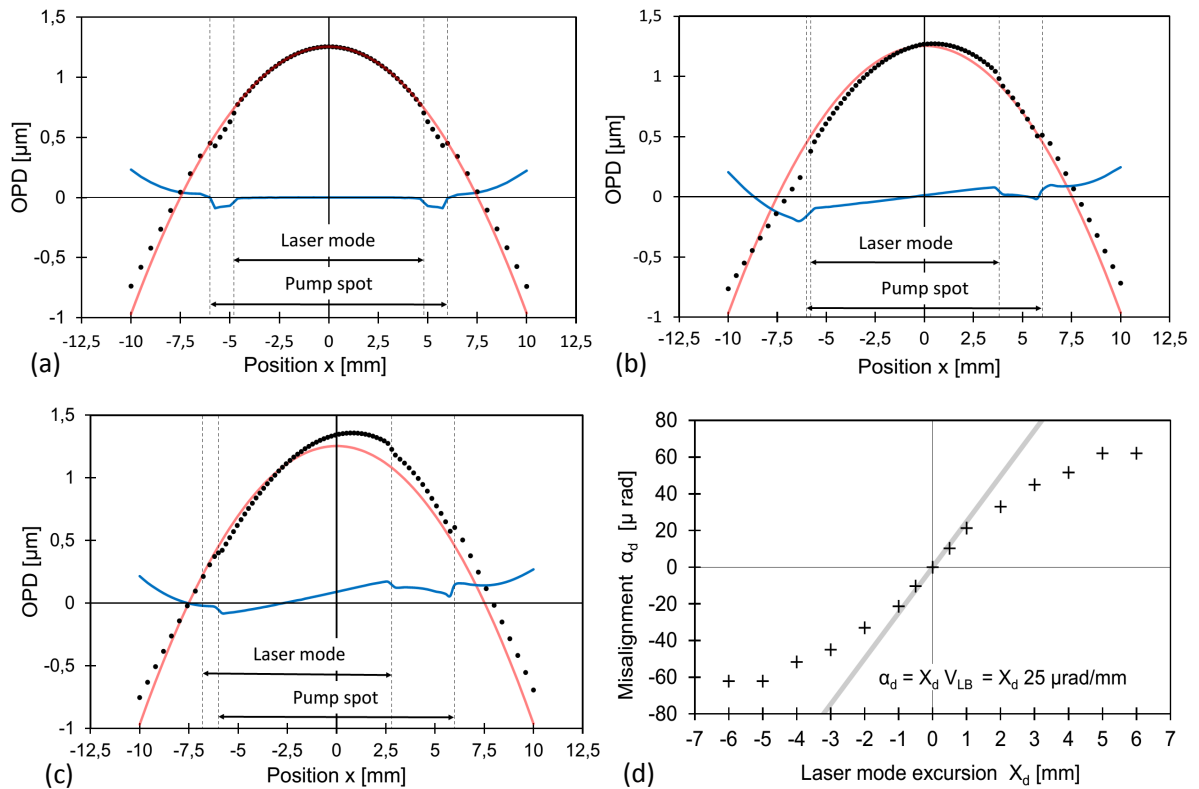


Figure 113: (a) The black points represent the one-dimensional optical phase difference (OPD) for a beam reflection at the disk computed with FEM methods as detailed in the Appendix. The pump and the laser beam share the same axis. The red curve is a parabolic function fitted to the FEM results in the central region $x \in [-3;3]$ mm. This curve is used as a reference in the following panels. The blue line represents the difference between the fitted parabola and the simulated points. (b) Similar to (a) but in this case the laser beam impinges on the disk with an excursion of $X_d = 1$ mm from the disk–pumped-area axis. The red curve is taken from (a). (c) Similar to (b) with a beam excursion of $X_d = 2$ mm. (d) The crosses represent the angular tilt of the laser beam after a reflection at the disk caused by the change of the thermal lens due to the mode excursion X_d computed with FEM methods. The continuous line shows for comparison the prediction based on Eq. (137) with VLB obtained using the same FEM calculation.

Hence, in this region the disk acts as a lens whose focal strength is smaller than in Figure 112(b) as expected from the decrease of heat deposition in the laser mode. The more complex structure at the periphery is related to the superposition of the effect associated with the pump and the laser mode that have been assumed to have different diameters.

The black points of Figure 113 (b) show the OPD computed with FEM when a laser beam (laser eigenmode) impinges on the disk 1 mm off-axis (in x -direction) relative to the disk–pumped-area axis. By subtracting from these points the quadratic function fitted to the OPD where the laser beam and the pump spot are aligned (red curve in panel (a)) a residual (blue continuous line) is obtained whose central region shows a linear behavior. This linear behavior can be interpreted as a tilt of the disk. Therefore the FEM simulation indicates that a small excursion of the laser mode from the disk–pumped-area axis induces in leading order only a tilt of the disk, while the quadratic part (focal strength) remains unchanged. This tilt grows with increasing laser eigenmode excursion from the disk–pumped-area axis as is visible by comparing Figure 113(b) with (c) and as is summarized in (d).

In the following, we use a simplified model to show that an off-axis laser beam at the active medium induces a change of the OPD that can be well approximated by a linear function with slope different from

zero. The FEM simulations have shown that the OPD caused by the pump beam alone (fluorescence operation, see Figure 112 (b)) and by the pump beam combined with the lasing processes (see Figure 113 (a)) in the vicinity of the disk axis can be well approximated by parabolic profiles. Thus, we assume these OPDs to be of the form

$$OPD_{pump}(x) = A_{pump} + \frac{V_{pump}}{2}x^2 \text{ (fluorescence operation)} \quad (129)$$

$$OPD_{tot}^{ONaxis}(x) = A_{tot} + \frac{V_{tot}}{2}x^2 \text{ (laser operation)}, \quad (130)$$

where x is the variable describing the position relative to the optical axis, V_{pump} and V_{total} are the focal strengths of the parabolic profiles, and A_{pump} , A_{tot} constants describing a global (position independent) phase shift. The difference between these two OPDs is used to define the OPD arising from the laser beam (LB) only

$$OPD_{LB}(x) = OPD_{tot}^{ONaxis}(x) - OPD_{pump}(x) \quad (131)$$

$$OPD_{LB}(x) = (A_{tot} - A_{pump}) + \frac{V_{tot} - V_{pump}}{2}x^2 \quad (132)$$

For TDL the thermal lens is usually defocusing because it is dominated by the bending of the disk as shown in Figure 112(a) so that the disk acts as a convex mirror. Consequently, for TDL the focal strength associated with the laser beam only $V_{LB} = V_{tot} - V_{pump}$ is positive (focusing)⁷.

As a next step, we consider the OPD resulting from the pump process and a laser beam impinging off-axis on the active medium:

$$OPD_{tot}^{OFFaxis}(x) = OPD_{pump}(x) + OPD_{LB}(x - X_d) \quad (133)$$

$$= A_{tot} + \frac{V_{pump}}{2}x^2 + \frac{V_{LB}}{2}(x - X_d)^2 \quad (134)$$

where X_d is the excursion of the laser beam from the optical axis. A misalignment of the laser beam by X_d from the disk-pumped-area axis thus gives rise to an OPD variation given by

$$\Delta(OPD)(x) = OPD_{tot}^{ONaxis}(x) - OPD_{tot}^{OFFaxis}(x) \quad (135)$$

$$= \frac{V_{LB}}{2}x X_d - \frac{V_{LB}}{2}X_d^2 \quad (136)$$

The last term in Eq. (136) is a position-independent contribution that describes an overall phase shift that can be neglected in our treatment. The first term being linear in x represents the angular tilt α_d suffered by a laser beam after reflection at the disk

$$\alpha_d = V_{LB} X_d \quad (137)$$

Therefore, the simplified model predicts that a beam excursion X_d at the active medium induces a tilt of $\alpha_d/2$ of the active medium proportional to the beam excursion⁷. As well visible in Figure 113(d) for small

⁷ For rod lasers the thermal lens is usually focusing because the refractive index change versus temperature is positive ($dn/dT > 0$). Hence, the reduced heat load due to laser operation leads to a negative (defocusing) V_{LB} .

excursions ($X_d = 1$ mm) there is a good agreement between the tilt calculated using only the FEM and the tilt based on Eq. (137) with VLB also from the same FEM. For larger excursion, this agreement decreases.

Equation (137) represents the steady-state tilt of the disk caused by a fixed beam excursion. It also implies that a change of the beam excursion causes a change of the disk tilt. However, the adjustment of the disk tilt to the new beam excursion is not instantaneous but occurs with a time constant t given by the thermalization of the assembly of thin disk and heat sink. For example the variation of the temperature distribution for the assembly of thin disk and heat sink presented in the Appendix has been computed to have a time constant of $t = 5$ ms. Due to the linearity of Eq. (137) we can model the time variation of the disk tilt as⁸

$$\tau \frac{d\alpha_d}{dt} = V_{LB} X_d(t) - \alpha_d. \quad (138)$$

9.3. Resonator reaction for end-mirror misalignment

A geometrical ray propagating in an optical system can be described by its position $X_r(z)$ and its angle $\theta_r(z)$ with respect to the optical axis (z -axis) [20]. For an ideally aligned optical system the beam propagates along the optical axis of the system so that $X_r(z) = 0$ and $\theta_r(z) = 0$ are fulfilled everywhere. The ABCD-matrix formalism can be used to compute the beam propagation along the optical system if the initial beam position and angle are known. In a resonator, the eigenmode has to reproduce itself after a roundtrip with regard to its position, angle, waist and phase front curvature.

Starting from an ideally aligned laser resonator where the laser eigenmode is on-axis everywhere, we introduce a small misalignment of the first end-mirror by an angle $\alpha_r/2$. To have laser operation, the eigenmode position X_r and the angle θ_r at the first end-mirror must fulfill following equation

$$\begin{bmatrix} X_r \\ \theta_r \end{bmatrix} = \begin{bmatrix} D & B \\ C & A \end{bmatrix} \begin{bmatrix} A & B \\ C & D \end{bmatrix} \begin{bmatrix} X_r \\ \theta_r + \alpha_r \end{bmatrix} \quad (139)$$

where the second ABCD matrix describes the beam propagation from the first (tilted) end-mirror to the second end-mirror, and the first ABCD matrix the back-propagation from the second end-mirror to the first end-mirror. Note that the effective focal strength (thermal and non-thermal) of the disk is included in the two matrices. Using the condition that the determinant of each ABCD matrix is equal to one, the solution of these equations reads

⁸ Here we implicitly assumed that there is only a single thermalization time t , i.e. that t does not depend on the (x, y) position because the heat flow in the active material occurs in axial (z) direction. Diamond as substrate material shows also a radial heat flow given its large thermal conductivity (see Table 8). However, this high thermal conductivity and the low thermal expansion lead to a thermal-lens effect order of magnitude smaller than the one generated by the active material. Therefore, for a good approximation, only the heat flow in the laser crystal has to be considered which is along the z -axis due to the moderate thermal conductivity of the active material and its small thickness. For diamond substrates, the above assumption is thus justified. A metallic heat sink has a significantly lower thermal conductivity compared to diamond leading to a negligible heat flow in x and y directions (assuming large pump spots). Hence, the assumption of a single thermalization time t is also fulfilled for metallic heat sinks.

$$X_r = -\frac{\alpha_r D}{2 C} \quad (140)$$

$$\theta_r = -\frac{\alpha_r}{2}. \quad (141)$$

Because the resonator reaction time (10 ns time scale) is much shorter than the thermal lens adaptation time (ms time scale) we can assume that

$$X_r(t) = -\frac{\alpha_r(t) D}{2 C} \quad (142)$$

holds for any time t .

Equation (142) describes the time-dependent beam excursion at the resonator end-mirror that results as a consequence of the resonator response to a misalignment of the same end-mirror by an angle $\alpha_r/2$. This equation will be used in Sec. 9.4 to model the stability of a resonator having the disk as an end-mirror. For a disk used as bending mirror (for V-shaped resonators), an equation analogous to Eq. (142) has to be derived. This is accomplished in Sec. 9.5 and applied to resonator stability studies in Sec. 9.6.

9.4. Resonator stability for disk as end-mirror

We have seen previously that an excursion of the eigenmode at the disk position causes a change of the disk tilt (thermal lens effect), and that a tilt of the disk causes an excursion of the eigenmode at the disk position (resonator reaction). Until now, we neglected the interplay of these two effects. Their coupling causes a feedback loop that calls for a more detailed investigation.

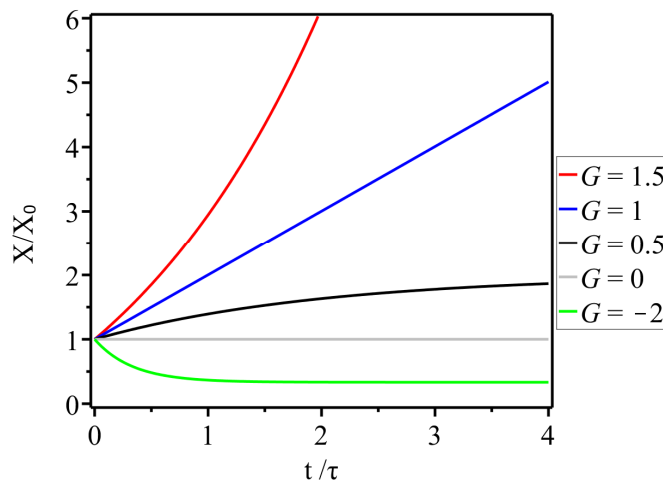


Figure 114: Time evolution of the eigenmode excursion from the disk–pumped-area axis caused by the interplay between resonator reaction and change of the thermal lens due to misalignments. An initial excursion X_0 can be either reduced or amplified to a finite or infinite value depending on the value of the G parameter.

Coupling of these two effects is realized by identifying

$$X \equiv X_d = X_r - X_0 \quad (143)$$

$$\alpha \equiv \alpha_d = \alpha_r. \quad (144)$$

Here we have assumed an initial eigenmode excursion X_0 at the disk position. The magnitude of this excursion is unimportant for the understanding of the effect we are modeling in this study as will become clear later (see Eq. (147)). It must simply have a non-vanishing value: $X_0 \neq 0$. Note that this condition is always valid in practice because of the imperfection (misalignment between pump and laser mode) intrinsic in the alignment of the resonator.

By combining Eqs. (138), (142), (143) and (144) and assuming $dX_0/dt = 0$ (static or slowly varying initial misalignment) we obtain

$$\tau \frac{dX(t)}{dt} = GX(t) - [X(t) - X_0], \quad (145)$$

where we have defined the parameter G as

$$G = -\frac{V_{LB} D}{2 C}. \quad (146)$$

The solution of Eq. (146) reads:

$$X(t) = \begin{cases} X_0 \frac{G e^{\frac{G-1}{\tau}t} - 1}{G - 1} & \text{for } G \neq 1 \\ X_0 \left(1 + \frac{t}{\tau}\right) & \text{for } G = 1 \end{cases}. \quad (147)$$

The time behavior $X(t)$ for various values of G is plotted in Figure 114. For $G < 0$ the initial excursion is reduced with time, for $G = 0$ it remains constant, and for $G > 0$ it is amplified. Furthermore, for $G < 1$ the initial excursion is amplified but saturates with time to a finite value, while for $G \geq 1$ the initial excursion increases continuously, $X(t \rightarrow \infty) \rightarrow \infty$.

The rate of change of the excursion $dX(t)/dt$ depends on G , X_0 and τ . Yet the fate of the excursion at large times $X(t \rightarrow \infty)$, i.e. whether it remains constant, damped or amplified only depends on the parameter G .

We close this section by listing the various assumptions and limits underlying the analytical solution of the time evolution of the eigenmode excursion given in Eq. (147). A linear dependence between excursion and tilt has been assumed which is only valid for small excursions ($X \leq 1$ mm) as demonstrated in Figure 113 (d). We also assume a space-independent time constant τ . Deviation from this behavior impacts in a minor way our model, as τ does not affect the fate of the beam excursion.

In this model, we neglect the decrease of the circulating laser intensity caused by a misalignment. On the one hand, this intensity decrease reduces V_{LB} and the tilt of the disk, on the other hand, the ratio D/C that depends on the thermal lens increases making this resonator more unstable.

In principle, our model could be extended to include all these effects and the soft-aperture effects naturally occurring in the pumped medium [52, 170]. This would lead to a very complex interplay obscuring the principle of the mechanism we are disclosing in this study and whose precise modeling goes beyond the scope of this paper. However, our simplified analytical model captures correctly the onset of this

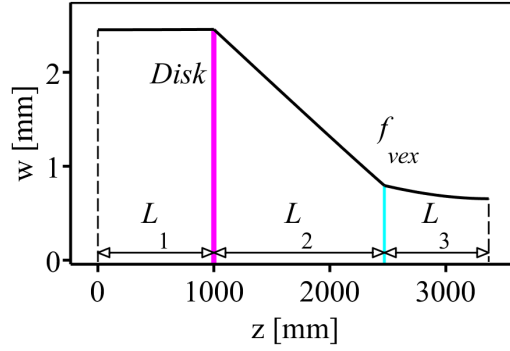


Figure 115: V-shaped resonator architecture consisting of a flat end-mirror, a free propagation of length L_1 , a disk with 0.5 dioptic power (in unpumped conditions), a free propagation of length L_2 , a convex lens (mirror) with focal length f_{vex} , a free propagation of length L_3 , and a flat end-mirror. The eigenmode waist w along the resonator for a particular set of values is also given to clarify the layout.

misalignment instability that causes a dramatic decrease of the laser performance (efficiency and stability). Thus, its predictive power for designing resonator remains unaffected.

9.5. Stability of V-shaped resonators

In this section, we investigate the stability properties of V-shaped resonators (widely used in the TDL sector [99, 116, 117, 259, 260]) with respect to the thermal-induced misalignment effect disclosed in this paper. More specifically, we model here the eigenmode excursion at the disk for a resonator where the disk is a folding mirror (not an end-mirror).

The roundtrip propagation in this resonator can be divided into two branches (right and left of the disk): from the tilted disk to the second end-mirror and back to the disk

$$\begin{bmatrix} X'_r \\ \theta'_r \end{bmatrix} = \begin{bmatrix} D_R & B_R \\ C_R & A_R \end{bmatrix} \begin{bmatrix} A_R & B_R \\ C_R & D_R \end{bmatrix} \begin{bmatrix} X_r \\ \theta_r + \alpha_r \end{bmatrix} \quad (148)$$

and from the tilted disk to the first end-mirror and back to the disk

$$\begin{bmatrix} X_r \\ \theta_r \end{bmatrix} = \begin{bmatrix} D_L & B_L \\ C_L & A_L \end{bmatrix} \begin{bmatrix} A_L & B_L \\ C_L & D_L \end{bmatrix} \begin{bmatrix} X'_r \\ \theta'_r + \alpha_r \end{bmatrix}. \quad (149)$$

The ABCD matrices describe the left (L) and the right (R) branches of the optical system similar to Eq. (139). The effective focal strength of the disk is included in the ABCD matrices: it can be included without loss of generality either in the left or in the right branches or even divided between the two branches. X_r and $\theta_r + \alpha$ represent the excursion and the angle for the beam leaving the tilted disk towards the second (right) end-mirror. We assume the disk to be tilted by an angle $\alpha_r/2$. X'_r and θ'_r are the excursion and angle of the beam returning to the disk (prior to reflection on the disk) after reflection on the second end-mirror, i.e., after a propagation in the right branch. The beam leaving the disk toward the first (left) end-mirror after

a reflection on the disk thus has an excursion and angle of X'_r and $\theta'_r + \alpha_r$, respectively. When it returns back at the disk after a propagation in the left branch it has an excursion X_r and an angle θ_r .

The eigenmode excursion at the disk position caused by a tilt of the disk by an angle $\alpha_r/2$ can be found by solving these two coupled equations and reads

$$X_r = -\alpha_r \frac{A_L D_R}{A_L C_R + C_L D_R}. \quad (150)$$

Following a similar argumentation as exposed in Sec. 9.4 we find that the time evolution of the excursion $X(t)$ at the disk follows Eq. (150) but with the parameter G defined as

$$G = -V_{LB} \frac{A_L D_R}{A_L C_R + C_L D_R}. \quad (151)$$

On that account, all the conclusions drawn in the previous section remain valid after the appropriate replacement of parameter G .

9.6. Impact on typical V-shaped resonators

One of the first steps when designing laser resonators is to study the influence of the thermal lens on the resonator stability. This is usually achieved by means of so called “stability plots” [178], i.e. by plotting the evolution of the eigenmode size at a given optical element for variations of the thermal lens. Given a resonator layout, stable laser operation is only achieved in a limited range of thermal lens values. This range is known as the “stability region”.

In this section, we illustrate the shrinkage of the effective stability region and the reduction of the output power caused by the thermal-induced misalignment mechanism. The impact of this misalignment mechanism will be illustrated for four resonator layouts, all based on the architecture sketched in Figure 115.

For the modeling of the output power and the thermal lens effect given in Figure 116, 123, 124, 125, 127 and 128 we have assumed the simplified situation summarized in Table 6. The thermal dioptric power of the disk in laser operation has been assumed to be 50% of the thermal dioptric power in fluorescence operation [146, 147, 148] with $V_{LB} > 0$ (valid for TDL). We further assumed that the dioptric power of the disk decreases linearly with the pump power density, and that the laser operates in the TEM₀₀ mode.

At zero pump power (i) the dioptric power of the disk is 0.5 diopters (assumption). With increasing pump power density the dioptric power decreases. When the pump power density reaches 0.3 kW/cm² (ii) laser operation starts. A further increase of in pump power density leads to an increase of the output power until the allowed maximal (due to optical damage) pump power density of 8 kW/cm² (vi) is reached. In this case, the laser resonator remains within the stability region independently of the laser pump power density. No limitations due to the above-described thermal-induced misalignment are noticeable in this layout.

Table 6: Parameters assumed to model the laser output power and the stability properties of Figs. 6, 7, 8, 9, 11 and 12. Notation: w_c is the waist of the eigenmode at the center of the stability region, P the pump power density and V the dioptric power of the disk.

Maximal pump power density	8 kW/cm ²
Pump power density at laser threshold	0.3 kW/cm ²
Slope efficiency	50%
Pump spot diameter	$D_{\text{pump}} = 3w_c$
Disk dioptric power (unpumped)	$V(\text{unpumped}) = 0.5 \text{ 1/m}$
Thermal dioptric power in fluorescence operation	$\frac{dV}{dP} = -0.017 \frac{1/\text{m}}{\text{kW}/\text{cm}^2}$ [148]
Thermal dioptric power in laser operation	$\frac{dV}{dP} = -0.0092 \frac{1/\text{m}}{\text{kW}/\text{cm}^2}$ [148]

Table 7: Description of significant states of the laser operation used in Figs. 6, 7, 8, 9, 11 and 12.

i	The disk is not pumped and its dioptric power is $V = 0.5 \text{ 1/m}$.
ii	The gain of the disk equals the losses at the out-coupler (other losses are neglected). Laser threshold is reached provided the resonator is within the “classical” stability region and the waist at the given dioptric power does not exceed 1.3 the layout value ($w \leq 1.3w_c$).
iii	The disk dioptric power in fluorescence operation gives rise to a stable resonator with $w = 1.3 w_c$. Laser operation is starting.
vi	The disk dioptric power in laser operation is within the stability region with $w \approx 1.3w_c$.
v	The parameter G becomes 1. Laser operation is disrupted giving rise to a rapid decrease of the disk dioptric power from the laser operation value to the fluorescence value (at the same pump power density).
iv	Laser operation at the allowed maximal pump power density of 8 kW/cm ² .
iv'	Laser operation at the allowed maximal pump power density of 8 kW/cm ² when the thermal induced misalignment mechanism is ignored.

Figure 115: shows the stability plot and the output power as a function of the disk dioptric power V for a resonator having an eigenmode waist at the disk of about 1.5 mm. V accounts for thermal and non-thermal (prior to pumping) lens effects. A qualitative understanding of the laser operation of this resonator can be obtained by considering some particular states of the laser operation indicated with Roman numbers from (i) to (vi) as summarized in

Table 7.

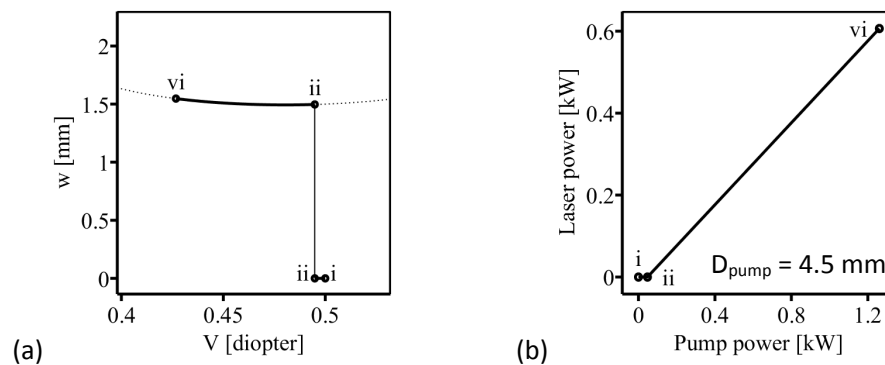


Figure 116: (a) eigenmode waist at the disk versus the disk dioptric power V for a resonator layout as in Figure 115 with $L_1 = 500 \text{ mm}$, $L_2 = 1470 \text{ mm}$, $L_3 = 100 \text{ mm}$ and $f_{\text{vex}} = -1500 \text{ mm}$. The dotted line represents the “classic” stability plot, i.e. the waist w for any V . The continuous black line indicates the beam waist versus dioptric power only for the dioptric power that retain the disk in the assumed running conditions: starting from $V = 0.5$ diopters for no pumping to $V \approx 0.42$ diopters for 8 kW/cm^2 . The value of $w = 0$ is used to indicate that at the given dioptric power there is no laser operation. The Roman numbers indicate specific states of the laser operation as described in the main text and summarized in Table 2. Between (i) and (ii) there is no laser operation because the gain at the disk in this pump power density range is still smaller than the out-coupler transmission. (b): Qualitative evolution of the output power for the resonator layout of (a) as a function of the pump power. The parameters of Table 1 have been used to model the output power evolution.

In Figure 117 the output power evolution and the stability plot are given for a resonator layout whose stability region is shifted compared with the layout of Figure 116. With increasing pump power and above the laser threshold (ii) the output power increases. However, at an output power of about 0.4 kW (v), laser operation stops because the parameter G becomes equal to 1. As a consequence, the thermal lens suddenly jumps from the laser operation value to its fluorescence value (while the pump power density remains constant). A further increase of the pump power worsens the situation because G increases further and the resonator moves out of the “classic” stability region. Also, in this case, provided that the laser operation would not be disrupted by the thermal misalignment effect, the resonator would stay inside the “classic” [14] stability region for all pump power densities from 0 (i) to 8 kW/cm^2 (vi'). But for this layout, the onset of the thermal-induced misalignment limits the effective stability region and the maximal output power as can be seen by comparing (v) with (vi').

Figure 118 shows the behavior of a resonator having a larger eigenmode waist of $w_c = 2.5 \text{ mm}$ (w_c denotes the waist at the center of the stability region). At point (ii), the disk gain becomes larger than the out-coupler losses, but there is no laser operation because the resonator lies outside of the stability region. With increasing pump power, the resonator becomes stable but laser operation only starts at point (iii) when the waist w of the eigenmode reaches a reasonable value that we assumed to be $w = 1.3w_c$. From (iv) to (v) the output power increases with the value given by the assumed slope efficiency and laser threshold, while from (iii) to (iv) a transition from fluorescence to efficient laser operation occurs. In this pump power density range the dioptric power of the disk can be assumed to be constant as the heat load caused by the increase of pump power density is compensated by the reduction of the heat load due to the fast-growing laser output power.

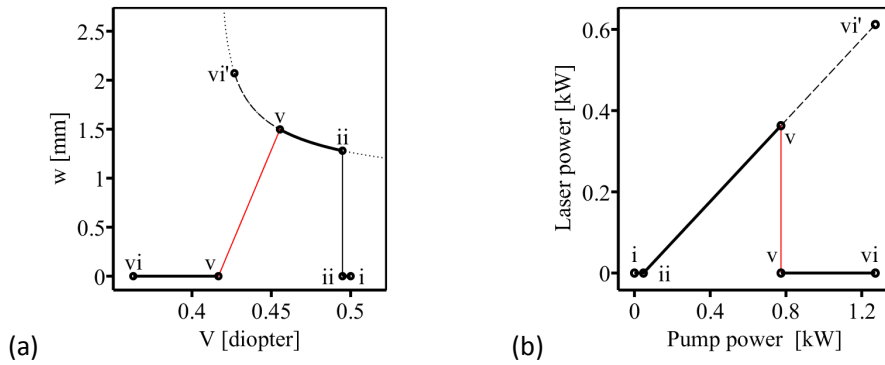


Figure 117: Similar to Figure 116 but for a resonator with $L_1 = 500$ mm, $L_2 = 900$ mm, $L_3 = 100$ mm and $f_{\text{vex}} = -1500$ mm. At position (v) the laser operation is disrupted by the onset of the thermal-induced misalignment mechanism and the dioptric power of the disk jumps from its laser operation value (0.45 diopters) to its fluorescence value (0.42 diopters) as indicated by the red line. Therefore, the maximal output power attainable is limited by the onset of the misalignment mechanism presented in this study. The absence of laser operation between (i) and (ii) is because the gain at the disk does not overcome the losses at the out-coupler, while the absence of laser operation between (v) and (vi) is due to the thermal-induced misalignment. The points (vi') indicate waist and output power hypothetically achievable when neglecting the thermal-induced misalignment.

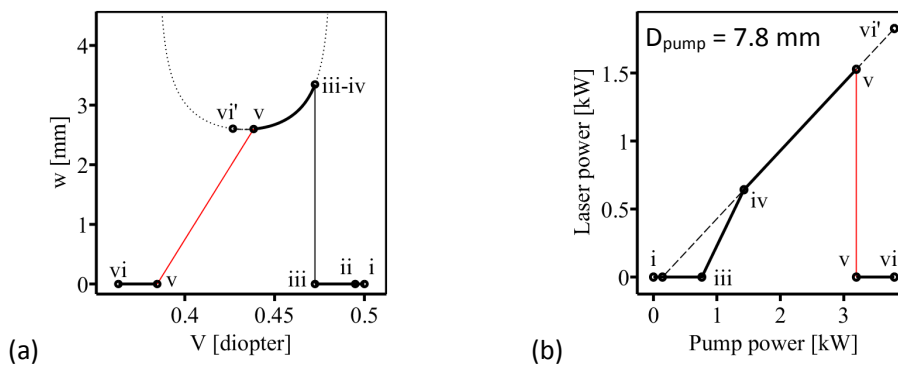


Figure 118: Similar to Figure 117 but for a resonator with $L_1 = 1000$ mm, $L_2 = 1600$ mm, $L_3 = 900$ mm and $f_{\text{vex}} = -1000$ mm. The absence of laser operation between (i) and (iii) has multiple origins: the gain at the disk does not overcome the losses at the out-coupler, or the resonator is outside the stability region, or the resonator is within the stability region but it has a waist $w > 1.3w_c$. The absence of laser operation between (v) and (vi) is due to the thermal-induced misalignment. The behavior between (iv) and (v) assumes a slope efficiency of 50% and a laser threshold of 0.3 kW/cm². Between (iii) and (iv) there is a transition from fluorescence to laser operation.

Also, in this case the output power of the laser is limited by the onset of thermal-induced misalignment instabilities that occurs at position (v) when G becomes equal to 1. Here the thermal lens of the disk rapidly mutates from the laser to the fluorescence value. In this case, the obtainable maximal laser output power does not significantly deviate from the value that could be obtained at the maximal pump power density of 8 kW/cm² (vi'). However, for a resonator with larger eigenmode (see Figure 119) the limitations induced by the thermal-induced misalignment become substantial.

Laser operation of the resonator given in Figure 119 follows the same dynamics as in Figure 118 but shows an increased limitation arising from the thermal-induced misalignment given the shrinkage of the “classic” stability region. In fact, it has been demonstrated [178] that the width of the stability region scales with $1/w_c^2$ where w_c represents the eigenmode width at the position of the thermal lens (disk). Hence, stable operation of high-power laser becomes increasingly challenging.

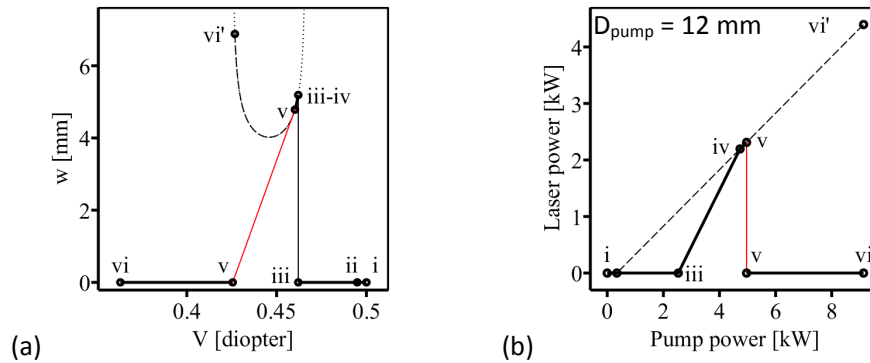


Figure 119: Similar to Figure 118 but for a resonator with $L_1 = 1000$ mm, $L_2 = 1600$ mm, $L_3 = 2000$ mm and $f_{vex} = -750$ mm.

The thermal-induced misalignment effect presented here further worsens the situation because a constant (in absolute terms and independent of w) range of the stability region becomes unusable reducing the “effective” stability region. This unusable range starts from the weak focusing edge of the “classic” stability region and has a width proportional to the pump power density. This unusable range with $G \geq 1$ within the “classic” stability region is related to the commonly applied rule of thumb that a laser resonator should be designed to remain inside the stability region also when the laser cavity is blocked.

No stable laser operation is possible and power scaling reaches its limit when the width of the “classical” stability region with increasing mode size shrinks to the width of the unusable range (due to thermal-induced misalignment instabilities). A decrease of the pump power density would reduce the width of the unusable range allowing the use of larger eigenmode and pump spots but the maximal output power would remain approximatively the same.

Possible non-linear variations of the thermal lens versus pump power densities [149] further amplify the limiting effect of the here disclosed effect. However, proper resonator designs as exposed in the next section can be used to circumvent this problem.

9.7. Resonator designs insensitive to the thermal-induced misalignment

In this section we present three resonator architectures which avoid the thermal-induced misalignment by keeping $G < 1$ (assuming $V_{LB} > 0$). The resonator shown in Figure 120 (a) has been obtained by replacing the free propagation of length L_1 on the left side of Figure 115 by an optical segment acting as a Fourier transform. Since the ABCD matrix of a Fourier transform based on a lens of focal length F reads

$$\begin{bmatrix} A_L & B_L \\ C_L & D_L \end{bmatrix} = \begin{bmatrix} 0 & F \\ -\frac{1}{F} & 0 \end{bmatrix}, \quad (152)$$

the G parameter of Eq. (151) becomes zero for all layouts. The physical origin of this stabilization arises from the fact that the back and forth propagation of the beam in the Fourier segment corresponds to a

4F-relay imaging from pass to pass on the disk. An on-axis laser beam reflected on the disk tilted by $\alpha_r = 2$ leaves the disk towards the Fourier segment at an angle $\theta_r = \alpha_r$. When the beam is coming back to the tilted disk after the propagation in the 4f-relay imaging system, its angle is inverted so that $\theta_r = -\alpha_r$. The subsequent reflection of the beam on the disk brings the beam back on axis ($\theta_r = 0$). The beam thus reproduces itself on the right side of the resonator independently of the disk tilt.

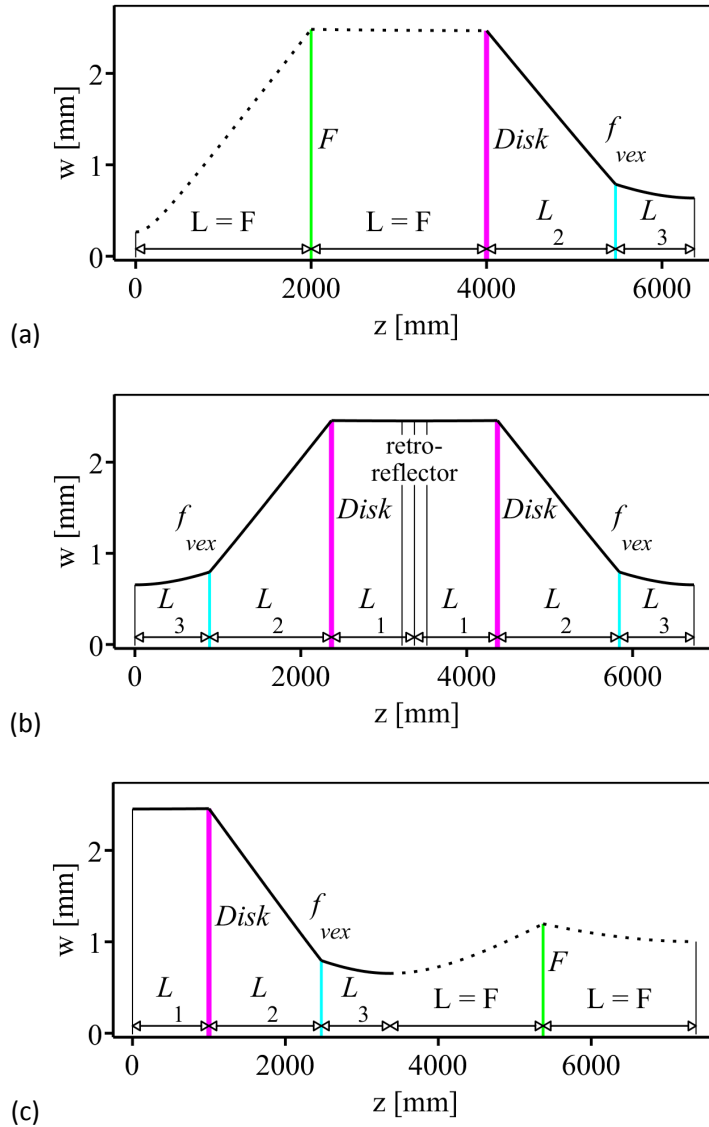


Figure 120: Resonator architectures with $G < 1$ (assuming $V_{LB} > 0$), i.e., unaffected by the thermal-induced misalignment. The vertical lines represent the position of the various optical elements. The eigenmode waist evolution along the resonator is also indicated. (a) This resonator has been obtained by replacing the left side (L_1) of the V-shaped resonator design of Figure 115 with a Fourier-transform segment. This is achieved by inserting a focusing element with focal length F at a distance F from the disk and from the end-mirror. (b) Resonator formed by combining two identical or quasi-identical optical segments, each of which having a layout of a V-shaped resonator as in Figure 115. A retro-reflector is placed between the two segments and the same disk has to be used in both segments [21]. (c) Similar to (a) but in this case the Fourier-transform segment is used to extend the right branch of the V-shaped resonator.

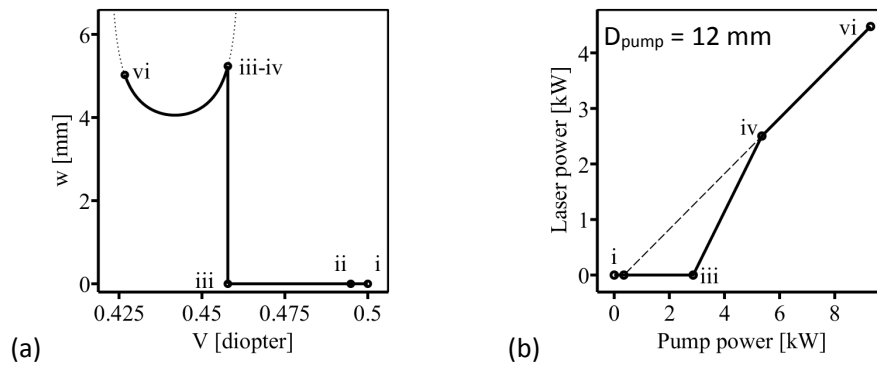


Figure 121: Similar to Figure 119 but with a resonator design based on Figure 120 with $L_2 = 1620$ mm, $L_3 = 2000$ mm and $f_{\text{vex}} = -750$ mm. As for this resonator $G < 1$ (assuming $V_{\text{LB}} > 0$), the thermal-induced misalignment presented in this study does not limit the maximal output power.

The drawback of this architecture is that for high power resonators the cavity becomes exceedingly long. This is caused by the requirement to have a large beam waist at all optical elements that calls for large F . However, the beam offset generated by the corner cube prevents the use of the corner cube as resonator end-mirror. For this reason in Figure 120 (b) the corner cube is used as folding mirror between two reflections on the same disk. This resonator layout thus corresponds to a multi-pass resonator (4 reflections on the same disk per roundtrip) exhibiting a larger gain compared to previous layouts. Note that the realization of this layout with two different disks would not provide any cancellation of the thermal-induced effect. Moreover, it has been demonstrated that the stability region of such multi-pass resonators having only one disk does not depend on the number of reflections at the disk and have thus been proposed to solve present energy scaling of mode-locked laser oscillators [52].

In Figure 120 (c) the Fourier-transform segment has been added to the right side of the resonator of Figure 121. This addition leads to a sign change of G . In such a way, G becomes negative stabilizing the resonator⁹.

The resonator adaptations presented in this section lead to larger output power and larger “effective” stability ranges as can be seen by comparing Figure 119 with Figure 121. This opens the way for a further increase of the waist w_c resulting in power scaling as shown in Figure 122.

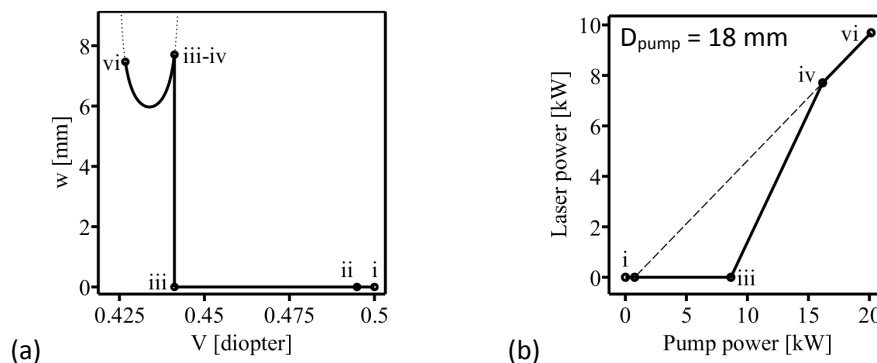


Figure 122: Similar to Figure 121 but with a resonator design with larger eigenmode waist ($L_2 = 1605$ mm, $L_3 = 5000$ mm and $f_{\text{vex}} = -750$ mm).

⁹ For active media having negative V_{LB} , like rod lasers, this design leads to $G > 0$ limiting the power scaling. By contrast, the design given in Figure 115 having $G < 0$ are power scalable for negative V_{LB} .

9.8. Conclusion

We have exposed for the first time a fundamental obstacle to power scaling of TDL related with self-driven growth of misalignment due to thermal-lens effects. We have found a parameter G which serves to evaluate the response of an optical resonator to an excursion of the laser eigenmode at the active medium position accounting for the changes of the OPD at the active medium caused by the excursion of the laser eigenmode itself. This parameter G can be computed using the ABCD-matrix formalism and the knowledge of the active medium thermal lens in laser and fluorescence operation.

When designing resonator layouts the region where $G \geq 1$ has to be avoided. This results for standard TDL design (V-shaped resonator) in a restriction of the “classic” stability region (where stable laser operation can be achieved). Hence, it becomes particularly limiting for high-power TDL.

This boundaries can be stretched by reducing the thermal-lens difference V_{LB} between laser operation and fluorescence operation which can be achieved by increasing the thermal conductivity of the assembly of thin disk and heat sink, by increasing the stiffness of the heat sink and by lowering the heat deposition for example by using zero-phonon line pumping [149]. However, this effect can be avoided completely by suited resonator layouts as presented in Sec. 9.7 or by implementing an active feedback as the beam excursion grows on a time scale of milliseconds.

9.9. Appendix: Simulations based on finite elements methods

The thermal-induced OPD difference (at the disk) between fluorescence (only pumped) and laser operation is at the core of this study. The model we have developed describing this interplay and providing a simple criterion to characterize the sensitivity of resonators to this phenomenon assumes that a change of the eigenmode position at the disk generates a change of its OPD that corresponds to a tilt of the disk. The FEM simulations presented in Figure 113 demonstrate the validity of this assumption for small beam excursion ($X = 1$ mm). In this appendix, we specify the geometry and parameters entering the FEM simulations underlying the OPD profiles of Figure 112 and Figure 113.

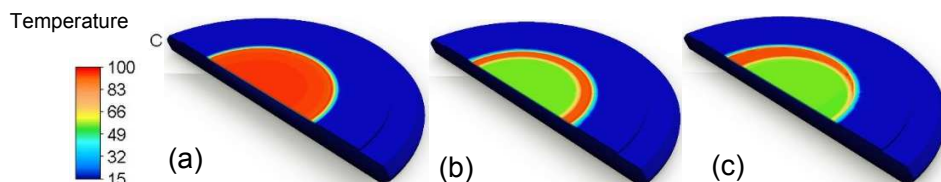


Figure 123: Temperature distributions of the assembly of thin disk and heat sink with the geometry and heat loads as specified in the main text. (a) Temperature distribution caused by the pump only. The laser is operated in fluorescence mode. (b) Laser operation reduces the heat deposited at the resonator eigenmode position. Here the laser eigenmode is centered relative to the pumped area while in (c) the laser eigenmode is 1 mm off from the disk-pumped-area axis.

To account for the asymmetry caused by the off-axis laser beam, 3D simulations must be performed. These differ from typical FEM simulations [102, 145, 248] of TDL which usually assume rotational symmetry and are thus performed only along a radial cut of the disk. To reduce computing time, however, only half of the disk is simulated and the appropriate symmetry conditions are used to extend the simulations to the whole disk. Autodesk Simulation Mechanical 2015 has been used.

The FEM simulations assume a diamond heat sink of 1.5 mm thickness and 25 mm diameter, and a Yb:YAG active material with 140 μm thickness and a diameter of 20 mm. The heat sink is supported at its edge, while its backside is held at a constant temperature of $T = 13\text{ }^\circ\text{C}$. Disk coatings and contacting layers have been neglected.

A flat-top pump beam of 12 mm diameter generates a heat load of 50 W/mm^2 in the active material while it is assumed that in the laser beam area (diameter of 9.6 mm) the laser beam reduces the heat load by a factor of 2. Such a reduction that strongly depends on running conditions, active medium material and pump wavelength has been observed for example in [146, 147, 148, 149, 101].

Figure 123 shows the temperature distribution at the disk surface for three different conditions computed with FEM using the parameters summarized in Table 8. In (a) the laser is in fluorescence mode, i.e., the active medium is pumped but no laser light is produced. In transverse direction, the temperature is constant within the pumped area. The heat-sink temperature is much lower compared to the disk due to the superior conductivity of the diamond relative to Yb:YAG. In (b) the laser is operating in optimal conditions. The laser eigenmode is perfectly aligned with the disk–pumped-area axis. As the circulating laser intensity reduces the thermal load [146, 147, 148, 149, 101] the region of superposition between pumped-area and laser eigenmode is colder. In (c) there is a 1 mm deviation between the laser eigenmode axis and the pumped-region axis that leads to an asymmetric temperature profile. It is this asymmetric temperature distribution that causes an asymmetric mechanical deformation of the disk backside that produces the tilt effects described above. Adding the axial expansion of the active medium and correcting for the temperature dependence of the active medium refractive index we obtain OPD profiles whose radial cuts are shown in Figure 112 and Figure 113.

Table 8: Parameters assumed in the FEM simulations to model the thermal lens of the disk contacted to the diamond substrate.

Yb:YAG (7%) thermal conductivity	7 W/mK
Yb:YAG Young's modulus	300 GPa
Yb:YAG avg. thermal expansion	$8 \cdot 10^{-6}$ 1/K
Yb:YAG refraction index change versus temperature (dn/dT)	$9 \cdot 10^{-6}$ 1/K
Diamond thermal conductivity	1900 W/mK
Diamond Young's modulus	1100 GPa
Diamond avg. thermal expansion	$9 \cdot 10^{-7}$ 1/K

10. Thin-disk laser pump schemes¹⁰

Thin-disk laser pump layouts yielding an increased number of passes for a given pump module size and pump source quality are proposed. These layouts result from a general scheme based on the merging of two simpler pump optics arrangements. Some peculiar examples can be realized by adapting standard, commercially available pump optics with an additional mirror pair. More pump passes yield better efficiency, opening the way for the usage of active materials with low absorption. In a standard multi-pass pump design, scaling of the number of beam passes brings about an increase in the overall size of the optical arrangement or an increase of the requirements for the beam quality of the pump source. Such increases are minimized in our scheme, making them eligible for industrial applications.

10.1. Motivation

The thin-disk laser [98, 99, 100] is a diode-pumped solid-state laser with high power and high pulse energy capabilities, high efficiency, and excellent beam quality. The thin-disk laser active medium, depicted in Figure 124 (a), is a thin disk with a typical thickness of 100-500 μm and a diameter up to a few cm. Lasing and cooling occurs along the disk axis, while pumping results in a quasi-end-pumped configuration. The rear side of the disk acts as a highly reflective (HR) mirror for pump and laser wavelengths, and it is thermally coupled to a heat sink (see Figure 124 (a)). Heat removal from the disk is efficient because of the large cooled-surface-to-active-volume ratio. Since the heat flux occurs along the laser axis, the thermally induced lens effects are minimized, resulting in small phase-front distortions for beams of large diameter [117, 102, 145, 148]. This cooling scheme thus allows for power and energy scaling [235, 236, 238, 248, 162, 115] simply by increasing the diameter of laser and pump spots, eventually limited by amplified spontaneous emission effects [117, 121, 261, 125]. Moreover, the efficient cooling allows pumping in the kW range and the use of quasi-three-level system materials having low quantum defect and high gain. To date, the paradigmatic material of choice, especially in industrial applications, is ytterbium-doped yttrium aluminum garnet (Yb:YAG) [206, 234, 237], but recently researchers have concentrated on finding new materials of higher thermal conductivity for higher output power and with larger bandwidth for ultrashort pulse generation or tunable lasers [105, 101, 247, 162, 262, 263, 264].

The small thickness of the disk guarantees excellent cooling and power scaling. Yet, in a single pass, only a small fraction of pump light is absorbed in the thin active medium. The light not absorbed in the disk in

¹⁰ This chapter is a reprint of [53]

the first pass is reflected by the HR coating onto a second pass in the active medium. Even so, the absorption in the resulting double pass is too small. This shortcoming can be compensated using a multi-pass scheme for the pump light, that is, by redirecting the (not absorbed) pump beam into the disk several times [265].

A well-defined pump region with sharp boundaries is fundamental, especially for three-level system materials due to the high lasing threshold. To generate a pump profile that minimizes radial tails, on the one hand the pump optics have to redirect the various passes at “exactly” the same position at the disk, and, on the other hand, each individual pump pass spot must have sharp boundaries. Relay 4f telecentric imaging with unitary magnification is commonly used for this purpose [265], as its propagation matrix is exactly the negative unity matrix.

The scheme ordinarily used for disk laser pumping is the first to homogenize a high-power diode laser by coupling it into either a multimode fiber or a rod homogenizer. The output face of this optical element is then imaged onto the disk with suitable magnification. The multi-pass propagation of the pump beam is realized using tele-centric 4f relay imaging with unitary magnification, that is, by imaging the pump spot at the disk position from pass to pass without changing its size. The imaging properties of the 4f imaging scheme “per definition” guarantees that the beam spot profile and its divergence are exactly reproduced from pass to pass (neglecting phase-front distortions occurring at the disk).

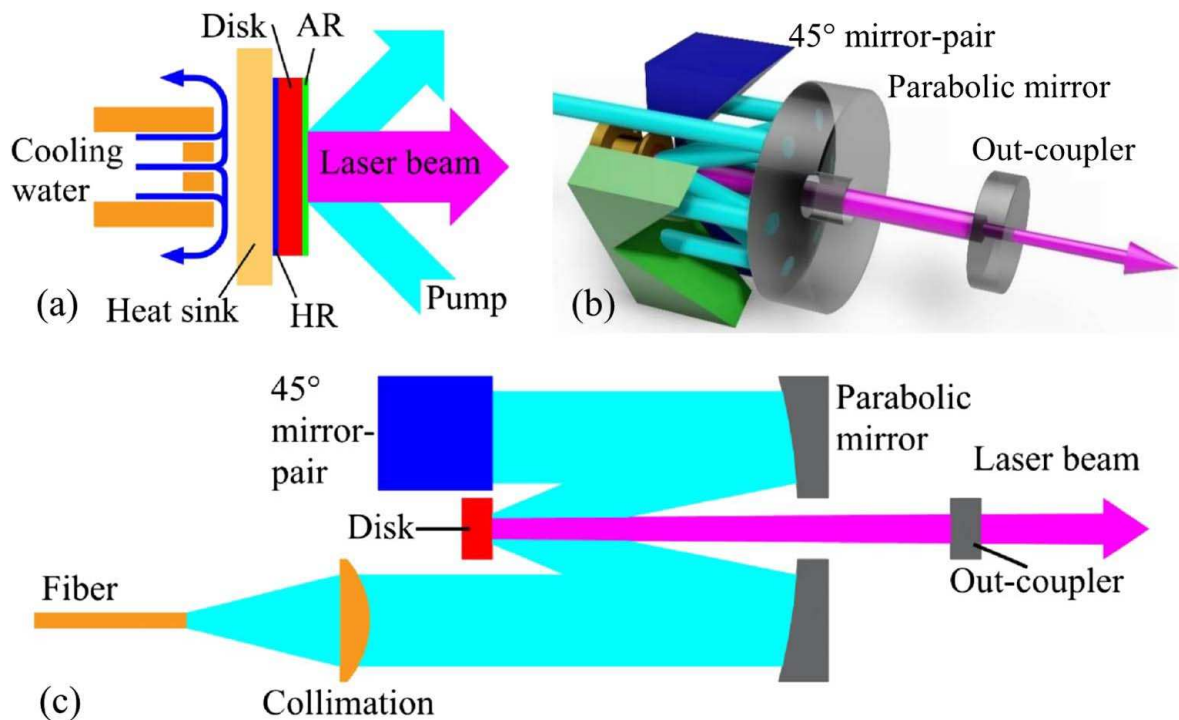


Figure 124: Working principle of a thin-disk laser and thin-disk laser pump arrangement. (a) Scheme of the thin disk active medium mounted on a water cooled heat sink. Lasing and cooling occur along the disk axis. (b) 3D schematic of the pump optics: heat sink (gold), parabolic mirror (gray), and prisms acting as mirror pairs (green and blue). (c) Pump light multi-pass arrangement. The light from a homogenizer is imaged onto the disk via a parabolic mirror. The multi-pass is realized via the disk, the parabolic mirror, and the 45° mirror pairs. The pump beam propagation in the multi-pass is given in cyan, the laser beam, in magenta. HR and AR stand for high reflector and anti-reflex layer, respectively.

Another practical advantage is given by the fact that 4f-imaging can be realized with only a few optical elements also for a large number of passes. Commonly it is realized [113, 265, 266, 267, 268, 269] using a parabolic mirror and a deflecting mirror system, as shown in Figure 124 (b) and Figure 124 (c). After collimation, the pump light from the homogenizer enters the pump optics and is directed to the disk by the parabolic mirror. The light not absorbed in the disk in the first double pass is reflected back to the parabolic mirror. At the parabolic mirror, the pump beam is collimated and sent to the mirror system (prisms), which after a double 90° reflection redirects the light back onto the parabolic mirror but at a different position. From there, the light proceeds to the disk for the second time. Iterating this scheme several times gives rise to a multi-pass pump pattern having several passes through the active medium.

The typical commercially available pump modules for thin disks [269, 270, 271] provide 24 or 48 passes. (Throughout this section, the number of passes N is defined to be twice the number of reflections at the disk.). A larger number of pump passes enables a reduction of the thin disk thickness and doping concentration while keeping the same pump light absorption. The smaller heat resistance that results from reducing the thin disk thickness brings about a lower average temperature for the active medium, which is advantageous for the three-level systems. Moreover, the thermal-lens effects (spherical and aspherical components) of the thin disk are reduced, leading to improved efficiency and beam quality. Similarly, reduced doping ensures higher active medium thermal conductance due to decreased scattering of the active medium phonons on the doping ions yielding more efficient cooling. The increase in pump passes also allows for the use of active medium materials with smaller absorption cross sections and smaller absorption bandwidths. However, such an increase in the pass number has to be attained without substantially increasing the requirements for the pump beam quality expressed by the beam parameters product P , which is defined as the product of the pump beam's divergence angle (half-angle in the far field) and beam waist (radius of the beam at its narrowest point). In this paper, possible realizations of multi-pass pump layouts suitable for thin-disk lasers are presented. We restrict the discussion to 4f imaging schemes. In Sec. 10.2 the 4f-imaging and the multi-pass concepts are introduced with the help of an exemplary simple pump layout. Sec. 10.3 describes the standard commercially available thin-disk pump optics and the related pump beam propagation. The layouts we are proposing in this work result from combining two multi-pass concepts: The first one is based on the standard pump module design described in Sec. 10.3; the second one is given in Sec. 10.4. The merging of these two concepts, which is described in Sec. 10.5, enables multi-pass systems to be realized with a large number of passes while only minimally increasing the complexity of the multi-pass system, the size of the optics, and the requirement for the pump source quality, making these schemes apt for industrial applications. A particular practical realization based on hexagonal mirror pairs and hexagonal ordered fiber-coupled diodes is presented in Sec. 10.6, followed by concluding remarks.

10.2. Simple example of a multi-pass scheme based on 4f relay imaging

A simple way to realize a multi-pass scheme based on 4f imaging is shown in Figure 125 [272, 273]. The setup consists of a thin disk, a lens with focal length f , and a pair of mirrors at a 45° angle relative to the

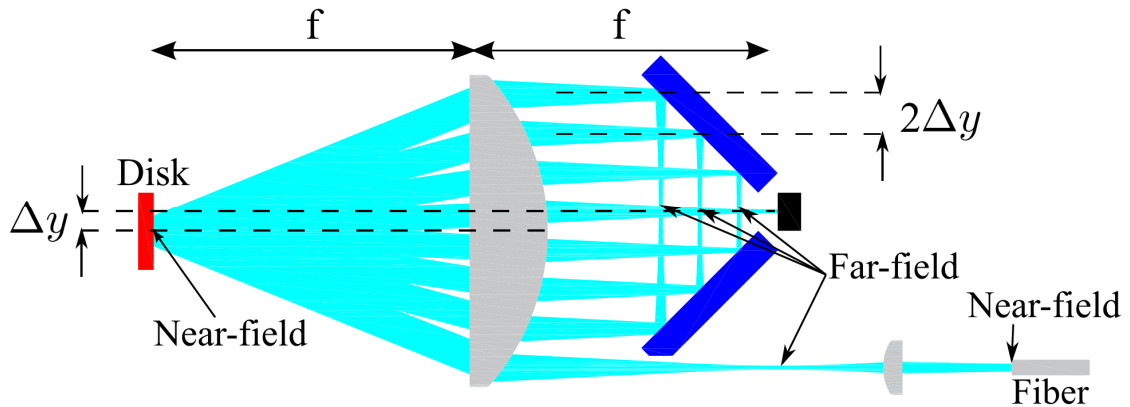


Figure 125: Schematic of a $4f$ multi-pass optical system realized with a 45° mirror pair (blue), a lens (gray), and a disk (red). The mirror pair axis is shifted by Δy relative to disk-lens axis. The pump beam multi-pass is given in cyan. The number of passes can be doubled by introducing a back-reflector (black).

optical axis. The spacing between disk and lens and between lens and the intersect of the mirror pair is f . Hence, the propagation from disk to mirror pair can be seen as imaging from the disk image plane to the mirror-pair Fourier plane and the full round trip from disk to disk as a $4f$ relay imaging. In other words, the near-field laser profile at the disk is imaged by the lens into the far field at the mirror-pair center and vice versa.

If the intercept (center) of the mirror pair was located on the disk-lens axis, the light would propagate in this optical system in a closed loop as in a resonator. However, by displacing the mirror-pair center by Δy , as shown in the figure, a multi-pass configuration can be realized. The resulting far-field spacing of the various beam passes is $2\Delta y$. The shift of the mirror-pair center relative to the common disk lens axis breaks the symmetry, which is necessary for the realization of a multi-pass scheme. The size of Δy controls the number of achievable passes, given constraints from the laser beam size, restrictions related with astigmatism, and the size of the various optical elements.

A common feature of multi-pass propagation is that the number of passes can be doubled by placing a back-reflector at its end, causing the beam to retrace itself traveling in the opposite direction. For pump beams, the residual beam not absorbed in the disk after the back-and-forth propagation is consequently sent back to the homogenizer of the pump diodes.

10.3. State of the art of the commercial multi-pass pump systems

A typical pump optics system for thin-disk lasers originally proposed in [265] and now available at TRUMPF, IFSW, and Dausinger + Giesen is shown in Figure 124. It consists of a disk, a large parabolic mirror with focal length f , and two mirror pairs (HR coated prism pairs). Similar to the previous example, the distances between disk and parabolic mirror, and between parabolic mirror and prisms intersects, are f . For the

realization of a multi-pass propagation, the symmetry of the optical layout has to be broken. Instead of shifting the mirror pair off-axis, as was done previously, in this case the symmetry is broken by rotating one prism pair by an angle ϕ_1 relative to the other pair, as depicted in Figure 126.

To understand the beam routing in the multi-pass pump optics, consider Figure 126 (b). The position of the pump beam at the mirror-pairs plane (and at the parabolic mirror as the collimated pump beams are parallel) is indicated by the numbering. Number 1 represents the position of the collimated in-coupled beam. After a reflection at the parabolic mirror the beam travels to the disk (red central circle). The remaining pump light reflected from the disk subsequently reaches position 2 at the first mirror pair after a second collimation at the parabolic mirror. From there the pump beam is redirected within the same mirror pair to reach position 3. Thereafter, it is sent toward the parabolic mirror, disk, parabolic mirror to reach position 4 on the second mirror pair. Via a path within this second mirror pair the beam reaches position 5 where it is redirected again toward the disk (third reflection at the disk) and from there eventually to position 6. At position 6 the beam is back-reflected, giving rise to a propagation in the opposite direction, which results in a doubling of the number of pump passes on the disk.

The relative rotation of the mirror-pair intercepts by an angle ϕ_1 gives rise to a rotational symmetric beam spot pattern with a spot-to-spot angle of $2\phi_1$. In this design, all far-field beams have the same radial distance from the optical axis, resulting in a central region free of pump-beam spots. (Near field is used for beams at the disk, far field for beams at the mirror pair plane, as defined in Figure 125.) Therefore, the mechanics holding the mirror pair can have a central aperture, as shown in Figure 126 (a), in which the thin disk can be placed. Similarly, the parabolic mirror can have a central aperture, as shown in Figure 124 (b) and (c), for laser beam access. In such a way, the radial symmetric beam pattern allows the use of a parabolic mirror instead of a lens, as in the example of Figure 125, which yields a folding of the beam propagation so that geometrically the plane of the mirror pair coincides with the disk plane. Thus, the utilization of a parabolic mirror reduces the size of the multi-pass pump optics, leads to smaller absorption losses, and offers the possibility of elegant laser beam coupling [see off-axis aperture in Figure 126 (a)]. The most natural way to increase the number of pump passes would be to reduce the angle ϕ_1 , as shown in Figure 126 (c).

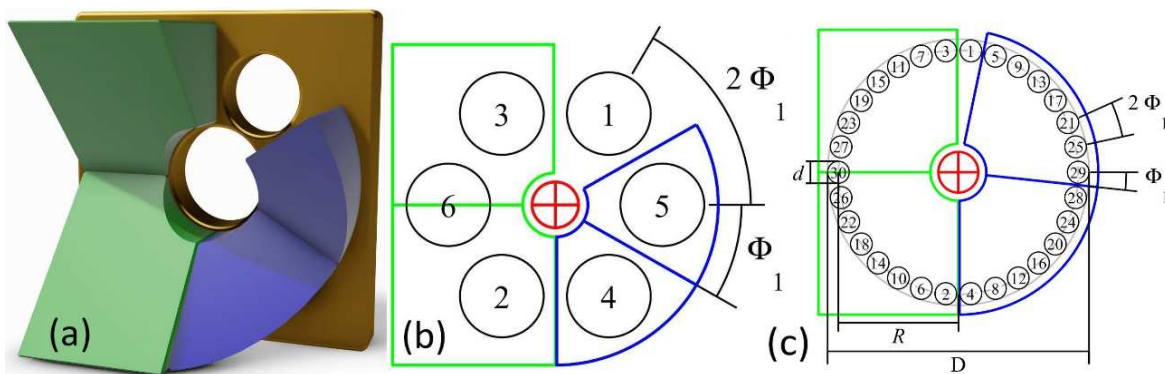


Figure 126: Schematics of the mirror pairs and multi-pass beam routing at the parabolic mirror and mirror-pairs plane. (a) 3D arrangement of the mirror (prism) pairs commercially available. (b) Mirror-pair contours and beam routing (which follows the given numbering) for six reflections (12 passes) at the disk. The disk position is given in red. The second mirror pair (blue) is rotated by an angle $\phi_1 = 30^\circ$ relative to the first mirror pair (green). At position 6 the beam is back-reflected, doubling the number of passes. (c) Schematic for 30 reflections (60 passes) at the disk achieved by decreasing the angle ϕ_1 .

The number of passes N is given by $N = 2 \times 180 / \phi_1$, where ϕ_1 is expressed in degrees. The factor of 2 originates from the fact that each reflection corresponds to two passes in the active material. Furthermore, this equation assumes that the pump beam propagates back and forth in the multi-pass segment due to the back-reflector [placed, e.g., at position 6 in Figure 126 (b), or at position 30 in Figure 126 (c)].

However, an increase of passes by decreasing the angle ϕ_1 (assuming the same parabolic mirror size and focal length f) can be realized only by decreasing the far-field beam spot size. Overlapping of the far-field spots (spots at the mirror-pairs plane) is not acceptable because it implies aperture losses at the beam in-coupling. For large N the maximal diameter d of a single far-field beam spot, as can be seen in Figure 126, is given by $d = 2\pi R / N$, where R is the radial distance of the pump beams from the optical axis at the parabolic mirror position. This implies $1/N$ scaling of the pump beam parameters product and a poor usage of the mirror pairs and parabolic mirror surfaces. However, if the total surface of the parabolic mirror was used, the diameter of the far-field spots would shrink approximately only as $N^{-1/2}$.

A scheme that makes use of a much larger fraction of the parabolic mirror surface is presented in Sec. 10.5. This scheme thus allows for scaling of the number of passes while only moderately increasing the demands on the quality of the pump source. Before describing this scheme, for didactic reasons in Sec. 10.4 a multi-pass layout is presented that forms one of the building blocks of the final schemes.

10.4. Two mirror pairs whose intersects meet off-axis

The generalized pump schemes we propose and which are detailed in the next section rest on two building blocks. The first one is given by the standard pump optics described in Sec. 10.3. The second one, described in this section, is a design also realized with only a disk, a parabolic mirror, and two mirror pairs, as shown in Figure 127.

Different from the layout of Figure 126, the second mirror pair is rotated relative to the first one by an angle ϕ_2 not around the disk axis but around an axis shifted by an offset ΔX , as shown in Figure 127 (a). The resulting distribution of the far-field spots is located on two separate circles. Similar to previous configurations, the number of passes is dictated by the angle of rotation, whereas the radius of these circles is given by the distance of the in-coupled beam to the center of the first mirror pair depicted in green.

The beam is traveling in between mirror pairs, parabolic mirror and disk. The beam routing starts from the aperture (slit between the green mirror pair) at position 1 of the first mirror pair and reaches position 2 at the second mirror pair (blue) after a reflection at the disk and two reflections at the parabolic mirror. From position 2, the beam is redirected within the second mirror pair to position 3. From position 3, it travels back to the first mirror pair via a reflection at the disk and two reflections at the parabolic mirror to reach position 4. Within the first mirror pair the beam travels from position 4 to 5, and from there it is sent again toward the disk. Iterating this scheme, several passes at the disk are realized, while the beam position at the mirror pairs travels the given numbering.

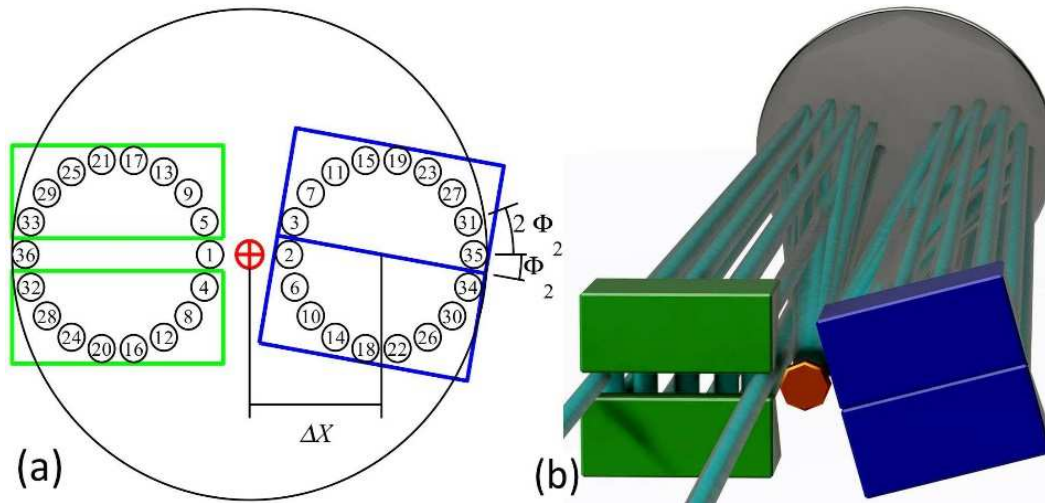


Figure 127: (a), multi-pass configuration resulting from two mirror pairs (prism pairs) whose intersects do not cross at the optical axis but at a point with ΔX offset. (b) Corresponding 3D drawings. Mirror pairs are given in blue and green, the disk in red, and the parabolic mirror in gray.

For a large number of passes, this multi-pass scheme requires large pump optics and shows a poor utilization of the parabolic mirror surface. Therefore, when used as shown in Figure 127, it is not suited for the realization of compact pump optics. However, when combined with other schemes as detailed in the next section, layouts with more efficient usage of the parabolic surface can be realized. Still, this scheme as such (as in Figure 127) can be used to design multi-pass laser amplifiers with a large number of passes, because of the typically better beam parameter products of the laser beams and the less stringent size limitations.

10.5. Design with many more passes

By merging the two concepts presented in Figure 126 and Figure 127, we can realize a multi-pass scheme with an increased number of passes while at the same time making efficient use of the surface of the parabolic mirror. Before proceeding to develop in a detailed way the ideas behind our configurations, the merging process yielding the simple layout of Figure 128 (d) is quickly introduced. The starting point is the setup of two mirror pairs (green and blue), as in Figure 128 (a), very similar to the setup in Figure 126. Adding two more mirror pairs (magenta and cyan) as shown in Figure 128 (b) results in an arrangement of four mirror pairs, as depicted in Figure 128 (c), which can be simplified to the three-mirror-pair setup shown in Figure 128 (d).

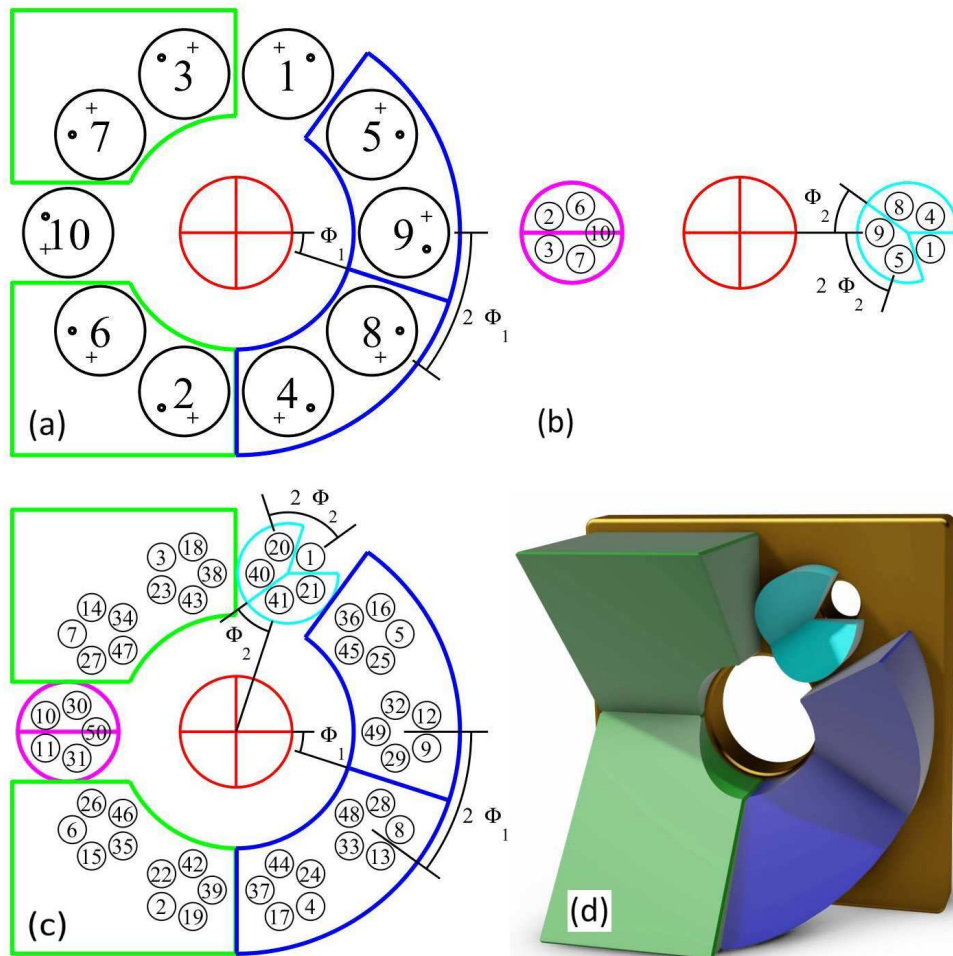


Figure 128: Principle of the merging of the two multi-pass schemes of Figure 126 and Figure 127. (a) Similar mirror-pair scheme as in Figure 126 for 20 passes. The slightly different position of the in-coupled light in region 1 is producing the pattern indicated by the black dots at the various numbered regions. The crosses represent the beam position after the first reflection at the mirror pair in region 10. (b) Similar mirror-pair scheme as given in Figure 127 for 20 passes. (c) The merging of the multi-pass scheme given in previous panels produces a beam propagation pattern of 100 passes. (d) 3D representation of the three mirror pairs needed to realize the 100 pass scheme of panel (c). The red circles represent the position of the thin disk; the blue, green, magenta, and cyan contours represent the first, second, third, and fourth mirror pairs, respectively.

In more detail, this merging proceeds in the following way. The panel (a) shows the same two mirror-pairs arrangement as in Figure 126, but contrarily to that situation, here the beam is not coupled in the center of region 1 but with a small displacement relative to the center of region 1. Starting from this initial position, the pump beam travels in the pump optics following the given numbering at the positions indicated by the black dots, until it eventually reaches region 10. At this position, a third mirror pair is placed, corresponding to the magenta mirror pair of panel (b). This third mirror pair reflects the beam within region 10, from the black dot to the black cross. From there, the beam undergoes a propagation indicated with the crosses back to region 1. At position 1, a fourth mirror pair corresponding to the cyan mirror pairs of the panel (b) is introduced, completing in this way the merging of the two concepts. The orientation of this fourth mirror pair is such as to reflect the beam within region 1 at the position indicated with the empty square. Similar to before, starting from this position, propagation until region 10 is followed. By iterating this scheme, a large number of passes on the disk can be realized.

Panel (c) of Figure 128 displays the arrangement of all optical elements resulting from the merging of the two multi-pass schemes of panels (a) and (b). The pump beam propagation follows the indicated numbering yielding $N = 2 n m = 2 (180/\phi_1) (180/\phi_2)$ passes, where ϕ_1 and ϕ_2 are the angular tilts in degrees of the second and fourth mirror pairs, respectively. In addition, in this case N accounts for back-and-forth propagation in the multi-pass segment. The needed back-reflection at position 50 in panel (c) is realized by the magenta mirror pair. The numbers n and m, which represent the number of reflections at the disk for the two separate multi-pass concepts, are used to classify the various configurations resulting from the merging process.

In this case, the third (magenta) mirror pair was introduced just for didactic reasons: to better highlight the principle of the merging process. In fact, in this particular case, its functionality can be realized by the first mirror pair [see panel (d)], but this does not apply generally [see, e.g., Figure 129 (a)].

In conclusion, by adding only a small mirror pair in the region of the in-coupled beam [see Figure 128(d)], the number of pump passes relative to a standard pump optics design can be increased by a factor of $(180/\phi_2)$. Moreover, the individual beam spots at the mirror pair and at the parabolic mirror are larger than in the standard configuration, assuming the same parabolic mirror and number of passes, because of the better usage of the parabolic mirror surface. Hence, the demands for the pump source phase-space quality or pump optics size are decreased relative to the standard configurations.

The merging described here can be interpreted as a generalization of the concept exploited already by TRUMPF [36] and shown in Figure 129 (b). In our scheme, the TRUMPF layout can be classified as an $n \times m = 6 \times 3$ configuration leading to 36 passes in the disk. In panel (a) a 10×2 and in panel (c) a $6 \times 3 \times 3$ configuration is shown. The latter demonstrates that our merging processes can be iterated several times. Moreover, our merging process can be applied for various initial configurations.

A comparison of the various configurations is shown in Figure 130, where the “filling factor” F is plotted against the number of pump passes. F is defined as the ratio of the beam spots area at the parabolic mirror over the parabolic mirror area: $F = N d^2/(2D^2)$, where d is the individual beam spot diameter in the far field and D the parabolic mirror diameter [see Figure 126 (c)]. F has been computed using the paraxial approximation. For the real situation, the “filling factor” differences between the various configurations are slightly larger due to the focal length increase of the parabolic mirror with increasing distance from the axis.

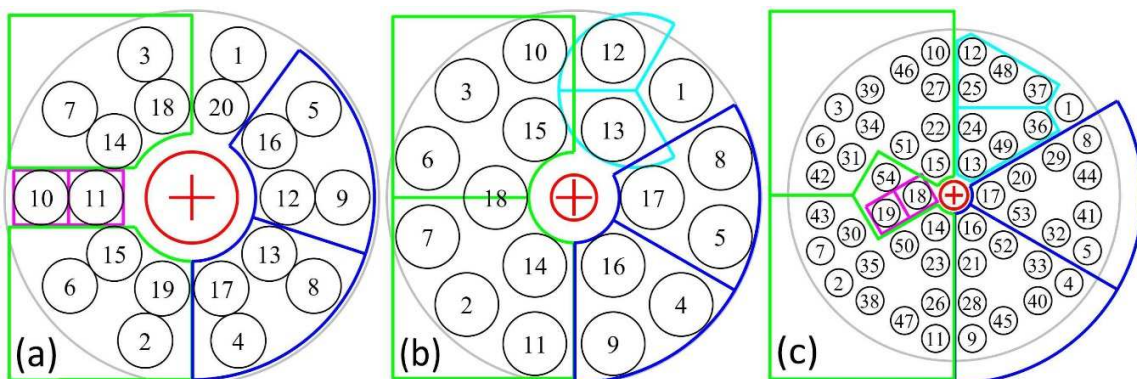


Figure 129: (a) 10×2 configuration yielding 40 passes. The third mirror pair in this case has been rotated by 90° compared to the merging process described above. (b) 6×3 configuration yielding 36 passes as implemented by TRUMPF and (c) $6 \times 3 \times 3$ configuration that results by iterating twice a merging process resulting in 108 passes.

For the standard design of Figure 126, $D = 2R + d$. For large N , $D \approx 2R$ and $R \approx Nd/(2\pi)$ applies. Thus, in this limit the “filling factor” scales as $F \sim 1/N$. For small N , these approximations do not apply and the “filling factor” increases with N , as is well visible from the plot.

Similar behavior versus N is found for other configurations. As a rule of thumb, with increasing m the maximal “filling factor” is reached for larger values of N . The overall maximal “filling factor” is obtained for the $N = 36$ design, resulting from the 6×3 configuration of TRUMPF depicted in Figure 129 (b). For $N = 108$, the configuration $6 \times 3 \times 3$ of Figure 129 (c) shows by far the highest “filling factor”.

Knowing the “filling factor” and the number of passes of a given configuration, it is possible to determine the minimal diameter D of the parabolic mirror and the maximal beam parameters product P of the pump source:

$$D > \sqrt{\frac{8N}{F}} \cdot \frac{Pf}{d_{pump}} \quad (153)$$

$$P < \sqrt{\frac{F}{8N}} \cdot \frac{Dd_{pump}}{f} \quad (154)$$

where d_{pump} is the pump spot diameter at the disk and f the focal length of the parabolic mirror. The optimal scheme that is used in each particular application is a trade-off between the number of passes needed, pump module size, and the quality and costs of the available pump source. Another aspect that must be considered is the misalignment sensitivity of the pump optics and the related required manufacturing precision. Figure 131 shows misalignment plots for various pump schemes. For an ideal alignment, each pump spot perfectly overlaps in the center of the disk. However, practically, deviations from the ideal situation occur: for example, the mirrors forming the mirror pairs may not be exactly orthogonal to each other, or the mirror-pair intersects may not be perfectly orthogonal to the symmetry axis.

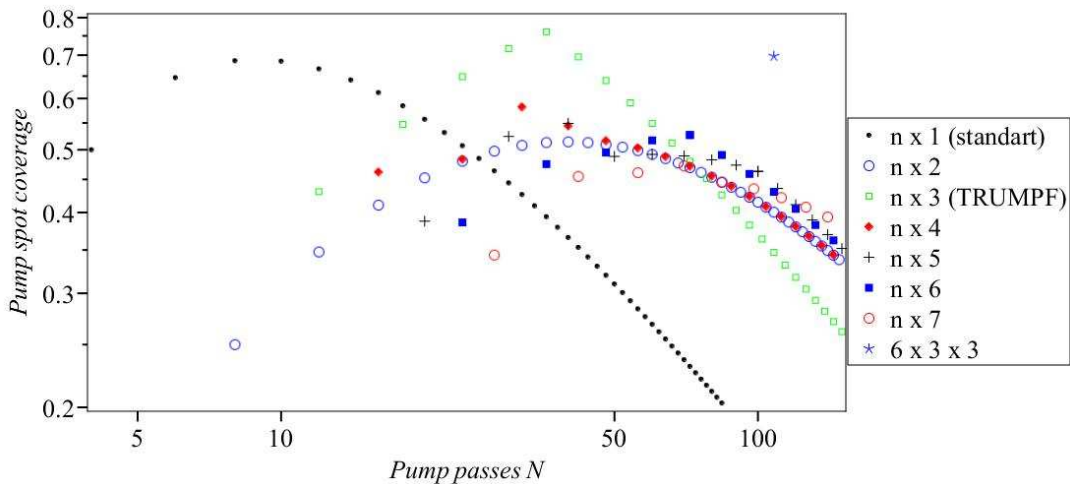


Figure 130: “Filling factor” F for various configurations versus number of passes N classified using the $n \times m$ nomenclature and computed using the paraxial approximation. The $n \times 1$ configuration represents the standard layout of Figure 126, the TRUMPF design corresponds to the maximum of the $n \times 3$ configuration, and the star represents the $6 \times 3 \times 3$ configuration of Figure 129 (c).

These misalignments give rise to deviations of the various pump spots from the center of the disk. Because of the rotation of the pump beam, compensation occurs while propagating in the standard pump optics so that the deviations of the pump spots from the ideal position first increase and then decrease, as indicated by the numbering in Figure 130. As the average deviation grows with the number of passes N , well visible by comparing the red circles with the green squares, misalignment effects become more severe for pump optics with large number of passes. However, in our design the large number of passes is reached starting from a standard design with a small number of passes. Thus, the deviations caused by misalignments are mitigated in our schemes compared with the standard design having the same number of passes so that the presently used manufacturing precision is sufficient.

10.6. Particular example based on a 6×6 configuration with triangular input aperture

Realization of 72-pass pump optics resulting from a 6×6 configuration is presented in Figure 132. Two large hexagonal mirror pairs, two small mirror pairs, and a flat end mirror are used in this configuration. The hexagonal mirrors, placed as shown in Figure 132 (a) 140 (b), naturally give rise to the central aperture necessary for the laser beam without the need for intensive manufacturing related with “internal” cutaways as, e.g., necessary for the prisms of Figure 128 (d). The beam losses occurring at position 6 of Figure 126 (b) or at position 50 of Figure 128 (c) at the mirror-pair intersects are not present in this configuration because at position 36 we are simply using a flat mirror as back-reflector (when high power is requested, frequently the commercially available pump optics based on the Figure 126 (b) design at position 6 (or equivalent positions) is equipped with a back-reflector to avoid losses that would be caused by the mirror-pair intersect.), qualifying this scheme for improved efficiency and power scaling.

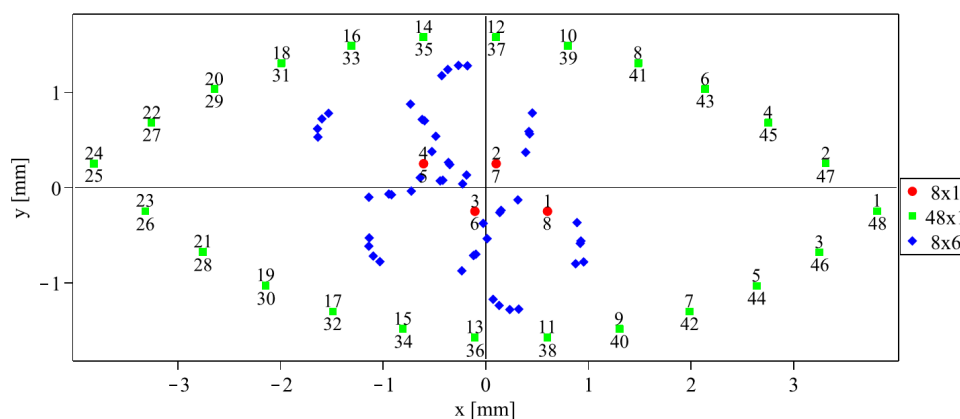


Figure 131: Example of a misalignment plot showing the deviation of the various pump beam passes at the position at the thin disk for a departure of the angle between the two mirrors forming the first mirror pair (given in green in all figures) by 2.5 mrad from 90°. The parabolic mirror has a focal length of 200 mm. The red points represent the deviation for the various passes in the standard 8×1 design with $N = 16$, the green squares for the standard 48×1 design with $N = 96$, and the blue diamonds for our 8×6 configuration also with $N = 96$. The numbering, which for clarity has been applied only to the standard configurations, represents the pass number along the pump beam propagation. Similar plots are obtained for other misalignments.

The triangular input aperture, which is successively imaged on the various hexagonal mirrors, seems strange for a pump optics design since the profile of commonly used homogenized pump radiation is usually rotationally symmetric. However, when high pump power is required, several collimated parallel beams could be combined to illuminate the triangular input aperture. The most homogeneous way to illuminate the triangular input aperture is achieved by placing 3, 6, 10, 15 or more pump diode homogenizer outputs on a hexagonal grid as shown in Figure 132 (c). Even though at the input-beam aperture (far field) the various parallel beams are located at different positions, the parabolic mirror merges them into a single round spot at the disk position. Large pump power density at the disk can be reached in this way, with pump diameter given by the individual pump source outputs characteristics (beam parameters product P).

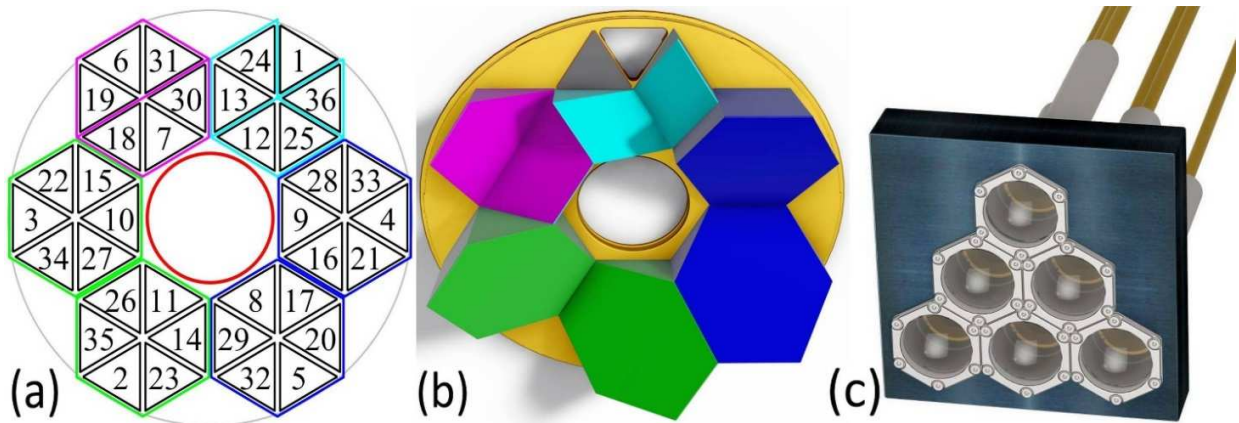


Figure 132(a): 6×6 configuration yielding 72 passes based on hexagonal mirror-pairs. (b) 3D drawings of the mirror pairs. These hexagonal-shaped mirror pairs are particularly suited for a triangular illumination that can be formed by merging several collimated beams arranged on a hexagonal lattice as shown in (c) and imaging them after appropriate magnification at the input beam triangular aperture (at position 1).

10.7. Conclusions

A general scheme for multi-pass $4f$ pump optics suited for thin-disk lasers has been presented here that can accommodate a large number of passes while keeping the requirements for the pump source beam quality moderate. A particular realization of this general scheme can be simply achieved by inserting a small additional mirror pair at the input beam position of a standard pump design. In such a way, the same pump optics can be operated, on the one hand, without this new additional mirror pair, for example, for high energy pulsed pumping and thick disks. On the other hand, by inserting a mirror pair at the in-coupling position tilted by 90° , 60° , and 30° , the number of passes can be increased by factors of 2, 3, and 6, respectively, for the case that larger numbers of passes are needed. Thus, it is straightforward to adapt the number of passes to the given pump source quality and active medium properties. We also presented some simple formulas that can be used to estimate the maximal beam parameters product that a pump source must have, or the minimal parabolic mirror diameter, given a certain configuration and number of passes.

The increased number of passes achievable by using the schemes presented here, which is particularly important for active media having small single pass absorption (due to smaller disk thickness, lower doping, lower active medium absorption cross section, and smaller absorption bandwidth), yields increased efficiency, enabling power scaling, lower lasing threshold, and development of a low-latency thin-disk laser system for the 2S – the use of different materials.

11. Appendix A: 2S-2P resonances in $\mu^3\text{He}$ and $\mu^4\text{He}$

In this appendix, we present the five resonances measured between the 2S and the 2P states in $\mu^4\text{He}$ and $\mu^3\text{He}$. Their linewidths are about 320 GHz at FWHM given by the lifetime of the 2P state. The absolute position of the resonance is not given, as the results are only preliminary. The data analysis for the $2S_{1/2} - 2P_{3/2}$ transition in $\mu^4\text{He}$ which is shown in Figure 133 is more advanced compared to the other resonances shown in Figure 134, Figure 135 and Figure 136 which were obtained using the online analyzer during data taking. We know from the analysis of the $2S_{1/2} - 2P_{3/2}$ transition in $\mu^4\text{He}$ that the signal to background ratio of these resonances will increase by about a factor of two when the analysis will be completed. For a detailed description of the analysis, the reader is referred to [76, 274].

The resonances were searched and scanned by stabilizing the laser frequency to a calibrated Fabry-Perot peak and then shooting the laser for about 1-2 h to record the laser induced 8 keV X-rays. The laser frequency was set to the same frequency point several times to average possible systematic effects related with the performance of the laser system. In each point 5-20 h of statistics were accumulated depending on the performance of the accelerator and of the laser system, the resonance addressed and the laser frequency relative to the center of the resonance.

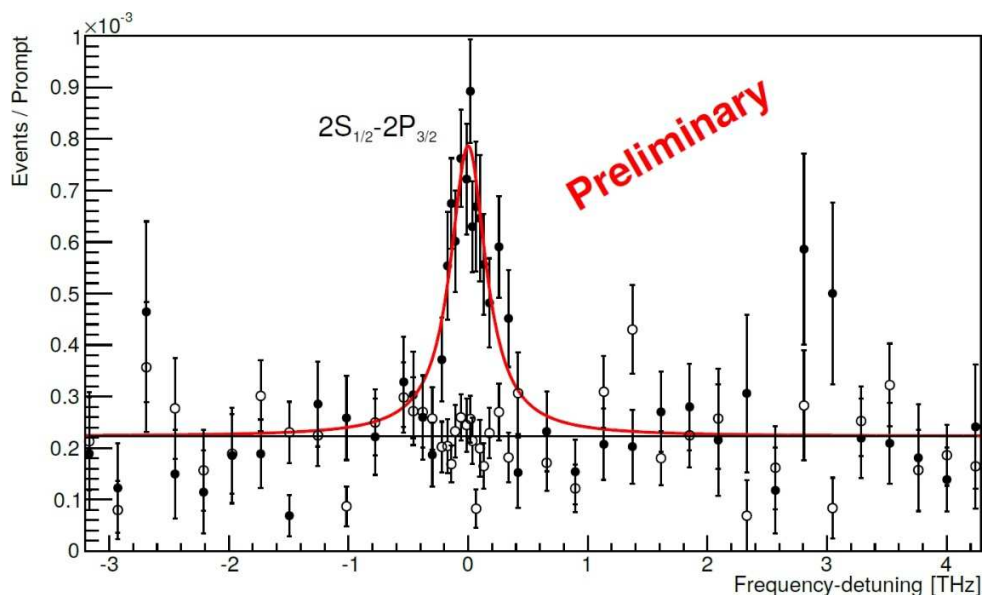


Figure 133: $2S_{1/2} - 2P_{3/2}$ resonance in $\mu^4\text{He}$ (black points). The red curve is a fit to these points using a Lorentzian line shape model. The final line shape model will account for fluctuations of the laser pulse energy. The hollow circles are measurements of the background collected at the same conditions but for muons when the laser was not fired. The background was fitted with a constant (black line).

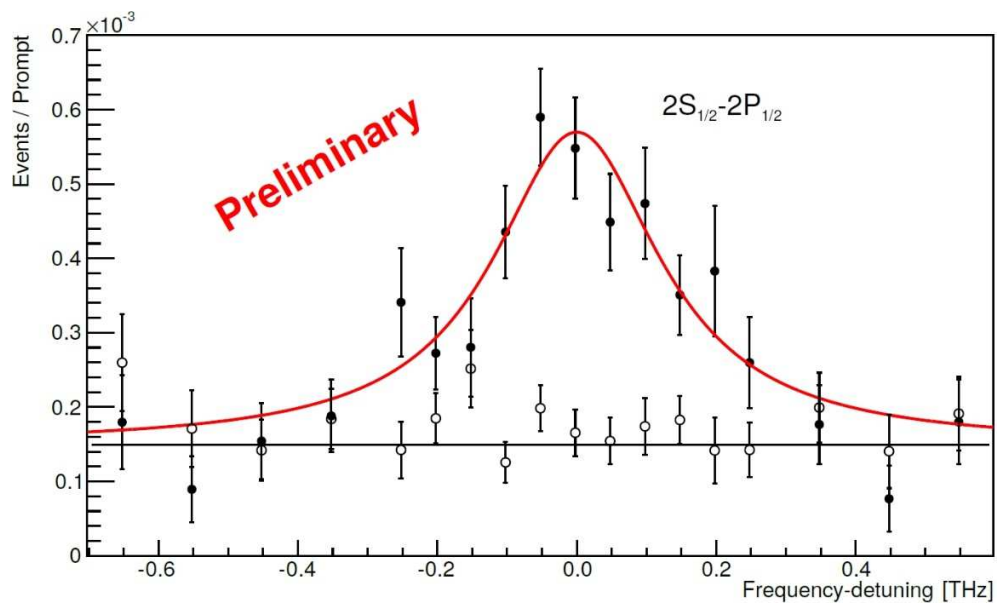


Figure 134: Similar to Figure 133 but for the $2S_{1/2} - 2P_{1/2}$ resonance in $\mu^4\text{He}$. The resonance was obtained using the online analyzer during data taking.

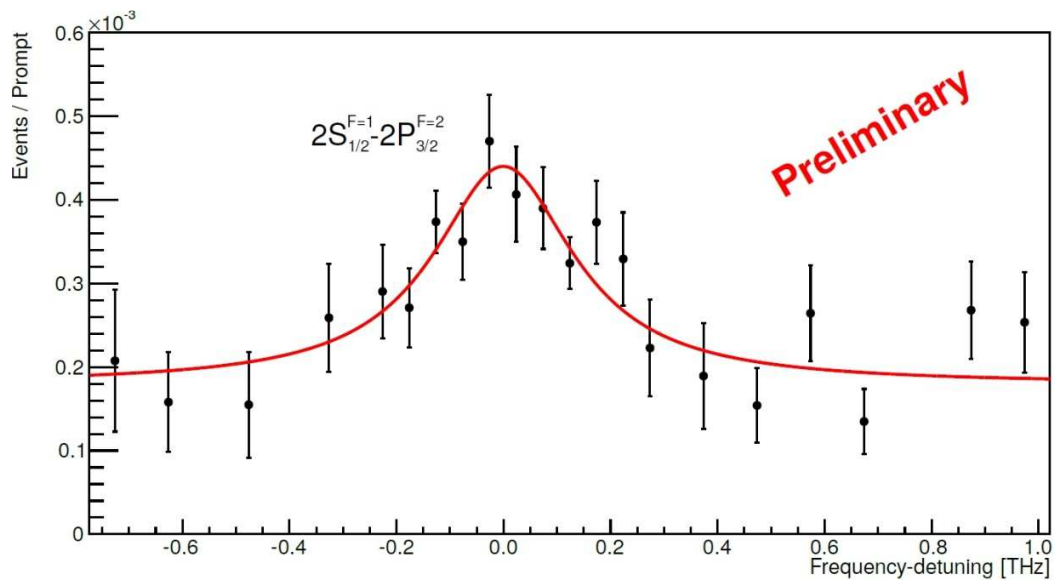


Figure 135: Similar to Figure 133 but for the $2S^{F=1}_{1/2} - 2P^{F=2}_{3/2}$ resonance in $\mu^3\text{He}$. The resonance was obtained using the online analyzer during data taking.

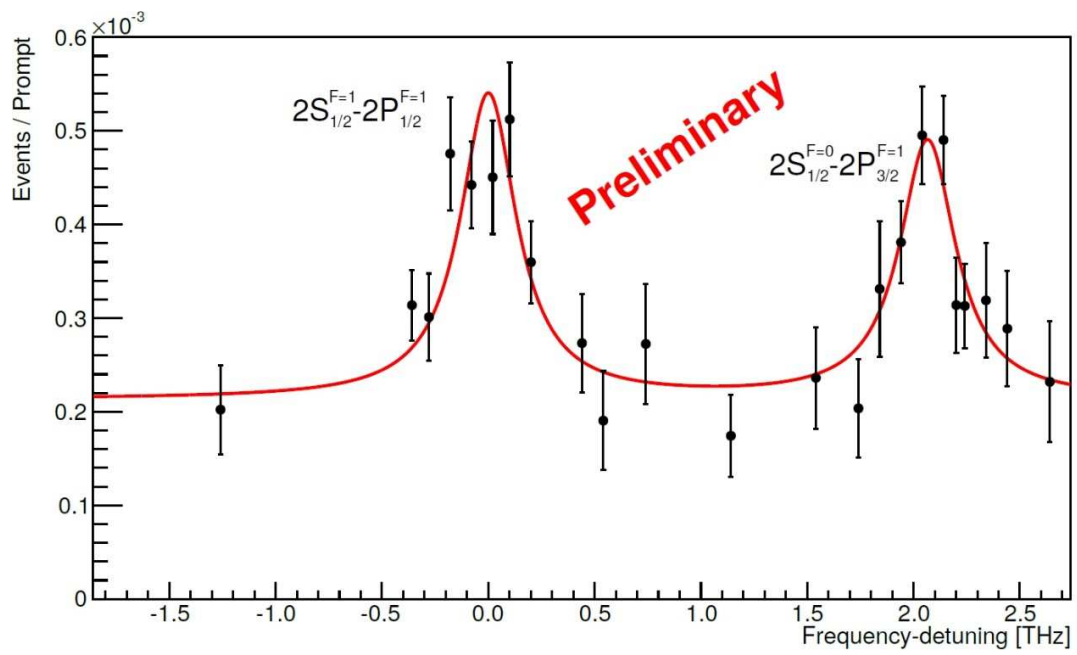


Figure 136: Similar to Figure 133 but for the $2S_{1/2}^{F=1} - 2P_{1/2}^{F=1}$ and $2S_{1/2}^{F=0} - 2P_{3/2}^{F=1}$ resonances in $\mu^3\text{He}$. The resonance was obtained using the online analyzer during data taking.

12. Appendix B: Interferometric measurement of the thermal lens

In this section, we present the experimental aspects related with the quantification of the thermal lens effect of a thin disk. A Twyman-Green interferometer [275, 276, 277], an imaging version of a Michelson interferometer [278], has been used for this purpose. In short, the thin disk is placed in one arm of the interferometer, and the reference mirror is placed in the other arm. The interferometric images resulting from the interference of the two beams have been recorded for small variations of the distance of the reference mirror, i.e. the interferometer was operated using the so-called phase-shift method [279, 280, 281]. In a next step, the position-dependent optical phase delay $OPD(x, y)$ experienced by a laser beam at the thin disk is retrieved from the interferograms. Finally, the $OPD(x, y)$ is fitted with a second order polynomial to extract the spherical component of the OPD which corresponds to the shape of the thin disk.

12.1.1. The Michelson interferometer

A sketch of a Michelson interferometer is displayed in Figure 137. An incoming laser beam is partially reflected and partially transmitted at a beam splitter (BS). The transmitted laser beam moves towards the mirror M1 (specimen, thin disk) while the reflected beam moves towards the reference mirror M2. Both mirrors M1 and M2 back-reflect the impinging laser beams. The reflected beams travel back to the beam splitter where each of them are partially reflected and partially transmitted.

As a result, there are two beams moving towards the detector and two beams moving back to the laser. Each pair of beams interfere according the optical phase accumulated in the two interferometer arms. Therefore, the measured intensity at the detector depends upon the difference of optical phase delay accumulated in the two arms. The intensity depends thus on the path length difference $d_1 - d_2$ where d_1 is the distance BS-M1 and d_2 the distance BS-M2.

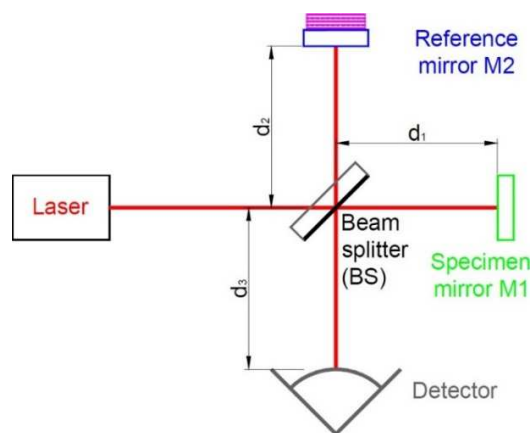


Figure 137: Michelson interferometer with the corresponding optical path.

Let us assume that the laser beam incident on the beam splitter has an amplitude $E_0 e^{i\omega t}$. The two beams leaving the beam splitter have an amplitude of $\sqrt{R_{BS}} E_0 e^{i(\omega t + \pi)}$ and $\sqrt{1 - R_{BS}} E_0 e^{i\omega t}$, respectively where R_{BS} is the reflectivity of the beam splitter. We assumed for simplicity and without loss of generality that both beams start from the beam splitter with phases equal to zero. The additional phase delay described by the factor of $e^{i\pi}$ in the reflected beam is arising because the reflection occurs at the interface between a medium with high refraction index and a medium of low refraction index with impinging and reflected beam remaining in the medium with high refraction index (see Figure 137).

After propagating in the two arms and returning to the beam splitter, the two beams acquire a phase delay that depends on the travelled path length so that their amplitudes before reaching the beam splitter are

$$E_{M1} = \sqrt{1 - R_{BS}} E_0 e^{i(\omega t - 2kd_1)} \quad (155)$$

and

$$E_{M2} = \sqrt{R_{BS}} E_0 e^{i(\omega t - 2kd_2 + \pi)}, \quad (156)$$

where k is the wave vector. Here we assumed a reflectivity of 100 % for the M1 and M2 mirrors. The amplitudes of the two beams reaching the detector after reflection and transmission at the beam splitter respectively are

$$E'_{M1} = \sqrt{R_{BS}(1 - R_{BS})} E_0 e^{i(\omega t - k(2d_1 + d_3))} \quad (157)$$

$$E'_{M2} = \sqrt{R_{BS}(1 - R_{BS})} E_0 e^{i(\omega t - k(2d_2 + d_3) + \pi)}, \quad (158)$$

where d_3 is the distance between the detector and the beam splitter. The reflection of the laser beam travelling back from the mirror M1, does not produce any phase jump of $e^{i\pi}$ because in this case the reflection occurs at the interface between a medium with low refraction index and a medium of high refraction index, with impinging and reflected beam remaining in the medium with low refraction index. Because the absolute value of both amplitudes is equal to

$$E_d = E_0 \sqrt{R_{BS}(1 - R_{BS})} \quad (159)$$

maximal interferometric contrast for any value of the reflectivity R_{BS} is obtained. The total amplitude at the detector position is given by the superposition of the two beams

$$E_{tot} = E_d [e^{i(\omega t - k(2d_1 + d_3))} + e^{i(\omega t - k(2d_2 + d_3) + \pi)}] = E_d \left[1 + e^{2ik(d_1 - d_2 + \frac{\pi}{2})} \right] e^{i(\omega t - k(2d_1 + d_3))}. \quad (160)$$

As the detector can measure only intensities, we evaluate the intensity produced by the total amplitude averaged over time

$$I_{det} = \langle |E_{tot}|^2 \rangle = 2E_d^2 \left[1 + \sin \left(2\pi \frac{2}{\lambda} (d_1 - d_2) \right) \right], \quad (161)$$

where $\lambda = 2\pi/k$ is the laser wavelength. As visible from Eq. (161), the intensity depends on the path difference $d_1 - d_2$ of the two arms of the interferometer. For a given value of λ , I_{det} , E_d and d_2 the distance d_1 can be evaluated. However, no unique solution exists, but two sets of solutions each with a periodicity of $\lambda/2$. This is usually not a problem because we are typically interested in small variations of the path length difference $d_1 - d_2$ and not in the absolute value of d_1 .

In practice, uncertainties have to be considered: the laser intensity is not precisely known, the sensitivity of the detector is usually not calibrated, there is background light and the mirrors M1 and M2 may not have the same reflectivities, spoiling intensity and contrast of the measured interference pattern. Hence, in the practical application the measured intensity takes the form

$$I_{exp} = I_{mean} + I_{mod} \sin\left(2\pi \frac{2}{\lambda}(d_1 - d_2)\right), \quad (162)$$

where the parameters I_{mean} and I_{mod} need to be determined experimentally. By measuring the intensity I_{exp} for various distances d_2 of the reference mirror M2, the three unknown parameters I_{mean} and I_{mod} and $d_1 - d_2$ (modulo $\lambda/2$) can be extracted. The measured intensity at the detector shows a sinusoidal modulation for variations of d_2 , which can be fitted to extract the unknown parameters assuming that λ is known. We also assume here that the variations of d_2 are known. To extract these three parameters at least three independent measurements for three different distances d_2 have to be performed.

Let us rewrite Eq. (162) using the total phase accumulated in the two arms: ϕ for the M1 arm and φ for the M2 arm:

$$I_{exp} = I_{mean} + I_{mod} \sin(\phi - \varphi). \quad (163)$$

N measurements of the intensity $I_n \equiv I_{exp,n}$ at the detector position for different mirror M2 positions lead to N equations of the form:

$$\frac{I_n - I_{mean}}{I_{mod}} = \sin(\phi - \varphi_n) = \sin(\phi) \cos(\varphi_n) - \cos(\phi) \sin(\varphi_n), \quad (164)$$

where n runs from $1 \dots N$, and φ_n is the accumulated phase delay for the M2 branch for the various $d_{2,n}$ distances. By making use of two measurements (a and b) and combining two equations of the type of Eq. (164) we obtain:

$$\sin(\phi) = \frac{I_{mean}(\cos(\varphi_a) - \cos(\varphi_b)) + I_b \cos(\varphi_a) - I_a \cos(\varphi_b)}{I_{mod} \sin(\varphi_b - \varphi_a)} \quad (165)$$

$$\cos(\phi) = \frac{I_{mean}(\sin(\varphi_a) - \sin(\varphi_b)) + I_b \sin(\varphi_a) - I_a \sin(\varphi_b)}{I_{mod} \sin(\varphi_b - \varphi_a)} \quad (166)$$

where I_a, I_b are the measured intensities, and φ_a, φ_b known phase shifts of the reference mirror M2. These equations can be rewritten as

$$I_{mod} \sin(\varphi_a - \varphi_b) \sin(\phi) = I_{mean}(\cos(\varphi_b) - \cos(\varphi_a)) + I_a \cos(\varphi_b) - I_b \cos(\varphi_a) \quad (167)$$

$$I_{mod} \sin(\varphi_a - \varphi_b) \cos(\phi) = I_{mean}(\sin(\varphi_b) - \sin(\varphi_a)) + I_a \sin(\varphi_b) - I_b \sin(\varphi_a). \quad (168)$$

Equations (167) and (168) are obtained using only two (independent) measurements. Similarly, Eq. (163) for N measurements we obtain

$$\sin(\phi) I_{mod} \sum_{n=1}^N \sin(\varphi_n - \varphi_{n+1}) = \sum_{n=1}^N (I_{mean}(\cos(\varphi_{n+1}) - \cos(\varphi_n)) + I_n \cos(\varphi_{n+1}) - I_{n+1} \cos(\varphi_n)), \quad (169)$$

where we define $\varphi_{N+1} = \varphi_1$ and $I_{N+1} = I_1$. Because

$$\sum_{n=1}^N (I_{mean} (\cos(\varphi_{n+1}) - \cos(\varphi_n))) = 0,$$

Eq. (169) simplifies to

$$\sin(\phi) I_{mod} \sum_{n=1}^N \sin(\varphi_n - \varphi_{n+1}) = \sum_{n=1}^N (I_n \cos(\varphi_{n+1}) - I_{n+1} \cos(\varphi_n)). \quad (170)$$

Similarly to Eq. (168) from Eq. (164) for N measurements we obtain

$$\cos(\phi) I_{mod} \sum_{n=1}^N \sin(\varphi_n - \varphi_{n+1}) = \sum_{n=1}^N (I_n \sin(\varphi_{n+1}) - I_{n+1} \sin(\varphi_n)). \quad (171)$$

Dividing Eq. (170) with (171) leads to [279, 280, 281]

$$\tan(\phi) = \frac{\sin(\phi)}{\cos(\phi)} = \frac{\sum_{n=1}^N (I_n \cos(\varphi_{n+1}) - I_{n+1} \cos(\varphi_n))}{\sum_{n=1}^N (I_n \sin(\varphi_{n+1}) - I_{n+1} \sin(\varphi_n))}. \quad (172)$$

Therefore, the phase ϕ related to the interferometer arm containing the specimen (thin disk) can be retrieved by measuring the intensities I_n at the detector for various known phases φ_n of the reference mirror M2.

As previously mentioned the minimal number of needed measurements is three. A larger number increases the measurement precision. An optimal fitting of the sinusoidal function requires an equidistant placement of the measurements for variations of d_2 up to $\lambda/2$. Other algorithms to retrieve the phase can be used even for unknown phase shifts [280, 281].

12.1.2. Twyman-Green interferometer

The Twyman-Green interferometer is the imaging version of the Michelson interferometer. As displayed in Figure 138 in the Twyman-Green interferometer the specimen surface is imaged using a large aperture lens to the detector that allows the recording of a 2D-intensity distribution. The detector thus records a position dependent intensity distribution $I(x,y)$ which can be used to reconstruct the “height-profile” of the specimen surface. More precisely, the measured intensities $I(x,y)$ can be used to retrieve the position-dependent optical phase delay $OPD = OPD(x,y)$ experienced by the laser beam when reflecting at the specimen. The x,y coordinates denote the transverse (w.r.t. the laser beam direction) coordinate at the specimen position.

For the realization of a Twyman-Green interferometer the laser beam has to be expanded, and large area plane optics need to be used for the beam-splitter. These optics need to be flat in the region of interest as any curvature would be misinterpreted as curvature (with opposite sign) of the specimen. The photodiode used in the Michelson interferometer is replaced by a CCD-detector.

Following the same procedure as described in previous section, for N values of the distance d_2 of the reference mirror M2 the corresponding 2D intensity profiles $I_n(x,y)$ are measured. An example of such intensity measurements is shown in Figure 139. The measurement of these interferograms and the

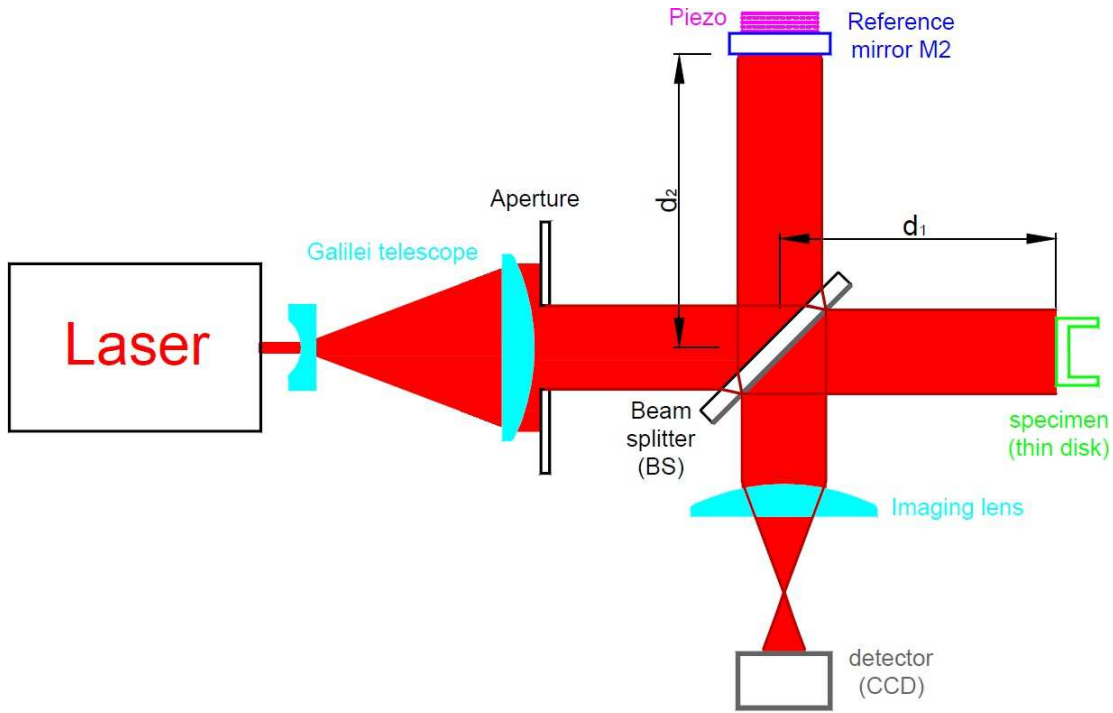


Figure 138: Schematic view of a Twyman-Green interferometer. The specimen surface is imaged with a lens onto the CCD detector.

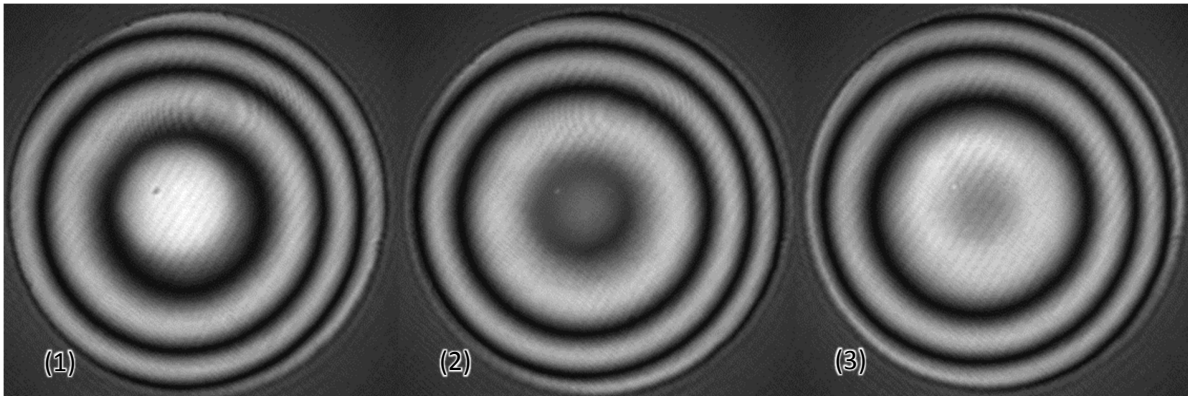


Figure 139: Three phase-shifted interferograms of a pumped thin disk recorded with a CCD detector. The phase unwrapping of these three intensity profiles $I_n(x,y)$ can be used to reconstruct the position-dependent $OPD(x,y)$ related to the thin disk.

knowledge of the phases φ_n of the reference mirror, allow reconstruction of a position-dependent phase $\phi(x, y)$. This is achieved using an adapted version of Eq. (172) [281]:

$$\tan(\phi(x, y)) = \frac{\sum_{n=1}^N (I_n(x, y) \cos(\varphi_{n+1}) - I_{n+1}(x, y) \cos(\varphi_n))}{\sum_{n=1}^N (I_n(x, y) \sin(\varphi_{n+1}) - I_{n+1}(x, y) \sin(\varphi_n))}. \tag{173}$$

From the phase $\phi(x, y)$ it is then possible to reconstruct the position-dependent $OPD(x, y)$ related to the reflective specimen as detailed in the next section.

12.1.3. Reconstruction of the OPD from interferometric measurements

To reconstruct the OPD at the specimen from the measured interferograms we perform following steps. First, from the various measured intensity distributions $I_n(x,y)$ and φ_n we compute $\phi(x,y)$ using Eq. (172). Similar to the Michelson interferometer, the reconstructed phase can be known only modulo 2π . Thus, as a second step, phase unwrapping is performed to deduce the position-dependent $OPD(x,y)$. The working principle of this unwrapping procedure is depicted in Figure 140 in 1D for the purpose of clarity. The panel (a) shows the phase $\phi(x)$, while the panel (b) shows the optical phase delay $OPD(x)$ reconstructed from the phase $\phi(x)$. Without losses of generality it is assumed that the optical phase delay at $x = 0$ is zero, i.e. $OPD(0) = 0$. In this specific case for $|x| < 1$ the OPD is simply given by

$$OPD(x) = \lambda \frac{\phi(x) - \phi(0)}{\pi}. \quad (174)$$

The discontinuities visible in Figure 140 (a) arise from the fact that the phase can be reconstructed only modulo 2π . These discontinuities are thus not related with physical “discontinuities” of the “height-profile” of the specimen. Hence, when reconstructing the OPD we have to require its continuity. This means that the OPD over the whole region of interest has to be determined using following expression:

$$OPD(x) = \lambda \frac{\phi(x) - \phi(0)}{\pi} + K\lambda, \quad (175)$$

where K is an integer number not known a priori. However, by requiring the $OPD(x)$ to be a continuous function, K can be fixed in for regions of continuous ϕ and by fitting several of these regions the OPD can be reconstructed over the whole area of interest.

This unwrapping procedure can be generalized for the two dimensional case. In this case, the expression to retrieve the OPD takes the form

$$OPD(x,y) = \lambda \frac{\phi(x,y) - \phi(0,0)}{\pi} + K\lambda. \quad (176)$$

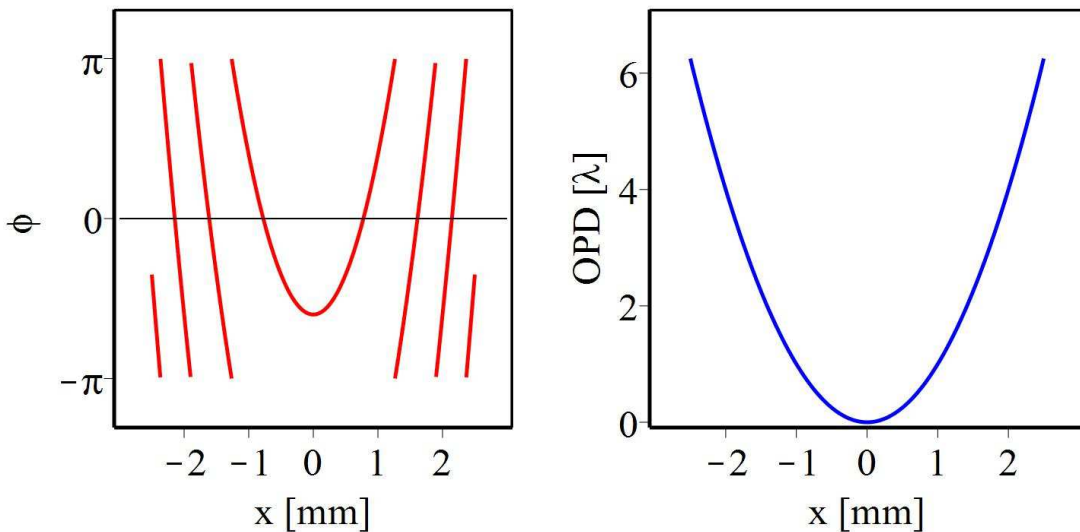


Figure 140: Example of the phase unwrapping procedure in one dimension to extract the position-dependent $OPD(x)$. The OPD at the origin has been assumed to be zero, i.e., $OPD(0) \equiv 0$.

This unfolding procedure is only possible when the OPD is adiabatically changing over the range of interest. Large fluctuations caused for example by large defects of the specimen surface could spoil this procedure. However, thin disk of sufficient qualities do not show these problems.

An example of an OPD of a pumped thin disk reconstructed from an interferometric measurement is presented in Figure 141. Its shape in the central region is approximately spherical. In fact, when subtracting its spherical component, the central region turns out to be flat as visible in Figure 142. This flat region corresponds approximately to the pumped region. Therefore, the interferometric measurements confirm the findings of the FEM simulations that within the pump region the thin disk can be accurately approximated with a spherical lens. Hence, also the interferometric results confirm that to avoid the excitation of higher-order beam components, the impinging laser beam should not exceed the pump region.

12.1.4. The practical realization of the interferometer

Since we are interested in the thermal lens of the thin disk, the thin disk has to be characterized in running conditions. For this purpose, the interferometer was realized within our laser and the pumped thin disk was placed at the specimen position. A picture of the setup realized is shown in Figure 143. The interferometric measurements were realized within the laser housing, i.e. in a thermally stabilized surrounding. To reduce vibrations of the thin disk that would cause instabilities of the interference fringes, a cooling system with stable water pressure and a pulsation damper was used.

As depicted in the Figure 138 and Figure 143 the Twyman Green interferometer includes a laser, a Galilean telescope, the beam splitter, the two arms with the reference mirror and the specimen, an imaging lens and a CCD detector. In the following, we describe some details needed for an adequate realization of the interferometer.

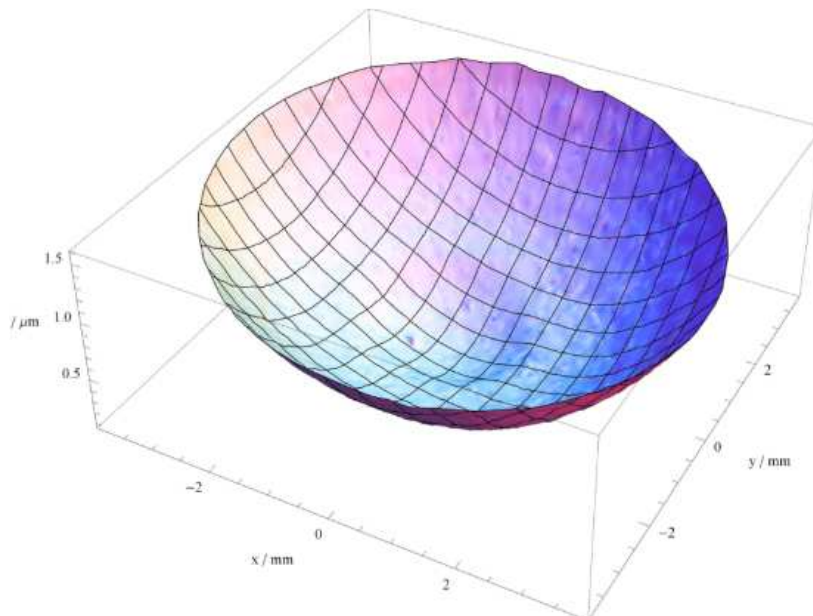


Figure 141: OPD of a pumped thin disk soldered to a metallic heat sink extracted from interferometric measurements after the phase unwrapping procedure. This OPD causes a defocusing of the impinging laser beam.

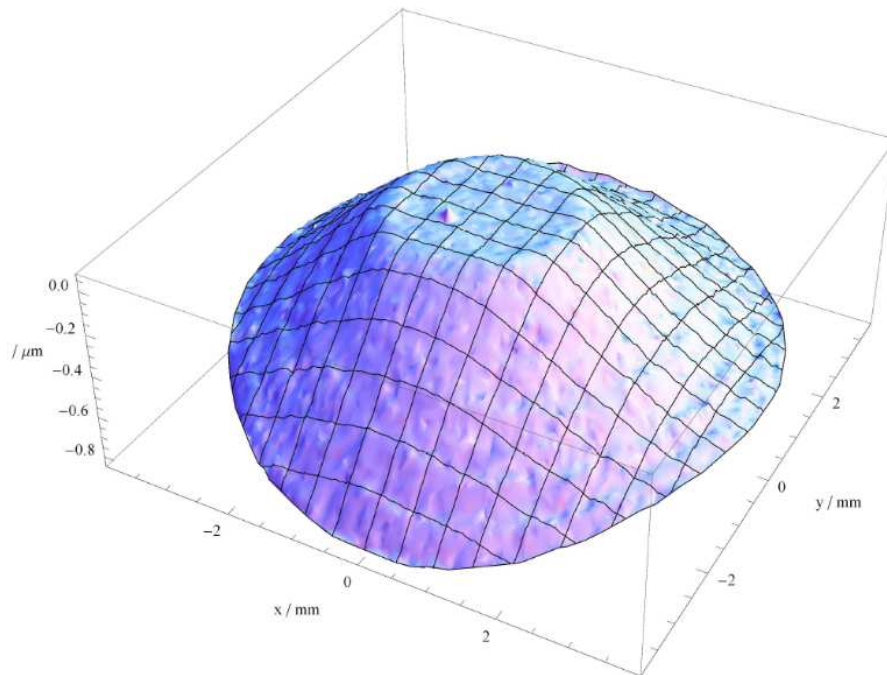


Figure 142: Residual between the OPD shown in Figure 141 and its fit with a parabolic function (fitted within the center of the pumped region). The flat profile in the central region demonstrates that in the central region the pumped disk acts as a spherical lens. The deviations which start at the periphery of the pumped region correspond to the aspherical (or higher-order) components denoted with $h_o(x)$ in Eq. (14). A defect (hot spot) is visible in the vicinity of the center.

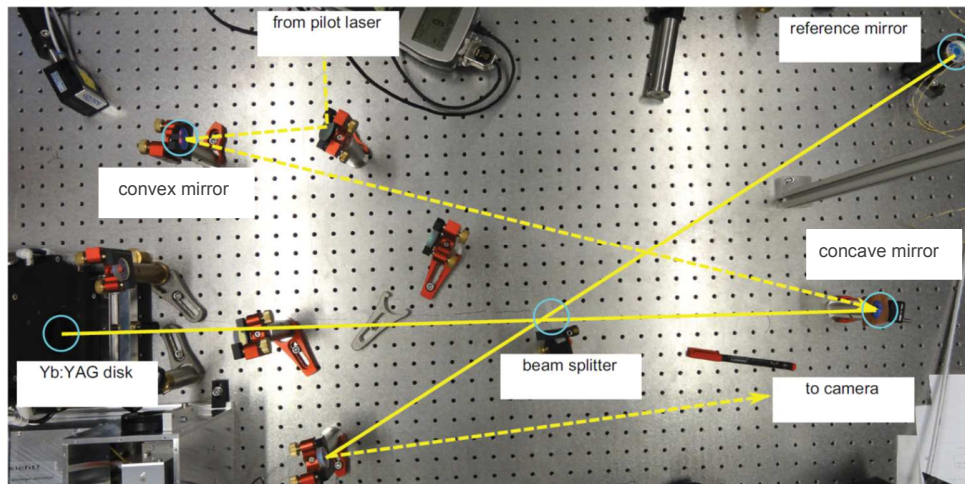


Figure 143: Picture of the interferometric setup.

- **The laser**

For the interferometric measurement, we used the single frequency thin-disk laser shown in Figure 144. Due to the relatively short laser cavity of about 20 cm, single frequency operation was realized with a single etalon with a thickness of $50\ \mu\text{m}$. The laser wavelength was $\lambda = 1030\ \text{nm}$. Therefore, a spectral separation between laser light and fluorescence light from the pumped disk was not possible. For this

reason, to have a good signal-to-background ratio at the CCD detector, the laser was operated at a high power (about 1 W).

- **The Galilean telescope and the beam size**

In the Galilean telescope, the laser beam was first expanded to be significantly larger than the area of interest and then collimated. In this way, the area of interest at the specimen position is illuminated with an approximately homogeneous intensity profile. The beam waist at the concave mirror of the telescope (see Figure 143) was much larger than the 1-inch mirror itself. This led to a strong truncation of the Gaussian beam resulting in a nearly flattop profile. With a diameter of 25 mm, the beam Rayleigh length is in the km range, i.e. much larger than the propagating distances in the interferometer of about 1 m. Therefore, the laser beam propagates basically collimated in both arms of the interferometer. The strong truncation given by the aperture of the concave mirror of the telescope leads to a high-order Fresnel diffraction pattern characterized by strong intensity modulations at the periphery of the beam. This effect can be neglected as they are outside the relevant range. However, in addition, it generates intensity minima and maxima at the beam center (similar to the point of Argo [282]) due to coherent interference of the diffracted light. This strongly distorts the fringe pattern in the region of interest.

The aperture of the collimating mirror projected perpendicular to the impinging laser beam is not perfectly round because the laser beam is not orthogonal to the mirror surface. This causes a slight dephasing of the diffracted light as visible in. As visible in Figure 145 (a), the intensity distortions show no rotational symmetric pattern and the intensity fluctuations are reduced significantly.

The placement of a serrated aperture [283] (shown in Figure 145 (b)) at the collimating mirror of the telescope significantly increases the dephasing of the diffracted light. This reduces the distortions at the beam center by orders of magnitude as shown in Figure 145 (c).

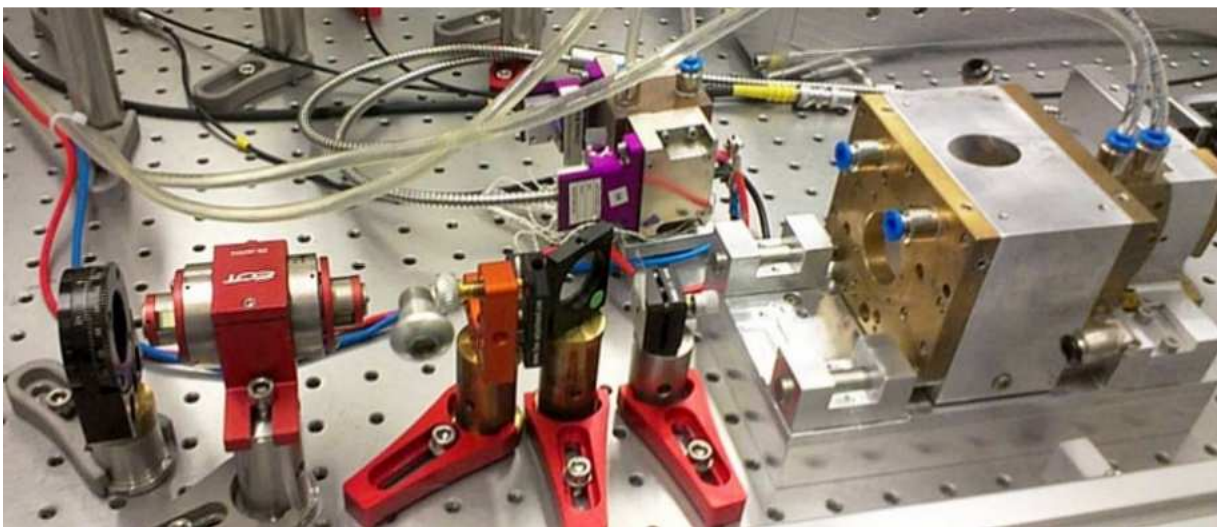


Figure 144: Picture of the single-frequency thin-disk laser used for the interferometric measurements. In operation, the cavity was covered with an aluminum cover to minimize instabilities.

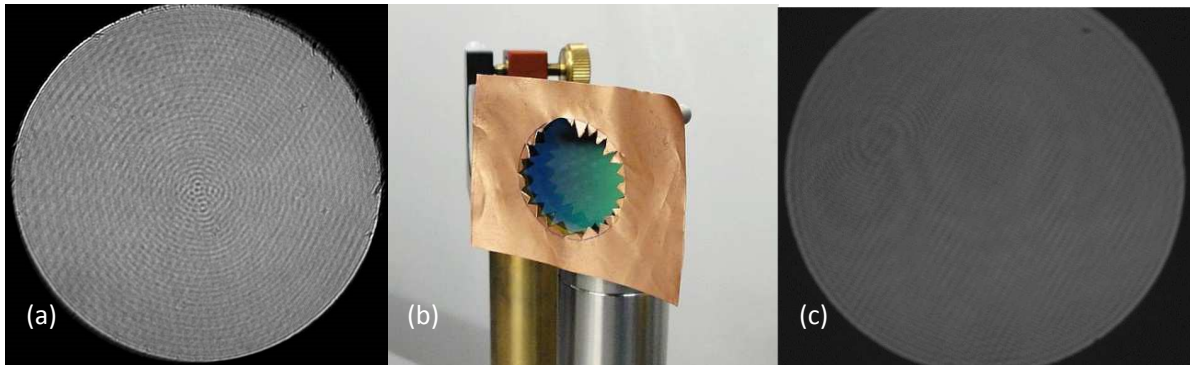


Figure 145: (a) Intensity distribution at the CCD-detector when the interferometer arm with the reference mirror M2 is blocked and without the serrated aperture at the concave mirror of the telescope. The structure with rotational symmetry is the Fresnel diffraction pattern caused by the round (elliptical) aperture of the collimating mirror of the telescope. The deviations from the rotational symmetry in the center are caused by the fact that the aperture is not perfectly circular (in the projection perpendicular to the laser beam). (b) Picture of the serrated aperture to suppress the “low-frequency” fringes caused by the Fresnel diffraction. (c) Same as in (a) but with the insertion of a serrated aperture at the concave mirror of the beam expander. This measurement was done using a different thin disk and a different laser intensity compared to (a).

The collimated beam is chosen to be smaller than the following optics to avoid diffraction effects at these elements. Because of this, the beam splitter and the imaging lens were chosen to be 2” in diameter. Contrarily, the size of the reference mirror M2 and the size of the thin disk is irrelevant because these two elements are imaged into the CCD-detector (at the image position the fringe pattern is suppressed).

- **The beam splitter**

The beam splitter is the central element of the interferometer. Independently of the interferometer design, both beams, the one travelling in the reference arm and the one travelling in the thin disk arm, experience one reflection and one transmission at the beam splitter (see Figure 146). As a result, independently of the reflectivity of the beam splitter the relative intensity of the two interfering beams at the CCD detector is equal provided the reflectivity of the specimen (thin disk) and reference mirror (M2) are equal. Maximal contrast is thus always guaranteed. Maximal intensity at the CCD-detector on the contrary is reached when the reflectivity of the beam splitter is 50 %. However, lower beam splitter reflectivities are advantageous because they suppress the background arising from the fluorescence light produced in the disk relative to the power of the illumination laser reaching the CCD detector.

The beam splitter is based on an extended glass substrate. One side has a partly reflective (PR) coating and therefore is the actual beam splitter, and the other side has an anti-reflective coating (AR). As an AR coating cannot fully suppress reflections, the substrate is wedged so that the residual reflections do not disturb the measurement (see Figure 146).

A collimated beam passing a wedge does not acquire any astigmatism [150]. Therefore, as the illumination beam at the beam splitter position is collimated, the usage of a wedged beam splitter seems uncritical. However, as we probe the position-dependent phase and amplitude distortions of the specimen, the beam reflected from the specimen has to be considered as a superposition of beams from point sources. Thus, it seems that a wedge beam splitter introduces astigmatism to the imaging. This problem can be suppressed by orienting the beam splitter so that the beam from the specimen is reflected towards the camera without crossing the substrate (see Figure 146).

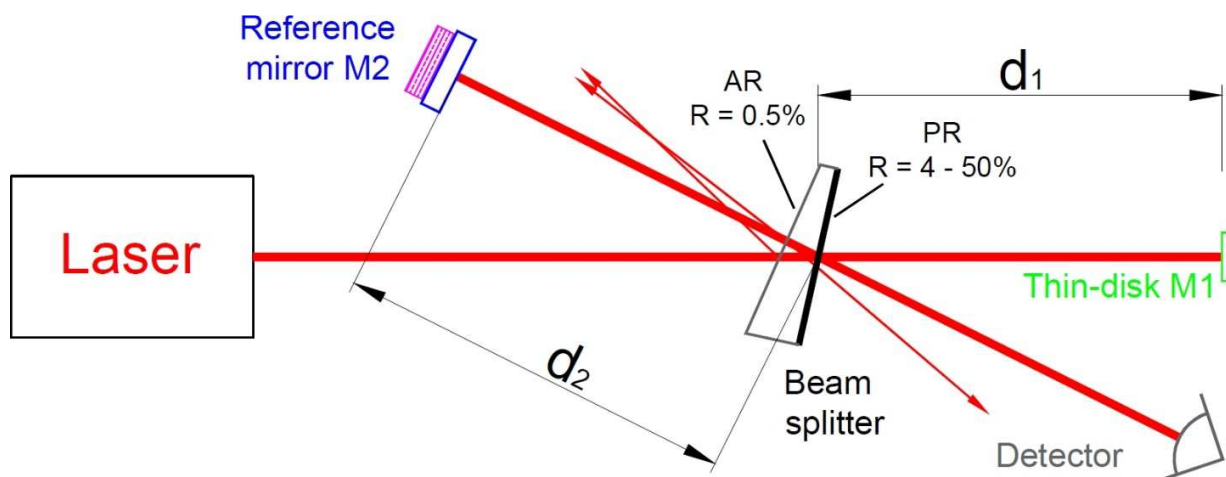


Figure 146: Details of the beam splitter used in the interferometer (PR = partial reflective, AR = anti reflective).

The beam splitter needs to have a large aperture and a homogeneous reflectivity. To maximize the usable aperture of the beam splitter in the practical realization we arranged it so that the angle of incidence of the input laser beam is about $10 - 30^\circ$ relative to the normal of the beam splitter surface as shown in Figure 146, and not at 45° as shown in the scheme of Figure 137.

The beam splitter needs to be flat as the curvature of the beam splitter fakes a curvature of the specimen of twice the strength. Assume for example that the PR coating in Figure 146 has a convex shape. In this case, the bended PR coating acts as a focusing element for the beam coming from the laser and being reflected to the reference mirror and as defocusing element for the beam coming from the specimen and being reflected to the detector. Thus, the focal strength of the beam splitter PR coating contributes twice to the interferometric measurement. As a result, when the measurement precision $< \lambda/x$ of the specimen has to be reached, the beam splitter needs to be manufactured to a precision of $< \lambda/2x$.

Yet, when merely the thermal lens effect of the thin disk needs to be determined, we are only interested in the difference of two interferometric measurements at pumped and at unpumped conditions. As the curvature of the beam splitter and reference mirror do not change in between the two measurements, their influence is cancelled out in the subtraction procedure.

12.1.5. Principle and setup of the space-resolved gain measurement

The above presented interferometric setup can be slightly modified to perform space-resolved gain measurements of the thin disk. In fact, the illumination laser we are using in the interferometric setup operates at a wavelength of 1030 nm i.e. the wavelength of maximal gain for Yb:YAG. For the measurement of the gain, three intensities distributions $I_n(x,y)$ have to be acquired with the CCD detector:

- $I_1(x, y)$ is the intensity distribution acquired using the setup shown in Figure 147 (d) where the beam travelling to the reference mirror M2 is blocked.
- $I_2(x, y)$ is the intensity distribution acquired without any laser beam as shown in Figure 147 (e). This image is used to quantify the background arising from the fluorescence of the thin disk.
- $I_3(x, y)$ is the intensity distribution acquired using the setup shown in Figure 147 (f) where the beam travelling to the thin disk is blocked. This image is used to normalize the laser intensity (and other background sources).

The space-resolved gain is then given by

$$g(x, y) = \frac{I_1(x, y) - I_2(x, y)}{I_3(x, y)}. \quad (177)$$

The intensity distribution $I_3(x, y)$ serves as a normalization because as we have seen previously the intensities of the two laser beams at the detector position after having travelled the two arms of the interferometer are identical (provided the reference mirror M2 and the thin disk have the same reflectivity). When measuring the intensity distribution $I_1(x, y)$ both the laser amplification and the fluorescence from the disk are recorded. The background produced by the fluorescence light must be subtracted by performing the measurement of the intensity distribution $I_2(x, y)$. The gain measurements shown in Figure 22 and 23 have been acquired using this setup and Eq. (176)

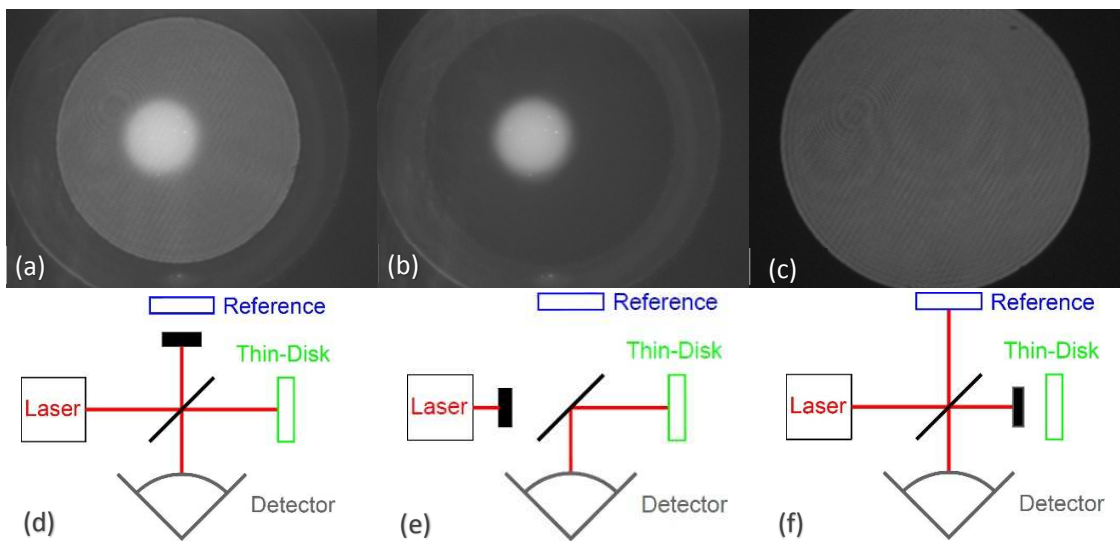


Figure 147: Setup and intensity distributions used to measure the position-dependent gain at the thin disk. The panel (a) shows the intensity distribution $I_1(x, y)$ acquired using the setup sketched in (d) for beveled thin disk soldered on a metallic heat sink. In this measurement, the pump spot was not perfectly aligned with the thin disk axis. The panel (b) shows the intensity distribution $I_2(x, y)$ acquired using the setup sketched in (e). The panel (c) shows the intensity distribution $I_3(x, y)$ recorded using the setup sketched in (e). The black optical elements represent 100 % absorbers.

References

- [1] R. Pohl, A. Antognini, F. Nez, F. D. Amaro, F. Biraben, J. M. R. Cardoso, D. S. Covita, A. Dax, S. Dhawan, L. M. P. Fernandes, A. Giesen, T. Graf, T. W. Hänsch, P. Indelicato, L. Julien, C.-Y. Kao, P. Knowles, E.-O. L. Bigot, Y.-W. Liu, J. A. M. Lopes, L. Ludhova, C. M. B. Monteiro, F. Mulhauser, T. Nebel, P. Rabinowitz, J. M. S. dos Santos, L. A. Schaller, K. Schuhmann, C. Schwob, D. Taqqu, J. F. C. A. Veloso and F. Kottmann, "The size of the proton," *Nature*, vol. 466, pp. 213-216, 2010.
- [2] A. Antognini, F. Nez, K. Schuhmann, F. D. Amaro, F. Biraben, J. M. R. Cardoso, D. S. Covita, A. Dax, S. Dhawan, M. Diepold, L. M. P. Fernandes, A. Giesen, A. L. Gouvea, T. Graf, T. W. Hänsch, P. Indelicato, L. Julien, C.-Y. Kao, P. Knowles, F. Kottmann, E. O. Le Bigot, Y. W. Liu, J. A. Lopes, L. Ludhova, C. M. Monteiro, F. Mulhauser, T. Nebel, P. Rabinowitz, J. M. dos Santos, L. A. Schaller, C. Schwob, D. Taqqu, J. F. Veloso, J. Vogelsang and R. Pohl, "Proton structure from the measurement of 2s-2p transition frequencies of muonic hydrogen," *Science*, vol. 339, pp. 417-420, 2013.
- [3] P. Mohr, Taylor, B. Barry and D. Newell, "CODATA recommended values of the fundamental physical constants: 2010," *Rev. Mod. Phys.*, vol. 84, pp. 1527-1605, 2012.
- [4] R. Pohl, R. Gilman, G. A. Miller and K. Pachucki, "Muonic Hydrogen and the Proton Radius Puzzle," *Annual Review of Nuclear and Particle Science*, vol. 63, pp. 175-204, 2013.
- [5] C. E. Carlson, "The proton radius puzzle," *Progress in Particle and Nuclear Physics*, vol. 82, pp. 59-77, 2015.
- [6] A. Antognini, K. Schuhmann, F. D. Amaro, P. Amaro, M. Abdou-Ahmed, F. Biraben, T.-L. Chen, D. S. Covita, A. J. Dax, M. Diepold, L. M. P. Fernandes, B. Franke, S. Galtier, A. L. Gouvea, J. Götzfried, T. Graf, T. W. Hänsch, M. Hildebrandt, P. Indelicato and L., "Experiments towards resolving the proton charge radius puzzle," *arXiv:1509.03235*, 2015.
- [7] A. Antognini, "Muonic atoms and the nuclear structure," *arXiv:1512.01765*, 2015.
- [8] R. Hill, "Review of experimental and theoretical status of the proton radius puzzle," *arXiv:1702.01189 (2017)*, 2017.
- [9] S. G. Karshenboim, D. McKeen and M. Pospelov, "Constraints on muon-specific dark forces," *Physical Review D*, vol. 90, 2014.

B The thin-disk laser for the 2S – 2P measurement in muonic helium

- [10] C. E. Carlson and M. Freid, "Extending theories on muon-specific interactions," *arXiv:1506.06631*, 2015.
- [11] P. Brax and C. Burrage, "Cosmological tests of coupled Galileons," *Phys. Rev. D*, vol. 91, no. 043515, 2015.
- [12] X. Zhan, K. Allada, D. Armstrong, J. Arrington, W. Bertozzi, W. Boeglin, J.-P. Chen, K. Chirapatpimol, S. Choi, E. Chudakov, E. Cisbani, P. Decowski, C. Dutta, S. Frullani, E. Fuchey, F. Garibaldi, S. Gilad, R. Gilman, J. Glister, K. Hafidi, B. Hahn, J.-O. Hansen, D. W. Higinbotham, T. Holmstrom, R. J. Holt, J. Huang, G. M. Huber, F. Itard, C. W. de Jager, X. Jiang, M. Johnson, J. Katich, R. de Leo, L. L. LeRose, R. Lindgren, E. Long, D. J. Margaziotis, S. May-Tal Beck, D. Meekins, R. Michaels, B. Moffit, B. E. Norum, M. Olson, E. Piasetzky, I. Pomerantz, D. Protopopescu, X. Qian, Y. Qiang, A. Rakhman, R. D. Ransome, P. E. Reimer, J. Reinhold, S. Riordan, G. Ron, A. Saha, A. J. Sarty, B. Sawatzky, E. C. Schulte, M. Shabestari, A. Shahinyan, R. Shneur, S. Širca, P. Solvignon, N. F. Sparveris, S. Strauch, R. Subedi, V. Sulkosky, I. Vilardi, Y. Wang, B. Wojtsekhowski, Z. Ye and Y. Zhang, "High-precision measurement of the proton elastic form factor ratio $\mu\text{pGE}/\text{GM}\mu\text{pGE}/\text{GM}$ at low Q^2 ," *Phys. Lett. B*, vol. 705, pp. 59-64, 2011.
- [13] R. J. Hill and G. Paz, "Model-independent extraction of the proton charge radius from electron scattering," *Phys. Rev. D*, vol. 82, p. 113005, 2010.
- [14] M. O. Distler, J. C. Bernauer and T. Walcher, "The RMS charge radius of the proton and Zemach moments," *Phys. Lett. B*, vol. 696, pp. 343-347, 2011.
- [15] I. Lorenz, U.-G. Meissner, H.-W. Hammer and Y.-B. Dong, "Theoretical constraints and systematic effects in the determination of the proton form factors," *Phys. Rev. D*, vol. 91, no. 014023, 2015.
- [16] J. C. Bernauer, M. O. Distler, J. Friedrich, T. Walcher, P. Achenbach, C. A. Gayoso, R. Böhm, D. Bosnar, L. Debenjak, L. Doria, A. Esser, H. Fonvieille, M. G. R. d. I. Paz, J. M. Friedrich, M. Makek, H. Merkel, D. G. Middleton, U. Müller, L. Nungesser, J. Pochodzalla, M. Potokar, S. Sánchez Majos, B. S. Schlimme, S. Širca and M. Weinriefer, "Electric and magnetic form factors of the proton," *Phys. Rev. C*, vol. 90, no. 015206, 2014.
- [17] I. Sick and D. Trautmann, "Proton root-mean-square radii and electron scattering," *Phys. Rev. C*, vol. 89, no. 012201(R), 2014.
- [18] G. Lee, J. R. Arrington and R. J. Hill, "Extraction of the proton radius from electron-proton scattering data," *Phys. Rev. D*, vol. 92, no. 013013, 2015.
- [19] M. Horbatsch and E. Hessels, "Evaluation of the strength of electron-proton scattering data for determining the proton charge radius," *arXiv:1509.05644*, 2015.

- [20] K. Griffioen, C. Carlson and S. Maddox, "Are Electron Scattering Data Consistent with a Small Proton Radius?," *arXiv:1509.06676*, 2015.
- [21] D. W. Higinbotham, A. A. Kabir, V. Lin, D. Meekins, B. Norum and B. Sawatzky, "The Proton Radius from Electron Scattering Data," *arXiv:1510.01293*, 2015.
- [22] I. Sick and D. Trautmann, "Reexamination of proton rms radii from low-q power expansions," *Phys. Rev. C*, vol. 95, no. 012501, 2017.
- [23] J. Bernauer and M. Distler, "Avoiding common pitfalls and misconceptions in extractions of the proton radius," *arXiv:1606.02159*, 2016.
- [24] S. G. Karshenboim, E. Y. Korzinin, V. A. Shelyuto and V. G. Ivanov, "Theory of Lamb Shift in Muonic Hydrogen," *Journal of Physical and Chemical Reference Data*, vol. 44, no. 031202, 2015.
- [25] A. A. Krutov and A. P. Martynenko, "Lamb shift in the muonic deuterium atom," *Phys. Rev. A*, vol. 84, no. 052514, 2011.
- [26] E. Borie, "Lamb Shift in Light Muonic Atoms - Revisited," *arXiv:1103.1772 v7*, 2014.
- [27] C. Peset and A. Pineda, "The Lamb shift in muonic hydrogen and the proton radius from effective field theories," *arXiv:1508.01948*, 2015.
- [28] B. J. Wundt and U. D. Jentschura, "Why three-body physics do not solve the proton radius puzzle," *Phys. Rev. J. D*, vol. 65, no. 357, 2012.
- [29] M. C. Birse and J. A. McGovern, "Proton polarisability contribution to the Lamb shift in muonic hydrogen at fourth order in chiral perturbation theory," *Eur. Phys. J. A*, vol. 48, no. 120, 1012.
- [30] C. E. Carlson and M. Vanderhaeghen, "Proton Structure from the Measurement of 2S-2P Transition Frequencies of Muonic Hydrogen," *Phys. Rev. A*, vol. 84, no. 020102, 2011.
- [31] G. A. Miller, "The Muon Scattering Experiment (MUSE) at PSI and the proton radius puzzle," *Phys. Lett. B*, vol. 718, no. 1078, 2013.
- [32] J. M. Alarcon, V. Lensky and V. Pascalutsa, "Chiral perturbation theory of muonic hydrogen Lamb shift: polarizability contribution," *Eur. Phys. J. C*, vol. 74, no. 2852, 2014.
- [33] A. Walker-Loud, C. E. Carlson and G. A. Miller, "Electromagnetic Self-Energy Contribution to M_p - M_n and the Isovector Nucleon Magnetic Polarizability," *Phys. Rev. Lett.*, vol. 108, no. 232301, 2012.

D The thin-disk laser for the 2S – 2P measurement in muonic helium

- [34] M. Gorchtein, "Forward sum rule for the 2γ -exchange correction to the charge-radius extraction from elastic electron scattering," *Phys. Rev. C*, vol. 90, no. 052201, 2014.
- [35] R. J. Hill and G. Paz, "Model Independent Analysis of Proton Structure for Hydrogenic Bound States," *Phys. Rev. Lett*, vol. 107, no. 160402, 2011.
- [36] C. Peset and A. Pineda, "The two-photon exchange contribution to muonic hydrogen from chiral perturbation theory," *Nuclear Physics B*, vol. 887, no. 69, 2014.
- [37] C. Peset and A. Pineda, "Model-independent determination of the Lamb shift in muonic hydrogen and the proton radius," *Eur. Phys. J. A*, vol. 51, no. 31, 2015.
- [38] F. Hagelstein, R. Miskimen and V. Pascalutsa, "Nucleon Polarizabilities: from Compton Scattering to Hydrogen Atom," *arXiv:1512.03765*, 2015.
- [39] A. Gasparian, "The PRad experiment and the proton radius puzzle," *EPJ Web Conf.*, vol. 73, no. 07006, 2014.
- [40] R. Gilman, E. Downie, G. Ron, A. Afanasev, J. Arrington, O. Ates, F. Benmokhtar, J. Bernauer, E. Brash, W. J. Briscoe, K. Deiters, J. Diefenbach, C. Djalali, B. Dongwi, L. E. Fassi, S. Gilad, K. Gnanvo, R. Gothe, D. Higinbotham, R. Holt, Y. Ilieva, H. Jiang, M. Kohl, G. Kumbartzki, J. Lichtenstadt, A. Liyanage, N. Liyanage, M. Meziane, Z.-E. Meziani, D. G. Middleton, P. Monaghan, K. E. Myers, C. Perdrisat, E. Piasezsky, V. Punjabi, R. Ransome, D. Reggiani, P. Reimer, A. Richter, A. Sarty, E. Schulte, Y. Shamai, N. Sparveris, S. Strauch, V. Sulkosky, A. S. Tadepalli, M. Taragin and L. Weinstein, "Studying the Proton "Radius" Puzzle with μp Elastic Scattering," *arXiv:1303.2160*, 2013.
- [41] H. Merkel, P. Achenbach, R. Böhm, D. Bosnar, J. Beričić, L. Debenjak, A. Denig, M. O. Distler, A. Esser, H. Fonvieille, I. Friščić, M. G. Rodríguez, K. Griffioen, S. Kegel, Y. Kohl, M. Mihovilović, U. Müller, J. Pochodzalla, T. R. Saito, B. S. Schlimme, M. Schoth, F. Schulz, C. Sfienti, I. Sick, S. Širca, M. Thiel and A. Weber, "Mainz Microtron MAMI," [Online]. Available: <http://wwwa1.kph.uni-mainz.de/A1/publications/proposals/MAMI-A1-01-2012.pdf>.
- [42] M. Mihovilović, H. Merkel and A. Weber, "Puzzling out the proton radius puzzle," *EPJ Web of Conf.* 81, vol. 81, no. 01009, 2014.
- [43] M. Mihovilović, A. B. Weber, P. Achenbach, T. Beranek, J. Beričić, J. C. Bernauer, R. Böhm, D. Bosnar, M. Cardinali, L. Correa, L. Debenjak, A. Denig, M. O. Distler, A. Esser, M. I. F. Bondy, H. Fonvieille, J. M. Friedrich, I. Friščić, K. Griffioen, M. Hoek, S. Kegel, Y. Kohl, H. Merkel, D. G. Middleton, U. Müller, L. Nungesser, J. Pochodzalla, M. Rohrbeck, S. Sánchez Majos, B. S. Schlimme, M. Schoth, F. Schulz, C. Sfienti, S. Širca, S. Štajner, M. Thiel, A. Tyukin, M. Vanderhaeghen and M. Weinriefer, "First measurement of proton's charge form factor at very low Q^2 with initial state radiation," *arXiv:1612.06707*, 2016.

- [44] A. C. Vutha, N. Bezginov, I. Ferchichi, M. C. George, V. Isaac, C. H. Storry, A. S. Weatherbee, M. Weel and E. A. Hessels, "Progress towards a new microwave measurement of the hydrogen $n=2$ Lamb shift: a measurement of the proton charge radius," in *Bull. Am. Phys. Soc.* 57(5):Q1.138, Orange County, California, 2012.
- [45] A. Beyer, J. Alnis, K. Khabarova, A. Matveev, C. G. Parthey, D. C. Yost, R. Pohl, T. Udem, T. W. Hänsch and N. Kolachevsky, "Precision spectroscopy of the 2S-4P transition in atomic hydrogen on a cryogenic beam of optically excited 2S atoms," *Annalen der Physik*, vol. 525, no. 671, 2013.
- [46] S. Galtier and et al., "Ultraviolet continuous-wave laser source at 205 nm for hydrogen spectroscopy," *Optics Communications*, vol. 324, pp. 34-37, 2014.
- [47] The Committee on Data for Science and Technology, [Online]. Available: <http://physics.nist.gov/cuu/Constants/>.
- [48] J. N. Tan, S. M. Brewer and N. D. Guise, "Experimental efforts at NIST towards one-electron ions in circular Rydberg states," *Phys. Scr.* T144:014009, 2011.
- [49] K. S. Khaw, A. Antognini, T. Prokscha, K. Kirch, L. Liskay, Z. Salman and P. Crivelli, "Spatial confinement of muonium atoms," *Phys. Rev. A*, vol. 94, no. 022716, 2016.
- [50] A. Antognini, F. Biraben, J. M. R. Cardoso, D. S. Covita, A. Dax, L. M. P. Fernandes, A. L. Gouvea, T. Graf, T. W. Hänsch, M. Hildebrandt, P. Indelicato, L. Julien, K. Kirch, F. Kottmann, Y.-W. Liu, C. M. B. Monteiro, F. Mulhauser, T. Nebel, F. Nez, J. M. F. Dos Santos, K. Schuhmann, D. Taqqu, J. F. C. A. Veloso, A. Voss and R. Pohl, "Illuminating the proton radius conundrum: the μHe^+ Lamb shift," *Canadian Journal of Physics*, vol. 89, no. 47, 2011.
- [51] K. Schuhmann, K. Kirch, F. Nez, R. Pohl and A. Antognini, "Thin-disk laser scaling limit due to thermal-lens," *Appl. Opt.*, vol. 55, pp. 9022-9032, 2016.
- [52] K. Schuhmann, K. Kirch and A. Antognini, "Multi-pass oscillator layout for high-energy mode-locked thin-disk lasers," *arXiv:1603.00404*, 2016.
- [53] K. Schuhmann, T. W. Hänsch, K. Kirch, A. Knecht, F. Kottmann, F. Nez, R. Pohl, D. Taqqu and A. Antognini, "Thin-disk laser pump schemes for large number of passes and moderate pump source quality," *Appl. Opt.* 54, pp. 9400-9408, Nov 2015.
- [54] K. Schuhmann, M. A. Ahmed, A. S. Antognini, T. Graf, T. W. Hänsch, K. Kirch, F. Kottmann, R. Pohl, D. Taqqu, A. Voss and B. Weichelt, "Thin-disk laser multi-pass amplifier," in *Proceedings of SPIE*, San Francisco, 2015.
- [55] J. Vogelsang, M. Diepold, A. Antognini, A. Dax, J. Götzfried, T. W. Hänsch, F. Kottmann, J. J. Krauth, Y.-W. Liu, T. Nebel, F. Nez, K. Schuhmann, D. Taqqu and R. Pohl, "Multipass laser cavity

for efficient transverse illumination of an elongated volume," *Optics Express*, vol. 22, pp. 13050-13062, 2014.

- [56] A. Antognini and K. Schuhmann, "High power multi-pass laser oscillator". Europe Patent EP15201707.5, 21 December 2015.
- [57] M. I. Eides, H. Grotch and V. A. Shelyuto, "Theory of light hydrogenlike atoms," *Physics Reports*, vol. 342, no. 63, 2001.
- [58] S. G. Karshenboim, "Precision physics of simple atoms: QED tests, nuclear structure and fundamental constants," *Phys. Rep.*, vol. 422, no. 1, pp. 1-63, 2005.
- [59] K. Pachucki, "Proton structure effects in muonic hydrogen," *Phys. Rev. A*, vol. 60, no. 3593, 1999.
- [60] A. Antognini, F. Kottmann, F. Biraben, P. Indelicato, F. Nez and R. Pohl, "Theory of the 2S–2P Lamb shift and 2S hyperfine splitting in muonic hydrogen," *Annals of Physics*, vol. 331, pp. 127-145, 2013.
- [61] P. J. Mohr, D. B. Newell and B. N. Taylor, "CODATA recommended values of the fundamental physical constants 2014," *Rev. Mod. Phys.*, vol. 88, no. 035009, 2016.
- [62] B. de Beauvoir, C. Schwob, O. Acef, L. Jozefowski, L. Hilico, F. Nez, L. Julien, A. Clairon and F. Biraben, "Metrology of the hydrogen and deuterium atoms: determination of the Rydberg constant and Lamb shifts," *Eur. Phys. J. D*, vol. 12, no. 61, 2000.
- [63] R. Pohl, F. Nez, L. M. P. Fernandes, F. D. Amaro, F. Biraben, J. M. R. Cardoso, D. S. Covita, A. Dax, S. Dhawan, M. Diepold, A. Giesen, A. L. Gouvea, T. Graf, T. W. Hänsch, P. Indelicato, L. Julien, P. Knowles, F. Kottmann, E.-O. Le Bigot, Y.-W. Liu, J. A. M. Lopes, L. Ludhova, C. M. B. Monteiro, F. Mulhauser, T. Nebel, P. Rabinowitz, J. M. F. dos Santos, L. A. Schaller, K. Schuhmann, C. Schwob, D. Taqqu, J. F. C. A. Veloso and A. Antognini, "Laser spectroscopy of muonic deuterium," *Science*, vol. 353, pp. 669-673, 2016.
- [64] Z. Epstein, G. Paz and J. Roy, "Model independent extraction of the proton magnetic radius from electron scattering," *Phys. Rev. D*, vol. 90, no. 074027, 2014.
- [65] U. Jentschura, "Proton radius, Darwin-Foldy term and radiative corrections," *Eur. Phys. J. D*, vol. 61, no. 7, 2011.
- [66] U. D. Jentschura, "Muonic bound systems, virtual particles, and proton radius," *Phys. Rev. A*, vol. 92, no. 012123, 2015.
- [67] G. A. Miller, "Nonperturbative lepton-sea fermions in the nucleon and the proton radius puzzle," *Phys. Rev. C*, vol. 91, no. 055204, 2015.

- [68] E. J. Salumbides, A. N. Schellekens, B. Gato-Rivera and W. Ubachs, "Constraints on extra dimensions from precision molecular spectroscopy," *New J. Phys.*, vol. 17, no. 033015, 2015.
- [69] J.-P. Karr, L. Hilico, J. Koelemeij and V. Korobov, "Hydrogen molecular ions for improved determination of fundamental constants," *Phys. Rev. A*, vol. 94, no. 050501, 2016.
- [70] M. O. Distler, T. Walcher and J. C. Bernauer, "Solution of the proton radius puzzle? Low momentum transfer electron scattering data are not enough," *arXiv:1511.00479*, 2015.
- [71] J. Grange, V. Guarino, P. Winter, K. Wood, H. Zhao, R. Carey, D. Gastler, E. Hazen, N. Kinnaird, J. Miller, J. Mott, B. Roberts, J. Benante, J. Crnkovic, W. Morse, H. Sayed, V. Tishchenko, V. Druzhinin, B. Khazin, I. Koop, I. Logashenko, Y. M. Shatunov, E. Solodov, M. Korostelev, D. Newton, A. Wolski, R. Bjorkquist, N. Eggert, A. Frankenthal, L. Gibbons, S. Kim, A. Mikhailichenko, Y. Orlov, D. Rubin, D. Sweigart, D. Allspach, G. Annala, E. Barzi, K. Bourland, G. Brown, B. C. Casey, S. Chappa, M. E. Convery, B. Drendel, H. Friedsam, T. Gadfort, K. Hardin, S. Hawke, S. Hayes, W. Jaskierny, C. Johnstone, J. Johnstone, V. Kashikhin, C. Kendziora, B. Kiburg, A. Klebaner, I. Kourbanis, J. Kyle, N. Larson, A. Leveling, A. Lyon, D. Markley, D. McArthur, K. Merritt, N. Mokhov, J. Morgan, H. Nguyen, J.-F. Ostiguy, A. Para, C. Polly M. Popovic, E. Ramberg, M. Rominsky, D. Schoo, R. Schultz, D. Still, A. Soha, S. Strigonov, G. Tassotto, D. Turrioni, E. Villegas, E. Voirin, G. Velev, D. Wolff, C. Worel, J.-Y. Wu, R. Zifko, K. Jungmann, C. Onderwater, P. Debevec, S. Ganguly, M. Kasten, S. Leo, K. Pitts, C. Schlesier, M. Gaisser, S. Haciomeroglu, Y.-I. Kim, S. Lee, M.-J. Lee, Y. Semertzidis, K. Giovanetti, V. Baranov, V. Duginov, N. Khomutov, V. Krylov, N. Kuchinskiy, V. Volnykh, C. Crawford, R. Fatemi, W. Gohn, T. Goringe, W. Korsch, B. Plaster, A. Anastasi, D. Babusci, S. Dabagov, C. Ferrari, A. Fioretti, C. Gabbanini, D. Hampai, A. Palladino, G. Venanzoni, T. Bowcock, J. Carroll, B. King, S. Maxfield, K. McCormick, A. Smith, T. Teubner, M. Whitley, M. Wormald, R. Chislett, S. Kilani, M. Lancaster, E. Motuk, T. Stuttard, M. Warren, D. Flay, D. Kawall, Z. Meadows, T. Chupp, R. Raymond, A. Tewlsey-Booth, M. Syphers, D. Tarazona, C. Ankenbrandt, M. Cummings, R. Johnson, C. Yoshikawa, S. Catalanotti, R. Di Stefano, M. Iacovacci, S. Mastroianni, S. Chattopadhyay, M. Eads, M. Fortner, D. Hedin, N. Pohlman, A. de Gouvea, H. Schellman, L. Welty-Rieger, T. Itahashi, Y. Kuno, K. Yai, F. Azfar, S. Henry, G. Alkhazov, V. Golovtsov, P. Neustroev, L. Uvarov, A. Vasilyev, A. Vorobyov, M. Zhalov, L. Cerrito, F. Gray, G. Di Sciascio, D. Moricciani, C. Fu, X. Ji, L. Li, H. Yang, D. Stöckinger, G. Cantatore, D. Cauz, M. Karuza, G. Pauletta, L. Santi, S. Baeßler, M. Bychkov, E. Frlez, D. Pocanic, L. Alonzi, M. Fertl, A. Fienberg, N. Froemming, A. Garcia, D. Hertzog, J. Kaspar, P. Kammel, R. Osofsky, M. Smith, E. Swanson, T. van Wechel and K. Lynch, "Muon (g-2) Technical Design Report," *arXiv:1501.06858*.
- [72] I. Sick and D. Trautmann, "On the rms radius of the deuteron," *Nucl. Phys. A*, vol. 637, no. 559, pp. 559-575, 1998.
- [73] C. G. Parthey, A. Matveev, J. Alnis, R. Pohl, T. Udem, U. D. Jentschura, N. Kolachevsky and T. W. Hänsch, "Precision Measurement of the Hydrogen-Deuterium 1S–2S Isotope Shift," *Phys. Rev. Lett.*, vol. 104, no. 233001, 2010.

H The thin-disk laser for the 2S – 2P measurement in muonic helium

- [74] R. Pohl, T. U. F. Nez, A. Antognini, A. Beyer, H. Fleurbaey, A. Grinin, T. Hänsch, L. Julien, F. Kottmann, J. Krauth, L. Maisenbacher, A. Matveev and F. Biraben, "Deuteron charge radius and Rydberg constant from spectroscopy data in atomic deuterium," *arXiv:1607.03165*, 2016.
- [75] B. Franke, J. J. Krauth, A. Antognini, M. Diepold, F. Kottmann and R. Pohl, "Theory of the n=2 levels in muonic helium-3 ions," *arXiv:1705.00352*.
- [76] M. Diepold, "The Lamb shift in muonic Helium ions," *PHD Ludwig-Maximilians-Universität München*, 2015.
- [77] I. Sick, "Precise root-mean-square radius of ^4He ," *Phys. Rev. C*, vol. 77, no. 941392, 2008.
- [78] B. Batell, D. McKeen and M. Pospelov, "New Parity-Violating Muonic Forces and the Proton Charge Radius," *Phys. Rev. Lett.*, vol. 107, no. 011803, 2011.
- [79] G. Carboni, G. Gorini, L. Palffy, F. Palmonari, G. Torelli and E. Zavattini, "Precise Measurement of the $2s(1/2) 2p(3/2)$ Splitting in the $(\mu^- \text{He-4}) + \text{Muonic Ion}$," *Nucl. Phys. A*, vol. 278, no. 381, 1977.
- [80] P. Hauser, H. P. von Arb, A. Bianchetti, H. Hofer, F. Kottmann, C. Lüchinger, R. Schaeren, F. Studer and J. Unternährer, "Search for the 2S-2P energy difference in muonic ^4He ions," *Phys. Rev. A*, vol. 46, no. 2363, 1992.
- [81] Z.-T. Lu, P. Mueller, G. W. F. Drake, W. Nörtershäuser, S. C. Pieper and Z.-C. Yan, "Laser probing of neutron-rich nuclei in light atoms," *Rev. Mod. Phys.*, vol. 81, no. 1383, 2013.
- [82] C. Ji, N. N. Dinur, S. Bacca and N. Barnea, "Nuclear Polarization Corrections to the $\mu^4\text{He}^+$ Lamb Shift," *Phys. Rev. Lett.* 111, 143402 (2013), vol. 111, no. 143402, 2013.
- [83] N. N. Dinur, C. Ji, S. Bacca and N. Barnea, "Nuclear structure corrections to the Lamb shift in $\mu^3\text{He}^+$ and $\mu^3\text{H}$," *arXiv:1512.05773*, 2015.
- [84] G. Hagen, A. Ekström, C. Forssén, G. R. Jansen, W. Nazarewicz, T. Papenbrock, K. A. Wendt, S. Bacca, N. Barnea, B. Carlsson, C. Drischler, K. Hebeler, M. Hjorth-Jensen, M. Miorelli, G. Orlandini, A. Schwenk and J. Simonis, "Charge, neutron, and weak size of the atomic nucleus," *arXiv:1509.07169*, 2015.
- [85] J. Carlson, S. Gandolfi, F. Pederiva, S. C. Pieper, R. Schiavilla, K. Schmidt and R. B. Wiringa, "Quantum Monte Carlo methods for nuclear physics," *Rev. Mod. Phys.*, vol. 87, no. 1067, 2015.
- [86] S. Bacca and S. Pastore, "Electromagnetic reactions on light nuclei," *J. Phys. G: Nucl. Part. Phys.*, vol. 41, no. 123002, 2014.

- [87] M. Piarulli, L. Girlanda, L. Marcucci, S. Pastore, R. Schiavilla and M. Viviani, "Electromagnetic structure of A=2 and 3 nuclei in chiral effective field theory," *Phys. Rev. C*, vol. 87, no. 014006, 2013.
- [88] L. Marcucci, F. Gross, M. Pena, M. Piarulli, R. Schiavilla, I. Sick, A. Stadler, J. V. Orden and M. Viviani, "Electromagnetic Structure of Few-Nucleon Ground States," *arXiv:1504.05063*, 2015.
- [89] R. van Rooij, J. S. Borbely, J. Simonet, M. D. Hoogerland, K. S. E. Eikema, R. A. Rozendaal and W. Vassen, "Frequency Metrology in Quantum Degenerate Helium: Direct Measurement of the 23S1 \rightarrow 21S0 Transition," *Science*, vol. 333, no. 196, 2011.
- [90] P. C. Pastor, L. Consolino, G. Giusfredi, P. D. Natale, M. Inguscio, V. A. Yerokhin and K. Pachucki, "Frequency Metrology of Helium around 1083 nm and Determination of the Nuclear Charge Radius," *Phys. Rev. Lett.*, vol. 108, no. 143001, 2012.
- [91] M. Herrmann, M. Haas, U. D. Jentschura, F. Kottmann, D. Leibfried, G. Saathoff, C. Gohle, A. Ozawa, V. Batteiger, S. Knünz, N. Kolachevsky, H. A. Schüssler, T. W. Hänsch and T. Udem, "Feasibility of coherent xuv spectroscopy on the 1S–2S transition in singly ionized helium," *Phys. Rev. A*, vol. 79, no. 052505, 2009.
- [92] D. Z. Kandula, C. Gohle, T. J. Pinkert, W. Ubachs and K. S. E. Eikema, "XUV frequency-comb metrology on the ground state of helium," *Phys. Rev. A*, vol. 84, no. 062512, 2011.
- [93] F. Dittus, Experimentelle Untersuchung über Bildung und Zerfall myonischer Heliumionen im metastabilen 2S-Zustand, Ph.D. thesis 7877, ETH Zurich, 1985.
- [94] H. P. von Arb, F. Dittus, H. Heeb, H. Hofer, F. Kottmann, S. Niggli, R. Schaeren, D. Taqqu, J. Unternährer and P. Egelhof, "Measurement of the lifetime and quenching rate of metastable 2S muonic helium ions," *Phys. Lett. B*, vol. 136, no. 232, 1984.
- [95] A. Antognini, "The Lamb Shift Experiment in Muonic Hydrogen," *PHD Ludwig-Maximilians-Universit at München*, 2005.
- [96] M. Diepold, L. M. P. Fernandes, J. Machado, P. Amaro, M. Abdou-Ahmed, F. D. Amaro, A. Antognini, F. Biraben, T.-L. Chen, D. S. Covita, A. J. Dax, B. Franke, S. Galtier, A. L. Gouvea, J. Götzfried, T. Graf, T. W. Hänsch, M. Hildebrandt, P. Indelicato, L. Julien, K. Kirch, A. Knecht, F. Kottmann, J. J. Krauth, L.-W. Liu, C. M. B. Monteiro, F. Mulhauser, B. Naar, T. Nebel, F. Nez, J. P. Santos, J. M. F. dos Santos, K. Schuhmann, C. I. Szabo, D. Taqqu, J. F. C. A. Veloso, A. Voss, B. Weichelt and R. Pohl, "Improved x-ray detection and particle identification with avalanche photodiodes," *Rev. Sci. Inst.*, vol. 86, no. 053102, 2015.
- [97] A. Antognini, F. Amaro, F. Biraben, J. Cardoso, C. Conde, D. Covita, A. Dax, S. Dhawan, L. Fernandes, T. Hänsch, V. Hughes, O. Huot, P. Indelicato, L. Julien, P. Knowles, F. Kottmann, Y.-W. Liu, J. Lopes, L. Ludhova, C. Monteiro, F. Mulhauser, F. Nez, B. N. Perry, R. Pohl, P.

j The thin-disk laser for the 2S – 2P measurement in muonic helium

- Rabinowitz, J. dos Santos, L. Schaller, C. Schwob, D. Taqqu and J. Veloso, "Powerful fast triggerable 6 μm laser for the muonic hydrogen 2S-Lamb shift experiment," *Optics Communications*, vol. 253, pp. 362-374, 2005.
- [98] A. Giesen, H. Hugel, A. Voss, K. Wittig, U. Brauch and H. Opower, "Scalable concept for diode-pumped highpower solid-state lasers," *Applied Physics B*, vol. 58, pp. 365-372, 1994.
- [99] U. Brauch, A. Giesen, M. Karszewski, C. Stewen and A. Voss, "Multiwatt diode-pumped Yb:YAG thin disk laser continuously tunable between 1018 and 1053 nm," *Opt. Lett.*, vol. 20, pp. 713-715, 1995.
- [100] C. Stewen, K. Contag, M. Larionov, A. Giesen and H. Hugel, "A 1-kW CW Thin Disc Laser," *IEEE journal of selected topics in quantum electronics*, vol. 6, pp. 650-657, 2000.
- [101] R. Peters, "Ytterbium-doped sesquioxides as highly efficient laser materials," *PHD Universitt Hamburg*, 2009.
- [102] J. Speiser and A. Giesen, "Numerical Modeling of High Power Continuous-Wave Yb:YAG Thin Disk Lasers, Scaling to 14 kW," in *Advanced Solid-State Photonics*, Vancouver, Canada, 2007.
- [103] Y. Peng, Y. Lim, J. Cheng, Y. Guo, Y. Cheah and K. Lai, "Near fundamental mode 1.1 kW Yb:YAG thin-disk laser," *Optics Letters*, vol. 38, no. 10, pp. 1709-1711, 2013.
- [104] J.-P. Negel, A. Loescher, A. Voss, D. Bauer, D. Sutter, A. Killi, M. A. Ahmed and T. Graf, "Ultrafast thin-disk multipass laser amplifier delivering 1.4 kW (4.7 mJ, 1030 nm) average power converted to 820 W at 515 nm and 234 W at 343 nm," *Opt. Express*, vol. 23, pp. 21064-21077, 2015.
- [105] R. Peters, C. Krnkel, K. Petermann and G. Huber, "Broadly tunable high-power Yb:Lu₂O₃ thin disk laser with 80% slope efficiency," *Opt. Express*, vol. 15, pp. 7075-7082, 2007.
- [106] I. I. Kuznetsov, I. B. Mukhin, D. E. Silin, A. G. Vyatkin, O. L. Vadimova and O. V. Palashov, "Thermal Effects in End-Pumped Yb:YAG Thin-Disk and Yb:YAG/YAG Composite Active Element," *IEEE Journal of Quantum Electronics*, vol. 50, pp. 133-140, 2014.
- [107] T. Y. Fan, "Optimizing the efficiency and stored energy in quasi-three-level lasers," *IEEE Journal of Quantum Electronics*, vol. 28, pp. 2692-2697, 1992.
- [108] C. Baer, O. Heckl, C. Saraceno, C. Schriber, C. Krnkel, T. Sudmeyer and U. Keller, "Frontiers in passively mode-locked high-power thin disk laser oscillators," *Optics Express*, vol. 20, no. 7, pp. 7054-7065, 2012.
- [109] A. Diebold, I. G. Z. Jia, F. E. Y. Yin, C. Saraceno, X. Tao and U. Keller, "Yb:GGG Thin-Disk Oscillator with High Power Continuous Wave Operation," in *Lasers Congress 2016 (ASSL, LSC, LAC)*, 2016.

- [110] K. S. Wentsch, B. Weichelt, F. Druon, M. A. Ahmed and T. Graf, "An Yb:CaF₂ thin-disk laser," in *CLEO EUROPE/IQEC*, 2013.
- [111] R. Peters, C. Kränkel, S. T. Fredrich-Thornton, K. Beil, K. Petermann, G. Huber, O. H. Heckl, C. R. E. Baer, C. J. Saraceno, T. Südmeyer and U. Keller, "Thermal analysis and efficient high power continuous-wave and mode-locked thin disk laser operation of Yb-doped sesquioxides," *Applied Physics B*, vol. 102, pp. 509-514, 2011.
- [112] K. Contag, S. Erhard, A. Giesen, M. Karszewski, C. Stewen and A. Voss, "Laser amplifying system". Germany Patent DE1998135108, 4 August 1998.
- [113] S. Erhard, A. Giesen, M. Karszewski, C. Stewen and A. Voss, "Laser amplifying system". Germany Patent DE1998135107, 4 August 2000.
- [114] K. Contag, M. Karszewski, C. Stewen, A. Giesen and H. Hügel, "Theoretical modelling and experimental investigations of the diode-pumped thin-disk Yb : YAG laser," *Quantum Electronics*, vol. 29, pp. 697-703, 1999.
- [115] J. Mende, E. Schmid, J. Speiser, G. Spindler and A. Giesen, "Thin disk laser: power scaling to the kW regime in fundamental mode operation," in *Proc. SPIE 7193 Solid State Lasers XVIII: Technology and Devices*, San Francisco, 2009.
- [116] F. Brunner, T. Südmeyer, E. Innerhofer, F. Morier-Genoud, R. Paschotta, V. E. Kisel, V. G. Shcherbitsky, N. V. Kuleshov, J. Gao, K. Contag, A. Giesen and U. Keller, "240-fs pulses with 22-W average power from a mode-locked thin-disk Yb:KY(WO₄)₂ laser," *Opt. Lett.*, vol. 27, pp. 1162-1164, 2002.
- [117] A. Antognini, K. Schuhmann, F. Amaro, F. Biraben, A. Dax, A. Giesen, T. Graf, T. Hänsch, P. Indelicato, L. Julien, C.-Y. Kao, P. Knowles, F. Kottmann, E. L. Bigot, Y.-W. Liu, L. Ludhova, N. Moschuring, F. Mulhauser, T. Nebel, F. Nez, P. Rabinowitz, C. Schwob, D. Taqqu and R. Pohl, "Thin-disk yb:yag oscillator-amplifier, laser ASE, and effective Yb:Yag lifetime," *IEEE Journal of Quantum Electronics*, vol. 45, pp. 993-1005, 2009.
- [118] J.-F. B. D. Kouznetsov, J. Dong and K. Ueda, "Surface loss limit of the power scaling of a thin-disk laser," *J. Opt. Soc. Am. B*, vol. 23, pp. 1074-1082, 2006.
- [119] Z. Lin, X. Zhu, G. Zhu, Y. Qiao, M. Wang, W. Zhao, H. Wang and L. Qi, "Amplified spontaneous emission model of thin disk laser with nonuniform temperature distribution," *J. Opt. Soc. Am. B*, vol. 34, pp. 625-632, 2017.
- [120] P. Peterson, A. Gavrielides, T. C. Newell, N. Vretenar and W. P. Latham, "ASE in thin disk lasers: theory and experiment," *Opt. Express*, vol. 19, pp. 25672-25684, 2011.

L The thin-disk laser for the 2S – 2P measurement in muonic helium

- [121] J. Speiser, "Scaling of thin-disk lasers—influence of amplified spontaneous emission," *J. Opt. Soc. Am. B*, vol. 26, pp. 26-35, 2009.
- [122] D. Kouznetsov, J.-F. Bisson, J. Dong and K. Ueda, "Surface loss limit of the power scaling of a thin-disk laser," *Opt. Soc. Am. B*, vol. 23, pp. 1074-1082, 2006.
- [123] A. Voss, *Der Scheibenlaser: theoretische Grundlagen des Dauerstrichbetriebs und erste experimentelle Ergebnisse anhand von Yb:YAG*, Stuttgart: Herbert Utz Verlag, 2002.
- [124] M. Karszewski, S. Erhard, T. Rupp and A. Giesen, "Efficient high power TEM 00 mode operation of diode-pumped Yb: YAG thin disk lasers," in *Advanced Solid State Lasers*, 2000.
- [125] H. Furuse, H. Chosrowjan, J. Kawanaka, N. Miyanaga, M. Fujita and Y. Izawa, "ASE and parasitic lasing in thin disk laser with anti-ASE cap," *Opt. Express*, vol. 21, pp. 13118-13124, 2013.
- [126] M. Larionov, *Laser in der Materialbearbeitung*, Stuttgart: Herbert Utz Verlag GmbH, 2009 .
- [127] EPO-TEK®377, "www.epotek.com," Jun 2015. [Online]. Available: http://www.epotek.com/site/administrator/components/com_products/assets/files/Style_Uploads/377.pdf.
- [128] W. H. Southwell, "Using apodization functions to reduce sidelobes in rugate filters," *Appl. Opt.*, vol. 28, pp. 5091-5094, 1989.
- [129] K. Ludewigt, "Solid-state laser cooling". Germany Patent DE19939774A1, 2002.
- [130] R. Woodcock, "Waveguide load". Patent US 3036280 A, 1962.
- [131] B. T. DeWitt and W. D. Burnside, "Electromagnetic scattering by pyramidal and wedge absorber," *IEEE Transactions on Antennas and Propagation*, vol. 36, pp. 971-984, 1988.
- [132] S. M. Spillane, T. J. Kippenberg, K. J. Vahala, K. W. Goh, E. Wilcut and H. J. Kimble, "Ultra-high-Q toroidal microresonators for cavity quantum electrodynamics," *Phys. Rev. A*, vol. 71, p. 013817, 2005.
- [133] S.-S. Schäd, C. Stolzenburg and A. Killi, "Festkörperlaseranordnung". Patent DE 102012214970 A1, 2014.
- [134] A. Giesen, "Thin Disk Lasers – Power scalability and beam quality," *Laser Technik Journal*, vol. 2, pp. 1863-9119, 2005.
- [135] D.-K. Ko, G. Lim, S.-H. Kim, B. H. Cha and J. Lee, "Self-seeding in a dual-cavity-type pulsed Ti:sapphire laser oscillator," *Optics Letters*, vol. 20, pp. 710-712, 1995.

- [136] W. P. Latham, A. Lobad, T. C. Newell and D. Stalnaker, "6.5 kW, Yb:YAG Ceramic Thin Disk Laser," in *Internationa symposium on high power laser ablation*, Santa Fe, (New Mexico), 2010.
- [137] K. Ludewigt, "Festkörperlaser (Scheibenlaser) mit direktem Kontakt des aktiven Mediums zu einer Kühlmittelflüssigkeit". Patent DE19939774C2, 21. August 1999.
- [138] J. Mende, J. Speiser, G. Spindler, W. L. Bohn and A. Giesen, "Mode dynamics and thermal lens effects of thin-disk lasers," in *Proc. SPIE 6871, Solid State Lasers XVII: Technology and Devices*, 2008.
- [139] M. A. Dehghan, M. H. Daemi, S. S. S. Zamani and M. Shayganmanesh, "Analysis of Yb:YAG thin disk laser resonator considering thermal lens effects: Experimentally and by Laser Cavity Analysis and Design," *Journal of Laser Applications*, p. 25, 2013.
- [140] D. Albach, G. LeTouzé and J.-C. Chanteloup, "Deformation of partially pumped active mirrors for high average–power diode–pumped solid–state lasers," *Opt. Express*, vol. 19, pp. 8413–8422, 2011.
- [141] K. S. Wentsch, B. Weichelt, S. Günster, F. Druon, P. Georges, M. A. Ahmed and T. Graf, "Yb:CaF₂ thin-disk laser," *Opt. Express*, vol. 22, pp. 1524–1532, 2014.
- [142] D. Blázquez-Sánchez, B. Weichelt, A. Austerschulte, A. Voss, T. Graf, A. Killi, H.-C. Eckstein, M. Stumpf, A. L. Matthes and U. D. Zeitner, "Improving the brightness of a multi-kilowatt single thin-disk laser by an aspherical phase front correction," *Opt. Lett.*, vol. 36, pp. 799–801, 2011.
- [143] S. Piehler, T. Dietrich, P. Wittmüss, O. Sawodny, M. A. Ahmed and T. Graf, "Deformable mirrors for intra-cavity use in high-power thin-disk lasers," *Opt. Express*, vol. 25, pp. 4254–4267, 2017.
- [144] J. Speiser and A. Giesen, "Scaling of Thin Disk Pulse Amplifiers," in *Solid State Lasers XVII: Technology and Devices*, San Jose, CA, 2008.
- [145] G. Zhu, X. Zhu, M. Wang, Y. Feng and C. Zhu, "Analytical model of thermal effect and optical path difference in end-pumped Yb:YAG thin disk laser," *Appl. Opt.*, vol. 53, pp. 6756–6764, 2014.
- [146] S. Chnais, F. Druon, S. Forget, F. Balembois and P. Georges, "On thermal effects in solid-state lasers: The case of ytterbium-doped materials," *Progress in Quantum Electronics*, vol. 30, pp. 89–153, 2006.
- [147] S. Chnais, F. Balembois, F. Druon, G. Lucas-Leclin and P. Georges, "Thermal Lensing in Diode-Pumped Ytterbium Lasers Part II: Evaluation of Quantum Efficiencies and Thermo-Optic Coefficients," *Journal of Quantum Electronics, IEEE*, vol. 40, p. 1235, 2004.

- [148] J. Perchermeier and U. Wittrock, "Precise measurements of the thermo-optical aberrations of an Yb:YAG thin-disk laser," *Opt. Lett.*, vol. 38, pp. 2422-2424, 2013.
- [149] M. Smrž, T. Miura, M. Chyla, S. Nagisetty, O. Novák, A. Endo and T. Mocek, "Suppression of nonlinear phonon relaxation in Yb:YAG thin disk via zero phonon line pumping," *Opt. Lett.*, vol. 39, pp. 4919-4922, 2014.
- [150] H. Stöcker, Taschenbuch der Physik, ISBN-13: 9783817115808: Harri Deutsch, 1998.
- [151] Crystran Ltd. , "www.crystran.co.uk," 2012. [Online]. Available: <http://www.crystran.co.uk/userfiles/files/yttrium-aluminium-garnet-yag-msds.pdf>.
- [152] WHS Sondermetalle e.K., "www.whs-sondermetalle.de," 01 2014. [Online]. Available: http://www.whs-sondermetalle.de/pdf/WCu_Wolfram-Kupfer_web.pdf.
- [153] Element Six, "http://www.e6.com/wps/wcm/connect/E6_Content_EN/Home," [Online]. Available: <http://www.e6.com/wps/wcm/connect/1a3f1905-2b90-4dd6-aa8c-c570e3416985/Optical+Grade+CVD.pdf?MOD=AJPERES&CACHEID=1a3f1905-2b90-4dd6-aa8c-c570e3416985>.
- [154] Element 6, "http://www.e6.com," [Online]. Available: <http://www.e6.com/wps/wcm/connect/919d538a-742f-4619-bca0-fd604ae888ad/Diamond+for+dressing+cutting.pdf?MOD=AJPERES&CACHEID=919d538a-742f-4619-bca0-fd604ae888ad>.
- [155] Xiamen Powerway Advanced Material Co., Ltd, "www.qualitymaterial.net," [Online]. Available: http://www.qualitymaterial.net/news_list85.html.
- [156] Precision Micro-Optics Inc., "www.pmoptics.com," [Online]. Available: http://www.pmoptics.com/silicon_carbide.html.
- [157] Wikipedia, "de.wikipedia.org," 29 2 2016 . [Online]. Available: <https://de.wikipedia.org/wiki/Aluminiumnitrid>.
- [158] American beryllia, "http://www.americanberyllia.com," [Online]. Available: http://www.americanberyllia.com/lit/Product_Spec_Sheet.pdf.
- [159] Wikipedia, [Online]. Available: <https://de.wikipedia.org/wiki/Aluminium>.
- [160] Wikipedia, [Online]. Available: https://en.wikipedia.org/wiki/Thermal_expansion.
- [161] Wikipedia, [Online]. Available: <https://en.wikipedia.org/wiki/Copper>.

- [162] A. Giesen and J. Speiser, "Fifteen years of work on thin-disk lasers: Results and scaling laws," *IEEE J. Sel. Top. Quantum Electron.*, vol. 13, pp. 598-609, 2007.
- [163] M. Larionov, *Kontaktierung und Charakterisierung von Kristallen für Scheibenlaser*, UTZ, 2009.
- [164] T. Y. Fan, "Aperture guiding in quasi-three-level lasers," *Opt. Lett.*, vol. 19, pp. 554-556, 1994.
- [165] A. G. F. a. T. Li, "Modes in a maser interferometer with curved and tilted mirrors," *Proceedings of the IEEE*, vol. 51, pp. 80-89, 1963.
- [166] S. A. Collins, "Lens-System Diffraction Integral Written in Terms of Matrix Optics," *J. Opt. Soc. Am.*, vol. 60, pp. 1168-1177, 1970.
- [167] R. L. Phillips and L. C. Andrews, "Spot size and divergence for Laguerre Gaussian beams of any order," *Appl. Opt.*, vol. 22, pp. 643-644, 1983.
- [168] O. Georg, "Use of the orthogonal system of Laguerre-Gaussian functions in the theory of circularly symmetric optical waveguides," *Appl. Opt.*, vol. 21, pp. 141-146, 1982.
- [169] J. P. Meunier, J. Pigeon and J. N. Massot, "A general approach to the numerical determination of modal propagation constants and field distributions of optical fibres," *Optical and Quantum Electronics*, vol. 13, pp. 71-83, 1981.
- [170] A. Siegmann, *Lasers*, Sausalito, California: Univ Science Books, 1986.
- [171] S. Feng and H. G. Winful, "Physical origin of the Gouy phase shift," *Opt. Lett.*, vol. 26, pp. 485-487, 2001.
- [172] P. Rambo, J. Schwarz, M. Kimmel and J. L. Porter, "Development of high damage threshold laser-machined apodizers and gain filters for laser applications," *High Power Laser Science and Engineering*, vol. 4, no. doi: 10.1017/hpl.2016.33, 2016.
- [173] M. Endo, M. Kawakami, K. Nanri, S. Takeda and T. Fujioka, "Two-dimensional simulation of an unstable resonator with a stable core," *Appl. Opt.*, vol. 38, pp. 3298-3307, 1999.
- [174] J. Kedmi and D. Treves, "Injection-locking optimization in unstable resonators," *Appl. Opt.*, vol. 20, pp. 2108-2112, 1981.
- [175] M. R. Siegrist, M. R. Green, P. D. Morgan and R. L. Watterson, "Mode structure in the unstable resonator of an optically pumped FIR laser: an investigation," *App. Opt.*, vol. 19, pp. 3824-3829, 1980.
- [176] H. Hügel and T. Graf, *Laser in der Fertigung*, Wiesbaden: Springer Vieweg, 2014.

- [177] H. Kogelnik, "On the Propagation of Gaussian Beams of Light Through Lenslike Media Inducing those with a Loss or Gain Variation," *Appl. Opt.*, vol. 4, pp. 1562-1569, 1965.
- [178] V. Magni, "Resonators for solid-state lasers with large-volume fundamental mode and high alignment stability," *Appl. Opt.*, vol. 25, pp. 107-117, 1986.
- [179] V. Magni, "Multielement stable resonators containing a variable lens," *J. Opt. Soc. Am. A* 4, pp. 1962-1969, 1987.
- [180] H. Zucker, "Optical Resonators With Variable Reflectivity Mirrors," *Bell Labs Technical Journal*, vol. 49, pp. 2349-2376, 1970.
- [181] A. Yariv and P. Yeh, "Confinement and stability in optical resonators employing mirrors with gaussian reflectivity tapers," *Optics Communications*, vol. 13, pp. 370-374, 1975.
- [182] M. Nazarathy, A. Hardy and J. Shamir, "Generalized mode theory of conventional and phase-conjugate resonators," *J. Opt. Soc. Am.*, vol. 73, pp. 576-586, 1983.
- [183] E. Hecht, *Optics*, Oldenbourg, 2001.
- [184] S. D. Silvestri, B. Majocchi, P. Laporta, V. Magni and O. Svelto, "Unstable laser resonators with super-Gaussian mirrors," *Opt. Lett.*, vol. 13, pp. 201-203, 1988.
- [185] H. Kogelnik, "Imaging of Optical Modes — Resonators with Internal Lenses," *Bell System Technical Journal*, vol. 44, pp. 1538-7305, 1965.
- [186] A. G. Fox and T. Li, "Resonant Modes in a Maser Interferometer," *Bell System Technical Journal*, vol. 40, pp. 1538-7305, 1961.
- [187] J. Dong, M. Bass, Y. Mao, P. Deng and F. Gan, "Dependence of the Yb³⁺ emission cross section and lifetime on temperature and concentration in yttrium aluminum garnet," *J. Opt. Soc. Am. B*, vol. 20, pp. 1975-1979, 2003.
- [188] P. Russbueldt, D. Hoffmann, M. Höfer, J. Löhring, J. Luttmann, A. Meissner, J. Weitenberg, M. Traub, T. Sartorius, D. Esser, R. Wester, P. Loosen and R. Poprawe, "Innoslab Amplifiers," *IEEE Journal of selected topics in quantum electronics*, vol. 21, 2015.
- [189] C. J. Koester and E. Snitzer, "Amplification in a Fiber Laser," *Appl. Opt.*, vol. 3, pp. 1182-1186, 1964.
- [190] A. Schawlow and C. Townes, "Infrared and Optical Masers," *Phys. Rev.*, vol. 112, pp. 1940-1949, 1958.

- [191] D. Hanna and Y.-W. Koo, "Stable single-mode operation of a Q-switched laser by a simple resonator length control technique," *Optics Communications*, vol. 43, pp. 414-418, 1982.
- [192] M. Schell, W. Utz, D. Huhse, J. Kässner and D. Bimberg, "Low jitter single-mode pulse generation by a self-seeded, gain-switched Fabry–Pérot semiconductor laser," *Appl. Phys. Lett.*, vol. 65, p. 3045, 2016.
- [193] G. T. Maker and A. I. Ferguson, "Single-frequency Q-switched operation of a diode-laser-pumped Nd:YAG laser," *Opt. Lett.*, vol. 13, pp. 461-463, 1988.
- [194] C. B. Dane, L. Hackel and F. B. Harris, "Self-seeded single-frequency solid-state ring laser and system using same". Patent US 7180918 B2, 16 May 2003.
- [195] LAYERTEC GmbH, "OPTICAL COATINGS," [Online]. Available: https://www.layertec.de/de/downloads/files/Layertec_Katalog_2015_Optical_Coatings.pdf.
- [196] K. Andringa, "Q-switched laser system". Patent US 3740663 A, 1973.
- [197] M. Larionov, F. Butze, D. Mueller, K. Schuhmann and A. Giesen, "12 mJ, 1 kHz single frequency thin disk regenerative amplifier," in *Conference on Lasers and Electro-Optics/Quantum Electronics and Laser Science Conference*, 2003.
- [198] S. Klingebiel, M. Schultze, C. Y. Teisset, R. Bessing, M. Haefner, S. Prinz, M. Gorjan, D. H. Sutter, K. Michel, H. G. Barros, z. Major, F. Krausz and T. Metzger, "220mJ Ultrafast Thin-Disk Regenerative Amplifier," in *CLEO*, 2015.
- [199] R. C. Jones, "A New Calculus for the Treatment of Optical Systems. I. Description and Discussion of the Calculus," *J. Opt. Soc. Am.*, vol. 31, pp. 488-493, 1941.
- [200] CASTECH INC., "Beta-Barium Borate Datasheet," [Online]. Available: http://www.castech.com/products_detail/&productId=100.html. [Accessed 27 May 2016].
- [201] F. Behlke, "Behlke Power Electronics GmbH," 28 September 2011. [Online]. Available: <http://www.behlke.com/pdf/160-01.pdf>. [Accessed 24 February 2017].
- [202] S. Xu, H. Cai and H. Zeng, "Interband photorefractive effect in β -BBO crystal due to multiphoton excitation by intense ultrashort optical pulses," *Opt. Express*, vol. 15, pp. 10576-10583, 2007.
- [203] Laser Components, "LITHIUM NIOBATE CRYSTAL (LiNbO₃)," [Online]. Available: http://www.lasercomponents.com/fileadmin/user_upload/home/Datasheets/divers-optik/laserstaebe_kristalle/linbo3.pdf. [Accessed 06. March 2017].

- [204] L. E. Zapata, H. Lin, A.-L. Calendron, H. Cankaya, M. Hemmer, F. Reichert, W. R. Huang, E. Granados, K.-H. Hong and F. X. Kärtner, "Cryogenic Yb:YAG composite-thin-disk for high energy and average power amplifiers," *Opt. Lett.*, vol. 40, pp. 2610-2613, 2015.
- [205] J. Neukum, "Wavelength stabilized high-power diode lasers and modules," in *High Power Diode Lasers and Systems Conference*, Coventry, United Kingdom, 2009.
- [206] TRUMPF GmbH, [Online]. Available: <http://www.trumpf-laser.com/de/produkte/festkoerperlaser/scheibenlaser/trudisk.htm>.
- [207] Universität Stuttgart, Institut für Strahlwerkzeuge (IFSW), Pfaffenwaldring 43; 70569 Stuttgart; Deutschland.
- [208] TRUMPF GmbH + Co. KG, Johann-Maus-Str. 2; 71254 Ditzingen; Deutschland.
- [209] C. Vorholt and U. Wittrock, "Spatial hole burning in Yb:YAG thin-disk lasers," *Applied Physics B*, vol. 120, pp. 711-721, 2015.
- [210] A. Berry, D. Hanna and C. Sawyers, "High power, single frequency operation of a Q-switched TEM₀₀ Mode Nd:YAG laser," *Optics Communications*, vol. 40, pp. 54-58, 1981.
- [211] A. L. Caprara and J.-M. Heritier, "Single longitudinal mode laser without seeding". Patent US 5412673 A, 22 December 1993.
- [212] G. Palmer, M. Schultze, M. Siegel, M. Emons, U. Bünting and U. Morgner, "Passively mode-locked Yb:KLu(WO₄)₂ thin-disk oscillator operated in the positive and negative dispersion regime," *Opt. Lett.*, vol. 33, pp. 1608-1610, 2008.
- [213] V. Evtuhov and A. E. Siegman, "A "Twisted-Mode" Technique for Obtaining Axially Uniform Energy Density in a Laser Cavity," *Appl. Opt.*, vol. 4, pp. 142-143, 1965.
- [214] P. Krehl and S. Engemann, "August Toepler — The first who visualized shock waves," *Shock Waves*, vol. 5, pp. 1-18, 1995.
- [215] H. Pan, S. Xu and H. Zeng, "Passively Q-switched Single-longitudinal-mode c-cut Nd:GdVO₄ laser with a twisted-mode cavity," *Opt. Express*, vol. 13, pp. 2755-2760, 2005.
- [216] Y. Ma, L. Wu, H. Wu, W. Chen, Y. Wang and S. Gu, "Single-longitudinal mode Nd:YVO₄ microchip laser with orthogonal-polarization bidirectional traveling-waves mode," *Opt. Express*, vol. 16, pp. 18702-18713, 2008.
- [217] T. Nebel, F. D. Amaro, A. Antognini, F. Biraben, J. M. R. Cardoso, D. S. Covita, A. Dax, L. M. P. Fernandes, A. L. Gouvea, T. Graf, T. W. Hänsch, M. Hildebrandt, P. Indelicato, L. Julien, K. Kirch,

- F. Kottmann, Y. -W. Liu, C. M. B. Monteiro, F. Nez, J. M. F. d. Santos and K. S, "The Lamb-shift experiment in Muonic helium," *Hyperfine Interactions*, pp. 195-201, 01 December 2012.
- [218] K. Schuhmann, A. Antognini, K. Kirch, T. Graf, M. A. Ahmed, A. Voss and B. Weichelt, "Thin-disk laser for the measurement of the radii of the proton and the alpha-particle," in *Advanced Solid State Lasers*, Paris, 2013.
- [219] M. D. J. Vogelsang, A. Antognini, A. Dax, J. Götzfried, T. Hänsch, F. Kottmann, J. Krauth, Y. Liu, F. N. T. Nebel, K. Schuhmann, D. Taqqu and R. Pohl, "Multipass laser cavity for efficient transverse illumination of an elongated volume," *Opt. Express*, pp. 13050-13062, 22 5 2014.
- [220] W. Paa, W. Triebel, C. Eigenbrod, M. Larionov and A. Giesen, "The "advanced disk laser" — An onboard laser diagnostics system for drop tower experiments," *Microgravity - Science and Technology*, vol. 17, no. 3, pp. 71-74, 2005.
- [221] M. D. Martinez, J. K. Crane, L. A. Hackel and F. A. P. a. D. F. Browning, "Optimized diode-pumped Nd:glass prototype regenerative amplifier for the National Ignition Facility (NIF)," in *SPIE 3267, Laser Resonators*, San Jose, 1998.
- [222] M. Schulz, High Energy High Rep etition-Rate Thin-Disk Amplifier for OPCPA Pumping, Hamburg: DESY-2013-00751, 2013.
- [223] B. Reagan, A. Curtis, K. Wernsing, F. Furch, B. Luther and J. Rocca, "Development of High Energy Diode-Pumped Thick-Disk Yb:YAG Chirped-Pulse-Amplification Lasers," *IEEE Journal of Quantum Electronics*, vol. 48, no. 6, pp. 827- 835, 2012.
- [224] S. Keppler, C. Wandt, M. Hornung, R. Bödefeld, A. Kessler, A. Sävert, M. Hellwing, F. Schorcht, J. Hein and M. C. Kaluza, "Multipass amplifiers of POLARIS," in *Proc. SPIE 8780, High-Power, High-Energy, and High-Intensity Laser* , Prague, 2013.
- [225] K. Schuhmann, F. Amaro, F. Biraben, A. Dax, A. Giesen, T. Graf, T. Hansch, P. Indelicato, L. Julien, C. Kao, P. Knowles, F. Kottmann, E. L. Bigot, Y. Liu, L. Ludhova, N. Moschuring, F. Mulhauser and T. Nebel, "Thin-Disk Yb:YAG Oscillator-Amplifier Laser, ASE, and Effective Yb:YAG Lifetime," *IEEE J. Quant. Electr. Vol. 45*, pp. 993-1005, 2009 No.8.
- [226] M. Schulz, R. Riedel, A. Willner, S. Düsterer, M. J. Prandolini, J. Feldhaus, B. Faatz, J. Rossbach, M. Drescher and F. Tavella, "Pulsed operation of a high average power Yb:YAG thin-disk multipass amplifier," *Opt. Express*, vol. 20, no. 5, pp. 5038-5043, 2013.
- [227] J. Tümmler, R. Jung, H. Stiel, P. V. Nickles and W. Sandner, "High-repetition-rate chirped-pulse-amplification thin-disk laser system with joule-level pulse energy," *Optics Letters*, vol. 34, no. 9, pp. 1378-1380, 2009.

- [228] J. Negel, A. Voss, M. A. Ahmed, D. Bauer, D. Sutter, A. Killi and T. Graf, "1.1 kW average output power from a thin-disk multipass amplifier for ultrashort laser pulses," *Optics Letters*, vol. 38, no. 24, pp. 5442-5445, 2013.
- [229] U. Keller, "Ultrafast solid-state laser oscillators: a success story for the last 20 years with no end in sight," *Applied Physics B*, vol. 100, pp. 15-28, 2010.
- [230] F. Krausz and M. Ivanov, "Attosecond physics," *Rev. Mod. Phys.* 81, p. 163–234, 2009.
- [231] T. Südmeyer, S. V. Marchese, S. Hashimoto, C. R. E. Baer, G. Gingras, B. Witzel and U. Keller, "Femtosecond laser oscillators for high-field science," *Nature Photon*, vol. 2, pp. 599-604, 2008.
- [232] A. Giesen, J. Speiser, R. Peters, C. Kränkel and K. Petermann, "Thin-Disk Lasers Come of Age," *Photonics Spectra*, 2007.
- [233] TRUMPF Scientific Lasers GmbH + Co. KG, [Online]. Available: <http://www.trumpf-scientific-lasers.com>.
- [234] T. Gottwald, C. Stolzenburg, D. Bauer, J. Kleinbauer, V. Kuhn, T. Metzger, S. Schad, D. Sutter and A. Killi, "Recent disk laser development at Trumpf," in *Proc. SPIE 8898*, San Francisco, 2012.
- [235] S. Piehler, B. Weichelt, A. Voss, M. A. Ahmed and T. Graf, "Power scaling of fundamental-mode thin-disk lasers using intracavity deformable mirrors," *Opt. Lett.*, no. 37, pp. 5033-5035, 2012.
- [236] H. Fattahi, H. G. Barros, M. Gorjan, T. Nubbemeyer, B. Alsaif, C. Y. Teisset, M. Schultze, S. Prinz, M. Haefner, M. Ueffing, A. Alismail, L. Vamos, A. Schwarz, O. Pronin, J. Brons, X. T. Geng, G. Arisholm, M. Ciappina, V. S. Yakovlev, D. E. Kim and A. M. Azz, "Third generation femtosecond technology," *Optica* 1, pp. 45-63, 2014.
- [237] M. Larionov and J. Neuhaus, "Regenerative thin disk amplifier with a pulse energy of 120 mJ at 1 kHz," in *Advanced Solid State Lasers*, Shanghai China, 2014.
- [238] C. Saraceno, F. Emaury, C. Schriber, A. Diebold, M. Hoffmann, M. Golling, T. Südmeyer and U. Keller, "Toward millijoule-level high-power ultrafast thin-disk oscillators," *Selected Topics in IEEE Journal of Quantum Electronics*, vol. 21, pp. 106-123, 2015.
- [239] J. Brons, V. Pervak, E. Fedulova, D. Bauer, D. Sutter, V. Kalashnikov, A. Apolonskiy, O. Pronin and F. Krausz, "Energy scaling of kerr-lens mode-locked thin-disk oscillators," *Opt. Lett.*, vol. 39, pp. 6442-6445, 2014.
- [240] J. Negel, A. Loescher, A. Voss, D. Bauer, D. Sutter, A. Killi, M. Ahmed and T. Graf, "Ultrafast thin-disk multipass laser amplifier delivering 1.4 kW (4.7 mJ, 1030 nm) average power

converted to 820 W at 515 nm and 234 W at 343 nm," *Opt. Express*, vol. 23, pp. 21064-21077, 2015.

- [241] N. Kanda, A. Eilanlou, T. Imahoko, T. Sumiyoshi, Y. Nabekawa, M. Kuwata-Gonokami and K. Midorikawa, "High-Pulse-Energy Yb:YAG Thin Disk Mode-Locked Oscillator for Intra-Cavity High Harmonic Generation," in *ASSP*, Paris, 2013.
- [242] O. Pronin, J. Brons, C. Grasse, V. Pervak, G. Boehm, M.-C. Amann, A. Apolonski, V. L. Kalashnikov and F. Krausz, "High-power Kerr-lens mode-locked Yb:YAG thin-disk oscillator in the positive dispersion regime," *Opt. Lett.*, vol. 37, pp. 3543-3545, 2012.
- [243] M. Richardson and A. Zoubir, "High intensity MHz mode-locked". USA Patent Patent US 7590156 B1, 2009.
- [244] C. Saraceno, F. Emaury, C. Schriber, M. Hoffmann, M. Golling, T. Südmeyer and U. Keller, "Ultrafast thin-disk laser with 80 μ J pulse energy and 242 W of average power," *Optics Letters*, vol. 39, no. 1, pp. 9-12, 2014.
- [245] D. Bauer, I. Zawischa, D. H. Sutter, A. Killi and T. Dekorsy, "Mode-locked yb:yag thin-disk oscillator with 41 μ J pulse energy at 145 W average infrared power and high power frequency conversion," *Opt. Express*, vol. 20, pp. 9698-9704, 2012.
- [246] C. Hönninger, R. Paschotta, F. Morier-Genoud, M. Moser and U. Keller, "Q-switching stability limits of continuous-wave passive mode locking," *J. Opt. Soc. Am. B*, p. 46–56, 1999.
- [247] B. Dannecker, X. Délen, K. S. Wentsch, B. Weichelt, C. Hönninger, A. Voss, M. A. Ahmed and T. Graf, "Passively mode-locked Yb:CaF₂ thin-disk laser," *Opt. Express*, vol. 22, pp. 22278-22284, 2014.
- [248] J. Speiser, "Thin disk laser-energy scaling," *Laser Physics*, vol. 19, pp. 274-280, 2009.
- [249] S. Gatz and J. Herrman, "Geometrical threshold zones and Gaussian modes in lasers with radially varying gain," *Opt. Lett.*, vol. 19, pp. 1696-1698, 1994.
- [250] L. W. Casperon and A. Yariv, "The Gaussian Mode in Optical Resonators with a Radial Gain Profile," *Appl. Phys. Lett.*, vol. 12, pp. 355-357, 1968.
- [251] L. W. Casperon and S. D. Lunnam, "Gaussian Modes in High Loss Laser Resonators," *Appl. Opt.*, vol. 14, pp. 1193-1199, 1975.
- [252] J. Herrman, "Theory of Kerr-lens mode locking: role of self-focusing and radially varying gain," *J. Opt.Soc. Am. B*, vol. 11, pp. 498-512, 1994.

- [253] D. V. Willetts and M. R. Harris, "Output Characteristics of a Compact 1 J Carbon Dioxide Laser with a Gaussian Reflectivity Resonator," *IEEE Journal of quantum electronics*, vol. 24, pp. 849-855, 1988.
- [254] V. Magni, "Perturbation theory of nonlinear resonators with an application to Kerr lens mode locking," *J. Opt. Soc. Am. B*, vol. 13, pp. 2498-2507, 1996.
- [255] M. Kumkar, "Laser amplifying system". Germany Patent DE 10140254 A1, 9 8 2001.
- [256] P. B. Lundquist, S. Sarkisyan, E. A. Wilson, R. M. Copenhaver, H. Martin and S. McCahon, "Off axis walk off multi-pass amplifiers". US Patent US 8605355 B2, 24 11 2009.
- [257] J. Mende, G. Spindler, E. Schmid, J. Speiser and A. Giesen, "Thin-Disk Lasers with Dynamically Stable Resonators," in *Advanced Solid-State Photonics OSA Technical Digest Series (CD)* (Optical Society of America, 2009).
- [258] J. Wang and D. Silva, "Wave-front interpretation with Zernike polynomials," *Appl. Opt.*, vol. 19, pp. 1510-1518, 1980.
- [259] R. Paschotta, J. A. d. Au, G. Spühler, S. Erhard, A. Giesen and U. Keller, "Passive mode locking of thin-disk lasers: effects of spatial hole burning," *Appl. Phys. B*, vol. 72, pp. 267-278, 2001.
- [260] C. Baer, C. Kränkel, C. Saraceno, O. Heckl, M. Golling, R. Peters, K. Petermann, T. Sdmeyer, G. Huber and U. Keller, "Femtosecond thin-disk laser with 141 W of average power," *Opt. Lett.*, vol. 35, pp. 2302-2304, 2010.
- [261] P. Peterson, A. Gavrielides, T. C. Newell, N. Vretenar and W. P. Latham, "ASE in thin disk lasers: theory and Experiment," *Opt. Express*, vol. 19, pp. 25672-25684, 2011.
- [262] M. Siebold, M. Loeser, F. Roeser, M. Seltmann, G. Harzendorf, I. Tsybin, S. Linke, S. Banerjee, P. D. Mason, P. J. Phillips, K. Ertel, J. C. Collier and U. Schramm, "High-energy, ceramic- disk Yb:LuAG laser amplifier," *Opt. Express*, vol. 20, pp. 21992-22000, 2012.
- [263] C. J. Saraceno, C. Schriber, F. Emaury, O. H. Heckl, C. R. R. Baer, M. Hoffmann, K. Beil, C. Kränkel, M. Golling, T. Südmeyer and U. Keller, "Cutting-edge high-power ultrafast thin disk oscillators," *Appl. Sci.*, vol. 3, pp. 355-395, 2013.
- [264] S. Ricaud, A. Jaffres, P. Loiseau, B. Viana, B. Weichelt, M. Abdou-Ahmed, A. Voss, T. Graf, D. Rytz, M. Delaigue, E. Mottay, P. Georges and F. Druon, "Yb:CaGdAlO₄ thin-disk laser," *Opt. Lett.*, vol. 36, pp. 4134-4136, 2011.
- [265] S. Erhard, M. Karszewski, C. Stewen, A. Giesen, K. Contag and A. Voss, "Pumping schemes for multi-kW thin disk lasers," in *Advanced Solid State Laser*, Davos, 2000.

- [266] K. Contag, U. Brauch, A. Giesen, I. Johannsen, M. Karszewski, U. Schiegg, C. Stewen and A. Voss, "Multihundred-watt diode-pumped Yb:YAG thin disc laser," *Solid State Lasers VI*, 2, 31. 03. 1997.
- [267] S. Erhard, A. Giesen and C. Stewen, "Laser amplifying system". Patent DE 2000105195, 5 February 2001.
- [268] S. Erhard and A. Giesen, "Laser amplifying system". Patent DE 2000105194, 5 February 2001.
- [269] Dausinger + Giesen GmbH, [Online]. Available: <http://www.dausinger-giesen.de/tdm-10-hp-lab..>
- [270] Dausinger + Giesen GmbH, [Online]. Available: <http://www.dausinger-giesen.de/tdm-10-0>.
- [271] Institut für Strahlwerkzeuge, [Online]. Available: http://www.ifsw.uni-stuttgart.de/produkte/pdf/1406_IFSW_HO_TDPumpModules_end.pdf.
- [272] A. Giesen, M. Larionov and K. Schuhmann, "Laserverstärkersystem". Patent DE 201110075274, 4 May 2012.
- [273] Dausinger + Giesen GmbH, [Online]. Available: <http://www.dausinger-giesen.de/tdm-005>.
- [274] J. J. Krauth, The Lamb shift of the muonic helium-3 ion and the helion charge radius, Dissertation, LMU München, 2017.
- [275] F. Twyman and A. Green. British Patent Patent 103832, 1916.
- [276] E. P. Goodwin and J. C. Wyant, "Field Guide to Interferometric Optical Testing," *SPIE Press*, 2006.
- [277] D. Malacara, Optical Shop Testing Chap 2 Twyman–Green Interferometer, John Wiley & Sons, Ltd, 2006.
- [278] A. Michelson and E. Morley, "On the Relative Motion of the Earth and the Luminiferous Ether," *American Journal of Science*, vol. 34, pp. 333-345, 1887.
- [279] P. d. Groot, "Phase Shifting Interferometry," *Optical Measurement of Surface Topography*, Vols. DOI 10.1007/978-3-642-12012-1_8, pp. 167-186, 2011.
- [280] X. Chen, M. Gramaglia and J. A. Yeazell, "Phase-shifting interferometry with uncalibrated phase shifts," *Appl. Opt.*, vol. 39, pp. 585-591, 2000.

- [281] J. Li, L. Zhong, S. Liu, Y. Zhou, J. Xu, J. Tian and X. Lu, "An advanced phase retrieval algorithm in N-step phase-shifting interferometry with unknown phase shifts," *(Nature) Scientific Reports*, 2017.
- [282] J. Harvey and J. Forgham, "The spot of Arago: New relevance for an old phenomenon," *American Journal of Physics*, vol. 52, pp. 243-247, 1984.
- [283] M. Gu and X. S. Gan, "Fresnel diffraction by circular and serrated apertures illuminated with an ultrashort pulsed-laser beam," *J. Opt. Soc. Am. A*, vol. 13, pp. 771-778, 1996.
- [284] J. H. Bruning, D. R. Herriott, J. E. Gallagher, D. P. Rosenfeld, A. D. White and D. J. Brangaccio, "Digital Wavefront Measuring Interferometer for Testing Optical Surfaces and Lenses," *Appl. Opt.*, vol. 13, pp. 2693-2703, 1974.
- [285] J. Speiser, "Scaling of thin-disk lasers—influence of amplified spontaneous emission," *J. Opt. Soc. Am. B*, vol. 26, pp. 26-35, 2009.
- [286] F. Twyman and A. Green, "Method and apparatus for finishing prisms or lenses or combinations of the same". Patent US1252512 A, 1918.
- [287] A. Michelson and E. Morley, "On the Relative Motion of the Earth and the Luminiferous Ether," *American Journal of Science*, vol. 34, pp. 333-345, 1887.
- [288] M. Gerber and T. Graf, "Generation of Super-Gaussian modes in Nd:YAG lasers with a graded-phase mirror," *IEEE Journal of Quantum Electronics*, vol. 40, pp. 741-746, 2004.

Curriculum vitae



Full name: Karsten Reinhard Fürchtegott Schuhmann
Birth date: 06.07.1974
Place of birth: Bad Homburg, Germany
Nationality: German
Marital status: Married, two children: Timo(14), Leon(7)

Education

1996-2002: Undergraduate student in physics, Johann Wolfgang Goethe University, Frankfurt (Final grade = 1).
2002-2009 Laser developer at the IFSW Stuttgart, Stuttgart, Germany
2007-2009 Participated at the measurement of the proton radius from muonic hydrogen at the Paul Scherrer Institute, Villigen, Switzerland
2009-2012 Laser developer at Dausinger-Giesen GmbH, Stuttgart, Germany
2012-2017 PHD student at the ETH, Zürich, Switzerland

z The thin-disk laser for the 2S – 2P measurement in muonic helium

Patents

- since 2016: K. Schuhmann and A. Antognini, High power multi-pass laser oscillator, Patent EP15201707 submitted to European Patent Office.
- 2013: K. Schuhmann, Vapor pressure controlled adaptive mirror, Patent DE 102013102736, 18.3.2013.
- 2011: A. Giesen, M. Larionov and K. Schuhmann, Laserverstärkersystem, Patent DE201110075274, 04.05.2011

Main Skills

- Design of optical system and resonators
- Development of high-power thin-disk laser
- Interferometry
- Analog electronics
- Non-linear optical processes

Main Achievements

- Several patent declarations. The one submitted via the ETH (and PSI) could have a very large impact in the field of mode-locked lasers which is an important industrial sector.
- Found a new power and energy-scaling limit arising from misalignment instabilities caused by thermal lens effects and proposed a method to avoid it.
- Proposed a new multi-pass resonator architecture for energy scaling of mode-locked lasers.
- Systematic study of pump optics geometries for thin-disk lasers to increase the number of pump passes while minimizing the size of the needed optics. This leads to better efficiencies and open the possibility to the usage of novel active materials.
- Development of the thin-disk laser for the muonic helium experiment at PSI that has led to the successful measurement of 5 transition frequencies. Data analysis is ongoing.
- Development of a thin-disk laser operated in vacuum with 418 W in TEM₀₀ mode.
- Development of a high-power pump-optic module for thin-disk lasers up to 30 kW pump power.
- Development of a simple pump-optic module for low power thin-disk lasers.
- Development of a single frequency thin-disk laser with intracavity doubling with optical-to-optical efficiency of 30 %.
- Realization of commercial interferometers.
- Development of the thin-disk laser which has led to the measurement of the proton radius from muonic hydrogen spectroscopy and the so called “proton radius puzzle”.
- Participation of the EU-Project “Innovative NDT concepts for aerospace industry”.

List of publications

- K. Schuhmann, K. Kirch and A. Antognini, “Multi-pass resonator design for energy scaling of mode-locked thin-disk lasers,” Proc. SPIE 10082, Solid State Lasers XXVI: Technology and Devices, 100820J (2017) doi:10.1117/12.2251913
- R. Pohl, F. Nez, L.M.P. Fernandes, F. D. Amaro, F. Biraben, J. M.R. Cardoso, D. S. Covita, A. Dax, S. Dhawan, M. Diepold, A. Giesen, A. L. Gouvea, T. Graf, T.W. Hänsch, P. Indelicato, L. Julien, P. Knowles, F. Kottmann, E.-O. Le Bigot, Yi-Wei Liu, J.A.M. Lopes, L. Ludhova, C.M.B. Monteiro, F. Mulhauser, T. Nebel, P. Rabinowitz, J. M.F. dos Santos, L. Schaller, K. Schuhmann, C. Schwob, D. Taqqu, J. F.C.A. Veloso, A. Antognini, “Laser spectroscopy of muonic deuterium,” Science 353, 669-673 (2016).
- F. Nez, F. D. Amaro, A. Antognini, F. Biraben, J. M. R. Cardoso, D. S. Covita, A. Dax, S. Dhawan, M. Diepold, L. M. P. Fernandes, A. Giesen, A. L. Gouvea, T. Graf, T. W. Hänsch, P. Indelicato, L. Julien, P. Knowles, F. Kottmann, E. O. Le Bigot, Y. W. Liu, J. A. M. Lopes, L. Ludhova, C. M. B. Monteiro, F. Mulhauser, T. Nebel, . Rabinowitz, J. M. F. dos Santos, L. Schaller, K. Schuhmann, C. Schwob, D. Taqqu, J. F. C. A. Veloso and R. Pohl, “Laser spectroscopy of muonic deuterium: New contribution to the proton puzzle, 2016 Conference on Precision Electromagnetic Measurements (CPEM 2016), DOI: 10.1109/CPEM.2016.7540776 (2016).
- R. Pohl, F. Nez, L.M.P. Fernandes, M. Abdou Ahmed, F.D. Amaro, P. Amaro, F. Biraben, J.M.R. Cardoso, D.S. Covita, A. Dax, S. Dhawan, M. Diepold, B. Franke, S. Galtier, A. Giesen, A.L. Gouvea, J. Götzfried, T. Graf, T.W. Hänsch, M. Hildebrandt, P. Indelicato, L. Julien, K. Kirch, A. Knecht, P. Knowles, F. Kottmann, J.J. Krauth, E.-O. Le Bigot, Yi-Wei Liu, J.A.M. Lopes, L. Ludhova, J. Machado, C.M.B. Monteiro, F. Mulhauser, T. Nebel, P. Rabinowitz, J.M.F. dos Santos, J.P. Santos, L.A. Schaller, K. Schuhmann, C. Schwob, C.I. Szabo, D. Taqqu, J. F.C.A. Veloso, A. Voss, B. Weichelt, A. Antognini, “Laser Spectroscopy of Muonic Atoms and Ions,” arXiv:1609.03440 (2016).
- K. Schuhmann, K. Kirch, F. Nez, R. Pohl, A. Antognini, “Thin-disk laser scaling limit due to thermal-lens induced misalignment instability,” Applied Optics 55, 9022-9032 (2016).
- K. Schuhmann, K. Kirch, A. Antognini, “Multi-pass oscillator layout for high-energy mode-locked thin-disk lasers,” arXiv:1603.00404 (2016).
- K. Schuhmann and A. Antognini, “High power multi-pass laser oscillator,” Patent declaration EP15201707 (2016).
- K. Schuhmann, T. W. Hänsch, K. Kirch, F. Kottmann, R. Pohl, D. Taqqu and A. Antognini, “Thin-disk laser pump schemes for large number of passes and moderate pump source quality,” Applied Optics 54, 9400-9408 (2015). DOI: 10.1364/AO.54.009400
- Antognini, K. Schuhmann, F. D. Amaro, P. Amaro, M. Abdou-Ahmed, F. Biraben, T.-L. Chen, D.S. Covita, A. J. Dax, M. Diepold, L. M. P. Fernandes, B. Franke, S. Galtier, A. L. Gouvea, J. Götzfried, T. Graf, T. W. Hänsch, M. Hildebrandt, P. Indelicato, L. Julien, K. Kirch, A. Knecht, F. Kottmann, J. J. Krauth, Y.-W. Liu, J. Machado, C. M. B. Monteiro, F. Mulhauser, F. Nez, J. P. Santos, J. M. F. dos Santos, C. I. Szabo, D. Taqqu, J. F. C. A. Veloso, A. Voss, B. Weichelt and R. Pohl, “Experiments towards resolving the proton charge radius puzzle,” arXiv:1509.03235 (2015).
- M. Diepold, L. M. P. Fernandes, J. Machado, P. Amaro, M. Abdou-Ahmed, F. D. Amaro, A. Antognini, F. Biraben, T.-L. Chen, D. S. Covita, A. J. Dax, B. Franke, S. Galtier, A. L. Gouvea, J. Götzfried, T. Graf,

- T. W. Hänsch, M. Hildebrandt, P. Indelicato, L. Julien, K. Kirch, A. Knecht, F. Kottmann, J. J. Krauth, Y.-W. Liu, C. M. B. Monteiro, F. Mulhauser, B. Naar, T. Nebel, F. Nez, J. P. Santos, J. M. F. dos Santos, K. Schuhmann, C. I. Szabo, D. Taqqu, J. F. C. A. Veloso, A. Voss, B. Weichelt and R. Pohl, "Improved X-ray detection and particle identification with avalanche photodiodes," *Rev. Sci. Inst.* 86, 053102 (2015). DOI: 10.1063/1.4921195
- K. Schuhmann, M. A. Ahmed, T. Graf, T. W. Hänsch, K. Kirch, F. Kottmann, R. Pohl, D. Taqqu, A. Voss, B. Weichelt and A. Antognini, "Thin-disk laser multi-pass amplifier," *Proc. of SPIE* 9342, 93420U (2015), arXiv:1509.05731. DOI: 10.1117/12.2078858
 - J. Vogelsang, M. Diepold, A. Antognini, A. Dax, J. Götzfried, T. W. Hänsch, F. Kottmann, J. J. Krauth, Y.-W. Liu, T. Nebel, F. Nez, K. Schuhmann, D. Taqqu, and R. Pohl, "Multipass laser cavity for efficient transverse illumination of an elongated volume," *Optics Express* 22, 13050-13062 (2014). DOI: 10.1364/OE.22.013050.
 - M. Diepold, F. D. Amaro, A. Antognini, F. Biraben, J. M. R. Cardoso, D. S. Covita, A. Dax, S. Dhawan, L. M. P. Fernandes, A. Giesen, A. L. Gouvea, T. Graf, T. W. Hänsch, P. Indelicato, L. Julien, C.-Y. Kao, P. Knowles, F. Kottmann, E.-O. Le Bigot, Y.-W. Liu, J. A. M. Lopes, L. Ludhova, C. M. B. Monteiro, F. Mulhauser, T. Nebel, F. Nez, P. Rabinowitz, J. M. F. dos Santos, L. A. Schaller, K. Schuhmann, C. Schwob, D. Taqqu, J. F. C. A. Veloso, J. Vogelsang and R. Pohl, "Lifetime and population of the 2S state in muonic hydrogen and deuterium," *Phys. Rev. A* 88, 042520 (2013). DOI 10.1103/PhysRevA.88.042520
 - Antognini, F. Nez, K. Schuhmann, F. D. Amaro, F. Biraben, J. M. R. Cardoso, D. S. Covita, A. Dax, S. Dhawan, M. Diepold, L. M. P. Fernandes, A. Giesen, A. L. Gouvea, T. Graf, T. W. Hänsch, P. Indelicato, L. Julien, C.-Y. Kao, P. Knowles, F. Kottmann, E.-O. Le Bigot, Y.-W. Liu, J. A. M. Lopes, L. Ludhova, C. M. B. Monteiro, F. Mulhauser, T. Nebel, P. Rabinowitz, J. M. F. dos Santos, L. A. Schaller, C. Schwob, D. Taqqu, J. F. C. A. Veloso, J. Vogelsang and R. Pohl, "Proton structure from the measurement of the 2S-2P transition frequencies of muonic hydrogen," *Science* 339, 417-420 (2013). DOI: 10.1126/science.1230016
 - R. Pohl, A. Antognini, F. D. Amaro, F. Biraben, J. M. R. Cardoso, D. S. Covita, A. Dax, S. Dhawan, M. Diepold, L. M. P. Fernandes, A. Giesen, A. L. Gouvea, T. Graf, T. W. Hänsch, P. Indelicato, L. Julien, C.-Y. Kao, P. Knowles, J. A. M. Lopes, E.-O. Le Bigot, Y.-W. Liu, L. Ludhova, C. M. B. Monteiro, F. Mulhauser, T. Nebel, F. Nez, P. Rabinowitz, J. M. F. dos Santos, L. A. Schaller, K. Schuhmann, C. Schwob, D. Taqqu, J. F. C. A. Veloso, J. Vogelsang and F. Kottmann, "Laser spectroscopy of muonic hydrogen," *Annalen der Physik* 525, 1521-3889 (2013). DOI: 10.1002/andp.201300058.
 - M. Larionov and K. Schuhmann, "VBG stabilization of efficient high-power frequency-doubled disk laser," in *OSA Advanced Solid-State Lasers*, Paris France (2013).
 - K. Schuhmann, "Vapor pressure controlled adaptive mirror," Patent DE 102013102736 (2013).
 - T. Nebel, F.D. Amaro, A. Antognini, F. Biraben, J.M.R. Cardoso, D.S. Covita, A. Dax, L.M.P. Fernandes, A.L. Gouvea, T. Graf, T.W. Hänsch, M. Hildebrandt, P. Indelicato, L. Julien, K. Kirch, F. Kottmann, Y.-W. Liu, C.M.B. Monteiro, F. Nez, J.M.F. dos Santos, K. Schuhmann, D. Taqqu, J.F.C.A. Veloso, A. Voss and R. Pohl, "The Lamb-shift experiment in muonic helium," *Hyperfine Interactions*, 212, 195-201 (2012).

- T. Nebel, F.D. Amaro, A. Antognini, F. Biraben, J.M.R. Cardoso, D.S. Covita, A. Dax, L.M.P. Fernandes, A.L. Gouvea, T. Graf, T.W. Hänsch, M. Hildebrandt, P. Indelicato, L. Julien, K. Kirch, F. Kottmann, Y.-W. Liu, C.M.B. Monteiro, F. Nez, J.M.F. dos Santos, K. Schuhmann, D. Taqqu, J.F.C.A. Veloso, A. Voss, and R. Pohl, “The size of the proton: from the Lamb-shift in muonic hydrogen,” *Hyperfine Interactions* 212, 185-194 (2012). DOI: 10.1007/s10751-011-0386-5.
- Antognini, R. Pohl, F.D. Amaro, F. Biraben, J.M.R. Cardoso, D.S. Covita, A. Dax, S. Dhawan, L.M.P. Fernandes, A. Giesen, A.L. Gouvea, T. Graf, T.W. Hänsch, M. Hildebrandt, P. Indelicato, L. Julien, C.-Y. Kao, K. Kirch, P. Knowles, E.-O. Le Bigot, Y.-W. Liu, J.A.M. Lopes, L. Ludhova, C.M.B. Monteiro, F. Mulhauser, T. Nebel, F. Nez, P. Rabinowitz, J.M.F. dos Santos, L.A. Schaller, K. Schuhmann, C. Schwob, D. Taqqu, J.F.C.A. Veloso, A. Voss, F. Kottmann, “The Lamb Shift in Muonic Hydrogen and the Proton Radius,” *Science Direct, Physics Procedia* 17, 10-19 (2011). DOI: 10.1016/j.phpro.2011.06.012
- Giesen, M. Larionov and K. Schuhmann, “Laserverstärkersystem,” Patent DE201110075274 (2011).
- Antognini, F. Nez, F. D. Amaro, F. Biraben, J. M. R. Cardoso, D. S. Covita, A. Dax, S. Dhawan, L. M. P. Fernandes, A. Giesen, T. Graf, T. W. Hänsch, P. Indelicato, L. Julien, C.-Y. Kao, P. Knowles, J. A. M. Lopes, E.-O. Le Bigot, Y.-W. Liu, L. Ludhova, C. M. B. Monteiro, F. Mulhauser, T. Nebel, R. Pohl, P. Rabinowitz, J. M. F. dos Santos, L. A. Schaller, K. Schuhmann, C. Schwob, D. Taqqu, J. F. C. A. Veloso and F. Kottmann, “Muonic Hydrogen Spectroscopy: The Proton Radius Puzzle,” *Proceedings of SPIE*, 7993, (2011). DOI: 10.1117/12.881629.
- F. Nez, A. Antognini, F.D. Amaro, F. Biraben, J.M.R. Cardoso, D. Covita, A. Dax, S. Dhawan, L. Fernandes, A. Giesen, T. Graf, T.W. Hänsch, P. Indelicato, L. Julien, C.-Y. Kao, P.E. Knowles, E. Le Bigot, Y.-W. Liu, J.A.M. Lopes, L. Ludhova, C.M.B. Monteiro, F. Mulhauser, T. Nebel, P. Rabinowitz, J.M.F. dos Santos, L. Schaller, K. Schuhmann, C. Schwob, D. Taqqu, J.F.C.A. Veloso, F. Kottmann and R. Pohl, “Is the proton radius a player in the redefinition of the International System of Units?,” *Phil. Trans. R. Soc. A* 28, 4064-4077 (2011). DOI: 10.1098/rsta.2011.0233
- R. Pohl, F. D. Amaro, A. Antognini, F. Biraben, J. M. R. Cardoso, D. S. Covita, A. Dax, S. Dhawan, L. M. P. Fernandes, A. Giesen, T. Graf, T. W. Hänsch, P. Indelicato, L. Julien, C.-Y. Kao, P. Knowles, J. A. M. Lopes, E.-O. Le Bigot, Y.-W. Liu, L. Ludhova, C. M. B. Monteiro, F. Mulhauser, T. Nebel, F. Nez, P. Rabinowitz, J. M. F. dos Santos, L. A. Schaller, K. Schuhmann, C. Schwob, D. Taqqu, J. F. C. A. Veloso and Franz Kottmann, “The size of the proton and the deuteron,” *Journal of Physics Conference Series*, 264, 012008 (2011). DOI: 10.1088/1742-6596/264/1/012008.
- Antognini, F. Biraben, J. M. R. Cardoso, D. S. Covita, A. Dax, L. M. P. Fernandes, A. L. Gouvea, T. Graf, T. W. Hänsch, M. Hildebrandt, P. Indelicato, L. Julien, K. Kirch, F. Kottmann, J. A. M. Lopes, E.-O. Le Bigot, Y.-W. Liu, C. M. B. Monteiro, F. Mulhauser, T. Nebel, F. Nez, J. M. F. dos Santos, K. Schuhmann, D. Taqqu, J. F. C. A. Veloso, A. Voss and R. Pohl, “Illuminating the proton radius conundrum: the muonic helium Lamb shift,” *Can. J. Phys.* 89, 47-57 (2011). DOI: 10.1139/P10-113.
- R. Pohl, A. Antognini, F. Nez, F. D. Amaro, F. Biraben, J. M. R. Cardoso, D. S. Covita, A. Dax, S. Dhawan, L. M. P. Fernandes, A. Giesen, T. Graf, T. W. Hänsch, P. Indelicato, L. Julien, C.-Y. Kao, P. Knowles, J. A. M. Lopes, E.-O. Le Bigot, Y.-W. Liu, L. Ludhova, C. M. B. Monteiro, F. Mulhauser, T. Nebel, P. Rabinowitz, J. M. F. dos Santos, L. A. Schaller, K. Schuhmann, C. Schwob, D. Taqqu, J. F. C. A. Veloso and F. Kottmann, “The Lamb shift in muonic hydrogen,” *Can. J. Phys.* 89, 37-45 (2011). DOI: 10.1139/P10-109

- R. Pohl, A. Antognini, F. Nez, F. D. Amaro, F. Biraben, J. M. R. Cardoso, D. S. Covita, A. Dax, S. Dhawan, L. M. P. Fernandes, A. Giesen, T. Graf, T. W. Hänsch, P. Indelicato, L. Julien, C.-Y. Kao, P. Knowles, E.-O. Le Bigot, Y.-W. Liu, J. A. M. Lopes, L. Ludhova, C. M. B. Monteiro, F. Mulhauser, T. Nebel, P. Rabinowitz, J. M. F. dos Santos, L. A. Schaller, K. Schuhmann, C. Schwob, D. Taqqu, J. F. C. A. Veloso and F. Kottmann, “The size of the proton,” *Nature* 466, issue 7303, 213-216 (2010), also appeared as the cover of the *Nature Journal* in July 2010 issue and reviewed in *News and Views*. DOI: 10.1038/nature09250.
- Antognini, K. Schuhmann et al. “Thin-Disk Yb:YAG Oscillator-Amplifier Laser, ASE, and Effective Yb:YAG Lifetime,” *IEEE J. Quant. Electr.* 45, 993 (2009).
- M. Larionov, K. Schuhmann, J. Speiser, C. Stolzenburg and A. Giesen, “Nonlinear Decay of the Excited State in Yb:YAG,” in *OSA Advanced Solid-State Photonics*, Vienna, (2005).
- F. Butze, M. A. Larionov, K. Schuhmann, C. Stolzenburg and A. Giesen, “Nanosecond pulsed thin disk Yb:YAG lasers,” in *OSA Advanced Solid-State Photonics*, Santa Fe, (2004).
- M. Larionov, F. Butze, K. Schuhmann, D. Müller and A. Giesen, “12 mJ, 1 kHz single frequency thin disk regenerative amplifier,” in *OSA Conference on Lasers and Electro-Optics*, Baltimore, (2003).